Modeling Land Surface Processes of the Midwestern United States: Predicting Soil Moisture Under a Warmer Climate

by

Jonathan M. Winter

B.S., SUNY College of Environmental Science and Forestry (2003)
S.M., Massachusetts Institute of Technology (2006)

Submitted to the Department of Civil and Environmental Engineering
in partial fulfillment of the requirements for the degree of

Doctor of Philosophy in the Field of Civil and Environmental Engineering

at the

MASSACHUSETTS INSTITUTE OF TECHNOLOGY

June 2010

Author .....
Department of Civil and Environmental Engineering
February 15, 2010

Certified by .....
Elfatih A.B. Eltahir
Professor of Civil and Environmental Engineering
Thesis Supervisor

Accepted by .....
Daniele Veneziano
Chairman, Departmental Committee for Graduate Students

Modeling Land Surface Processes of the Midwestern United States: Predicting Soil Moisture Under a Warmer Climate

by

Jonathan M. Winter

Submitted to the Department of Civil and Environmental Engineering
on February 15, 2010, in partial fulfillment of the
requirements for the degree of
Doctor of Philosophy in the Field of Civil and Environmental Engineering

Abstract

This dissertation seeks to quantify the response of soil moisture to climate change in the midwestern United States. To assess this response, a dynamic global vegetation model, Integrated Biosphere Simulator, was coupled to Regional Climate Model version 3 (RegCM3-IBIS). IBIS has several key advantages over the native surface physics scheme used in RegCM3, Biosphere-Atmosphere Transfer Scheme 1e (BATS1e), most notably superior subsurface hydrology and partitioning of runoff.

A series of 22-year numerical experiments were completed to evaluate the ability of RegCM3-IBIS and RegCM3-BATS1e to simulate the energy and water budgets of the American Midwest. Several errors in both RegCM3 and IBIS were identified and corrected, including a significant warm bias, an underestimation of root zone soil moisture, and an overestimation of incident surface shortwave radiation, net longwave radiation, and total runoff. In addition, an agricultural plant functional type was added to RegCM3-IBIS to better represent the current vegetation cover of the midwestern United States.

The sensitivity of latent heat flux to available energy plays an important role in determining the effects of climate change on regional hydrologic cycles. An intuitive framework based on the Penman-Monteith equation was developed that identifies deficiencies in model parameterizations of latent heat flux and provides a consistent comparison of the sensitivity of evapotranspiration between models and observations. For Illinois, RegCM3-IBIS and RegCM3-BATS1e tend to overestimate the sensitivity of latent heat flux to available energy in May and June, but underestimate the sensitivity of latent heat flux to available energy in the late summer.

The response of soil moisture in RegCM3-IBIS and RegCM3-BATS1e to a surrogate climate change scenario and the ECHAM5 GCM A1B climate change scenario was evaluated. RegCM3-IBIS and RegCM3-BATS1e simulate increased rainfall, evapotranspiration, and runoff during the spring and summer. Soil moisture is unchanged throughout the growing season as enhanced precipitation offsets increased evaporative demand. Negligible changes in soil moisture are robust across surface physics schemes, large-scale forcings, and convective closure assumptions.

Thesis Supervisor: Elfatih A.B. Eltahir
Title: Professor of Civil and Environmental Engineering

Acknowledgments

I would first and foremost like to acknowledge the contributions of my advisor, Elfatih Eltahir, to all aspects of this research. My committee, which includes Jeremy Pal, Rafael Bras, and Adam Schlosser, provided key insights and valuable feedback on my work. Collaborations with Jeremy Pal and Filippo Giorgi were essential to the early stages of this research. Past and present members of the Eltahir group have been instrumental in assisting me, especially Anke Hildebrandt and Marc Marcella. I would like to thank the broader Parsons Laboratory community for helping shape my MIT experience. I would also like to acknowledge Charles Kroll and Charles Driscoll for encouraging me to pursue graduate studies.

I am fortunate enough to have an amazing network of family and friends. My parents, Richard and Marlene, have always been there for me; my girlfriend, Teresa, has helped me every step of the way; and the rest of my family has offered continuous support. Finally, I would like to thank my friends, who always supplied welcome distractions from work.

This research was funded by the National Science Foundation (Award Number: EAR-04500341), the Linden Fellowship, the Martin Family Fellowship, and the International Centre for Theoretical Physics.

Contents

List of Figures

List of Tables

Chapter 1

Introduction

1.1 Background

In January 1981, the *New York Times* article "Down on the Farm, Higher Prices" predicted a 10%-15% increase in the average U.S. consumer food bill resulting from a lack of rainfall in 1980. In 1988, a severe drought during the spring and summer reduced crop yields in the United States by approximately 37%, prompting a $3-billion Congressional bailout for farmers [Rosenzweig et al., 2001]. Agricultural productivity is strongly correlated with soil moisture (Figure 1-1), and as the world's food supply continues to be taxed by population growth and rapidly developing economies, a greater percentage of arable land will need to be utilized and land currently producing food must become more efficient (Figure 1-2) [Harrison et al., 2002].

The need for efficient use of arable land is clear; however, note that the estimates in Figure 1-2 assume a static environment and climate. Even in regions of the world where weather forecasts and climate prediction are most accurate, the fluctuations in rainfall (Figure 1-3) and temperature that dictate the productivity of agricultural areas are largely unpredictable beyond synoptic timescales at a useful resolution. Variability, both natural (e.g. El Niño, volcanic activity) and anthropogenic (e.g. CO_2, vegetation change), make the task of optimizing the use of arable land problematic.

Numerical modeling is one approach used to gain a better understanding of climate processes. In 1969, Manabe developed a model that explicitly integrated the effects of hy-

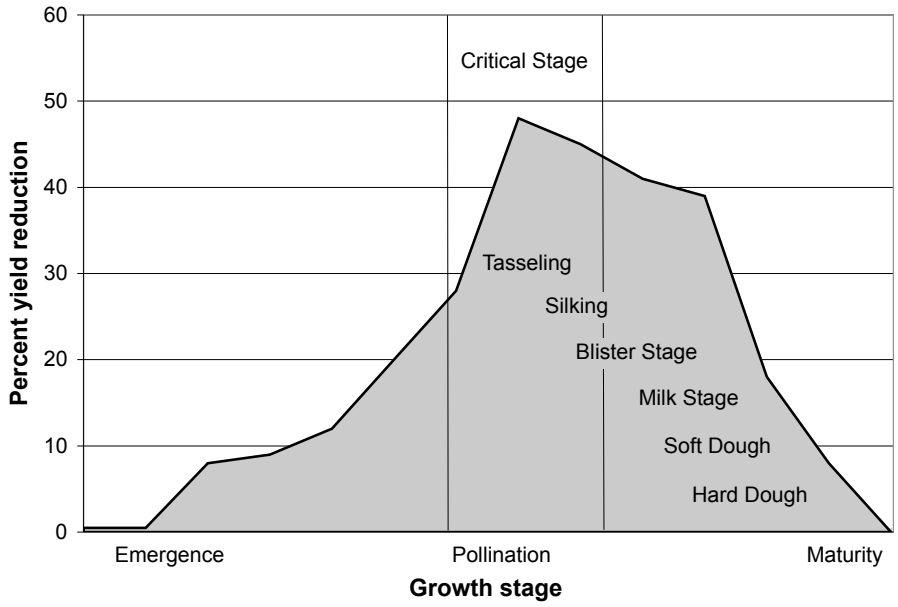

Figure 1-1: Reduction in corn yield due to moisture stress. Plants were subjected to four days of visible wilting [Claassen, 1995].

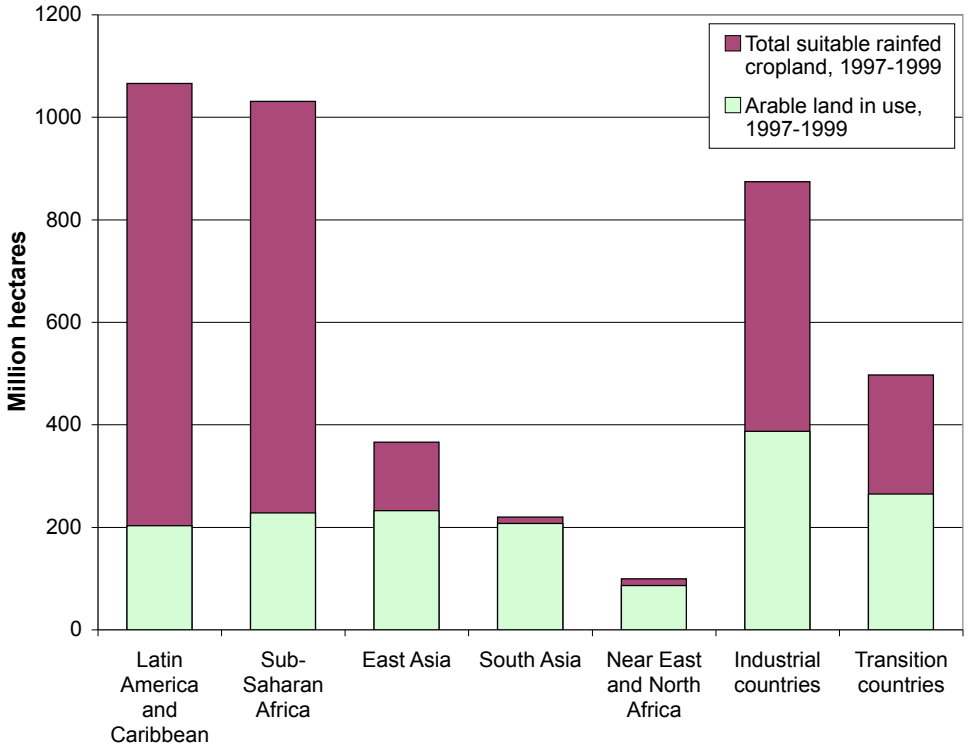

Figure 1-2: Cropland in use and total suitable land [Harrison et al., 2002].

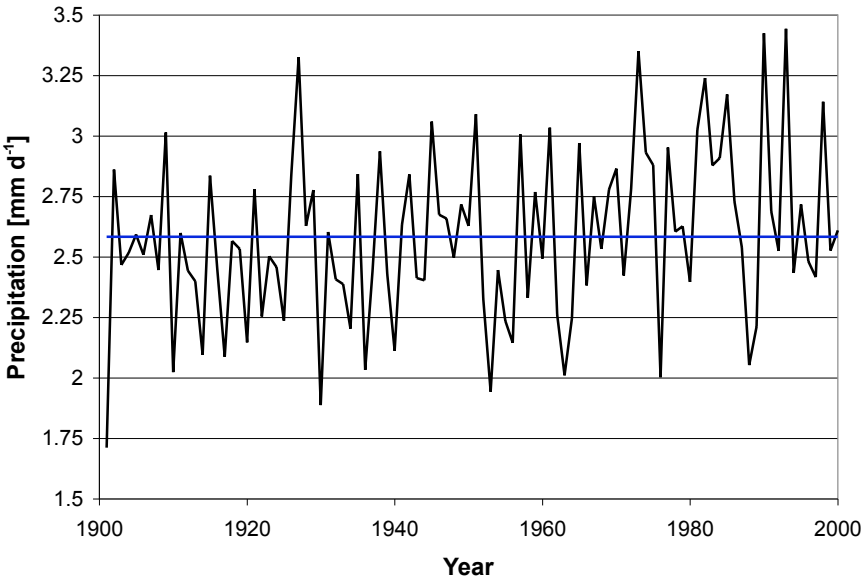

Figure 1-3: Annually-averaged precipitation over the Midwest (91.5°W:87.5°W, 37.0°N:42.5°N) for the years 1901-2000 [Mitchell et al., 2004].

drology into the Geophysical Fluid Dynamics Laboratory's (GFDL) General Circulation Model (GCM). Since this time, advances in computational power and the understanding of surface physics have led to the creation of many models capable of representing the coupled land-atmosphere system with increasing accuracy and detail. However, while GCMs provide fully coupled predictions of future climate, because of their large horizontal grid spacing ($\approx$200 km), they are unable to simulate changes in climate at fine spatial scales [Giorgi, 1990].

Assessing the local and regional impacts of changing climate is vital to formulating intelligent adaptation and mitigation strategies for the agricultural industry. This is reflected in the demands for information by policymakers. The summary from the twenty-eighth session of the Intergovernmental Panel on Climate Change (IPCC) in April 2008 states that: "Another area where substantial work needs to be done by the research community to provide adequate inputs for the IPCC is in respect to the regional aspects of climate modeling." This sentiment was echoed by the demand for IPCC Technical Reports: "Topics for Special Reports which were most frequently mentioned were regional assessments of adaptation and mitigation and an update of the 1997 'The Regional Impacts of Climate Change: An Assessment of Vulnerability'."

Regional climate models (RCMs) are used to downscale GCM output to societally relevant scales [Leung et al., 2003]. Though limited in predictive ability by the use of boundary conditions and prescribed sea surface temperatures (SSTs), RCMs are able to simulate important processes at sub-GCM resolutions and produce predictions of future climate on a smaller horizontal grid scale ($\approx$50 km). For example, Pal et al. [2004] used a regional climate model to quantify and describe European summer drying projected by the Prediction of Regional Scenarios and Uncertainties for Defining European Climate Change Risks and Effects (PRUDENCE) project, and Bell et al. [2004] used an RCM to assess regional changes in extreme climatic events over California.

However, from the "bucket model" of Manabe to state-of-the-science global and regional circulation models, numerical modeling of complex natural systems is inexact. This fact is clearly illustrated by the need for ensemble forecasts in numerical weather prediction and the range of year 2100 temperatures presented in the IPCC Third Assessment Report

(Figure 1-4).

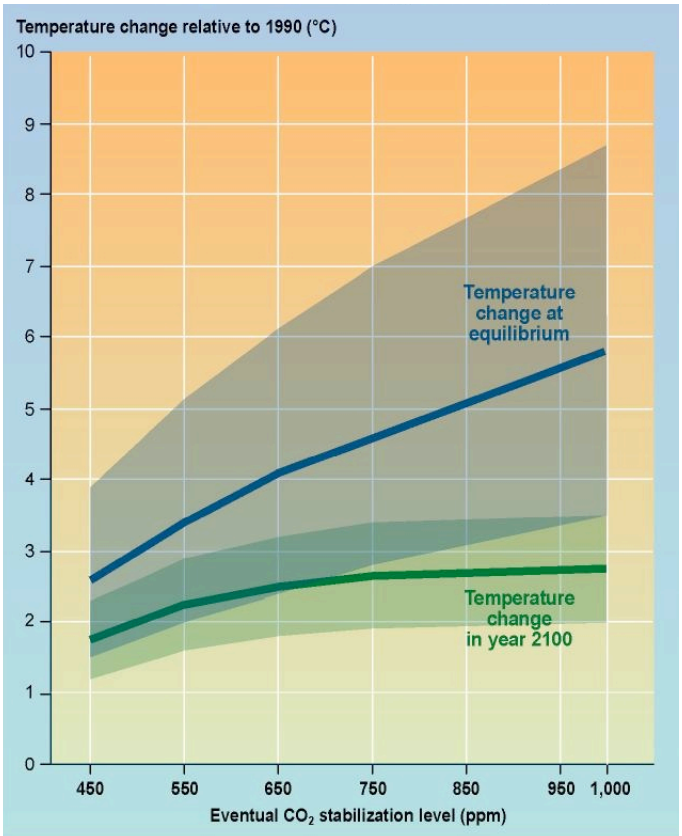

Figure 1-4: Uncertainty in global average temperature predictions from the 2001 IPCC Third Assessment Report [Folland et al., 2001].

The reason for this is simple: Error is implicit in all modeling results. Even given a perfect model (one that exactly and completely describes a system) and perfect initial conditions (a full and flawless assessment of the current state of a system), numerical inaccuracies in computation will skew results. In reality neither perfect initial conditions nor a perfect model exist. In surface physics models, the description of a significant portion of environmental processes are parameterizations: approximations devised to represent the true dynamics of the system best given limited knowledge and computational resources.

From this problem emerges doubt regarding the performance and response of models. One uncertainty in particular, the sensitivity of the coupled land-atmosphere system to an increase in available energy, is especially salient as it directly impacts the predicted effects of climate change.

1.2 Problem Statement

Climate change is likely to accelerate the hydrologic cycle, leading to enhanced global precipitation and evapotranspiration. In areas where the increase in evapotranspiration significantly exceeds that of precipitation, drought conditions will become more common. This could have extensive impacts on the entire world community if the newly created droughts occur in the midwestern United States or southern Europe, regions of substantial agricultural productivity. However, if the increase in precipitation exceeds that of evapotranspiration, little or no drying will occur.

1.3 Thesis Structure

To gain a more complete understanding of land surface processes and the way in which agricultural areas respond to climate change, Integrated Biosphere Simulator (IBIS) was coupled to Regional Climate Model version 3 (RegCM3). The ability of RegCM3-IBIS and RegCM3 with its native surface physics scheme, Biosphere-Atmosphere Transfer Scheme 1e (RegCM3-BATS1e), to simulate the current hydroclimatology of the American Midwest was tested extensively. RegCM3-IBIS and RegCM3-BATS1e were then forced using future climate scenarios to examine the impact of climate change on agricultural areas of the midwestern United States. The response of each component of the water and energy budgets relevant to the simulation of soil moisture over the American Midwest (Fig. 1-5) were explored.

Chapter 2 introduces RegCM3, BATS1e, IBIS, and describes the coupling of IBIS to RegCM3. Chapter 3 examines the ability of RegCM3-IBIS and RegCM3-BATS1e to simulate the hydroclimatology of the midwestern United States. Chapter 4 assesses the sensitivity of latent heat flux to available energy in regional climate models and observations. Chapter 5 explores the water and energy budgets of the American Midwest under a warmer climate. Chapter 6 summarizes results and provides guidance for future work.

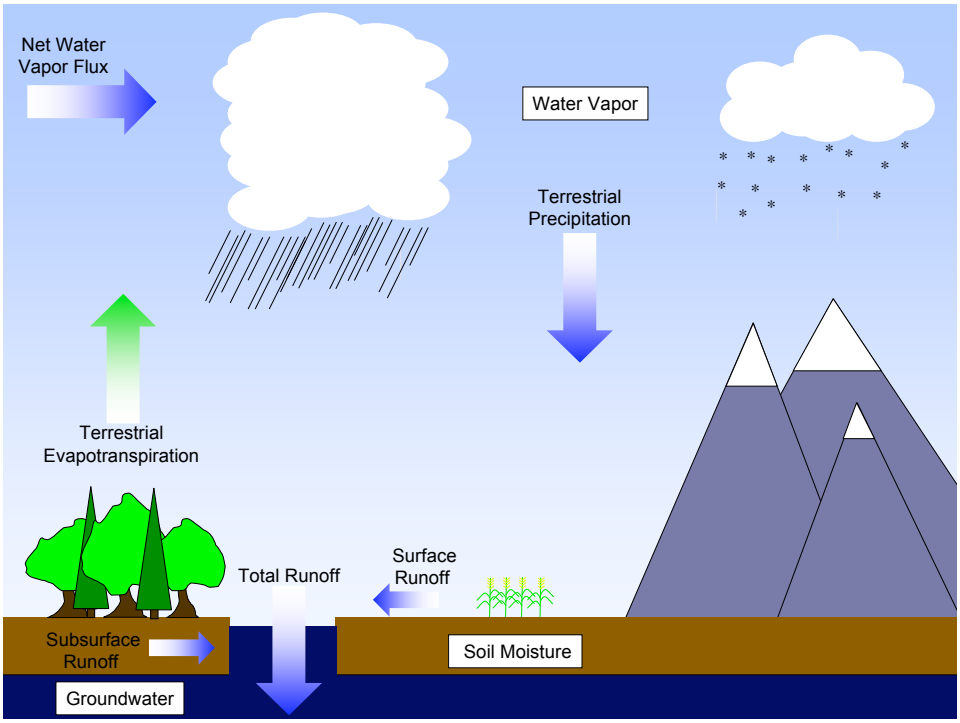

Figure 1-5: Components of the hydrologic cycle relevant to the simulation of soil moisture over the American Midwest.

Chapter 2

Model Description and Development

2.1 Regional Climate Model Version 3

Regional Climate Model version 3 (RegCM3) was chosen for this study because of its ability to accurately simulate the energy and water dynamics of North America [Pal, 2001]. Additionally, RegCM3 has been used in a variety of climate studies, including an exploration of the sensitivity of regional climate to deforestation in the Amazon basin [Eltahir and Bras, 1994], the implementation of a large-scale cloud/precipitation scheme and model verification using satellite and station based datasets [Pal et al., 2000], an examination of the effects of subcloud evaporation over the Middle East [Marcella and Eltahir, 2008], and an assessment of the land surface coupling of the West African monsoon [Steiner et al., 2009].

RegCM3 is a 3-dimensional, sigma-coordinate, hydrostatic, compressible regional climate model originally created at the National Center for Atmospheric Research (NCAR) and currently maintained at the International Centre for Theoretical Physics (ICTP) [Pal et al., 2007]. RegCM3 is a descendant of NCAR RegCM, which was developed from the work of Dickinson et al. [1989], Giorgi and Bates [1989], and Giorgi [1990]. RegCM was primarily built using the dynamical core of the Penn State University/NCAR Mesoscale Model version 4 [Anthes et al., 1987].

Key components of RegCM3 include: the atmospheric radiation transfer computations of NCAR Community Climate Model version 3 [Kiehl et al., 1996]; the planetary bound-

ary layer (PBL) scheme of Holtslag et al. [1990]; Biosphere-Atmosphere Transfer Scheme 1e (BATS1e) for land surface processes [Dickinson et al., 1993]; the ocean flux parameterization of Zeng et al. [1998]; Subgrid Explicit Moisture Scheme (SUBEX), a resolvable scale (non-convective) cloud and precipitation formulation created by Pal et al. [2000]; and four convection parameterization packages, the Betts-Miller cumulus convection scheme [1986], the Emanuel scheme [1991], the Grell scheme [1993], and the Kuo scheme of Anthes [1977].

More information on the history, parameterizations, and applications of RegCM3 can be found in Winter [2006].

2.2 Biosphere-Atmosphere Transfer Scheme 1e

Biosphere-Atmosphere Transfer Scheme 1e (BATS1e) is a comprehensive model of land surface processes that can be run offline, coupled to a GCM, or coupled to RegCM3 [Dickinson et al., 1993]. BATS1e performs seven major tasks, the overall structure of which is shown in Figure 2-1.

The first function of BATS1e is to assign vegetation and soil characteristics to each grid cell. Vegetation is assigned using the United States Geological Survey (USGS) Global Land Cover Characterization (GLCC) dataset [USGS, 1997]. In BATS1e, soil characteristics are assigned by vegetation type. For example, a desert grid point would be assigned a coarse, sandy soil, while for a deciduous forest, a finer soil with silt and clay would be specified.

Second, BATS1e sets the albedos of sea ice, bare soil, and vegetation. The albedo of a vegetated surface is determined by the vegetation type (Table 2.1), with albedos for each type drawn from a variety of studies, mainly Monteith [1976]. Soil albedo, A_{LBG}, is determined in part by soil type, but is also dependent on soil moisture.

$$A_{LBG} = A_{LBGO} + \Delta\alpha_g(S_{sw}) \tag{2.1}$$

A_{LBGO} is the albedo for a saturated soil and $\Delta\alpha_g(S_{sw})$ is a function of the surface soil

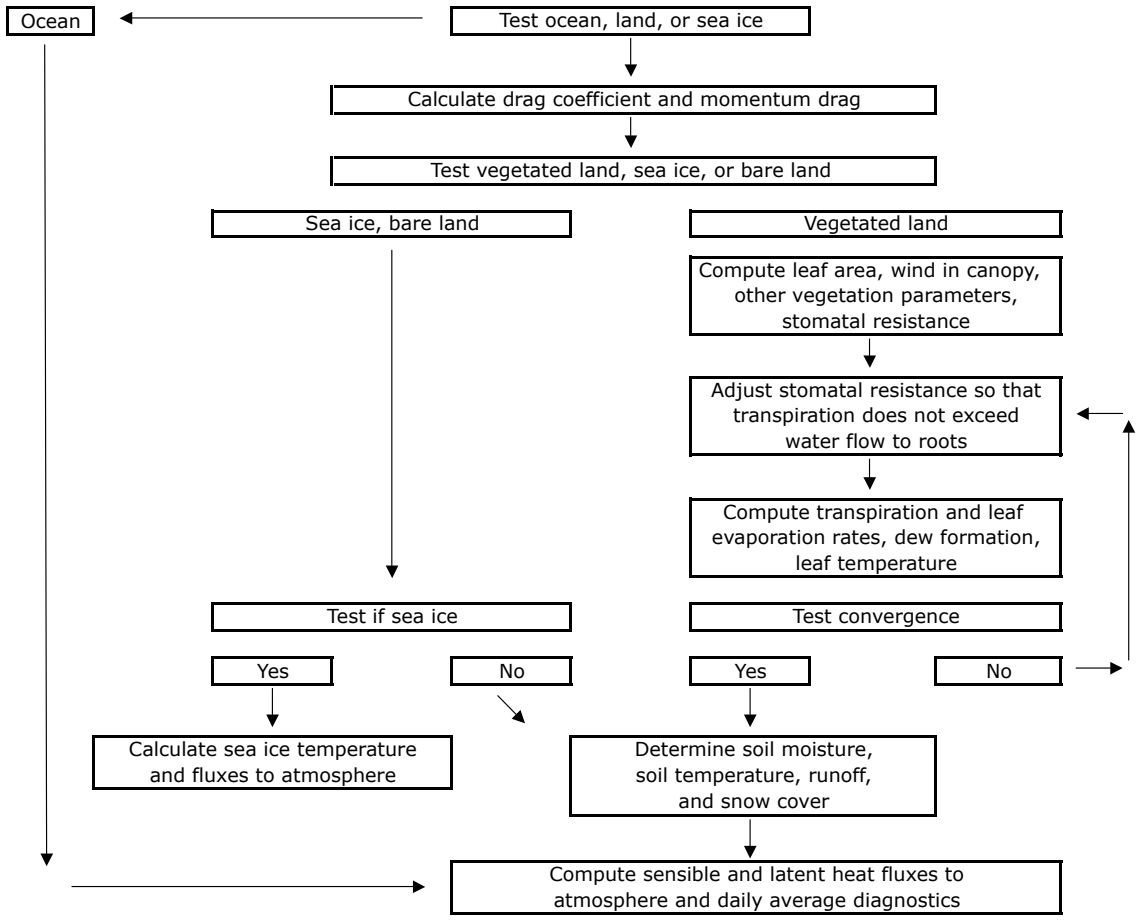

Figure 2-1: Flow chart for Biosphere-Atmosphere Transfer Scheme 1e (BATS1e) [Dickinson et al., 1993].

Table 2.1: Vegetation types for BATS1e [Dickinson et al., 1993].

Land Cover	Class	Vegetation albedo $\lambda < 0.7$ μm	Vegetation albedo $\lambda > 0.7$ μm
Crop/Mixed Farming	1	0.10	0.30
Short Grass	2	0.10	0.30
Evergreen Needleleaf	3	0.05	0.23
Deciduous Needleleaf	4	0.05	0.23
Deciduous Broadleaf	5	0.08	0.28
Evergreen Broadleaf	6	0.04	0.20
Tall Grass	7	0.08	0.30
Desert	8	0.20	0.40
Tundra	9	0.10	0.30
Irrigated Crop	10	0.08	0.28
Semi-Desert	11	0.17	0.34
Ice Cap/Glacier	12	0.80	0.60
Bog/Marsh	13	0.06	0.18
Inland Water	14	0.07	0.20
Ocean	15	0.07	0.20
Evergreen Shrub	16	0.05	0.23
Deciduous Shrub	17	0.08	0.28
Mixed Woodland	18	0.06	0.24
Forest/Field Mosaic	19	0.06	0.18
Water/Land Mixture	20	0.06	0.18

water content, S_{sw}, and upper soil layer depth, which gives the increase of albedo due to the dryness of the surface soil [Dickinson et al., 1993].

The third major computation that BATS1e performs is the surface drag coefficient, C_D, which is a function of the drag coefficient for neutral stability, C_{DN}, and the surface bulk Richardson number, Ri_B [Dickinson et al., 1993].

$$\begin{aligned} C_D &= C_{DN}(1 + 24.5(-C_{DN}Ri_B)^{1/2}) && Ri_B < 0 \\ &= C_{DN}/(1 + 11.5Ri_B) && Ri_B > 0 \end{aligned} \tag{2.2}$$

C_{DN} is calculated from mixing-length theory:

$$C_{DN} = \left[\frac{k}{ln(z_1/z_0)}\right]^2, \tag{2.3}$$

where k is the von Karman constant, z_0 is the roughness length, and z_1 is the height of the lowest model level [Dickinson et al., 1993].

All plant water budget calculations, including foliage and stem water fluxes, resistance limited transpiration, and precipitation interception are handled by the fourth set of calculations. A simplistic scheme is used in conjunction with the drip formulae of Massman [1980] to calculate rainfall interception.

$$\tilde{L}_w = \left(\frac{W_{dew}}{W_{DMAX}}\right)^{2/3} \tag{2.4}$$

$\tilde{L}_w$ is the fractional area of leaves covered by water, W_{dew} is the total water intercepted by the canopy, and W_{DMAX} is the maximum amount of water the canopy can hold.

In BATS1e, interception both allows evaporation from the wet leaf surfaces while simultaneously suppressing transpiration from leaves [Dickinson et al., 1993]. Root resistance follows from the work of Federer [1979], Hillel [1980], and Molz [1981]. The two aforementioned factors, along with specific environmental variables, such as solar radiation, temperature, soil moisture, and vapor pressure deficit are weighted and combined following the methodology of Jarvis [1976] and Hinckley et al. [1978] to find stomatal resistance r_s, and are ultimately used in a similar manner as presented by Monteith [Thom

and Oliver, 1977] to calculate transpiration [Dickinson et al., 1993].

$$r_s = r_{smin} \times R_f \times S_f \times M_f \times V_f \tag{2.5}$$

Here, r_{smin} is the minimum stomatal resistance, R_f gives the dependence of r_s on solar radiation, S_f is the seasonal temperature factor, M_f is a function of soil moisture and root uptake of water, and V_f gives the dependence of r_s on vapor pressure deficit [Dickinson et al., 1993].

Transpiration, E_{tr}, is calculated by the fifth set of equations. Here, a scheme similar to the one-layer formulation credited to Monteith is used [Thom and Oliver, 1977]. Differences include the ability to have a partially wetted canopy, as well as explicitly separate equations and resistances for energy fluxes between foliage and air within the canopy, and between air within the canopy and air above the canopy [Dickinson et al., 1993]. E_{tr} is given by:

$$E_{tr} = \delta(E_f^{WET}) L_d \left(\frac{r_{la}}{r_{la} + r_s} \right) E_f^{WET}, \tag{2.6}$$

where r_{la} is the resistance for heat and water vapor flux, E_f^{WET} is the evaporation rate of water from leaves and stems per unit wetted area, L_d is the fraction of foliage allowed to transpire, and δ is a step function that is 1 or 0 when the argument E_f^{WET} is positive or negative, respectively [Dickinson et al., 1993]. Foliage temperature is calculated iteratively, and is mainly dependent on the transfer of heat and moisture within the canopy [Dickinson et al., 1993].

The sixth task computes soil, snow, and sea ice temperature as dictated by radiation inputs, soil/snow heat capacity, and thermal conductivity [Dickinson et al., 1993]. The soil temperature model is an adaptation of the force restore method of Deardorff [1978], and is explicitly documented in Dickinson and Sellers [1988]. A relatively simple scheme handles sea ice, and primarily models a constant heat conduction from the ocean, following the works of Maykut and Untersteiner [1971], and Semtner Jr. [1976]. Surface soil

temperature, T_{g1}, is calculated by:

$$C\Delta t\frac{\partial T_{g1}}{\partial t} + 2AT_{g1} = B. \tag{2.7}$$

A is a function of the diurnal frequency, B is a term proportional to net surface heating, C is dependent on the thermal inertia of freezing, and Δt is the timestep in seconds.

Finally, the last set of formulae determine soil moisture, evaporation, surface runoff, and groundwater runoff. Soil is represented by three reservoirs (layers) in BATS1e, a 10 cm surface soil layer, a 1-2 m root layer, and a 3 m deep soil layer. As precipitation is applied to the soil (via snowmelt or rain), it is either partitioned to runoff or infiltration, and is then allowed to move between the three reservoirs based predominantly on vegetation and soil properties [Dickinson et al., 1993]. Bare soil evaporation is parameterized using a scheme dependent on the aerodynamic characteristics of the soil surface and the hydraulic conductivity [Dickinson et al., 1993]. Determining runoff and infiltration is primarily a function of soil moisture, where little runoff occurs from a soil at field capacity, and almost all water is sent to runoff for a saturated soil [Dickinson et al., 1993].

Infiltration is dictated by diffusivity, D:

$$D = K_{wo}\phi_o B s^{B+2}. \tag{2.8}$$

K_{wo} is the hydraulic conductivity, s is the volume of water divided by the volume of water at saturation, B is the Clapp and Hornberger [1978] exponent, and ϕ_o is the minimum soil suction [Dickinson et al., 1993]. At larger length scales infiltration can be influenced by the subsoil drainage [Dickinson et al., 1993]. Runoff, R_s, is given by:

$$\begin{aligned} R_s &= (\rho_w/\rho_{wsat})^4 G && T_{g1} \geq 0^\circ C \\ &= (\rho_w/\rho_{wsat}) G && T_{g1} < 0^\circ C, \end{aligned} \tag{2.9}$$

where ρ_w is the soil water density weighted toward the top layer, ρ_{wsat} is the saturated soil water density, and G is the net water applied to the surface [Dickinson et al., 1993].

2.3 Integrated Biosphere Simulator

Integrated Biosphere Simulator (IBIS), which was developed by Foley et al. [1996] at the University of Wisconsin-Madison, is a terrestrial biosphere model that uses a modular, physically consistent framework to perform integrated simulations of water, energy, and carbon fluxes. A summary of the model's core features, as well as descriptions of some parameterizations and formulae are included below. Full documentation of IBIS can be found in Foley et al. [1996]. Additionally, a complete description of the biophysical processes contained in IBIS is provided by Pollard and Thompson [1995].

IBIS includes four modules organized with respect to their temporal scale: land surface processes (energy, water, carbon, and momentum balance), soil biogeochemistry (carbon and nitrogen cycling from plants through soil), vegetation dynamics, and vegetation phenology (Figure 2-2).

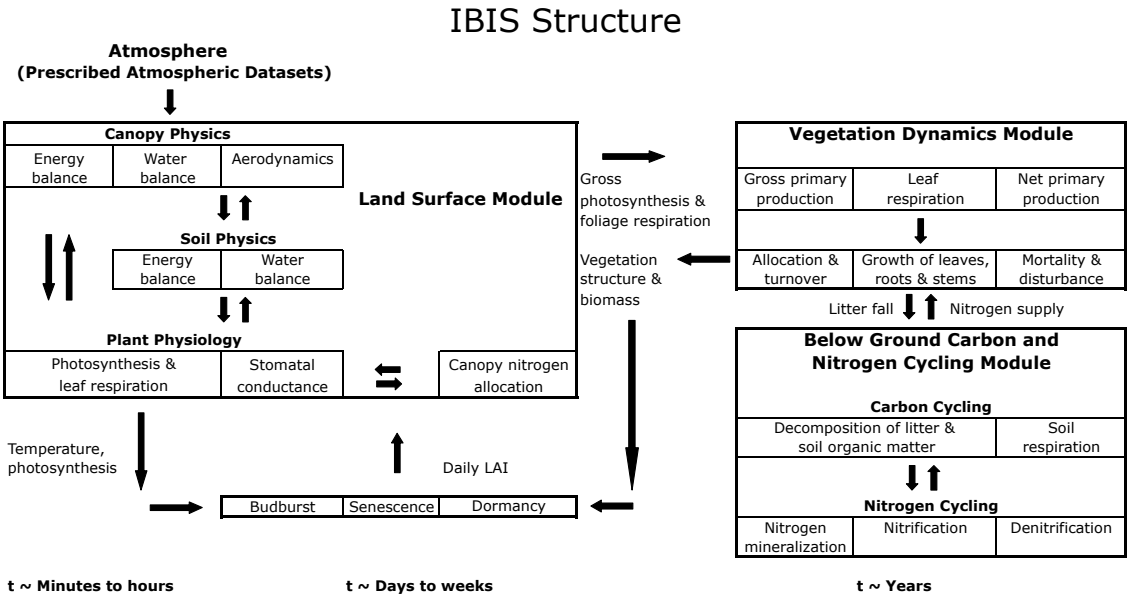

Figure 2-2: Schematic of IBIS. The characteristic timescales of the processes are indicated at the bottom of the figure [Kucharik et al., 2000].

2.3.1 Land Surface Physics

Based on Land Surface Transfer model [Thompson and Pollard, 1995a,b], the IBIS land surface module simulates energy, water, carbon, and momentum balances of the soil-

vegetation-atmosphere system [Kucharik et al., 2000]. The land surface module contains two vegetation layers, three snow layers, and up to six soil layers. This allows the land surface module to resolve changes in state variables both within the lower (shrubs, grasses) and upper (trees) canopies, as well as each individual layer of soil and snow [Kucharik et al., 2000]. Accordingly, in all formulae presented in this chapter, the subscripts u, s, and l refer to upper canopy leaves, upper canopy stems, and lower canopy vegetation, respectively. The subscripts a, 1, 12, 2, 3, 34, 4 are heights that reference the atmospheric forcing height, top of the upper canopy, middle of the upper canopy, bottom of the upper canopy, top of the lower canopy, middle of the lower canopy, bottom of the lower canopy, respectively [Pollard and Thompson, 1995].

IBIS uses separate calculations for solar and infrared radiation. Solar radiation is subdivided into two wavelength bands (visible from 0.4 μm to 0.7 μm and near infrared from 0.7 μm to 4.0 μm) within each vegetation layer. The amount of infrared radiation (IR) reflected, absorbed, and transmitted by a plant is a function of its foliage density and I_b, the net upward flux of IR from the surface.

$$I_b = (1 - f_u)I^{\uparrow} + f_u[(1 - \epsilon_u)(1 - \epsilon_s)I^{\uparrow} + \epsilon_u \sigma T_u^4 + \epsilon_s(1 - \epsilon_u)\sigma T_s^4 \tag{2.10}$$

Here, f_u is fractional cover, $I^{\uparrow}$ is the upward IR flux between the upper and lower canopies, ϵ_u and ϵ_s are emissivities, σ is the Stefan-Boltzmann constant, and T_u and T_s are temperatures [Foley et al., 1996].

Within each canopy layer, turbulent fluxes and wind speed are calculated using a diffusive model, the general solution of which is:

$$u(z)^2 = Ae^{\lambda z} + Be^{-\lambda z}. \tag{2.11}$$

In this formula, $u(z)$ is mean horizontal wind speed at height z, λ is a function of the effective drag coefficient and effective diffusion coefficient within the canopy, and A and B are arbitrary constants determined by boundary conditions [Pollard and Thompson, 1995].

Above and between layers, $u(z)$ is modeled using mixing-length logarithmic profiles

[Foley et al., 1996]. Between z_a, z_1:

$$u(z) = \sqrt{\frac{\tau}{\rho}} \frac{1}{k} ln \left(\frac{z - d_u}{z_{0u}} \right) F_{mu}^{-1/2} \tag{2.12}$$

and between z_2, z_3:

$$u(z) = \sqrt{\frac{\tau}{\rho}} \frac{1}{k} ln \left(\frac{z - d_l}{z_{0l}} \right) F_{ml}^{-1/2}, \tag{2.13}$$

where τ is the horizontal wind stress; ρ is air density neglecting height variation; k is the von Karman constant; d_u, d_l are zero-plane displacement heights; z_{0u}, z_{0l} are roughness lengths; and F_{mu}, F_{ml} are non-neutral stratification corrections [Pollard and Thompson, 1995]. Below the lowest canopy layer an empirically derived linear function is used to describe wind speed [Kucharik et al., 2000].

Evapotranspiration is calculated as the sum of evaporation from the soil surface, evaporation from water intercepted by the canopy, and plant transpiration. Evaporation from the soil surface is a function of wind speed and the relative humidity at the surface, which is itself dependent on soil temperature and soil moisture [Foley et al., 1996]. Evaporation from intercepted precipitation is simulated using a parameterization that describes the cascading of rain and snow through the canopy. Transpiration is calculated independently for each plant functional type (PFT), and depends primarily on stomatal conductance, a variable explained in more detail below. Evapotranspiration is expressed as:

$$E_u = \rho s_u \left[f_u^{wet} + \frac{(1 - f_u^{wet}) f_u^{sto}}{1 + r_u s_u} \right] (q_{sat}(T_u) - q_{12}), \tag{2.14}$$

$$E_s = \rho s_s f_s^{wet} (q_{sat}(T_s) - q_{12}), \tag{2.15}$$

$$E_l = \rho s_l \left[f_l^{wet} + \frac{(1 - f_l^{wet}) f_l^{sto}}{1 + r_l s_l} \left(\frac{LAI_l}{LAI_l + SAI_l} \right) \right] \times (q_{sat}(T_l) - q_{34}), \tag{2.16}$$

where ρ is the density of near surface air; s_u, s_s, s_l are transfer coefficients; f_u^{wet}, f_s^{wet},

f_l^{wet} are wetted fractions; f_u^{sto}, f_l^{sto} are 0.5 for leaves with stomata on one side and 1 for leaves with stomata on both sides; r_u, r_l are stomatal resistances; $q_{sat}(T_u)$, $q_{sat}(T_s)$, $q_{sat}(T_l)$ are saturation specific humidities at temperatures T_u, T_s, T_l, respectively; q_{12}, q_{34} are specific humidities; LAI_l is the leaf area index; and SAI_l is the stem area index [Pollard and Thompson, 1995].

To capture the diurnal and seasonal cycles of moisture and temperature in the soil, each layer is independently resolved and defined by temperature, fractional liquid water content relative to ice-free pore space (soil moisture), and fractional ice content relative to total pore space (soil ice) [Foley et al., 1996]. Time dependent changes in soil moisture are calculated using Richard's equation, and Darcy's law is used to diagnose the vertical flux of water. Soil matric potentials, required by Darcy's equations, are derived from soil moisture and texture using the parameterization of Clapp and Hornberger [1978]. The soil water budget is defined by the rate of infiltration, evaporation of water from the surface, transpiration, and redistribution of water within the soil profile [Kucharik et al., 2000]. The lower boundary of the soil allows no heat or water diffusion, and drainage is a user-defined function bounded by no drainage and free drainage. The attributes of snow layers (temperature, fractional coverage, and total snow thickness) are calculated using a thermodynamic model.

Also included in the land surface module is canopy physiology, which regulates water vapor and carbon dioxide fluxes between the vegetation and atmosphere. While most surface physics models use empirical relationships between light, temperature, and water vapor pressure to determine the photosynthetic rate and stomatal conductance, IBIS employs a mechanistically based approach for photosynthesis [Farquhar et al., 1980; Farquhar and Sharkey, 1982] and stomatal conductance [Ball et al., 1986; Lloyd, 1991; Lloyd and Farquhar, 1994; Friend, 1995; Leuning, 1995] . Consistent with the physics in the aforementioned papers, photosynthesis in IBIS is a function of absorbed light, leaf temperature, CO_2 concentration in the leaf, and the Rubisco enzyme capacity for photosynthesis; stomatal conductance is dependent on photosynthetic rate, CO_2 concentration, and water vapor concentration [Foley et al., 1996].

The gross rate of photosynthesis per unit leaf, A_g, for C_3 plants is assumed to be limited

by light, Rubisco activity, or utilization of triose phosphate, expressed as:

$$A_g \approx min(J_e, J_c, J_s). \tag{2.17}$$

The light-limited rate of photosynthesis, J_e, is:

$$J_e = \alpha_3 Q_p \left(\frac{C_i - \Gamma_*}{C_i + 2\Gamma_*} \right), \tag{2.18}$$

where α_3 is the intrinsic quantum efficiency for CO_2 uptake in C_3 plants, Q_p is the flux density of photosynthetically active radiation absorbed by the leaf, C_i is the concentration of CO_2 in the intercellular air spaces of the leaf, and Γ_* is the compensation point for gross photosynthesis.

$$\Gamma_* = \frac{[O_2]}{2\tau} \tag{2.19}$$

In Equation 2.19, $[O_2]$ is the concentration of atmospheric oxygen and τ describes the partitioning of enzyme activity to carboxylase or oxygenase function [Foley et al., 1996]. The Rubisco-limited rate of photosynthesis, J_c, is given by:

$$J_c = \frac{V_m(C_i - \Gamma_*)}{C_i + K_c \left(1 + \frac{[O_2]}{K_o}\right)}, \tag{2.20}$$

where V_m is the maximum capacity of Rubisco to perform the carboxylase function, K_c is the Michaelis-Menten coefficient for CO_2, and K_o is the Michaelis-Menten coefficient for O_2 [Foley et al., 1996]. Finally, the triose phosphate utilization-limited photosynthetic rate J_s, which restricts photosynthesis during periods of high intercellular CO_2 and irradiance, is:

$$J_s = 3T \left(1 - \frac{\Gamma_*}{C_i}\right) + \frac{J_p \Gamma_*}{C_i}. \tag{2.21}$$

T is the rate of triose phosphate utilization and J_p is a function of empirical constants and the other two limiting photosynthetic rates [Foley et al., 1996]. To allow for colimitation, a

quadratic equation is used to link the three photosynthetic rates [Foley et al., 1996].

Photosynthesis in C_4 plants follows a similar structure.

$$A_g \approx min(J_i, J_e, J_c) \tag{2.22}$$

The compensation point of C_4 plants is assumed to be zero, so the limiting photosynthetic rates are reduced to:

$$J_i = \alpha_4 Q_p, \tag{2.23}$$

$$J_e = V_m, \tag{2.24}$$

$$J_c = kC_i, \tag{2.25}$$

where J_i is the light-limited rate of photosynthesis, J_e is the Rubisco-limited rate of photosynthesis, J_c is the CO_2-limited rate of photosynthesis, α_4 is the intrinsic quantum efficiency for CO_2 uptake in C_4 plants, and k is a parameter based on V_m [Foley et al., 1996]. The final gross photosynthetic rate is again calculated by a quadratic equation that combines the above three rates.

Stomatal conductance, g_s, of water vapor is given by:

$$g_s = \frac{mA_n}{(C_s - \Gamma_*)\left(1 + \frac{D_s}{D_o}\right)} + b. \tag{2.26}$$

A_n is the net leaf assimilation rate, C_s is the CO_2 concentration at the leaf surface, D_s is the water vapor mole fraction difference between the leaf and the air, D_o is a reference value, and m and b are the slope and intercept of the conductance-photosynthesis relationship [Foley et al., 1996].

The following two equations link photosynthesis and stomatal conductance via the CO_2

concentration:

$$C_s = C_a - \frac{A_n}{g_b}, \tag{2.27}$$

$$C_i = C_s - \frac{1.6A_n}{g_s}, \tag{2.28}$$

where C_a is the atmospheric mole fraction of CO_2 and g_b is the CO_2 boundary layer conductance [Foley et al., 1996]. This framework has been tested extensively against gas exchange measurements by Delire and Foley [1999].

To account for shading within and between the two canopy layers, the formulation of Norman [1993] is employed. Individual calculations of photosynthesis and stomatal conductance are computed using the shaded and sunlit fractions of each PFT and then averaged (weighted average) to find fluxes for the entire canopy.

2.3.2 Vegetation Phenology

Run daily, the vegetation phenology module contains a set of rule-based formulations that describe the relationship between seasonal changes in vegetation and seasonal climatic conditions. This encompasses the annual leaf cycle of deciduous trees, the response of trees to drought, and changes in the physiological activity of evergreens [Kucharik et al., 2000]. Leaves of winter-deciduous plants are stripped when the daily average temperature falls below a critical threshold and repopulated when the temperature rises in spring [Foley et al., 1996]. The equation for senescence, assuming that the average 10-day temperature is less than the temperature threshold is given by:

$$L_{disp} = max(0.0, T_{thresh} - d_{frac}), \tag{2.29}$$

where the temperature threshold, T_{thresh}, is:

$$T_{thresh} = max(0, T_c + 5^{\circ}C). \tag{2.30}$$

L_{disp} is a fraction used to update leaf area index (LAI) and canopy fractions, T_c is the coldest average monthly temperature, and d_{frac} is the inverse of the number of days to affect phenology change [Foley et al., 1996].

The leaves of drought-deciduous plants (tropical deciduous trees) are removed during the least two productive months of the year based on the previous year's carbon cycle.

2.3.3 Vegetation Dynamics

At initialization, one of fifteen biomes is specified for each land point in an IBIS simulation using a vegetation input dataset. Then, based on specific climate variables, also contained in input datasets, vegetation cover for both the upper and lower canopies is assigned using a distribution of one or more of the twelve PFTs (Table 2.2).

Table 2.2: Vegetation types for IBIS [Foley et al., 1996].

Biome	Plant Functional Type	Index
Tropical Evergreen	Tropical Broadleaf Evergreen	1
Tropical Deciduous	Tropical Broadleaf Drought Deciduous	2
Temperate Evergreen Broadleaf	Warm Temperate Broadleaf Evergreen	3
Temperate Evergreen Conifer	Temperate Conifer Evergreen	4
Temperate Deciduous	Temperate Broadleaf Cold Deciduous	5
Boreal Evergreen	Boreal Conifer Evergreen	6
Boreal Deciduous	Boreal Broadleaf Cold Deciduous	7
Mixed Forest/Woodland	Boreal Conifer Cold Deciduous	8
Savanna	Evergreen Shrubs	9
Grassland/Steppe	Cold Deciduous Shrubs	10
Dense Shrubland	Warm (C4) Grasses	11
Open Shrubland	Cool (C3) Grasses	12
Tundra		13
Desert		14
Polar Desert/Rock/Ice		15
Ocean		16
Inland Water		17

Identified by LAI and the amount of carbon in the leaves, roots, and stems, PFTs are assigned key characteristics, including basic classification (trees, shrubs, grasses), leaf cycle (deciduous, evergreen), leaf type (broadleaf, needleleaf), and physiology (C_3 pathway,

C_4 pathway) [Kucharik et al., 2000]. Geographic bounds for each PFT are defined by climatic constraints [Kucharik et al., 2000]. Any number of PFTs may exist in each grid cell and IBIS explicitly allows different PFTs to compete for resources such as light, water, and nutrients. When running in dynamic vegetation mode, IBIS updates the assignment of biomes annually based on the distribution of LAI among each of the PFTs. For example, in an area where the dominant tree type is temperate broadleaf deciduous, if the LAI allocated to trees is high, medium, or low, then the area will be designated as a temperate deciduous forest, savanna, or grassland, respectively.

2.3.4 Biogeochemistry

Summing hourly fluxes of carbon (gross photosynthesis and respiration rates) yields the annual carbon balance, which is calculated for each PFT. Gross primary productivity, GPP, and net primary productivity, NPP, are also calculated for each PFT i.

$$GPP_i = \int A_{g,i} dt \tag{2.31}$$

$$NPP_i = (1 - \eta) \int (A_{g,i} - R_{leaf,i} - R_{stem,i} - R_{root,i}) dt \tag{2.32}$$

Here, η is the fraction of carbon lost in the construction of net plant material because of growth respiration [Amthor, 1984] and R_{leaf}, R_{stem}, and R_{root} are the leaf, stem, and root maintenance respiration, respectively [Foley et al., 1996].

IBIS contains three basic biomass pools in which carbon may reside: leaves, transport tissue, and fine roots. Changes in each biomass pool, mortality, and tissue turnover are simulated by assigning residence times to each biomass compartment. LAI is found by dividing the carbon in the leaf biomass pool by the specific leaf area [Foley et al., 1996].

2.4 Convection Schemes

The parameterization of convection plays a central role in simulating precipitation. Because of its relevance to the numerical experiments presented in this thesis, a brief introduction to the Grell scheme is provided. The Grell scheme is a basic representation of convective precipitation similar in structure to the Arakawa & Schubert scheme [1974]. Shown in Fig. 2-3, the Grell scheme models clouds as two steady-state circulations, an updraft and a downdraft [Grell et al., 1994].

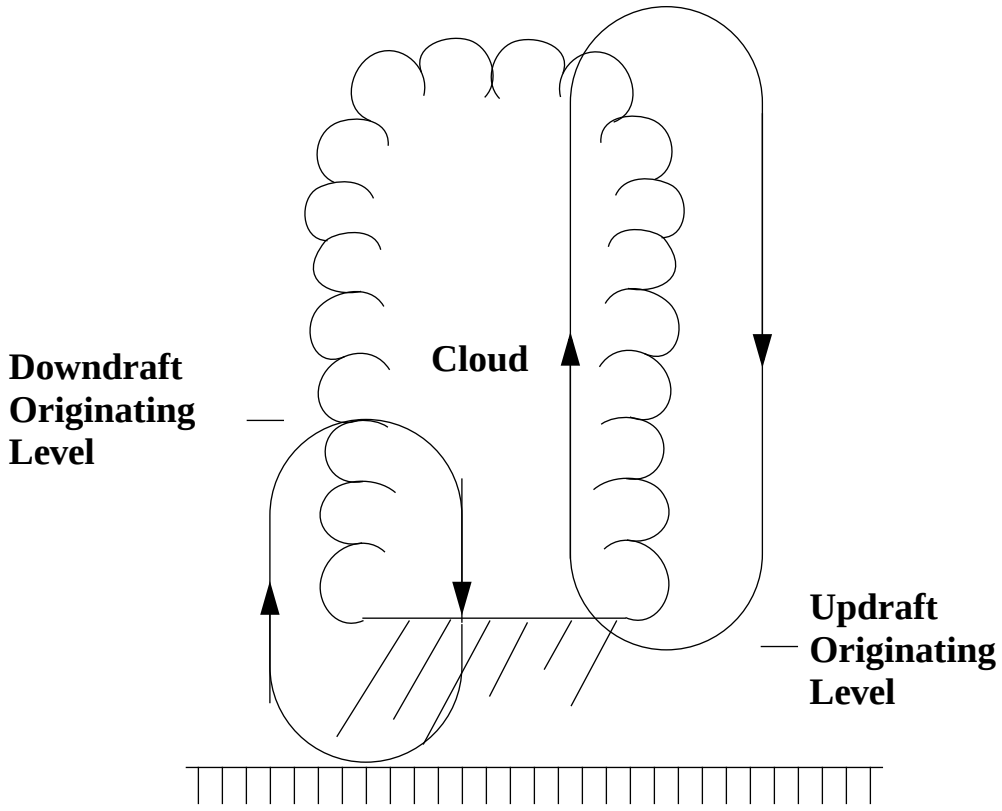

Figure 2-3: Conceptual diagram of the Grell scheme [Grell et al., 1994].

Mixing is not allowed between the cloudy air and the environment along the length of the column, only at the top and bottom of the circulations [Grell et al., 1994]. Mass flux is constant with height z and no entrainment or detrainment occurs along the edges of the

cloud, or:

$$m_u(z) = m_u(z_b) = m_b \tag{2.33}$$

and

$$m_d(z) = m_d(z_0) = m_0, \tag{2.34}$$

where m_u and m_d are the updraft and downdraft mass flux, respectively; z_b is the originating level of the updraft mass flux; z_0 is the originating level of the downdraft mass flux; and m_b and m_0 are the mass fluxes of the updraft and downdraft at their originating levels [Grell et al., 1994]. The originating level is a function of maximum and minimum moist static energy, h, calculated at height z by:

$$h(z) = C_p T(z) + gz + L_v q(z). \tag{2.35}$$

C_p is the specific heat of air, $T(z)$ is the temperature of air at height z, g is the acceleration due to gravity, L_v is the latent heat of vaporization of water, and $q(z)$ is the specific humidity at height z.

Given boundary conditions, the originating mass flux of the downdraft can be put in terms of the updraft mass flux at the originating level and the precipitation efficiency, yielding:

$$m_0 = \frac{\beta I_1 m_b}{I_2}, \tag{2.36}$$

where I_1 is the normalized updraft condensation, I_2 is the normalized downdraft evaporation, and β is the fraction of the updraft condensation that re-evaporates in the downdraft [Pal, 1997]. The precipitation efficiency, which depends on wind shear, is $(1-\beta)$. Rainfall, R, using the Grell scheme is given by:

$$R = I_1 m_b (1 - \beta). \tag{2.37}$$

The Grell scheme calculates heating and moistening as a function of mass fluxes and detrainment at the top and bottom of the cloud [Pal, 1997]. Additionally, to avoid zero-order sources of error, the cooling effects of moist convective downdrafts are included, as well as an upper limit on lateral mixing [Grell et al., 1994].

The simplicity of the Grell scheme allows for two different closure assumptions. The quasi-equilibrium Arakawa & Schubert convective closure (AS74) assumes that clouds stabilize the environment at the same rate that non-convective processes destabilize it [Grell et al., 1994]. This can be expressed as:

$$\frac{dAB}{dt} = \frac{dAB_{LS}}{dt} + \frac{dAB_{CU}}{dt} \approx 0, \tag{2.38}$$

where AB is the available buoyant energy, LS is the subscript for large-scale, and CU is the subscript for cumulus convention [Pal, 1997]. Expressed as a mass flux, the relationship is:

$$m_b = \frac{AB'' - AB}{NA\Delta t}. \tag{2.39}$$

AB'' is the buoyant energy generated by non-convective processes available for convection over the time period Δt and NA is the rate of change of AB per unit m_b.

The other Grell scheme closure assumption, Fritsch & Chappell (FC80), assumes that convection removes available buoyant energy as follows:

$$m_b = \frac{AB}{NA\tau}, \tag{2.40}$$

where τ is the AB removal time scale [Fritsch and Chappell, 1980].

While both closure schemes strike a statistical equilibrium between convection and large-scale processes, they do so different ways. While the AS74 closure scheme relates convective fluxes to tendencies in the state of the atmosphere, the FC80 closure assumption relates convective fluxes to instability in the atmosphere.

2.5 Coupling of Integrated Biosphere Simulator to Regional Climate Model Version 3

Building on the work of J.S. Pal (2002, personal communication) and Delire et al. [2002], IBIS was coupled to RegCM3 with one subroutine responsible for interfacing the two models, as well as additional minor changes to the RegCM3 and IBIS source codes [Winter et al., 2009].

The coupling of RegCM3 and IBIS involved five primary tasks: initialization, passing variables from RegCM3 to IBIS, passing variables from IBIS to RegCM3, restart, and output. Consideration was given to future developments of each model, and when possible, changes to the original IBIS and RegCM3 code were avoided.

The offline version of IBIS creates its input variables from seven files containing monthly mean climatologies that are perturbed by a weather generator and used by the rest of the model. None of the datasets used by the offline version of IBIS are needed in RegCM3-IBIS except at initialization, where climatic conditions and biomes are required for the allocation of PFTs within the domain. Instead, twelve forcing fields are passed from RegCM3 to IBIS at every timestep. These variables are listed in Figure 2-4. The transfer of data from IBIS to RegCM3 is handled in much the same way as the input. A list of variables passed from IBIS to RegCM3 is included in Figure 2-4. The coupling timescale of RegCM3 and IBIS is a user-defined value based on the timestep of the simulation.

The vegetation dataset of the offline version of IBIS was added to the RegCM3 preprocessor, allowing IBIS biomes to be assigned during initialization. Two additional biomes, inland water and ocean, were added to the set of biomes contained in the offline version.

Soil types in RegCM3-IBIS are defined by reading in two files from the Global Soil Data Task of the International Geosphere-Biosphere Programme, one containing the percentage of clay and the other the percentage of sand [Global Soil Data Task, International Geosphere-Biosphere Programme, Data and Information System, 2000]. These data are then interpolated to the RegCM3 grid and assigned physical properties such as porosity, albedo, density, etc., based on clay and sand fractions.

While the coupling of IBIS to Regional Climate Model version 3 (RegCM3-IBIS) intro-

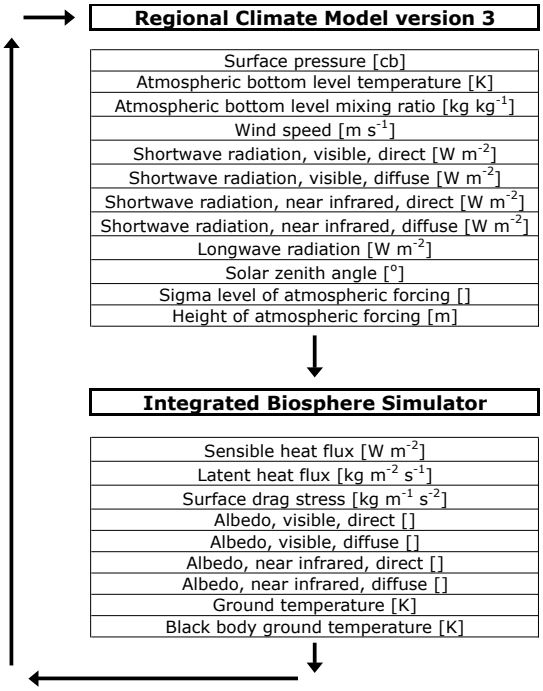

Figure 2-4: Flow chart of RegCM3-IBIS, including passed variables and their associated units.

duced several key advantages to RegCM3, errors were identified in RegCM3-IBIS, including a significant warm bias and an overestimation of incident surface shortwave radiation, net longwave radiation, and sensible heat flux [Winter et al., 2009].

Multiple changes were made to RegCM3-IBIS to address these deficiencies. The overestimation of incident surface shortwave radiation was reduced by updating the optical properties of water vapor, including background aerosols, and using the Arakawa & Schubert closure assumption for the Grell parameterization of convection. The resulting improvements in the simulation of water and energy fluxes over the midwestern United States are detailed in Section 3.3.1.

Aerosols were added by simply applying a visible optical depth uniformly across the domain. This implementation of aerosols had been included in earlier versions of RegCM3, but was deactivated for the development of a more sophisticated aerosol and atmospheric chemistry parameterization. Background aerosols were also added to RegCM3-BATS1e. In both models, the inclusion of aerosols improved the simulation of top of atmosphere albedo and incident shortwave radiation at the surface when compared to observations.

Parameters for the absorption of incident shortwave radiation by water vapor in RegCM3 were originally derived from NCAR Community Climate Model 3, which used a 1982 Air Force Geophysical Laboratory (AFGL) study by Rothman et al. [1983]. While these parameters were revised in the release of NCAR Community Atmosphere Model 3 to reflect the newest AFGL data as described in Collins et al. [2006], they were not changed in RegCM3. Coefficients for the absorption of shortwave radiation by water vapor were updated in RegCM3-IBIS and RegCM3-BATS1e, resulting in better simulations of incident surface shortwave radiation.

A large portion of the examined domain is cultivated; however, IBIS only contains parameterizations for natural vegetation. To address this problem, a simplistic crop scheme was implemented in RegCM3-IBIS. The potential vegetation of dataset of Ramankutty [1999] was modified to include crops in areas consistent with the GLCC dataset [USGS, 1997]. This allowed for the assignment of a cropland biome to cultivated areas of the domain at initialization. Normally this biome would then be populated with multiple PFTs, but croplands are a monoculture, so each cropland biome grid cell is completely and exclusively inhabited by a crop plant functional type. Because the primary agricultural product of the midwestern United States is corn, the crop PFT is modeled in a very similar manner to C_4 grasses, with parameters derived from the maize PFT of Kucharik and Brye [2003]. Finally, the beginning of the planting cycle is accounted for by not allowing crops to grow from January 1^{st} to March 31^{st}. The end of the growing season is defined by phenological factors, including drought and temperature.

Chapter 3

Simulating the Hydroclimatology of the American Midwest

3.1 Introduction

There have been numerous studies examining the ability of general circulation models (GCMs), regional climate models (RCMs), and probabilistic models to simulate the climate of the midwestern United States. Delworth et al. [2002] evaluated the GFDL R30 coupled climate model used in Manabe et al. [2004] against observed temperature and precipitation data. The model simulated a significant warm bias, $\approx$8°C, and underestimated precipitation by $\approx$1 mm day^{-1} over the American Midwest during the summer (June, July, August) [Delworth et al., 2002].

Wang [2005] examined drought using data from 15 GCMs that participated in the Intergovernmental Panel on Climate Change (IPCC) Fourth Assessment Report. Precipitation was the only variable evaluated against observations; the bias in the 15-model precipitation average over the midwestern United States during the summer was between 1-2 mm day^{-1} [Wang, 2005].

Seneviratne et al. [2002] analyzed four 1-year control experiments over the American Midwest using the NCAR Regional Climate Model (RegCM), and found that precipitation was overestimated by approximately 0.5 mm day $^{-1}$ during the months of March, April, and May. Precipitation was well modeled through the rest of the summer and underestimated

slightly in September [Seneviratne et al., 2002]. Simulated values of latent heat flux were in reasonable agreement with a 10-year climatology of evapotranspiration derived using an atmospheric and soil water balance; however, evapotranspiration was overestimated by $\approx$0.5 mm day^{-1} in April and May [Seneviratne et al., 2002]. Note that the terms "latent heat flux" and "evapotranspiration" are used interchangeably throughout this thesis.

One of the most complete assessments of a numerical model over the midwestern United States was completed by Pal et al. [2000] using a modified version of RegCM. Simulated temperature, precipitation, outgoing longwave radiation, incident surface shortwave radiation, and precipitation were evaluated for six 1-year numerical experiments. Temperature agreed well with observations throughout the year [Pal et al., 2000]. Precipitation was modeled accurately on average, but was overestimated during the spring [Pal et al., 2000]. Simulated values for outgoing longwave radiation and incident surface shortwave radiation were similar to observations for practically all months examined [Pal et al., 2000].

In the analysis presented below, the ability of RegCM3-IBIS and RegCM3-BATS1e to simulate the surface water and energy budgets–including temperature, precipitation, evapotranspiration, shortwave radiation, longwave radiation, runoff, and soil moisture–was extensively tested. The following sections detail three control experiments that were completed to assess and improve the capacity of RegCM3-IBIS and RegCM3-BATS1e to simulate the hydroclimatology of the American Midwest.

3.2 Design of Experiments

All three control experiments are centered at 40°N, 95°W and use a Rotated Mercator projection. The domain spans 100 points zonally, 60 points meridionally at a horizontal grid spacing of 60 km, covering all of the United States as well as parts of Mexico and Canada (Figure 3-1). Simulations were initialized April 1st, 1982 and allowed to spin-up for 21 months. The years evaluated (1984-2005) were chosen for maximum overlap with observational datasets. The region assessed is shown by the 4.0° x 5.5° shaded box contained in Figure 3-1, and was also chosen for maximum overlap with observational datasets.

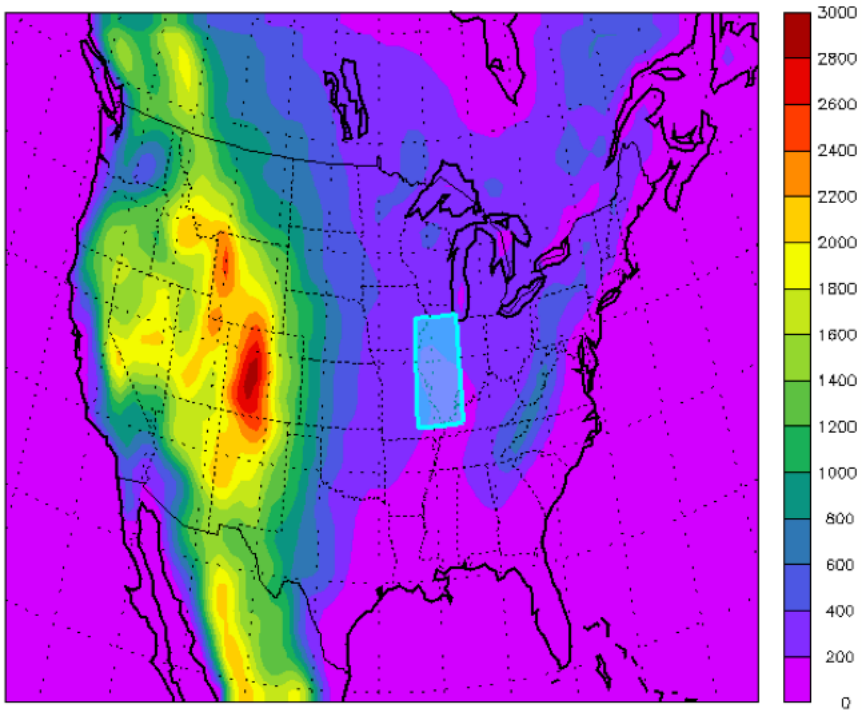

Figure 3-1: Domain and topography [m] of control experiments with a 4.0° x 5.5° cyan shaded box delineating the extent of spatial averaging over Illinois.

In RegCM3-BATS1e, vegetation classes were directly assigned using the Global Land Cover Characterization (GLCC) dataset of the United States Geological Survey (USGS) [1997]. In RegCM3-IBIS, the potential global vegetation dataset of Ramankutty [1999] was used to initialize biomes, and then each grid box was populated with plant functional types (PFTs) based on the biome and two datasets: monthly mean climatology of temperature [New et al., 1999] and minimum temperature ever recorded at a location minus the average temperature of the coldest month [Bartlein, 2000]. Croplands were then defined in RegCM3-IBIS using the USGS GLCC dataset. Topography for both models was given by the USGS Global 30-arc second elevation dataset [1996] aggregated to a 0.5° x 0.5° spatial resolution.

Although RegCM3-IBIS is capable of simulating dynamic vegetation, in all numerical experiments presented static vegetation was used. First, this creates a more consistent comparison between RegCM3-IBIS and RegCM3-BATS1e, which does not contain vegetation dynamics. Second, the analyses conducted focus primarily on agricultural areas, which are not natural systems in which vegetation would be allowed to evolve. And finally, the time

period examined, chosen for maximum overlap with observational datasets, is somewhat short for a reasonable simulation of dynamic vegetation.

At initialization, soil temperature was set by the surface temperature boundary condition and soil moisture was assigned based on vegetation type in RegCM3-BATS1e. Soil moisture, soil temperature, and soil ice in RegCM3-IBIS were initialized using the monthly average for April of the last year of a global 20-year 0.5° x 0.5° offline IBIS simulation. The monthly mean climatology variables required to run the offline version of IBIS are cloudiness, precipitation rate, relative humidity, temperature, wet days per month, near-surface wind speed, and temperature range, which are all products of the Climate Research Unit (CRU) Climatology 1.0 (CL1.0) dataset [New et al., 1999].

Because initialization of soil moisture has been shown by Fischer et al. [2007b] to be important in the modeling of European heatwaves, a pair of 4-year numerical experiments were conducted over the United States using two different types of soil moisture initialization. In the first RegCM3-IBIS simulation, soil moisture, soil temperature, and soil ice were initialized using the method described above. In the second simulation, RegCM3-IBIS with RegCM3-BATS1e soil moisture initialization (RegCM3-IBIS BSMI), the soil moisture and temperature fields at initialization were set identical to those of RegCM3-BATS1e. Appended Figure A-1 describes the summer seasonal cycles of surface and root zone soil moisture in RegCM3-IBIS, RegCM3-IBIS BSMI, and RegCM3-BATS1e. Overall the results of RegCM3-IBIS and RegCM3-IBIS BSMI are very similar, which suggests that for this set of experiments soil moisture initialization is not an important source of variability in the modeling results. Figure A-2 is included to illustrate the absence of trends in surface and root zone soil moisture over the years examined.

RegCM3-IBIS and RegCM3-BATS1e were assessed using the National Aeronautics and Space Administration (NASA) Surface Radiation Budget dataset [NASA, 2006], data compiled by Yeh [2003], and the Climate Research Unit Time Series 2.1 [Mitchell et al., 2004].

The National Aeronautics and Space Administration Surface Radiation Budget (SRB) dataset, obtained from the NASA Langley Research Center Atmospheric Science Data Center, was used to evaluate shortwave and longwave radiative fluxes for dates available (1984-

2004) [NASA, 2006]. Post processing, the dataset has a 1.0° x 1.0° spatial resolution on a regular latitude-longitude grid. NASA SRB is primarily derived from two sources: the International Satellite Cloud Climatology Project C1 dataset, which provides information on cloud amount and distribution [Rossow and Schiffer, 1991]; and the NASA Earth Radiation Budget Experiment dataset, which contains satellite-based measurements of top of atmosphere (TOA) fluxes [Barkstrom, 1984]. Documentation of the NASA SRB dataset estimates errors in the shortwave and longwave radiation budgets to be approximately 5 W m^{-2} and 10 W m^{-2}, respectively.

The dataset constructed by Yeh [2003] contains a number of observed and reanalysis sources, as well as monthly estimates of evapotranspiration based on regional ($\approx 10^5$ km^2) water balances. Daily precipitation and snow data are derived from the Midwest Climate Center, with additional estimates of precipitation obtained from EarthInfo, Inc. [Yeh, 2003]. The Illinois State Water Survey provided information for soil moisture and water table depth [Yeh, 2003]. Daily streamflow data was measured by the USGS, and wind and humidity fields were derived from National Centers for Environmental Prediction (NCEP)/NCAR Reanalysis 1 [Yeh, 2003]. Two estimates of evapotranspiration were calculated from these data, one using an atmospheric water balance and the other using a soil water balance; correlation between the two methods is 0.79 [Yeh, 2003]. Presented values for evapotranspiration in all figures were calculated by averaging the atmospheric and soil water balance estimates. Errors in determining evapotranspiration using the regional water balance methods described above were found to be $\approx 10\%$ [Yeh et al., 1998]. Negative evapotranspiration estimates during the winter are primarily attributable to an underestimation in precipitation measurements [Yeh et al., 1998]. While total runoff is based on USGS streamflow data, surface runoff is calculated by scaling observed precipitation using an empirically-derived surface runoff coefficient (0.06) [Yeh, 2003]. Groundwater runoff was computed by taking the difference between total runoff and surface runoff. For clarity, all observations used to estimate evapotranspiration, as well as the evapotranspiration values themselves, are referred to as ISWS data.

Temperature and precipitation values are provided by the Climate Research Unit (CRU) Time Series 2.1 (TS2.1). This dataset contains observed surface temperature and precipi-

tation resampled on a 0.5° x 0.5° regular latitude-longitude grid [Mitchell et al., 2004].

In addition to the RegCM3 and IBIS improvements discussed in Section 2.5, the number of soil layers and total soil depth in RegCM3-IBIS were changed in order to better represent the subsurface hydrology of the American Midwest. The default configuration for number of soil layers and total soil depth in IBIS is 6 and 4 m, respectively. However, because no explicit representation for groundwater exists, this forces unsaturated soils to a depth of 4 m. Observations show that the water table is rarely more than 4 m deep in the midwestern United States [Yeh, 2003]. Accordingly, the bottom soil layer was removed from the model, leaving 5 soil layers and a total soil depth of 2 m.

3.2.1 NCEP-DOE Reanalysis 2

In the first two control experiments, RegCM3-IBIS and RegCM3-BATS1e were forced using boundary conditions compiled from the NCEP-Department of Energy (DOE) Reanalysis 2 (NNRP2) dataset [Kanamitsu et al., 2002] under the exponential relaxation of Davies and Turner [1977]. NNRP2 is global in coverage with a resolution of 2.5° x 2.5°, and is provided by the Physical Sciences Division of the Earth System Research Laboratory. SSTs were prescribed using the National Oceanic and Atmospheric Administration (NOAA) Optimum Interpolation SST (OISST) dataset, which has a spatial resolution of 1.0° x 1.0° and is averaged on a weekly basis [Reynolds et al., 2002]. This dataset relies on in situ and satellite SSTs, as well as SSTs simulated from sea-ice cover [Reynolds et al., 2002].

Previous numerical experiments revealed that both RegCM3-IBIS and RegCM3-BATS1e were sensitive to convective closure assumption. To examine the model configuration variability of the NNRP2 control experiments, RegCM3-IBIS and RegCM3-BATS1e were run using the Grell parameterization of convection and both the Fritsch & Chappell (FC80) [Fritsch and Chappell, 1980] and the Arakawa & Schubert (AS74) [Grell et al., 1994] convective closure assumptions. This produced an ensemble of four simulations: RegCM3-IBIS using AS74 (IBIS-AS), RegCM3-BATS1e using FC80 (BATS-FC), RegCM3-IBIS using FC80 (IBIS-FC), and RegCM3-BATS1e using AS74 (BATS-AS). Additional details

on the Grell parameterization of convection and convective closure assumptions are provided in Section 2.4.

3.2.2 ECHAM5 GCM

While the NNRP2 dataset provides useful boundary conditions for assessing the ability of RegCM3-IBIS and RegCM3-BATS1e to simulate the current climate, it cannot describe future climate. General circulation models, however, are capable of producing unconstrained predictions of future climate. The ECHAM5 GCM (EH5OM) is a fully-coupled atmosphere-ocean general circulation model with a horizontal grid spacing of 1.875° x 1.875°. EH5OM is currently maintained at the Max Plank Institute for Meteorology in Germany and additional model details can be found in [Roeckner et al., 2003]. EH5OM was chosen based on its ability to accurately simulate the climate of the continental United States in the Intergovernmental Panel on Climate Change Fourth Assessment Report [Randall et al., 2007]. Boundary conditions for 1982-2000 were derived from the 20^{th} century simulation with observed anthropogenic forcings (i.e. CO_2, CH_4, N_2O, CFCs, O_3, and SO_4) [Roeckner et al., 2006a]. Because the final year of the 20^{th} century simulation is 2000, the last five years of boundary conditions (2001-2005) were compiled from a simulation of EH5OM under the A1B emissions scenario [Roeckner et al., 2006b]. Additional details regarding the EH5OM A1B experiment are provided in Section 5.2.2.

EH5OM control simulations were run using the configuration for convection in RegCM3-IBIS and RegCM3-BATS1e that best simulated the hydroclimatology of Illinois in the NNRP2 experiments described above. RegCM3-IBIS was run with the AS74 convective closure (IBIS-AS) and RegCM3-BATS1e was run using the FC80 convective closure (BATS-FC).

3.3 Results

3.3.1 NCEP-DOE Reanalysis 2

Presented results are 4.0° x 5.5° spatial averages over the box contained in Figure 3-1. Figures 3-2 through 3-10 show the performance of RegCM3-IBIS over the state of Illinois before (IBIS-08) and after (IBIS-AS) the modifications discussed in Sections 2.5 and 3.2. Improvements to IBIS-AS relative to IBIS-08 are summarized in Table 3.1.

Table 3.1: Key differences between IBIS-AS and IBIS-08

IBIS-AS	IBIS-08
Arakawa & Schubert convective closure	Fritsch & Chappell convective closure
5 soil layers, 2-m depth	6 soil layers, 4-m depth
Water vapor coeff. of Collins et al. [2006]	Water vapor coeff. of Rothman et al. [1983]
Potential vegetation and croplands	Potential vegetation only
Background aerosols	No aerosols

The IBIS-08 numerical experiment described in this section has an atmospheric and surface physics model timestep of 200 seconds and 600 seconds, respectively. In all other RegCM3-IBIS (and RegCM3-BATS1e) simulations, the atmospheric model timestep is 150 seconds and the surface physics model timestep is 450 seconds. IBIS-AS was run using both sets of timesteps (150 seconds, 450 seconds as well as 200 seconds, 600 seconds) and no significant differences were found between the simulations. Therefore, the IBIS-AS numerical experiment with an atmospheric model timestep of 150 seconds and a surface physics model timestep 450 seconds was used in the analysis below.

RegCM3-IBIS and RegCM3-IBIS-08

Figures 3-2 to 3-7 present each variable using a pair of panels, where the left panel shows the simulated and observed seasonal cycles, and the right panel shows the difference between the simulated and observed seasonal cycles.

The simulation of incident surface shortwave radiation is dramatically improved in IBIS-AS relative to IBIS-08, especially during the summer months (June, July, August)

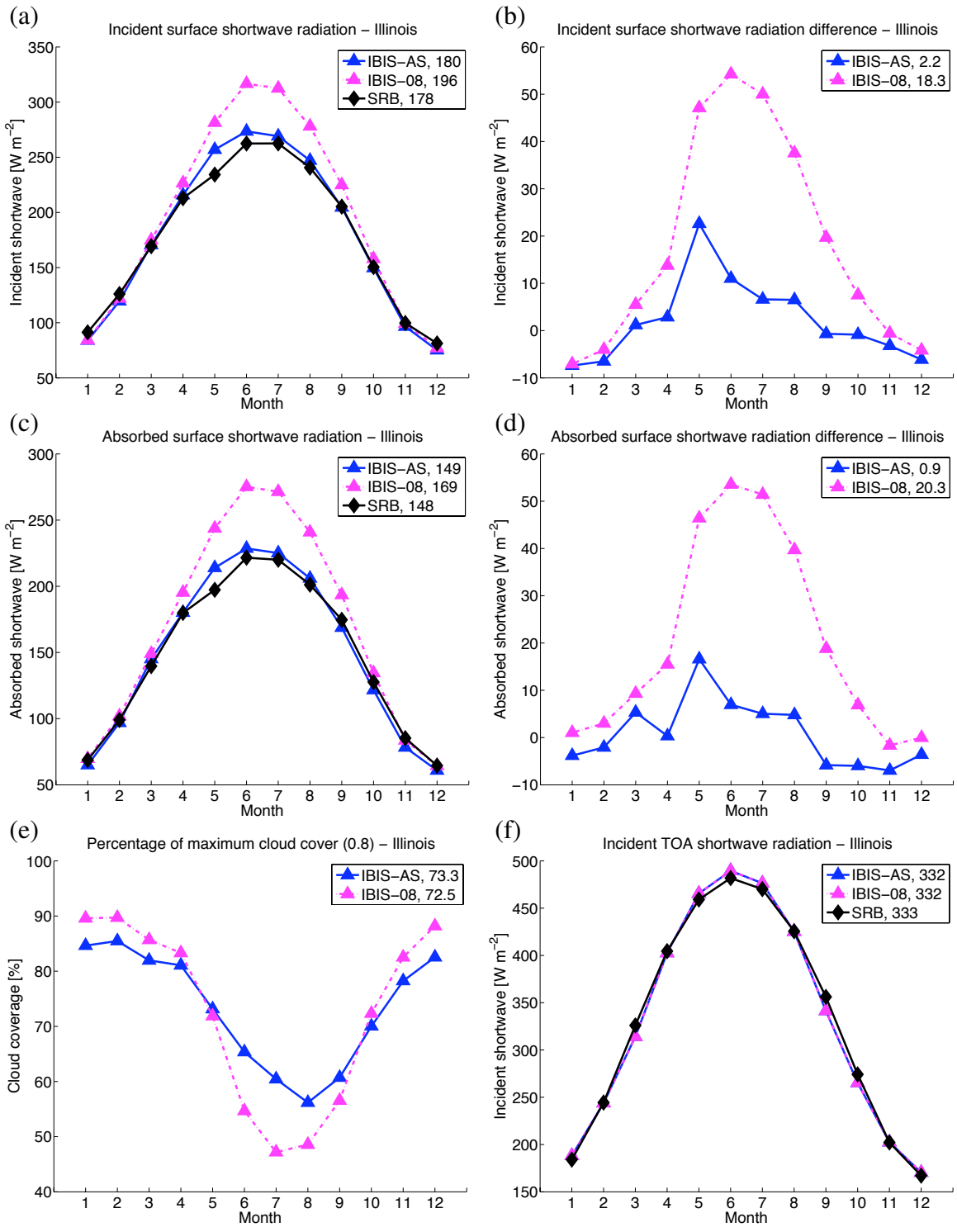

Figure 3-2: NNRP2 control and observed seasonal cycles of: (a) incident surface shortwave radiation, (c) absorbed surface shortwave radiation, (e) percentage of maximum model fractional cloud cover (0.8), (f) incident top of atmosphere (TOA) shortwave radiation; and the difference between NNRP2 control and observed seasonal cycles of: (b) incident surface shortwave radiation, (d) absorbed surface shortwave radiation for 1984-2004. Annual averages for each variable examined are provided in the legend.

where reductions average 40 W m^{-2} (Figure 3-2). Increasing the absorption of shortwave radiation by water vapor, implementing a simplistic representation of aerosols, modifying the vegetation cover to more accurately reflect current landuse, and increasing cloudiness by changing the convective closure assumption all contribute to reducing the overestimation of incident surface shortwave radiation. The increase in cloudiness during the summer months is illustrated in Figure 3-2.

Corresponding improvements in IBIS-AS absorbed surface shortwave radiation are shown in Figure 3-2, and suggest that the overestimation of absorbed surface shortwave radiation in IBIS-08 is primarily a result of incident surface shortwave radiation errors.

Incident top of atmosphere shortwave radiation is well simulated by IBIS-AS and IBIS-08. A function primarily of planetary geometry, the small differences in the modeled and observed values of incident top of atmosphere shortwave radiation are likely due to averaging over datasets with different spatial resolutions and map projections.

Corrections to the shortwave radiation budget are reflected in an improved simulation of 2-m temperature. The overestimation of 2-m temperature in IBIS-08 is reduced by 3.5°C during the summer months in IBIS-AS (Figure 3-3). It is expected that if the incident surface shortwave radiation could be lowered to match observations, 2-m temperature would agree well with observations.

IBIS-AS winter (December, January, February) and summer downward longwave radiation is $\approx$6 W m^{-2} less than IBIS-08 winter and summer downward longwave radiation, as shown in Figure 3-3. This is a slight degradation in model performance and is likely a product of increased cloud cover.

Relative to IBIS-08, the simulation of net longwave radiation (defined as positive upward) in IBIS-AS is reduced during the spring (March, April, May), summer, and fall (September, October, November) to more closely match observations. Cooler surface temperatures are largely responsible for this improvement.

While the annual average of IBIS-AS evapotranspiration is the same as the annual average of IBIS-08 evapotranspiration (Figure 3-4), the shape of the IBIS-AS evapotranspiration seasonal cycle matches observations better, a result of reduced incident surface shortwave radiation during the late spring and early summer as well as an increase in July

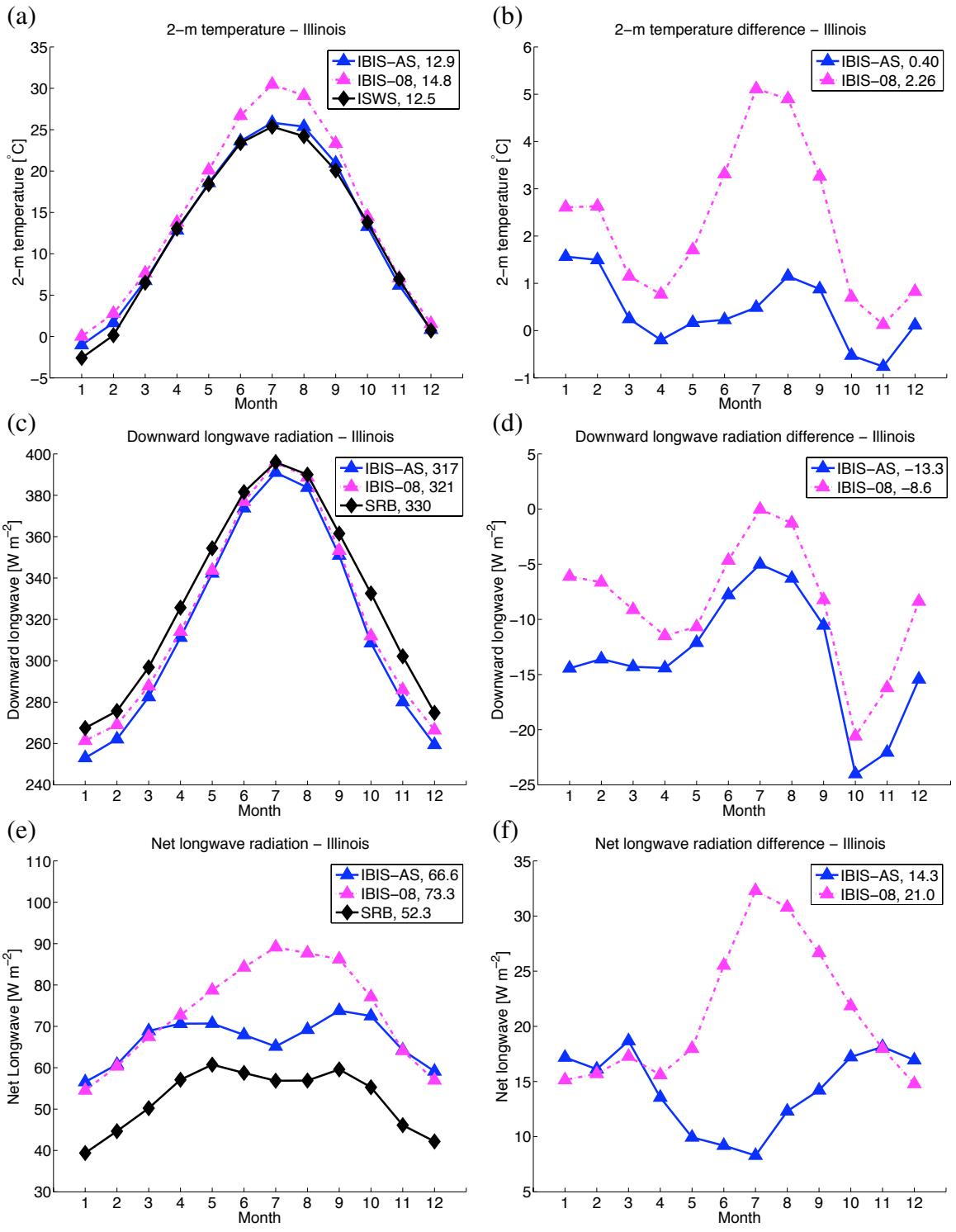

Figure 3-3: NNRP2 control and observed seasonal cycles of: (a) 2-m temperature, (c) downward longwave radiation, (e) net longwave radiation (defined as positive upward); and the difference between NNRP2 control and observed seasonal cycles of: (b) 2-m temperature, (d) downward longwave radiation, (f) net longwave radiation (defined as positive upward) for 1984-2004 (2-m temperature 1984-2005). Annual averages for each variable examined are provided in the legend.

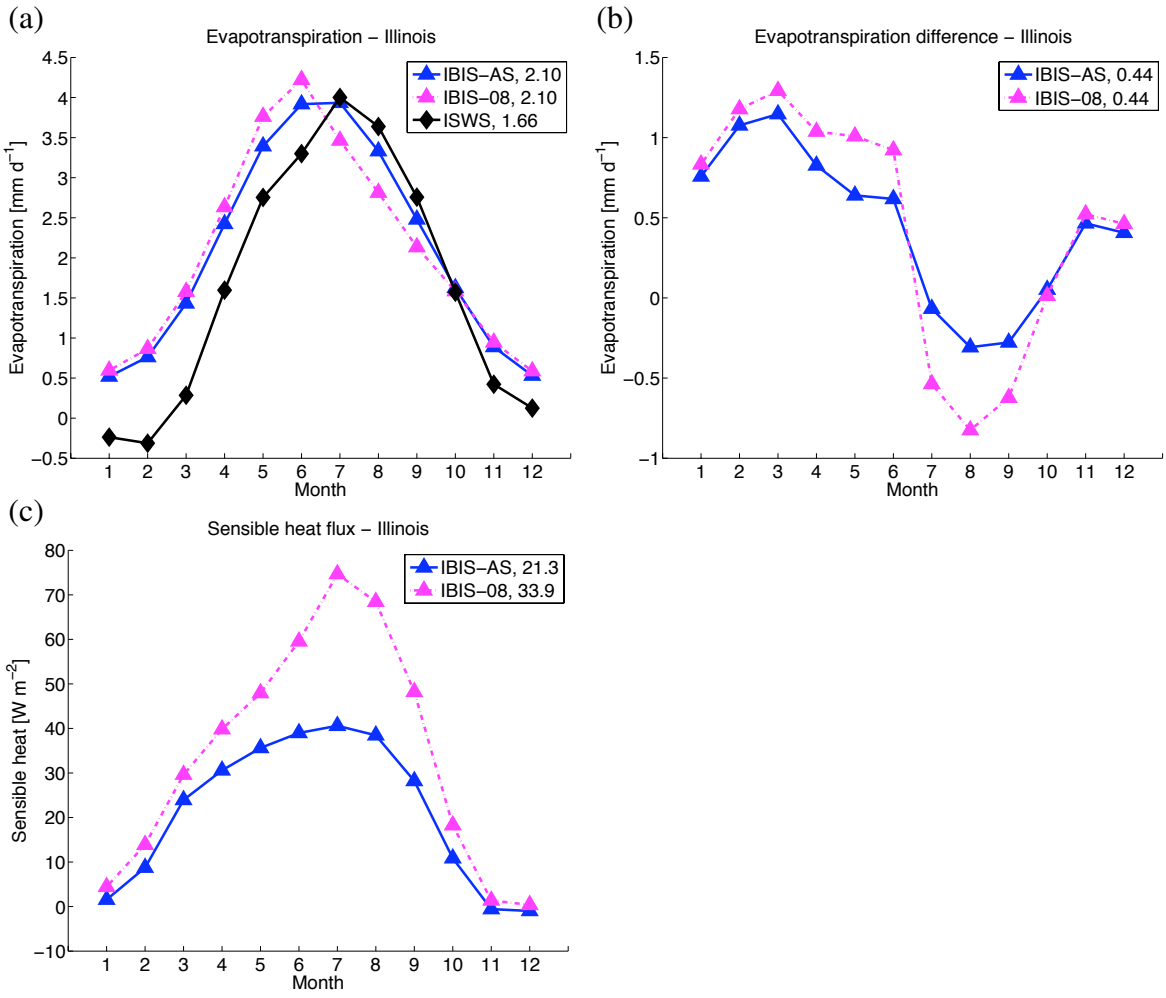

Figure 3-4: NNRP2 control and observed seasonal cycles of: (a) evapotranspiration, (c) sensible heat flux; and the difference between NNRP2 control and observed seasonal cycles of: (b) evapotranspiration for 1984-2005. Annual averages for each variable examined are provided in the legend.

precipitation. Currently, no regional-scale observations of sensible heat flux exist; however, a comparison of the IBIS-AS and IBIS-08 sensible heat flux seasonal cycles is shown in Figure 3-4. Cooler surface temperatures result in an overall reduction in sensible heat flux in IBIS-AS, especially during the summer.

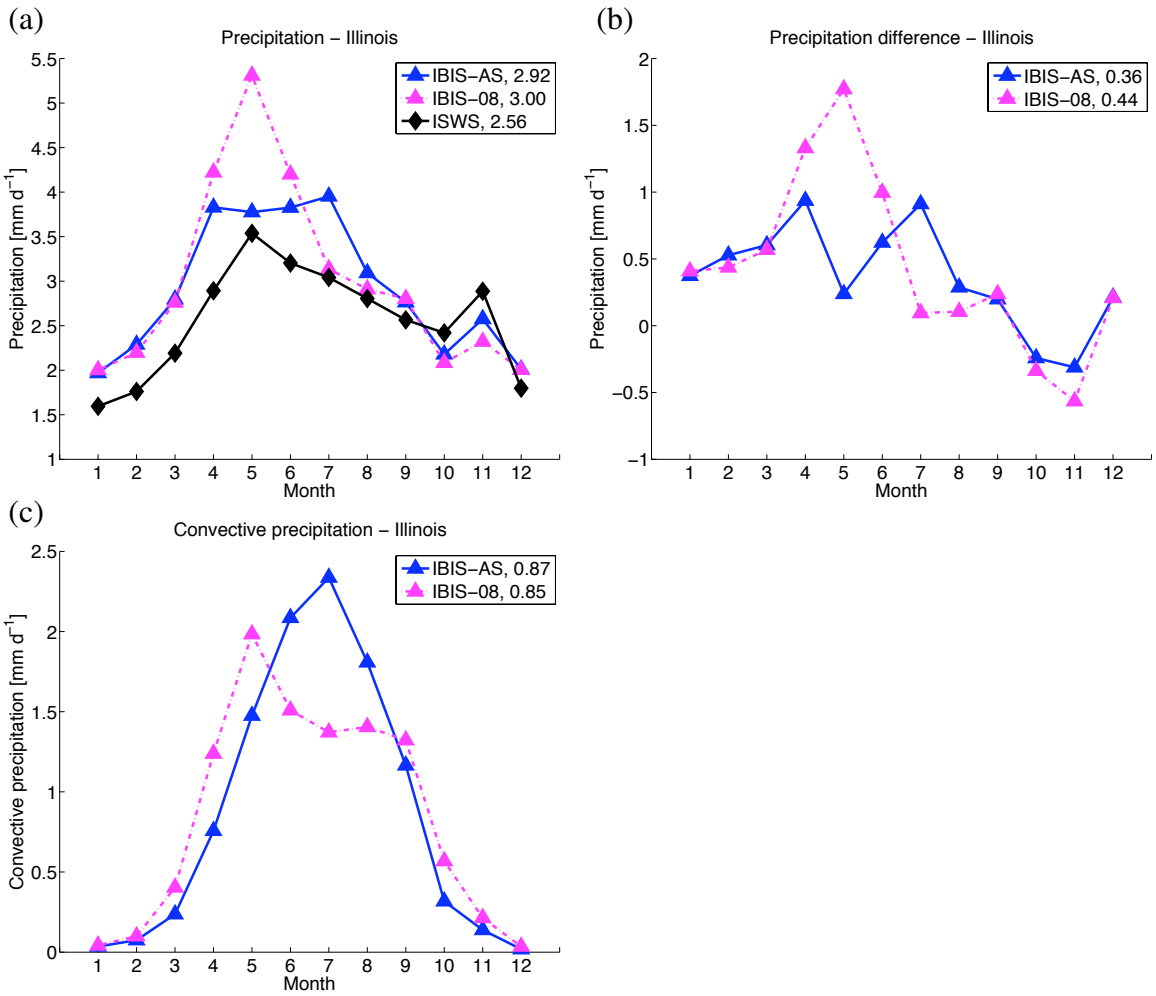

Figure 3-5: NNRP2 control and observed seasonal cycles of: (a) precipitation, (c) convective precipitation; and the difference between NNRP2 control and observed seasonal cycles of: (b) precipitation for 1984-2005. Annual averages for each variable examined are provided in the legend.

IBIS-08 simulates a large wet bias during April, May, and June across the midwestern United States, shown in Figure 3-5. This was mitigated partially in IBIS-AS by changing the convective closure assumption, which increased cloudiness and reduced convective precipitation in April and May. However, the simulation of precipitation in IBIS-AS for the month of July is degraded when compared with IBIS-08, a result of overestimated con-

vective precipitation.

Significant improvements were made to the subsurface hydrology of IBIS-AS, illustrated in Figure 3-6. The simulation of IBIS-AS May and June rainfall is more accurate than the simulation of IBIS-08 May and June rainfall, decreasing the overestimation of total runoff and surface runoff in IBIS-AS during the summer. Changes in groundwater runoff are largely a product of modifying the soil depth in IBIS-AS. IBIS-08 specifies a 4-m unsaturated zone, which was found to be too deep when compared to the observations of Yeh [2003]; the water table in Illinois is generally closer to the surface. To address this deficiency, the lowest soil layer, which is 2-m in depth, was removed from the model. This allowed the groundwater runoff to respond more readily to increases in precipitation during the early spring, improving both the simulation of groundwater and total runoff.

The seasonal cycle of surface soil moisture simulated by IBIS-08 is well correlated with observations (Figure 3-7). IBIS-AS surface soil moisture shows degraded performance. Enhanced late summer precipitation and increased root zone soil moisture in IBIS-AS results in a wet bias during the summer in surface soils.

Root zone soil moisture is markedly improved in IBIS-AS relative to IBIS-08. In IBIS-08, the lowest soil layer (2-4 m) acted as unsaturated storage. By eliminating this unrealistic reservoir, more water was allowed to be retained in the root zone.

The distribution of soil moisture with depth is shown in Figure 3-8. Annually, IBIS-08 underestimates soil moisture throughout the entire soil column. In addition, the distribution of soil moisture with depth is poorly represented in IBIS-08. While IBIS-AS simulates the distribution of annually-averaged soil moisture better, it overestimates soil moisture in the first two soil layers and underestimates soil moisture in the bottom three soil layers.

During the summer IBIS-08 does an excellent job of simulating soil moisture in the first two layers; however, below that soils are too dry. Summer soil moisture in IBIS-AS is overestimated near the surface and underestimated with depth, but overall IBIS-AS captures the observed summer soil moisture profile much better than IBIS-08.

Figures 3-9 and 3-10 reveal the performance of both models on a monthly basis. This yields important information about the variability of the climate system, as well as each model's skill in capturing that variability.

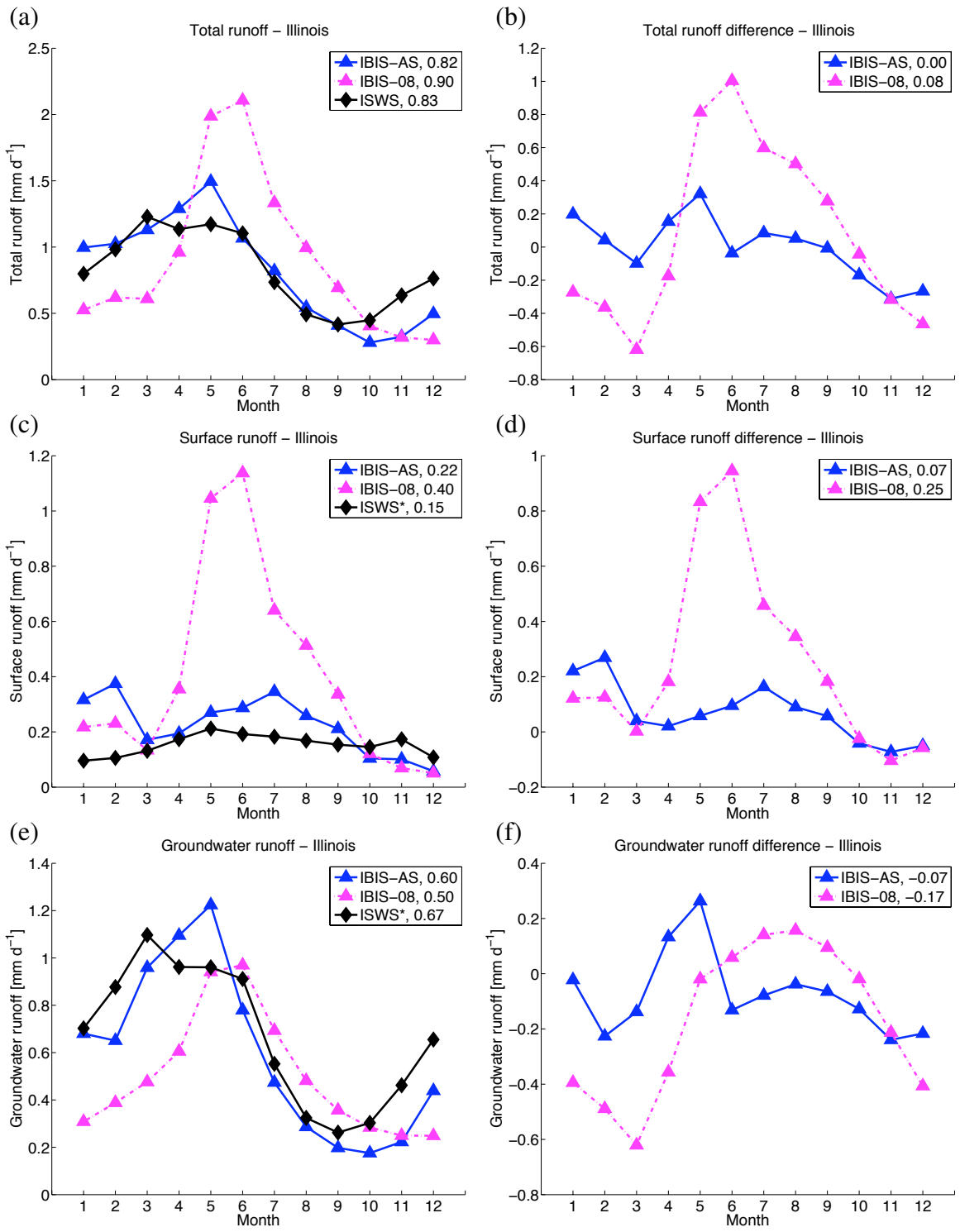

Figure 3-6: NNRP2 control and observed seasonal cycles of: (a) total runoff, (c) surface runoff, (e) groundwater runoff; and the difference between NNRP2 control and observed seasonal cycles of: (b) total runoff, (d) surface runoff, (f) groundwater runoff for 1984-2005. Annual averages for each variable examined are provided in the legend. *estimate of runoff as described in Section 3.2

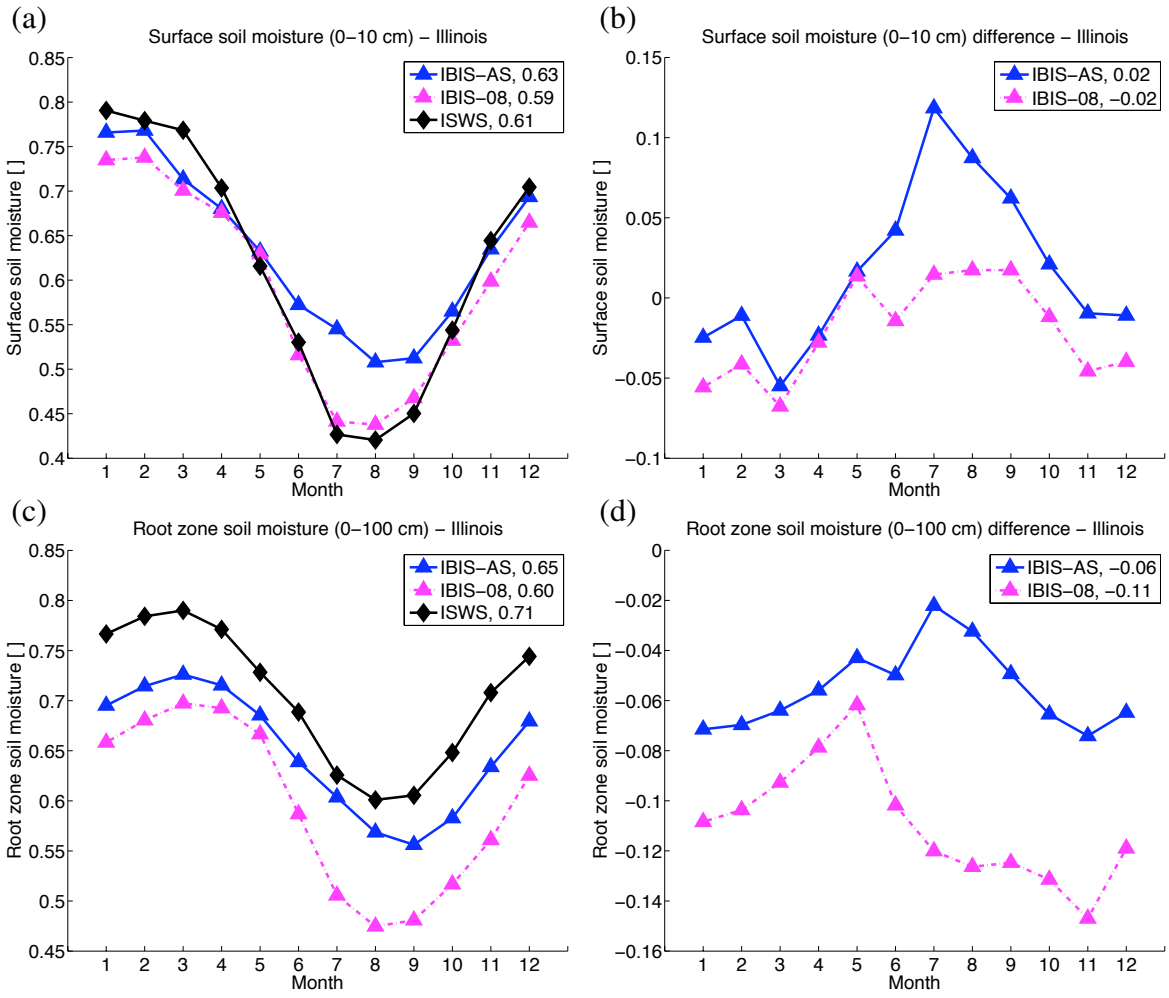

Figure 3-7: NNRP2 control and observed seasonal cycles of: (a) surface soil moisture, (c) root zone soil moisture; and the difference between NNRP2 control and observed seasonal cycles of: (b) surface soil moisture, (d) root zone soil moisture for 1984-2003. Annual averages for each variable examined are provided in the legend.

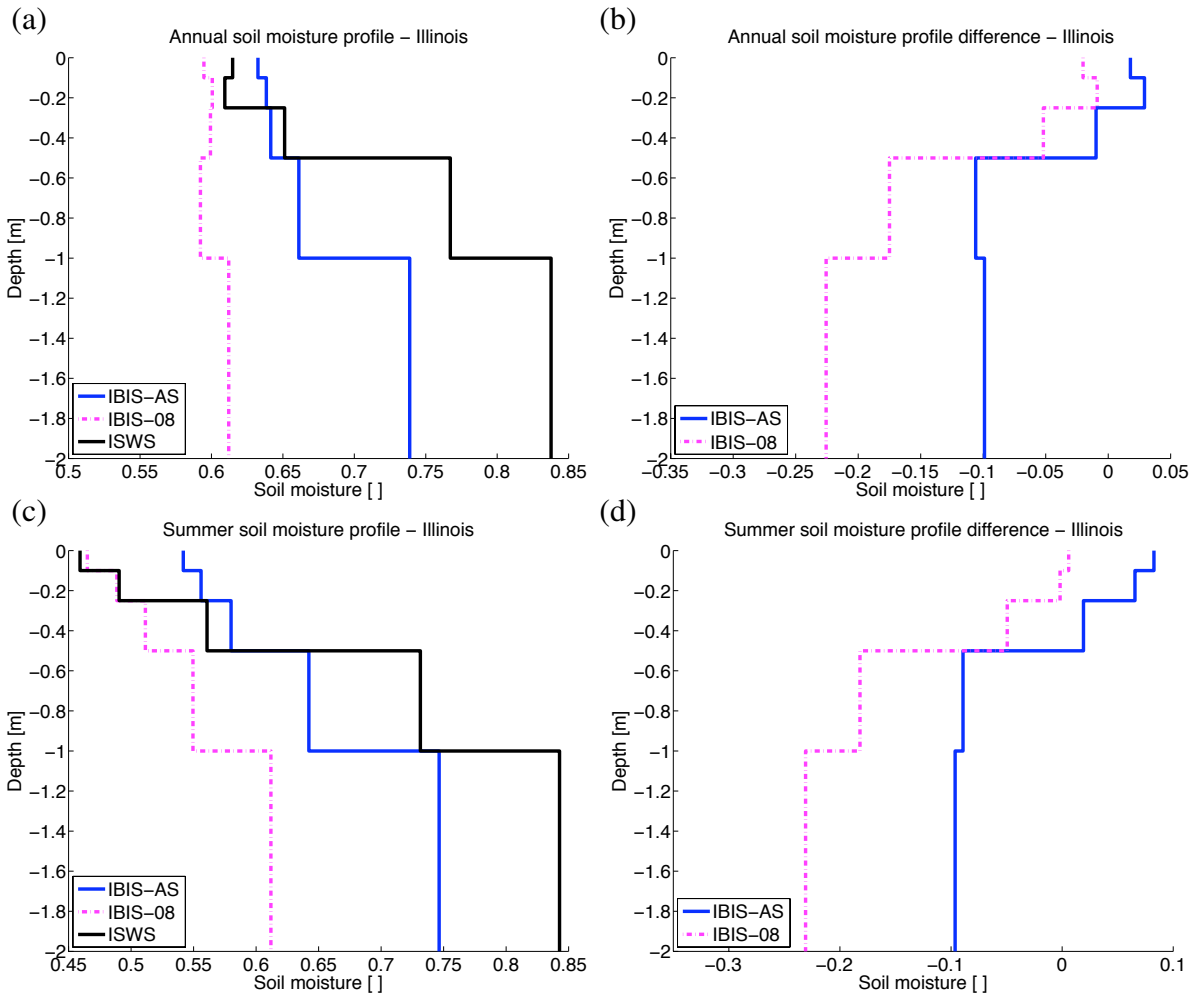

Figure 3-8: NNRP2 control and observed (a) annual, (c) summer (June, July, August) soil moisture profiles; and the difference between NNRP2 control and observed (b) annual, (d) summer (June, July, August) soil moisture profiles for 1984-2003.

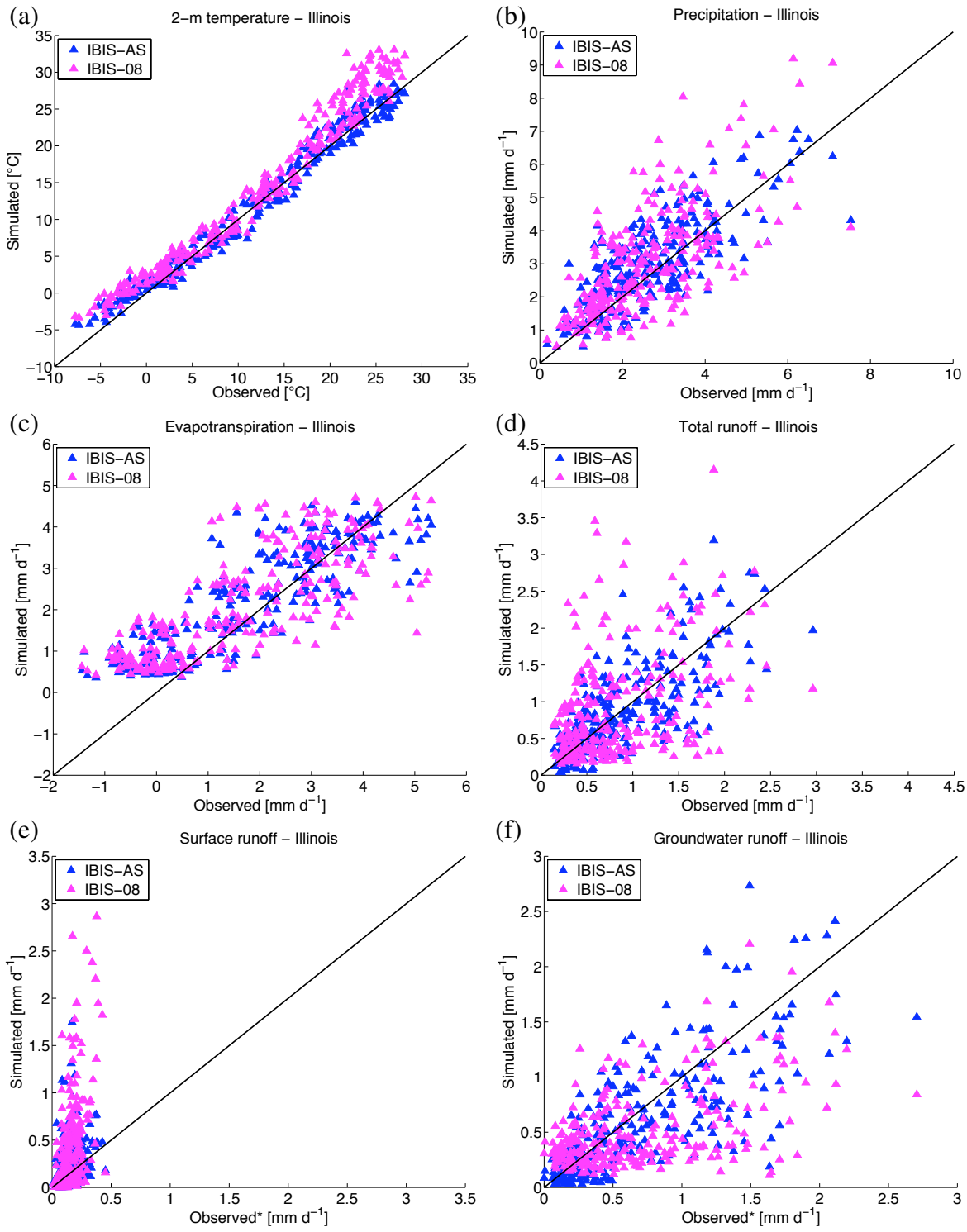

Figure 3-9: Scatter plots of: (a) temperature, (b) precipitation, (c) evapotranspiration, (d) total runoff, (e) surface runoff, (f) groundwater runoff using NNRP2 boundary conditions. Each point is a monthly average for 1984-2005. *estimate of runoff as described in Section 3.2

The warm bias in IBIS-AS is significantly less than that of IBIS-08, especially during the summer months (Figure 3-9). While the overall distribution and scatter of precipitation is similar for IBIS-AS and IBIS-08, IBIS-AS does contain less extreme precipitation events.

Evapotranspiration is relatively unchanged between the IBIS-AS and IBIS-08 simulations. Note that negative values for observed evapotranspiration are artifacts of the surface and atmospheric water balance as described in Section 3.2. The scatter in IBIS-AS total runoff is less than the scatter in IBIS-08 total runoff, indicating that IBIS-AS simulates monthly values of total runoff better than IBIS-08. In addition, some unrealistically large runoff events present in IBIS-08 are eliminated. IBIS-AS also shows increased skill in simulating surface runoff relative to IBIS-08, again removing erroneously large runoff events. Groundwater runoff is underestimated by IBIS-08 on average, and this bias is partially mitigated in IBIS-AS.

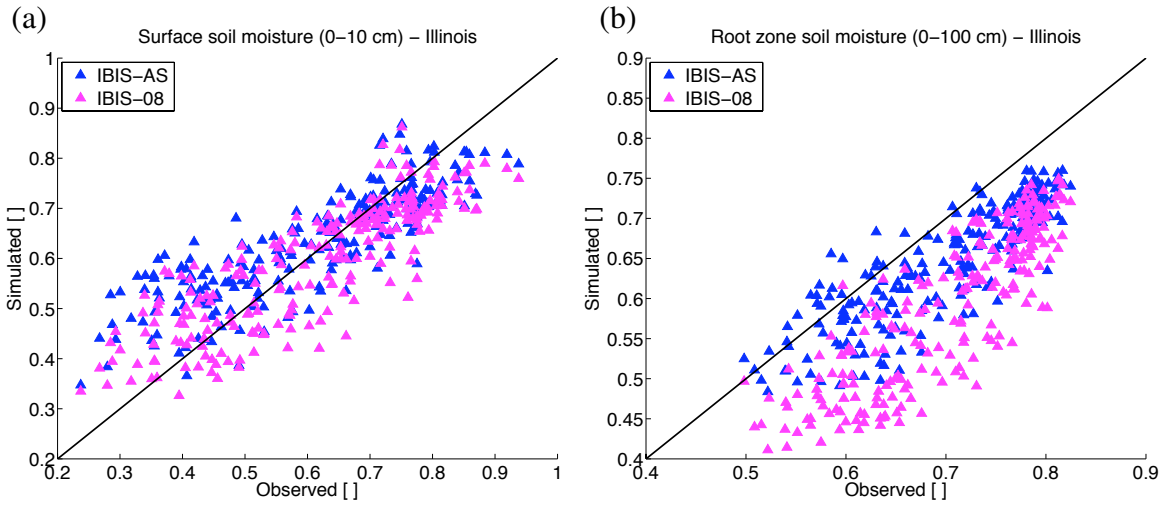

Figure 3-10: Scatter plots of: (a) surface soil moisture, (b) root zone soil moisture using NNRP2 boundary conditions. Each point is a monthly average for 1984-2003.

The simulation of surface soil moisture in IBIS-AS is degraded relative to IBIS-08, with the overestimation of surface soil moisture especially evident during drier soil conditions (summer months). The simulation of root zone soil moisture, however, is improved in IBIS-AS (Figure 3-10). While both IBIS-AS and IBIS-08 underestimate root zone soil moisture, the dry bias is significantly less in IBIS-AS.

RegCM3-IBIS and RegCM3-BATS1e

Figures 3-11 to 3-16 present each variable using a pair of panels, where the left panel shows the simulated and observed seasonal cycles, and the right panel shows the difference between the simulated and observed seasonal cycles.

IBIS-AS simulates the seasonal cycle of incident surface shortwave radiation best overall, as shown in Figure 3-11. However, IBIS-AS does overestimate incident surface shortwave radiation in the early summer months (May, June, July) by 13.4 W m^{-2}. BATS-FC overestimates incident surface shortwave radiation in summer (June, July, August) by as much as 23 W m^{-2} and underestimates incident surface shortwave radiation in spring (March, April, May), winter (December, January, February), and fall (September, October, November) by about 19 W m^{-2} on average. During the summer months, the shortwave radiation budget is strongly affected by convective closure, where the FC80 convective closure assumption produces significantly less clouds than the AS74 convective closure assumption. In the winter, incident surface shortwave radiation is primarily a function of surface physics model.

Biases in absorbed surface shortwave radiation are well correlated with biases in incident surface shortwave radiation, which implies an accurate simulation of surface albedo. Accordingly, IBIS-AS captures the observed seasonal cycle of absorbed surface shortwave radiation best.

Incident top of atmosphere shortwave radiation is included for completeness and is modeled accurately.

Biases in 2-m temperature are strong correlated with inaccuracies in the shortwave radiation budget, and are therefore influenced by surface physics model throughout the year and by convective closure assumption during the summer (Figure 3-12). IBIS-AS simulates 2-m temperature best, with a slight warm bias in the winter and summer, peaking at 1.6°C in the month of January. 2-m temperature is underestimated by BATS-FC by 2.5°C during the spring and throughout the year by 1.4°C.

Downward longwave radiation is underestimated in all models by approximately 12 W m^{-2} on an annual basis.

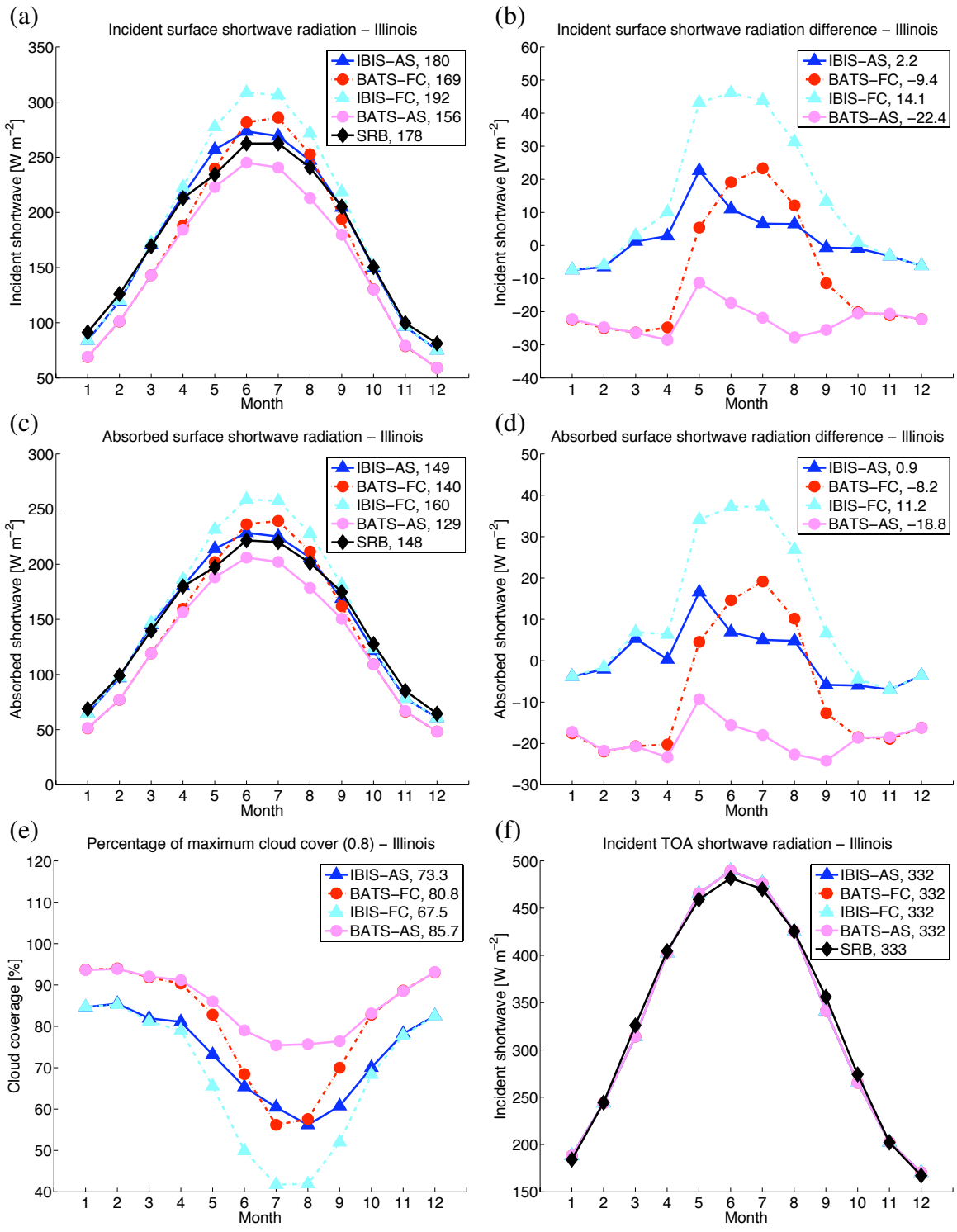

Figure 3-11: NNRP2 control and observed seasonal cycles of: (a) incident surface shortwave radiation, (c) absorbed surface shortwave radiation, (e) percentage of maximum model fractional cloud cover (0.8), (f) incident top of atmosphere (TOA) shortwave radiation; and the difference between NNRP2 control and observed seasonal cycles of: (b) incident surface shortwave radiation, (d) absorbed surface shortwave radiation for 1984-2004. Annual averages for each variable examined are provided in the legend.

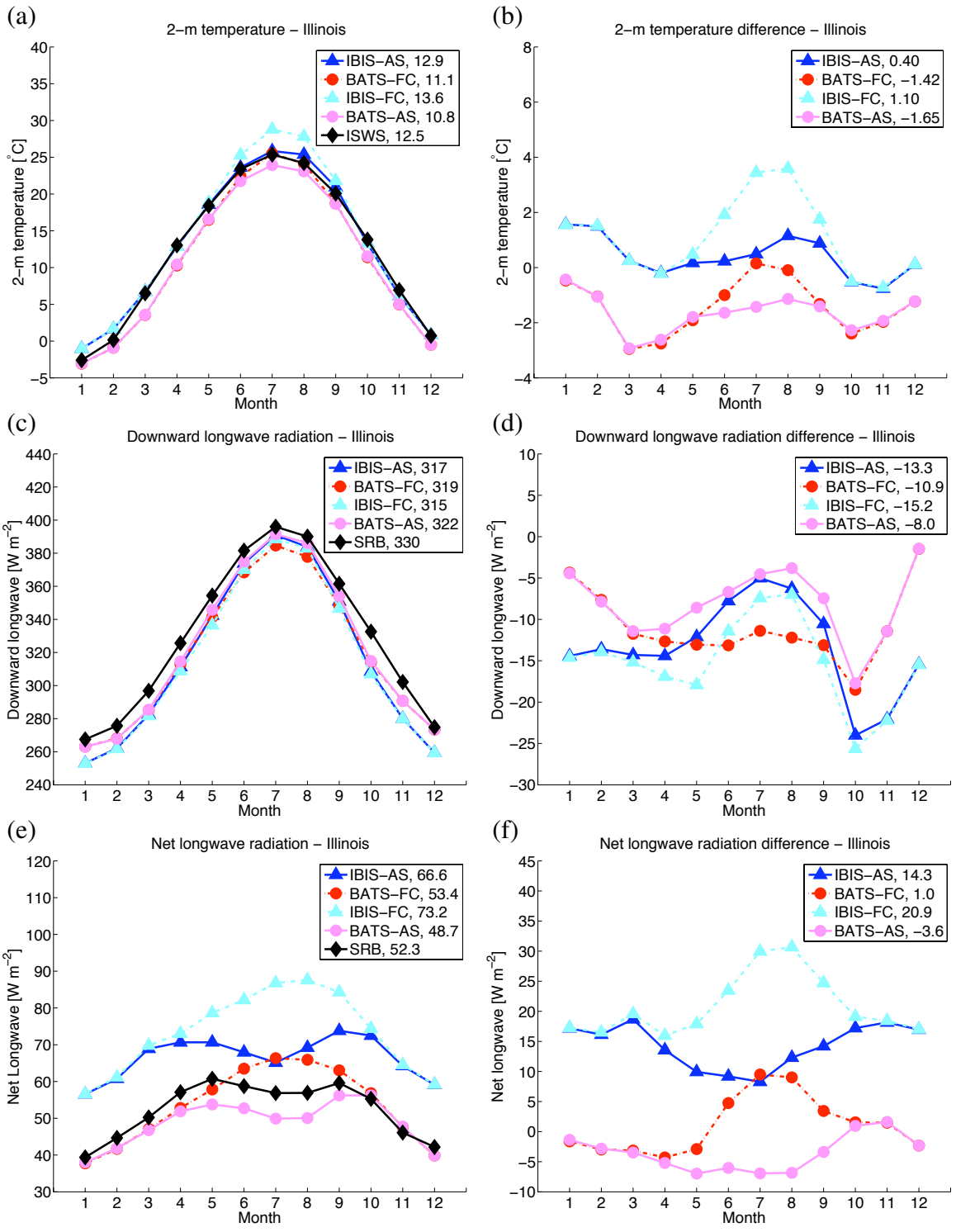

Figure 3-12: NNRP2 control and observed seasonal cycles of: (a) 2-m temperature, (c) downward longwave radiation, (e) net longwave radiation (defined as positive upward); and the difference between NNRP2 control and observed seasonal cycles of: (b) 2-m temperature, (d) downward longwave radiation, (f) net longwave radiation (defined as positive upward) for 1984-2004 (2-m temperature 1984-2005). Annual averages for each variable examined are provided in the legend.

BATS-FC simulates the annual average of net longwave radiation (defined as positive upward) best; however, the shape of the seasonal cycle does not match observations. While IBIS-AS is able to capture the shape of the net longwave radiation seasonal cycle, it consistently overestimates net longwave radiation by ≈14 W m^{-2} throughout the year. Net longwave radiation is influenced by convective closure via 2-m temperature. FC80 allows significantly more incident shortwave radiation to reach the surface during the summer, which warms the ground temperature and increases net longwave radiation.

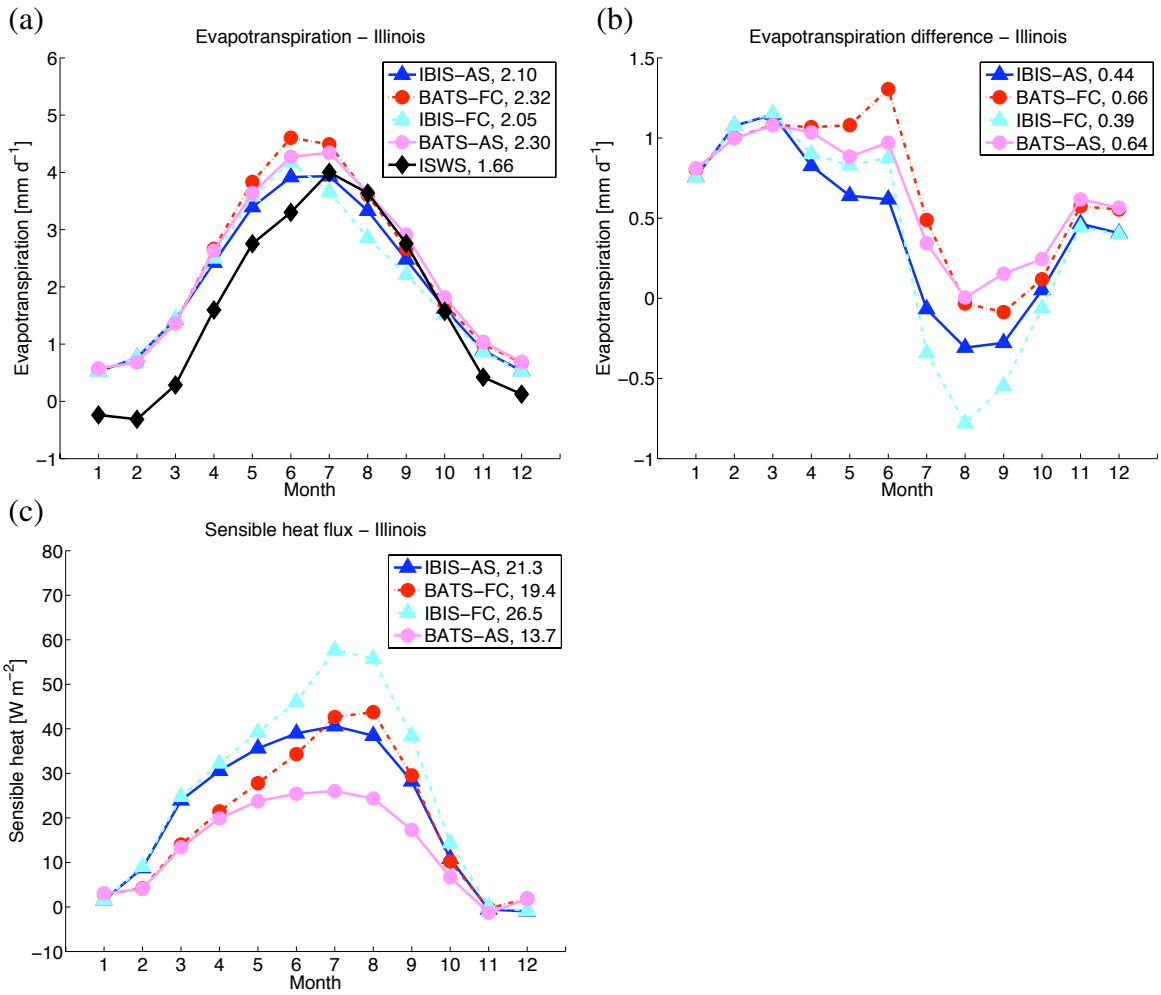

Figure 3-13: NNRP2 control and observed seasonal cycles of: (a) evapotranspiration, (c) sensible heat flux; and the difference between NNRP2 control and observed seasonal cycles of: (b) evapotranspiration for 1984-2005. Annual averages for each variable examined are provided in the legend.

Evapotranspiration is influenced primarily by surface physics scheme, and annually-averaged IBIS-AS and IBIS-FC simulate evapotranspiration better than BATS-FC and BATS-

AS. The seasonal cycle of evapotranspiration that is most consistent with observations is IBIS-AS; however, all models overestimate evapotranspiration in the winter, spring, and early summer. This overestimation of evapotranspiration is partially a result of the spring and summer wet biases of IBIS-AS, BATS-FC, IBIS-FC, and BATS-AS.

Sensible heat flux is influenced strongly by 2-m temperature, with the warmest model (IBIS-FC) producing the highest values of sensible heat flux and the coolest model (BATS-AS) the least. Unfortunately, no regional-scale observations of sensible heat flux exist for comparison.

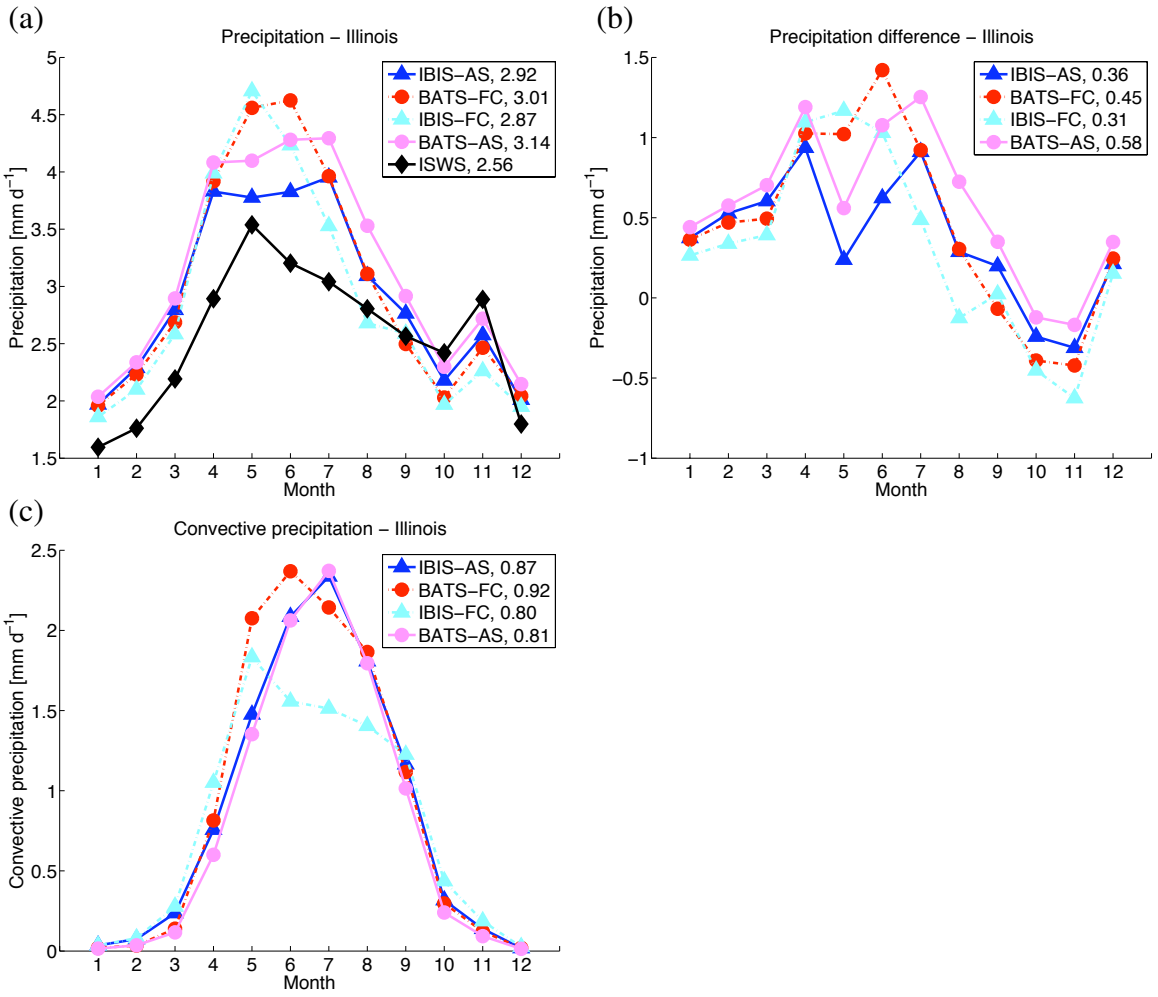

Figure 3-14: NNRP2 control and observed seasonal cycles of: (a) precipitation, (c) convective precipitation; and the difference between NNRP2 control and observed seasonal cycles of: (b) precipitation for 1984-2005. Annual averages for each variable examined are provided in the legend.

Precipitation is overestimated by all models during the spring and summer. No combi-

nation of convective closure assumption and surface physics scheme provides an accurate simulation of the seasonal cycle of precipitation. While FC80 grossly overestimates precipitation in May and June, AS74 simulates excessive precipitation in the late summer. IBIS-AS overestimates rainfall by 0.6 mm d^{-1} on average during the summer months (June, July, August). For those same months, the average wet bias in BATS-FC is 0.9 mm d^{-1}. Oddly, the FC80 closure assumption produces significantly different seasonal cycles convective precipitation in IBIS-FC and BATS-FC. In the FC80 closure assumption, warmer temperatures seem to reduce convective precipitation and increase large-scale precipitation. Errors in modeling precipitation represent a key uncertainty of this study.

Total runoff is well simulated by IBIS-AS, BATS-FC, and BATS-AS, as shown in Figure 3-15. IBIS-FC contains a large spike in precipitation that contributes to an overestimation of total runoff during May and June. IBIS-AS produces excess total runoff, 0.3 mm d^{-1}, in the month of May.

Surface runoff is a function of both precipitation and surface physics scheme. BATS-FC and BATS-AS grossly overestimate surface runoff throughout the year, on average 0.52 mm d^{-1}. This is a result of the inaccurate representation of surface and subsurface hydrology in RegCM3-BATS1e. IBIS-AS simulates surface runoff best, but still produces excessive surface runoff, especially during the winter and summer months.

Groundwater runoff is poorly simulated by BATS-FC and BATS-AS. On average, both models produce less than a sixth of observed runoff. Values for groundwater runoff in IBIS-AS generally agree with observations; however, too much groundwater runoff is simulated during the month of May, which is reflected in the overestimation of total runoff.

Figure 3-16 illustrates the dependence of surface soil moisture values on convective closure assumption. BATS-FC and IBIS-FC simulate surface soil moisture more accurately during the late summer (July, August, September) than IBIS-AS and BATS-AS. IBIS-AS overestimates surface soil moisture in the late summer by 0.09 on average. The minimum of the seasonal cycle for root zone soil moisture is delayed one month in IBIS-AS, BATS-FC, and BATS-AS. While IBIS-FC does simulate the shape of the seasonal cycle of root zone soil moisture best, it is too dry throughout the year. Averaged annually, IBIS-AS and BATS-FC underestimate root zone soil moisture by 0.06 and 0.13, respectively.

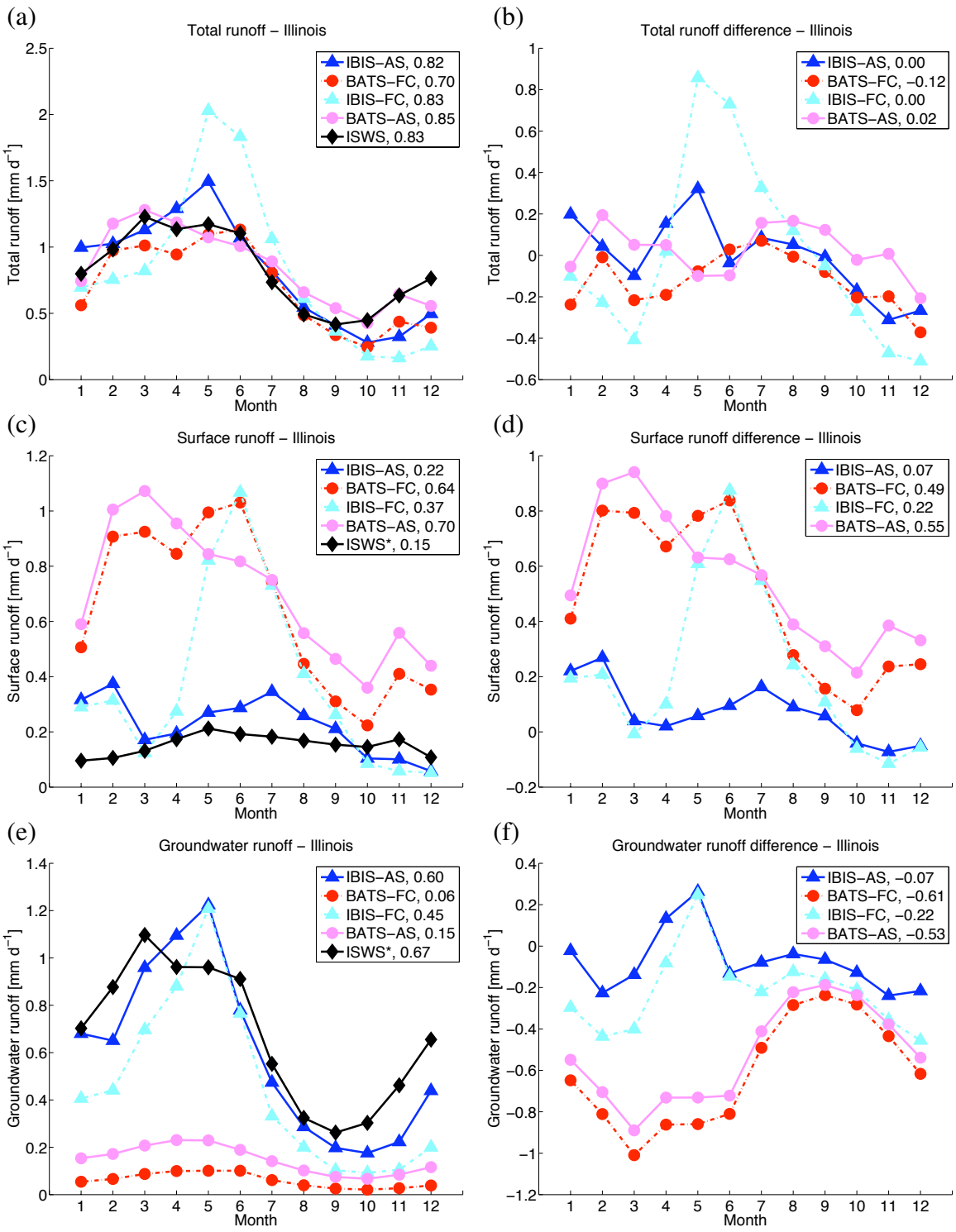

Figure 3-15: NNRP2 control and observed seasonal cycles of: (a) total runoff, (c) surface runoff, (e) groundwater runoff; and the difference between NNRP2 control and observed seasonal cycles of: (b) total runoff, (d) surface runoff, (f) groundwater runoff for 1984-2005. Annual averages for each variable examined are provided in the legend. *estimate of runoff as described in Section 3.2

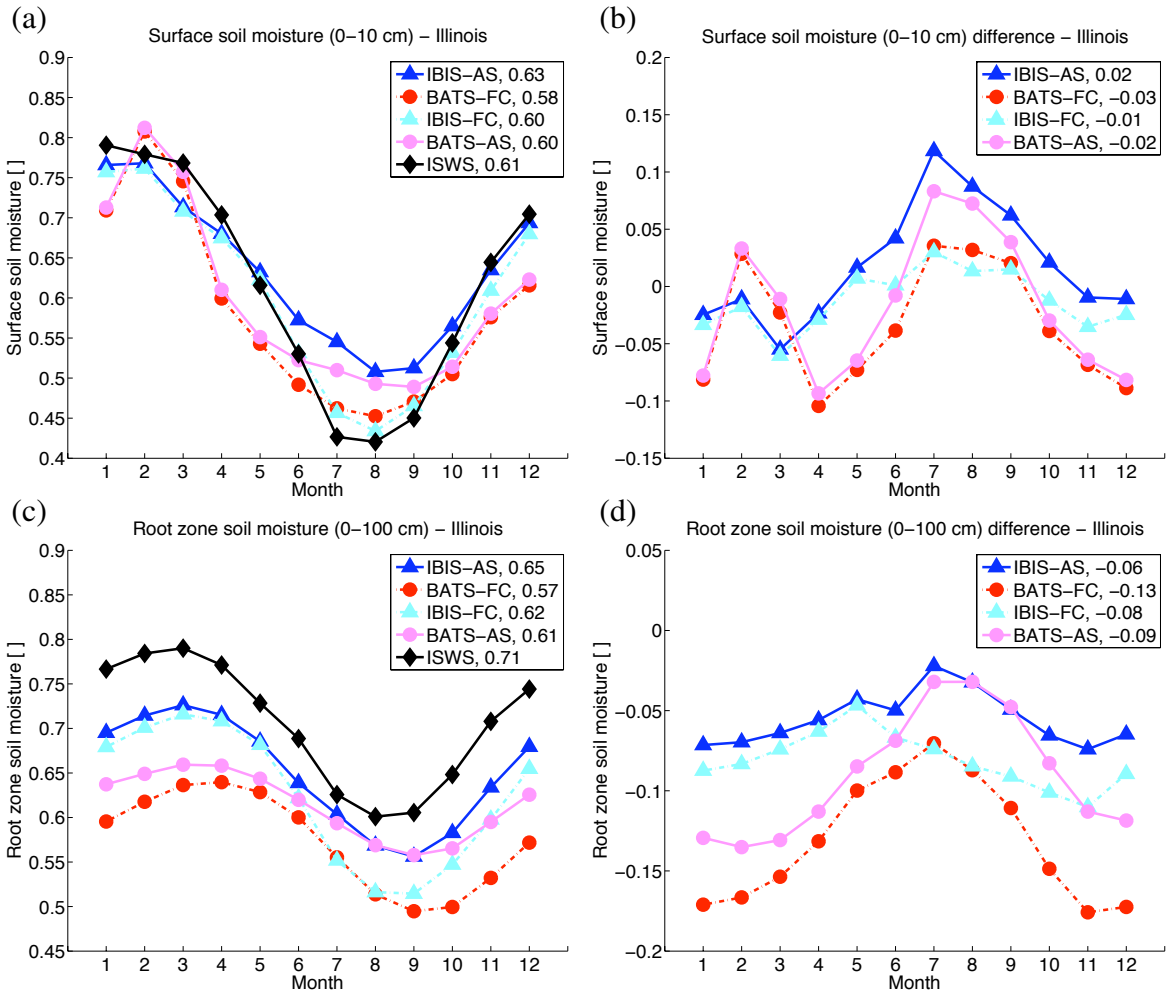

Figure 3-16: NNRP2 control and observed seasonal cycles of: (a) surface soil moisture, (c) root zone soil moisture; and the difference between NNRP2 control and observed seasonal cycles of: (b) surface soil moisture, (d) root zone soil moisture for 1984-2003. Annual averages for each variable examined are provided in the legend.

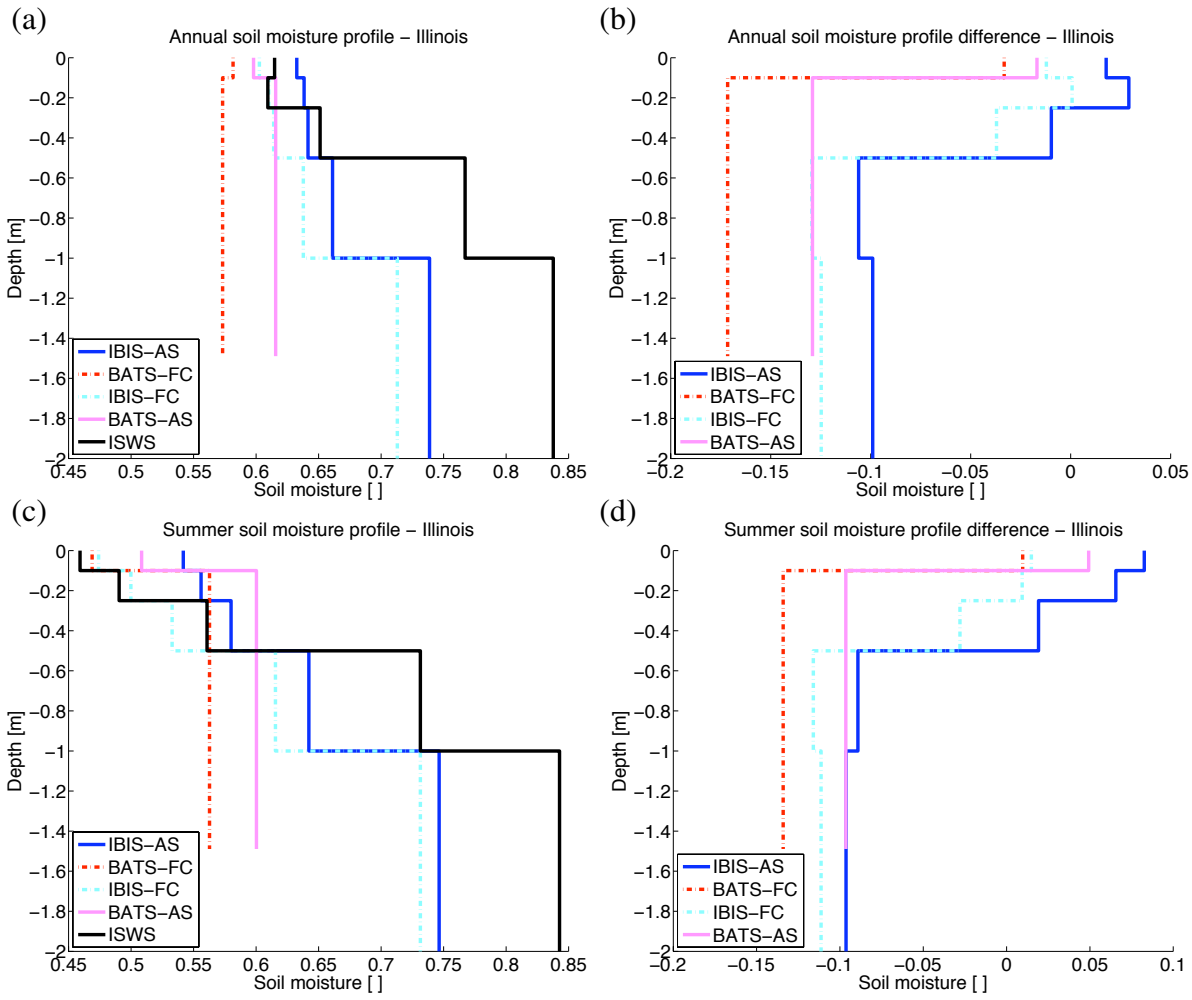

Figure 3-17: NNRP2 control and observed (a) annual, (c) summer (June, July, August) soil moisture profiles; and the difference between NNRP2 control and observed (b) annual, (d) summer (June, July, August) soil moisture profiles for 1984-2003.

The soil moisture profiles in Figure 3-17 are primarily a function of surface physics scheme; however, there is clearly an influence of convective closure assumption on soil moisture through precipitation, especially near the surface. Overall, IBIS-AS and IBIS-FC simulate soil moisture with depth much better than BATS-FC and BATS-AS. Averaged annually, IBIS-AS does capture the approximate shape of the soil moisture profile; however, the near-surface soil layers of IBIS-AS contain too much water, while at depth soils in IBIS-AS are drier than observations. BATS-FC underestimates soil moisture throughout the column. While all models simulate drying at the surface during the summer months, none are dry enough at the surface or wet enough in the lower soil layers. Note that while the depth of the root zone is fixed in IBIS-AS and IBIS-FC (0.1-2 m), in BATS-FC and BATS-AS it ranges from 0.1-1 m to 0.1-2 m based on vegetation type. The average depth of the root zone over the area considered is used to plot BATS-FC and BATS-AS soil moisture profiles.

Figures 3-18 and 3-19 reveal the performance of IBIS-AS and BATS-FC on a monthly basis. This yields important information about the variability of the climate system, as well as each model's skill in capturing that variability. This analysis was conducted using the two best performing model configurations from the above results: IBIS-AS and BATS-FC.

Both models simulate 2-m temperature well, with IBIS-AS overestimating slightly and BATS-FC underestimating slightly. The wet bias found in the seasonal cycles of both models is clearly visible in the Figure 3-18. While IBIS-AS and BATS-FC produce roughly the same range of monthly precipitation values as observations, on average both are too wet. The large scatter indicates that the ability of IBIS-AS and BATS-FC to produce the observed precipitation of any particular month is limited.

IBIS-AS and BATS-FC also overestimate evapotranspiration. Note that negative values for observed evapotranspiration are artifacts of the surface and atmospheric water balance as described in Section 3.2.

IBIS-AS and BATS-FC have difficulty simulating total runoff on a monthly basis (Figure 3-18). This is a result of total runoff being dependent in part on precipitation. Surface runoff is significantly overestimated by BATS-FC. This is shown by the proximity of BATS-FC data to the y-axis. Accordingly, values for groundwater runoff in BATS-FC are

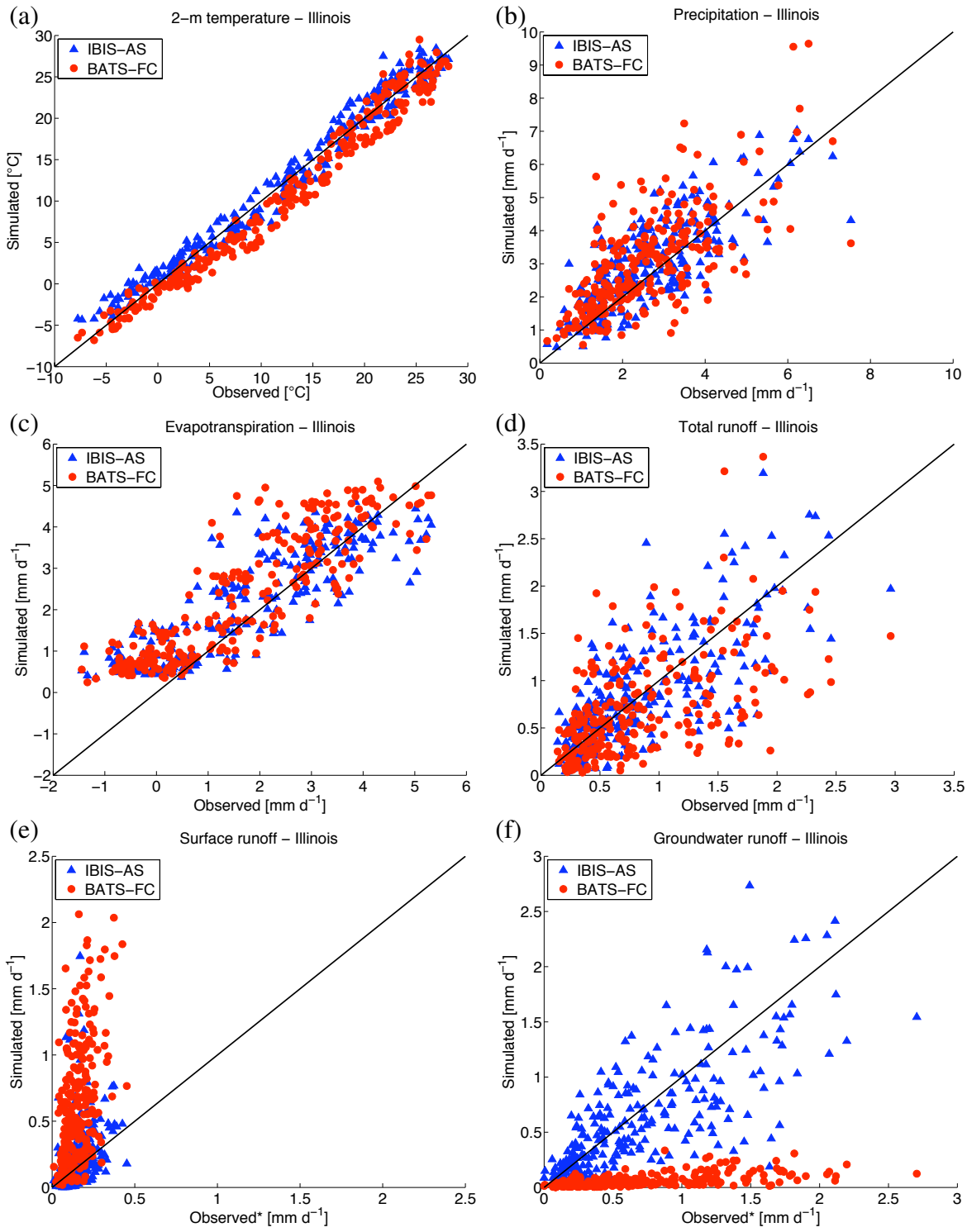

Figure 3-18: Scatter plots of: (a) temperature, (b) precipitation, (c) evapotranspiration, (d) total runoff, (e) surface runoff, (f) groundwater runoff using NNRP2 boundary conditions. Each point is a monthly average for 1984-2005. *estimate of runoff as described in Section 3.2

extremely low, and lie along the x-axis. IBIS-AS also overestimates surface runoff, and simulated extreme values of IBIS-AS surface runoff are larger than observations. On average, IBIS-AS simulates groundwater runoff much better; however, there is still significant scatter in the data.

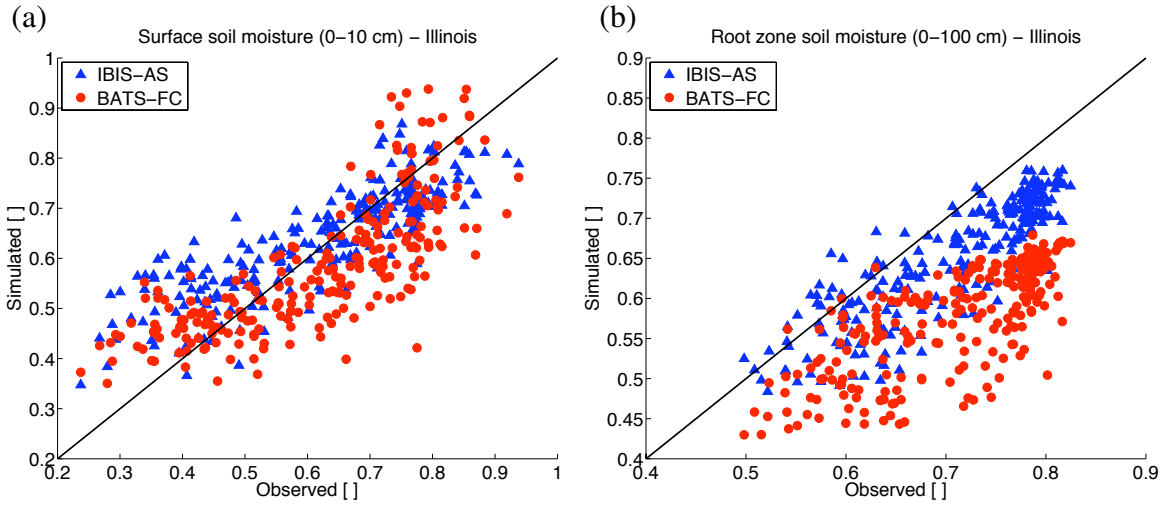

Figure 3-19: Scatter plots of: (a) surface soil moisture, (b) root zone soil moisture using NNRP2 boundary conditions. Each point is a monthly average for 1984-2003.

Surface soils in IBIS-AS are wetter than surface soils in BATS-FC, consistent with Figure 3-16. Figure 3-19 shows that IBIS-AS and BATS-FC overestimate surface soil moisture at low values (during the summer) and underestimate surface soil moisture at high values (during the winter). Root zone soil moisture is clearly underestimated by both models; however, IBIS-AS simulates root zone soil moisture better than BATS-FC.

The performance of IBIS-AS and BATS-FC throughout the contiguous United States during the summer (June, July, August) is shown in Figure 3-20. IBIS-AS overestimates summer 2-m temperature throughout much of the United States. This warm bias is especially pronounced along the west coast of California and the Baja Peninsula. BATS-AS also overestimates summer 2-m temperatures along the west coast of California and the Baja Peninsula, but simulates a cold bias over the northwestern and southeastern United States.

Summer precipitation is reasonably well simulated by IBIS-AS with the exception of an underestimation of June, July, August precipitation over the Gulf of Mexico coast and Florida. BATS-FC produces a wet bias across the majority of the United States, with

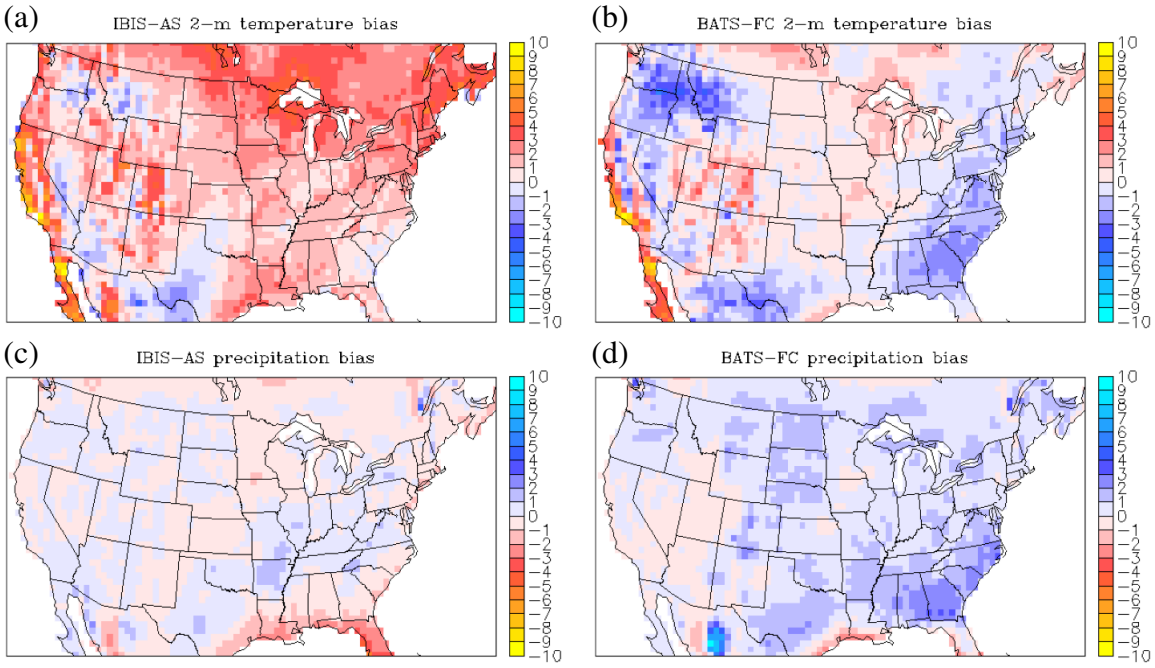

Figure 3-20: Summer (June, July, August) bias for: (a), (b) temperature; (c), (d) precipitation using NNRP2 boundary conditions. Each figure contains the difference between NNRP2 control and observed (CRU TS2.1) values for 1984-2002.

the largest overestimations of summer precipitation in the southeastern United States and northern Mexico.

3.3.2 ECHAM5 GCM

Presented results are 4.0° x 5.5° spatial averages over the box contained in Figure 3-1. Figures 3-21 to 3-29 contain a comparison of the two best performing model configurations from the NNRP2 numerical experiments: RegCM3-IBIS using the Arakawa & Schubert convective closure assumption (IBIS-AS) and RegCM3-BATS1e using the Fritsch & Chappell convective closure assumption (BATS-FC). IBIS-AS and BATS-FC were forced with boundary conditions derived from the EH5OM 20th century (1984-2000) and EH5OM A1B (2001-2005) simulations. In addition, the EH5OM model output for the domain examined is included for reference.

Figures 3-21 to 3-26 present each variable using a pair of panels, where the left panel shows the simulated and observed seasonal cycles, and the right panel shows the difference between the simulated and observed seasonal cycles.

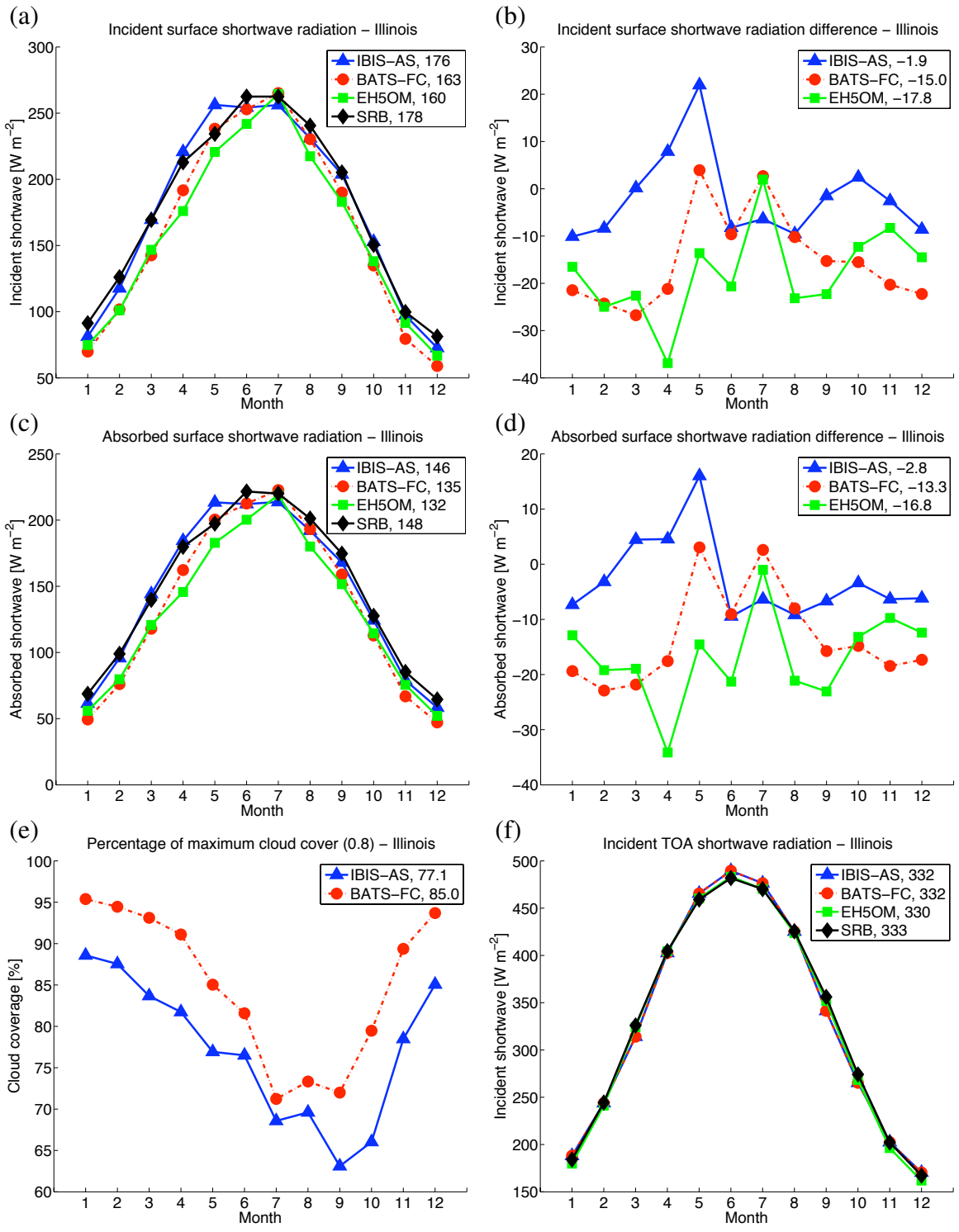

Figure 3-21: EH5OM control and observed seasonal cycles of: (a) incident surface shortwave radiation, (c) absorbed surface shortwave radiation, (e) percentage of maximum model fractional cloud cover (0.8), (f) incident TOA shortwave radiation; and the difference between EH5OM control and observed seasonal cycles of: (b) incident surface shortwave radiation, (d) absorbed surface shortwave radiation for 1984-2004. Annual averages for each variable examined are provided in the legend.

All three models do a reasonable job of capturing the observed seasonal cycle of incident surface shortwave radiation, as shown in Figure 3-21. BATS-FC and EH5OM underestimate incident surface shortwave radiation during the spring (March, April, May) by 15 W m^{-2} and 24 W m^{-2}, respectively. The values of incident surface shortwave radiation simulated by IBIS-AS are very similar NASA SRB, both averaged annually and monthly; however, IBIS-AS does overestimate incident surface shortwave radiation by 22 W m^{-2} during the month of May.

Errors in absorbed surface shortwave radiation are well correlated with incident surface shortwave radiation errors, suggesting a consistent surface albedo across models and observations. The ability of both IBIS-AS and BATS-FC to correctly simulate the shortwave radiation budget is consistent with the similarities in the seasonal cycle of cloud cover, shown in Figure 3-21.

Incident top of atmosphere shortwave radiation is well simulated by IBIS-AS, BATS-FC, and EH5OM, and is included for completeness.

EH5OM provides cooler boundary conditions than NNRP2. As a result, IBIS-AS simulates 2-m temperature correctly throughout most of the year, but underestimates summer (June, July, August) 2-m temperature slightly (Figure 3-22). BATS-FC develops a more significant cold bias, and produces 2-m temperatures that are consistently $\approx$2.3°C lower than observations.

Downward longwave radiation is underestimated throughout the year by BATS-FC (14.6 W m^{-2}) and IBIS-AS (16.5 W m^{-2}). EH5OM accurately simulates downward longwave radiation, except in the months of October and November.

BATS-FC simulates net longwave radiation (defined as positive upward) very well, benefitting from reduced surface temperatures during the months of June and July (Figure 3-22). This allows BATS-FC to capture both the correct magnitude and shape of the observed seasonal cycle. EH5OM reasonably approximates observations, with larger (and correct) values for downward longwave radiation, which reduces net longwave radiation. The simulation of net longwave radiation by IBIS-AS is improved slightly during the summer compared with NNRP2 experiments, but averaged annually IBIS-AS still overestimates net longwave radiation by 13 W m^{-2}. It is expected that correcting the bias in downward

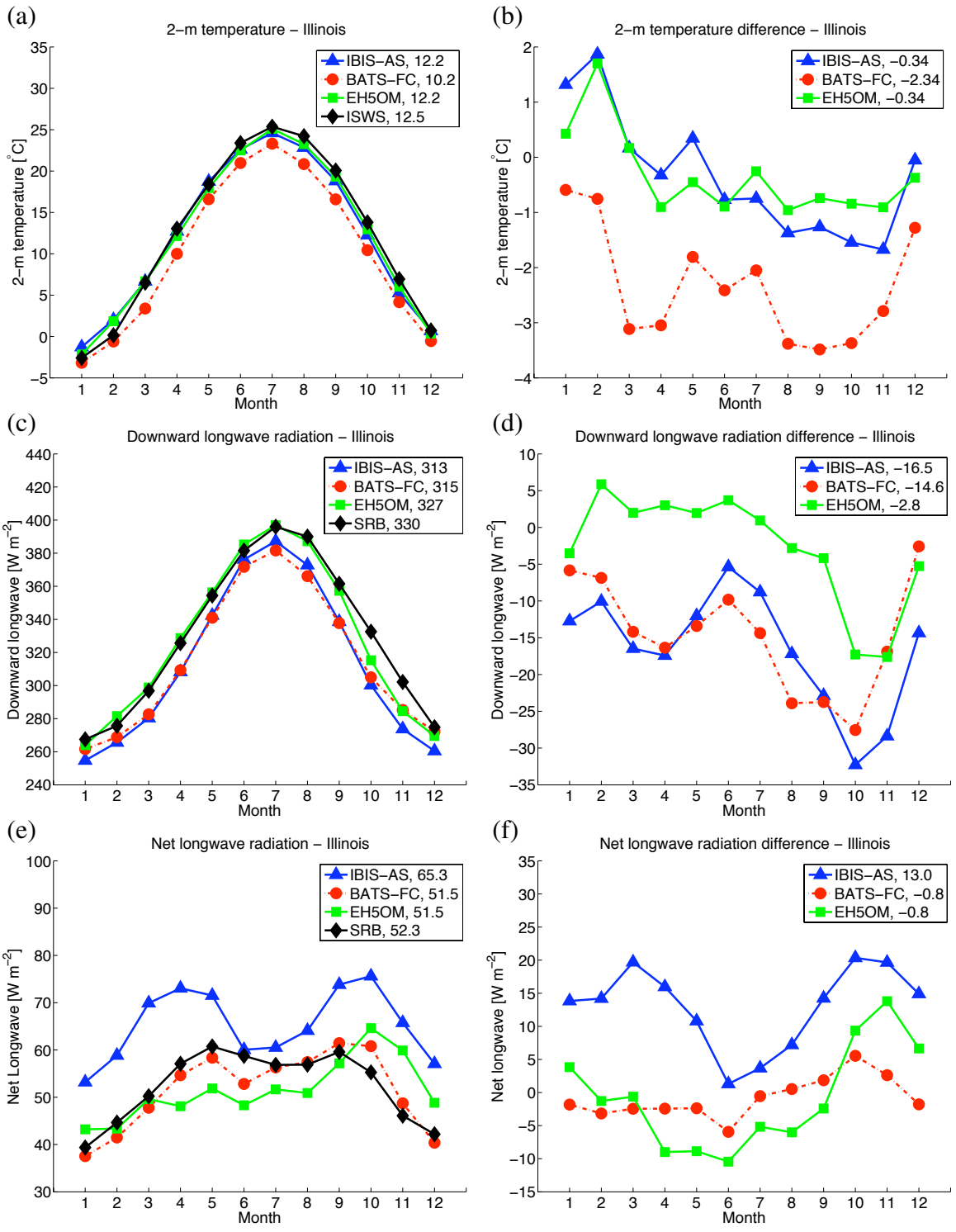

Figure 3-22: EH5OM control and observed seasonal cycles of: (a) 2-m temperature, (c) downward longwave radiation, (e) net longwave radiation (defined as positive upward); and the difference between EH5OM control and observed seasonal cycles of: (b) 2-m temperature, (d) downward longwave radiation, (f) net longwave radiation (defined as positive upward) for 1984-2004 (2-m temperature 1984-2005). Annual averages for each variable examined are provided in the legend.

longwave radiation in IBIS-AS would fix errors in net longwave radiation.

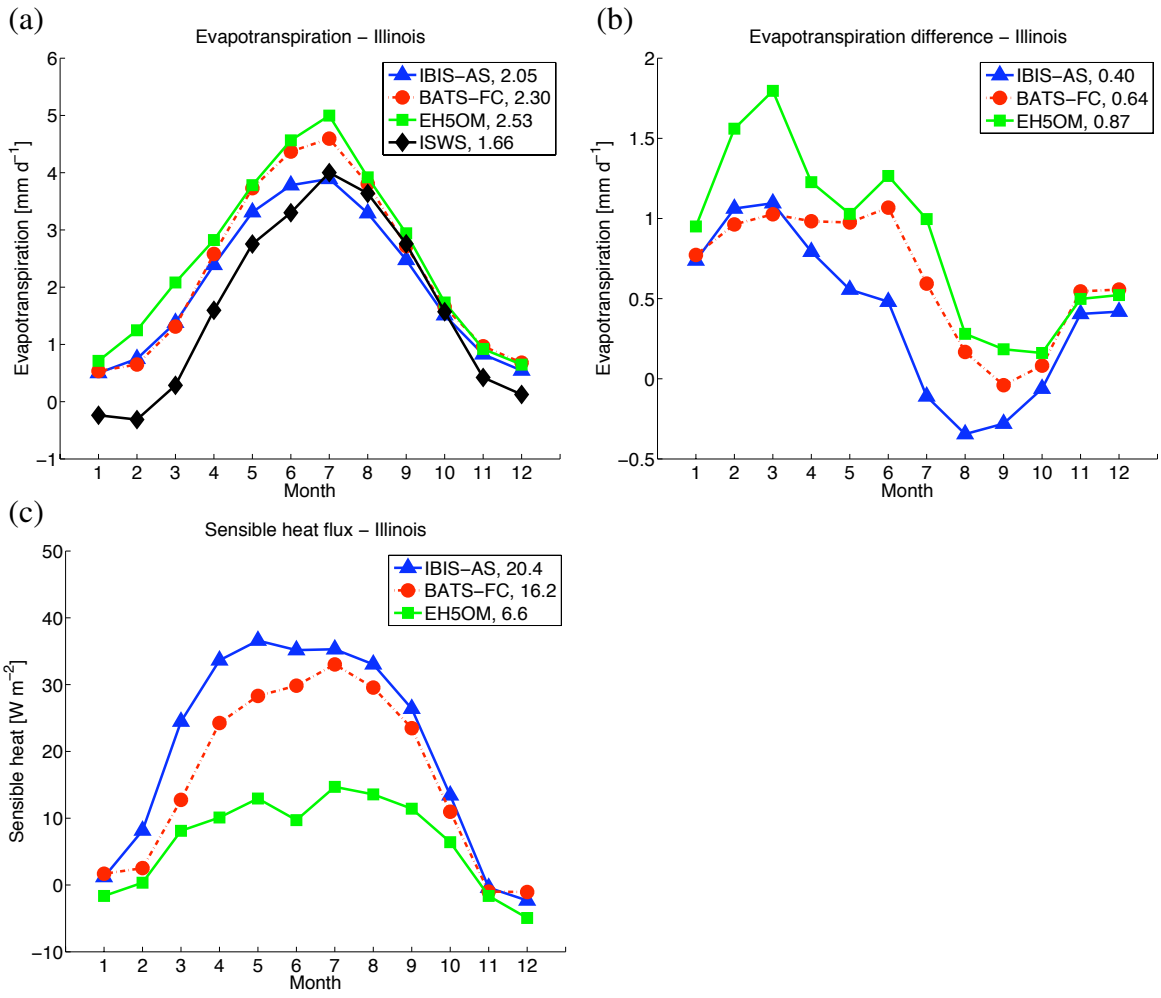

Figure 3-23: EH5OM control and observed seasonal cycles of: (a) evapotranspiration, (c) sensible heat flux; and the difference between EH5OM control and observed seasonal cycles of: (b) evapotranspiration for 1984-2005. Annual averages for each variable examined are provided in the legend.

The evapotranspiration seasonal cycles simulated by IBIS-AS and BATS-FC under EH5OM boundary conditions are very similar to the evapotranspiration seasonal cycles simulated by IBIS-AS and BATS-FC under NNRP2 boundary conditions. This suggests that evapotranspiration is heavily influenced by surface physics scheme (Figure 3-23). Accordingly, the seasonal cycle of evapotranspiration is significantly overestimated by IBIS-AS, BATS-FC, and EH5OM during the spring (March, April, May) and winter (December, January, February). BATS-FC and EH5OM also overestimate evapotranspiration during the summer.

Sensible heat flux decreases slightly in IBIS-FC and BATS-FC using EH5OM boundary conditions relative to IBIS-AS and BATS-FC using NNRP2 boundary conditions, a result of cooler 2-m temperatures. Unfortunately, no regional-scale observations of sensible heat flux exist for comparison.

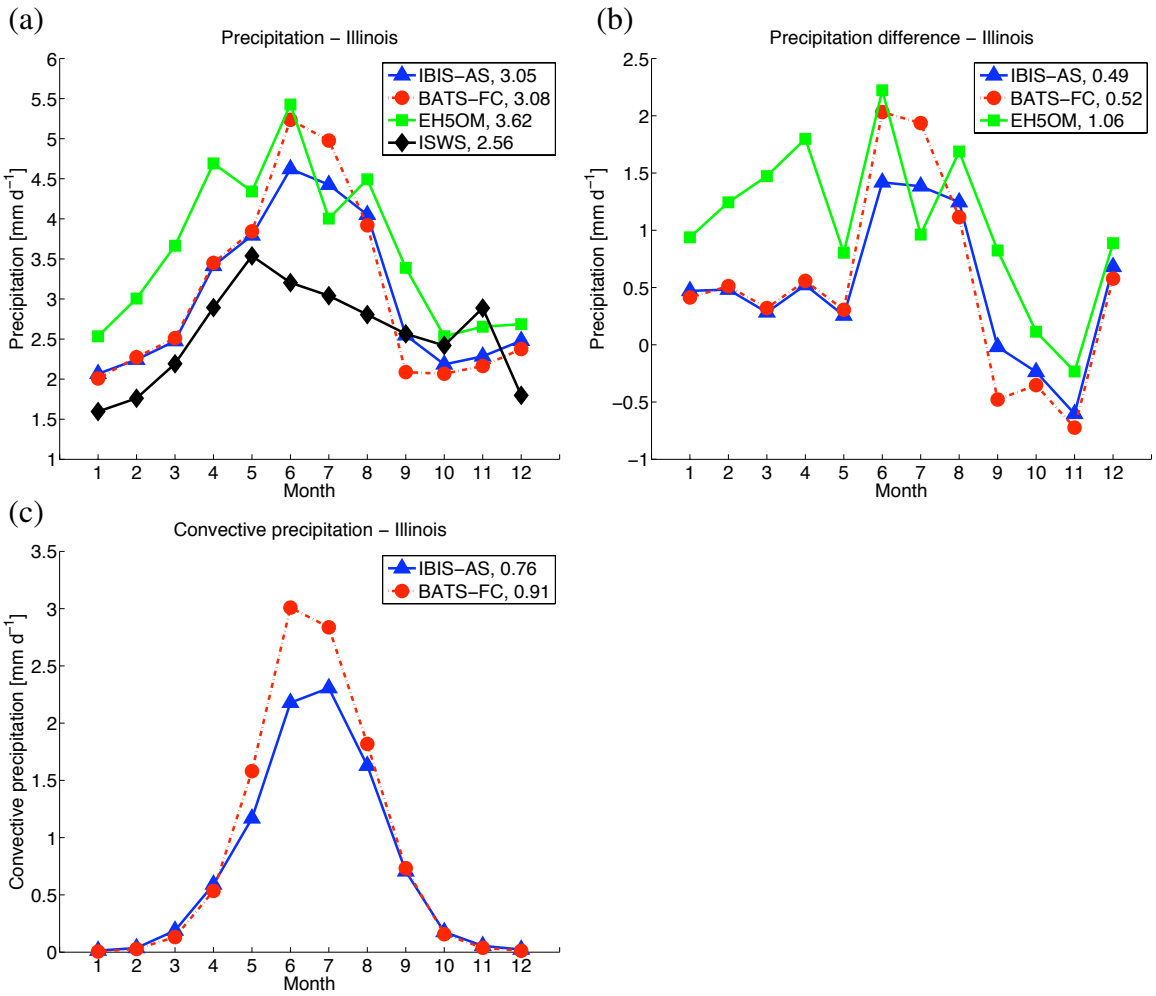

Figure 3-24: EH5OM control and observed seasonal cycles of: (a) precipitation, (c) convective precipitation; and the difference between EH5OM control and observed seasonal cycles of: (b) precipitation for 1984-2005. Annual averages for each variable examined are provided in the legend.

Precipitation is significantly overestimated by all three models. IBIS-AS and BATS-FC forced with EH5OM data simulate more rainfall during the summer than IBIS-AS and BATS-FC forced with NNRP2 data, suggesting wetter boundary conditions. This is consistent with the severe wet bias in the EH5OM simulation. The overestimation of precipitation seems largely independent of surface physics scheme and convective closure assumption.

While IBIS-AS does simulate the seasonal cycle of precipitation best, it contains a wet bias of 1.3 mm d^{-1} during the summer. BATS-FC and EH5OM overestimate precipitation in the summer by 1.7 mm d^{-1} and 1.6 mm d^{-1}, respectively. Differences in the simulation of rainfall during the summer between IBIS-AS and BATS-FC are primarily driven by convective precipitation.

While total runoff is well simulated by both regional climate models, the performance of IBIS-AS using EH5OM boundary conditions is degraded relative to the performance of IBIS-AS using NNRP2 boundary conditions, a result of increased precipitation. IBIS-AS and BATS-FC overestimate total runoff during the summer months by 0.34 mm d^{-1} and 0.26 mm d^{-1}, respectively (Figure 3-25). Annually averaged, BATS-FC simulates total runoff best. EH5OM also overestimates total runoff, a product of the wet bias in the model. Values are especially high during the spring, 0.44 mm d^{-1} larger than observations.

IBIS-AS, BATS-FC, and EH5OM simulate too much surface runoff. IBIS-AS captures the seasonal cycle of surface runoff best, with excessive values of surface runoff resulting from overestimated precipitation. BATS-FC and EH5OM simulate more than four times the observed surface runoff. Here, the overestimation of surface runoff is a function of both the overestimation of precipitation and errors in the representation of surface and subsurface hydrology.

Groundwater runoff is well simulated by IBIS-AS, however the peak and trough of the seasonal cycle both occur late. In addition, groundwater runoff during the months of July, August, and September is overestimated, likely driven by excess precipitation. BATS-FC vastly underestimates groundwater runoff, a result of its poor subsurface flow parameterization. EH5OM underestimates groundwater runoff throughout the year and simulates the annual minimum of groundwater runoff too early.

The seasonal cycle of surface soil moisture is shown in Figure 3-26. Surface soil moisture is overestimated by all three models during the summer. BATS-FC simulates summer surface soil moisture best, overestimating by only 0.06 on average during the months of July, August, and September. For that same period, IBIS-AS overestimates surface soil moisture by 0.14. Values of surface soil moisture simulated by EH5OM are considerably larger than observations, which is predominantly a result of the simplistic soil moisture

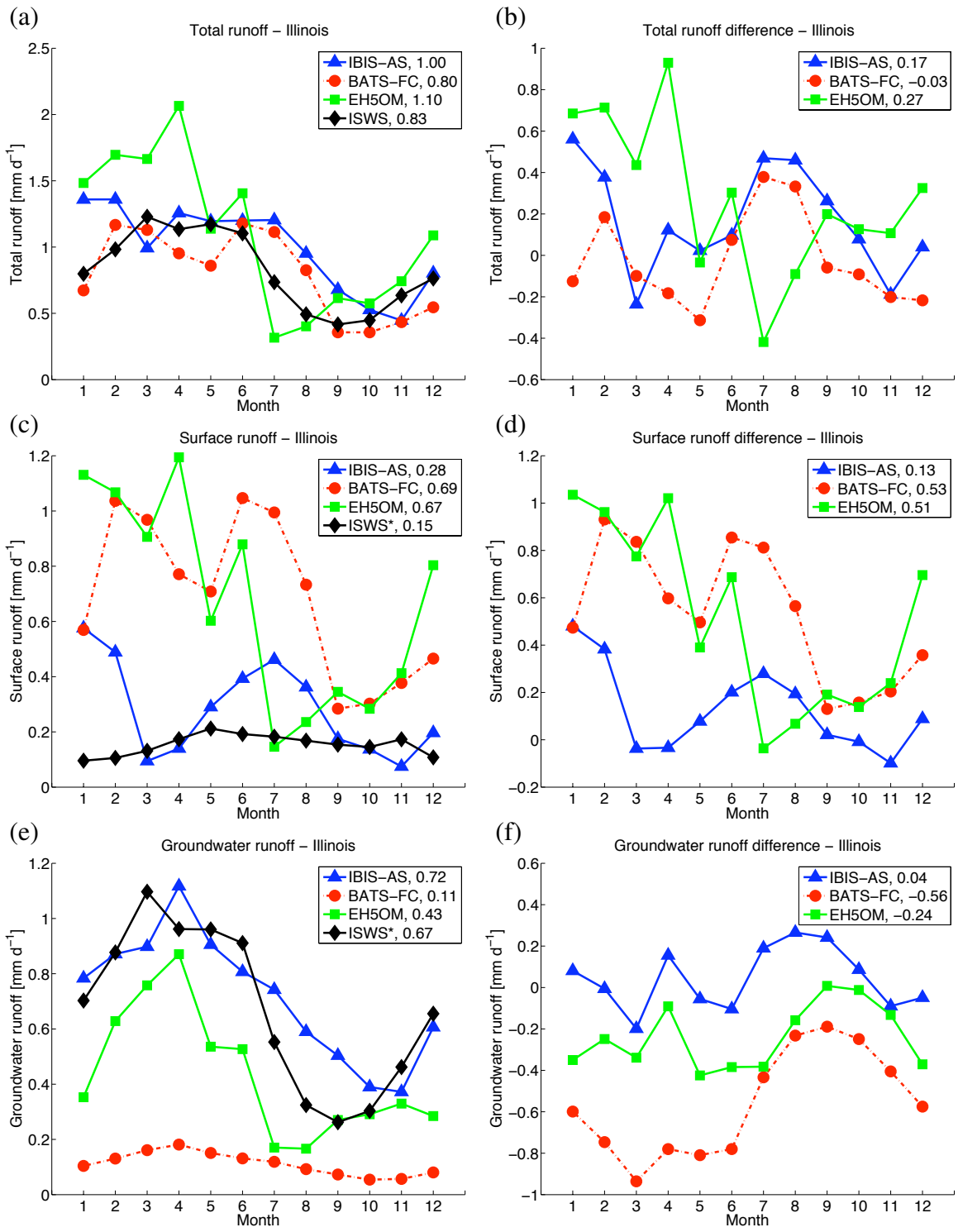

Figure 3-25: EH5OM control and observed seasonal cycles of: (a) total runoff, (c) surface runoff, (e) groundwater runoff; and the difference between EH5OM control and observed seasonal cycles of: (b) total runoff, (d) surface runoff, (f) groundwater runoff for 1984-2005. Annual averages for each variable examined are provided in the legend. *estimate of runoff as described in Section 3.2

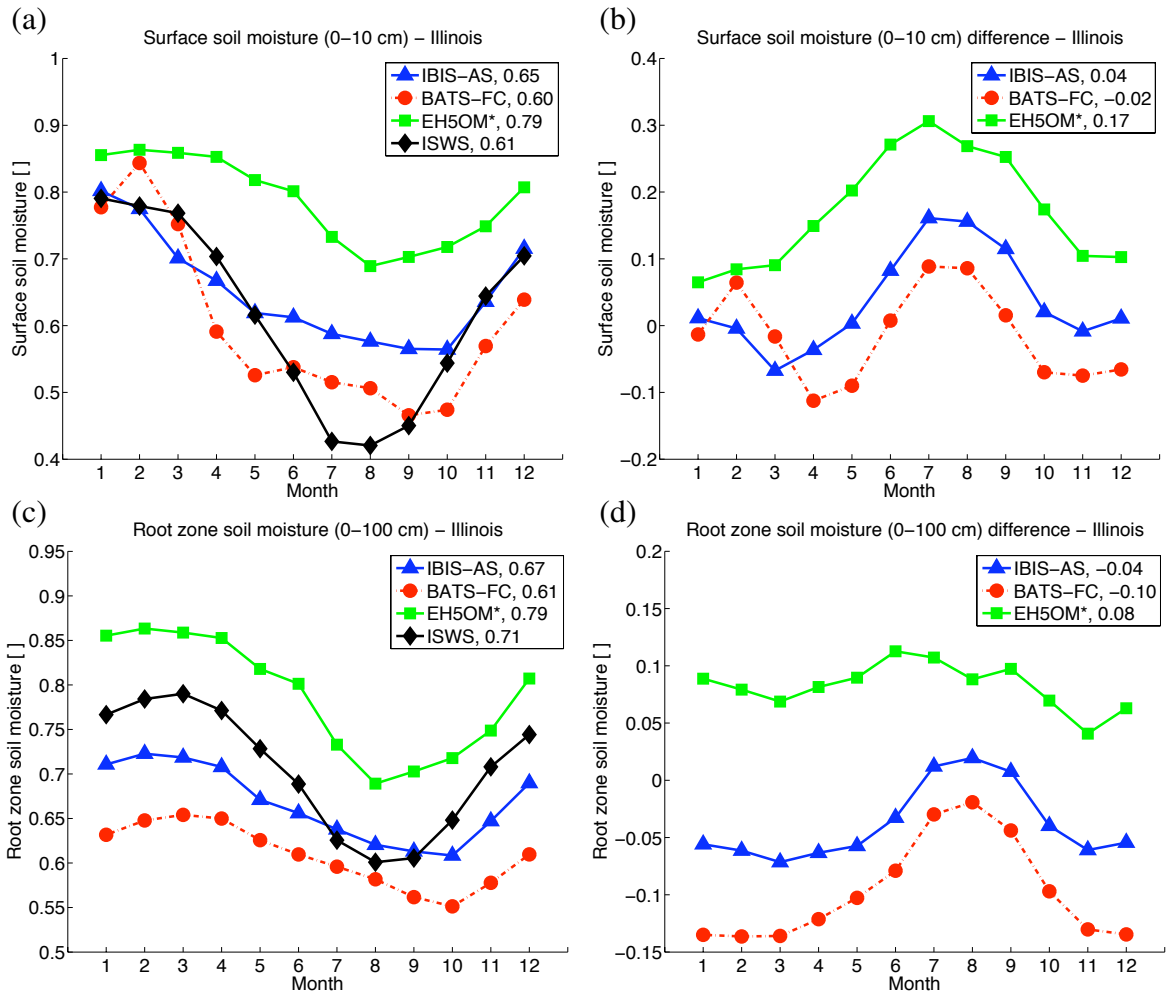

Figure 3-26: EH5OM control and observed seasonal cycles of: (a) surface soil moisture, (c) root zone soil moisture; and the difference between EH5OM control and observed seasonal cycles of: (b) surface soil moisture, (d) root zone soil moisture for 1984-2003. Annual averages for each variable examined are provided in the legend. *estimate of soil moisture as described in Section 3.3.2

representation in the ECHAM5 GCM.

EH5OM parameterizes soil moisture using a modified "bucket model". Soil moisture in EH5OM is the amount of water in the bucket relative to the total capacity of the bucket (field capacity of the soil). Because values for IBIS-AS and BATS-FC are given as fraction of total soil pore space containing liquid water, the soil moisture of EH5OM (which is relative to the soil field capacity) had to be scaled by the ratio of field capacity to total pore space derived from ISWS observations. Note that EH5OM simulates soil moisture as a singular bucket, so EH5OM values for surface and root zone soil moisture are always the same.

Root zone soil moisture is significantly overestimated by EH5OM (Figure 3-26), consistent with the excessive precipitation simulated by EH5OM and the simplistic representation of subsurface hydrology in EH5OM. IBIS-AS captures the seasonal cycle of root zone soil moisture best on average; however it is too dry in the winter and spring, the minimum of root zone soil moisture occurs two months late, and overall amplitude of the seasonal cycle is damped compared with observations. The seasonal cycle of BATS-FC is similar to that of IBIS-AS, but is drier overall. BATS-FC underestimates soil moisture for all months.

Annually averaged, BATS-FC simulates too little soil moisture throughout the soil column (Figure 3-27). IBIS-AS simulates too much soil moisture in the first three soil layers and not enough in the bottom two soil layers; however, the overall shape of the soil moisture profile is consistent with observations. During the summer months (June, July, August), IBIS-AS and BATS-FC simulate too much soil moisture near the surface and not enough at depth. Excessive soil moisture at the surface in IBIS-AS and BATS-FC is primarily a result of the overestimation of precipitation produced by both models. EH5OM does not model soil moisture changes in the vertical, so it is excluded from Figure 3-27. Note that while the depth of the root zone is fixed in IBIS-AS (0.1-2 m), in BATS-FC it ranges from 0.1-1 m to 0.1-2 m based on vegetation type. The average depth of the root zone over the area considered is used to plot BATS-FC soil moisture profiles.

Figures 3-28 and 3-29 reveal the performance of IBIS-AS and BATS-FC on a monthly basis. This yields important information about the variability of the climate system, as well as each model's skill in capturing that variability.

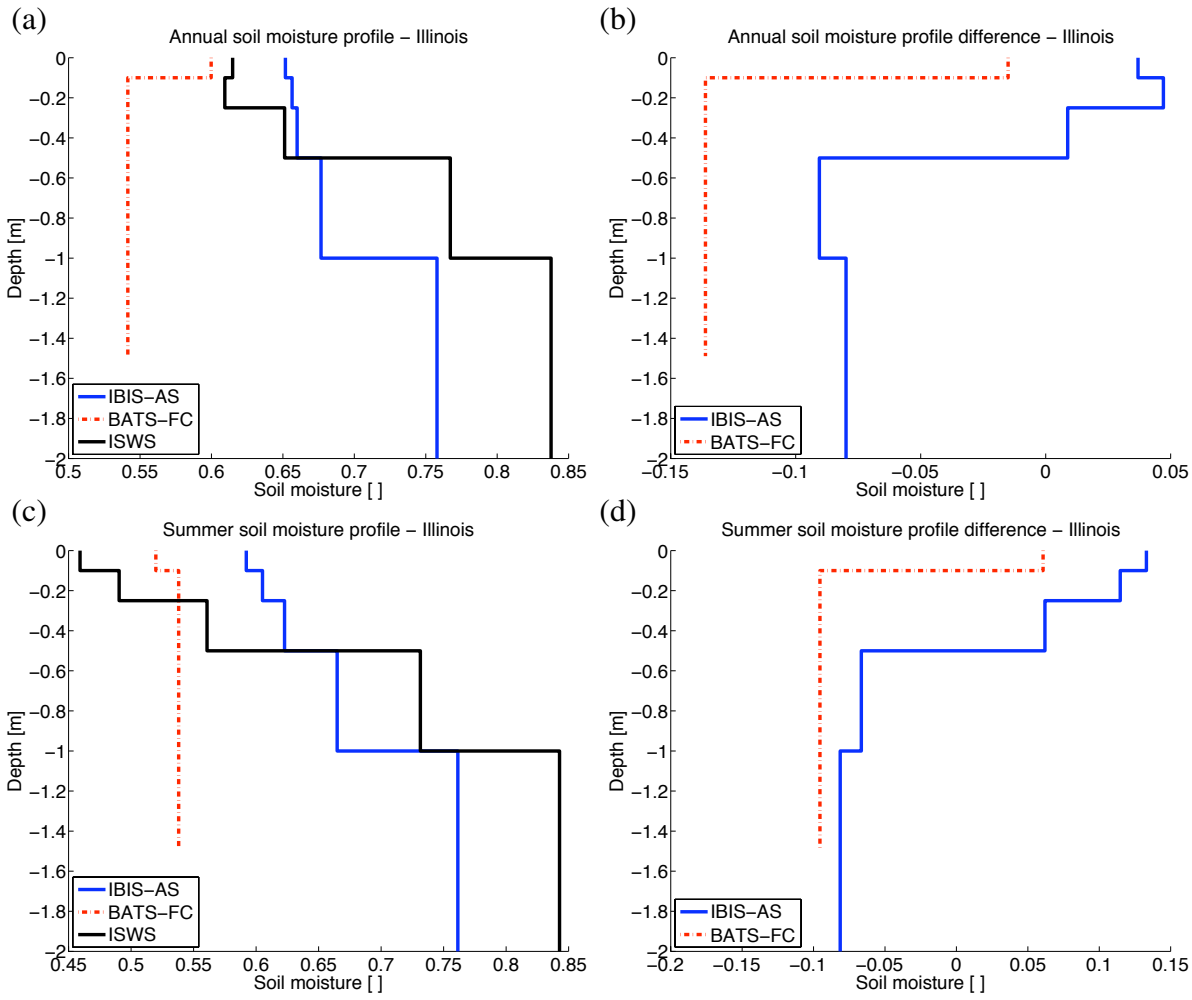

Figure 3-27: EH5OM control and observed (a) annual, (c) summer (June, July, August) soil moisture profiles; and the difference between the EH5OM control and observed (b) annual, (d) summer (June, July, August) soil moisture profiles for 1984-2003.

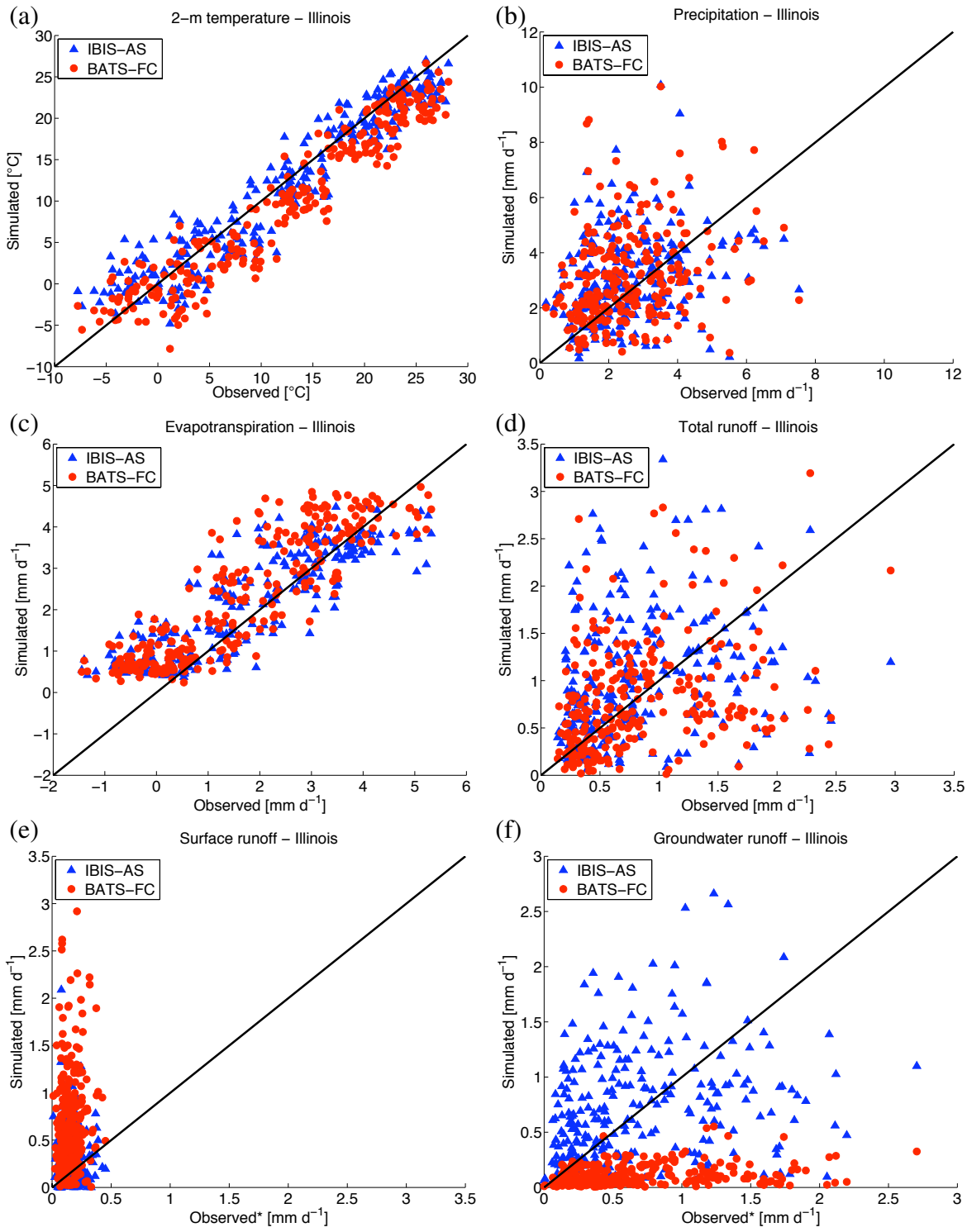

Figure 3-28: Scatter plots of: (a) temperature, (b) precipitation, (c) evapotranspiration, (d) total runoff, (e) surface runoff, (f) groundwater runoff using EH5OM boundary conditions. Each point is a monthly average for 1984-2005. *estimate of runoff as described in Section 3.2

Changing boundary conditions from NNRP2 to EH5OM significantly increases the scatter of IBIS-AS and BATS-FC 2-m temperature. BATS-FC shows a clear cold bias, consistent with its seasonal cycle, while on average IBIS-AS simulates 2-m temperature well. However, the increased scatter in both models indicates a reduced ability of IBIS-AS and BATS-FC to correctly model 2-m temperature. The simulation of precipitation in IBIS-AS and BATS-FC is degraded, including higher extreme values and larger biases, when EH5OM boundary conditions are used instead of NNRP2 boundary conditions.

The simulation of IBIS-AS and BATS-FC evapotranspiration shown in Figure 3-28 appears relatively unchanged from the NNRP2 experiments, suggesting that evapotranspiration is strongly controlled by the surface physics scheme and relatively unresponsive to changes in boundary conditions. Note that negative values for observed evapotranspiration are artifacts of the surface and atmospheric water balance as described in Section 3.2.

The scatter and bias of IBIS-AS and BATS-FC total runoff forced using EH5OM boundary conditions are larger than the scatter and bias of IBIS-AS and BATS-FC total runoff forced using NNRP2 boundary conditions. This result is consistent with the increases in scatter and bias of precipitation discussed above. While IBIS-AS and BATS-FC do capture the average of total runoff, the ability of both models to simulate total runoff on a monthly basis is modest. Surface runoff is overestimated by IBIS-AS and BATS-FC, although values for IBIS-AS are much closer to observations. Errors in the runoff parameterizations of BATS-FC are responsible for the majority of total runoff being partitioned to surface runoff. This same error leads to a gross underestimation of groundwater runoff in BATS-FC. IBIS-AS groundwater runoff does match observations reasonably well; however, the large scatter in Figure 3-28 indicates that IBIS-AS has difficulty simulating monthly groundwater runoff.

Surface soil moisture in IBIS-AS and BATS-FC is overestimated during dry conditions, especially in IBIS-AS. There is significant scatter in the surface soil moisture values of both models. Root zone soil moisture is underestimated for all but the driest of conditions in IBIS-AS and BATS-FC. The range of values in both models is smaller than observed. This suggests that soils are not allowed to adequately saturate during the winter and spring months, and do not lose enough water during the summer.

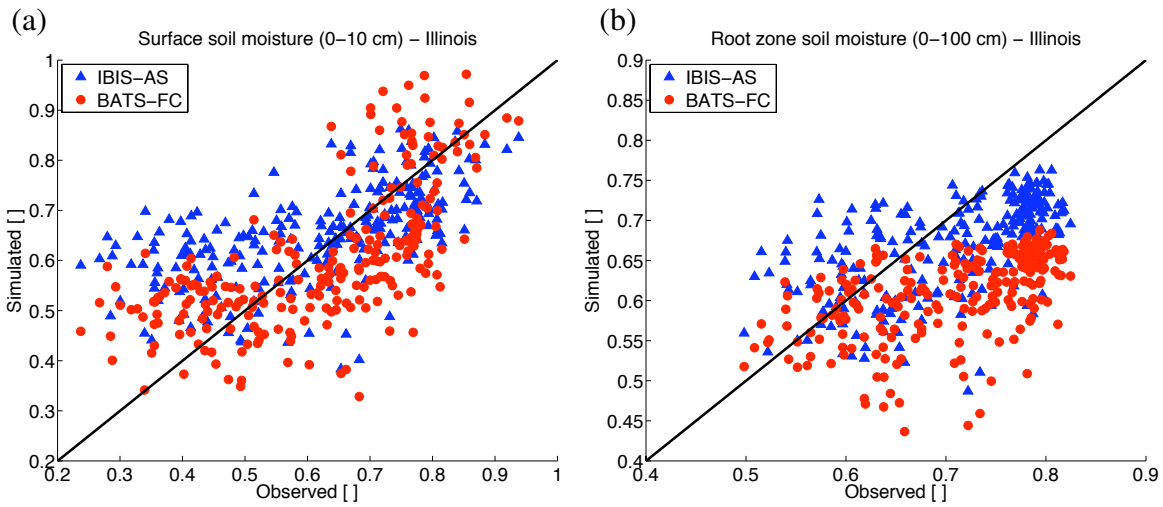

Figure 3-29: Scatter plots of: (a) surface soil moisture, (b) root zone soil moisture using EH5OM boundary conditions. Each point is a monthly average for 1984-2003.

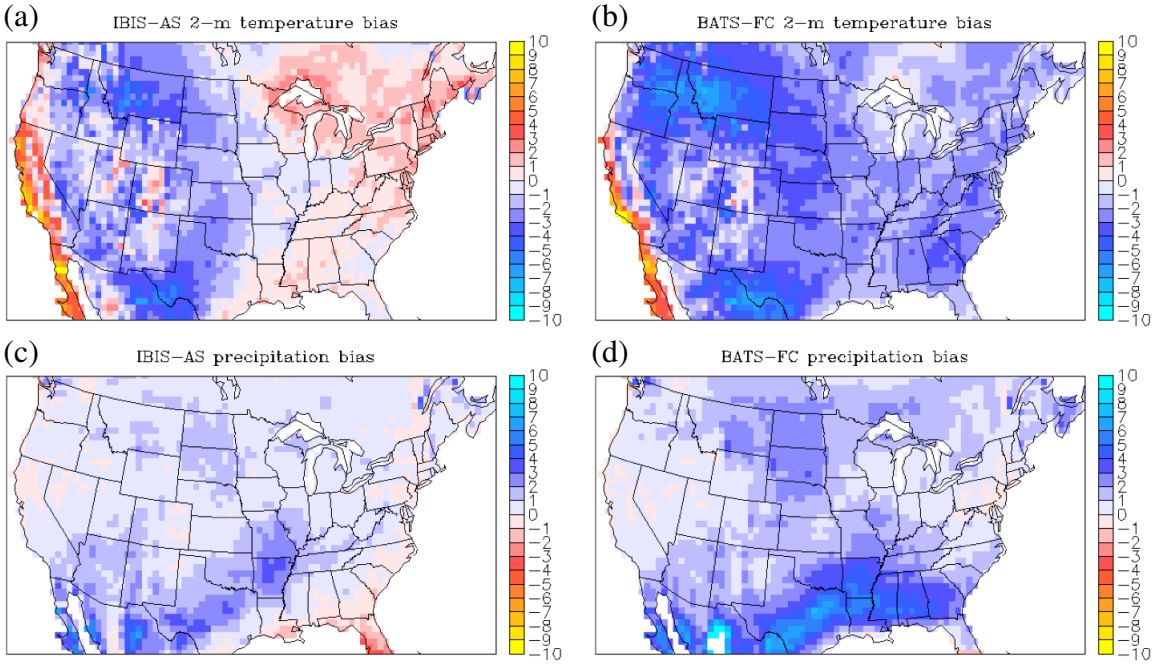

Figure 3-30: Summer (June, July, August) bias for: (a), (b) temperature; (c), (d) precipitation using EH5OM boundary conditions. Each figure contains the difference between EH5OM control and observed (CRU TS2.1) values for 1984-2002. White pixels surrounded by intense color (e.g. central Mexico in the lower right panel) denote biases that are larger or smaller than the colorbar limits.

The performance of IBIS-AS and BATS-FC throughout the contiguous United States during the summer (June, July, August) is shown in Figure 3-30. The summer 2-m temperature bias of IBIS-AS using EH5OM boundary conditions is smaller than the summer 2-m temperature bias of IBIS-AS using NNRP2 boundary conditions across the eastern half of the United States. IBIS-AS simulates a significant warm bias over the west coast of California and the Baja Peninsula, as well as a cold bias within Montana and northern Mexico. BATS-FC forced by EH5OM shows degraded performance in summer 2-m temperature relative to BATS-FC forced by NNRP2 boundary conditions. While BATS-FC does simulate a warm bias along the west coast of California, the rest of the domain in too cold when compared to CRU TS2.1, especially over Montana and northern Mexico.

Consistent with Figure 3-24, summer precipitation simulated by both IBIS-AS and BATS-FC increases throughout the United States when forced using EH5OM boundary conditions instead of NNRP2 boundary conditions. While the dry bias along the Gulf of Mexico and Florida in IBIS-AS is reduced, a series of wet biases are created across northern Mexico running up the central Mississippi Valley. EH5OM boundary conditions enhance the summer wet bias simulated by BATS-FC using NNRP2 data, particularly across the southern United States.

3.4 Conclusions

The performance of RegCM3-IBIS and RegCM3-BATS1e was comprehensively evaluated over the American Midwest. Temperature and precipitation, as well as the primary components of the shortwave radiation, longwave radiation, surface water, and subsurface water budgets, were examined. This chapter describes one of the most extensive assessments of a regional climate model over the United States to date.

The ability of IBIS-AS to simulate incident surface shortwave radiation, absorbed surface shortwave radiation, net longwave radiation, 2-m temperature, total runoff, surface runoff, groundwater runoff, and root zone soil moisture over Illinois is significantly improved relative to IBIS-08. These improvements were accomplished by updating the optical properties of water vapor, including background aerosols, using the Arakawa & Schubert

closure assumption for the Grell parameterization of convection, and adding a cropland biome and plant functional type.

Overall, the model that reproduces the observed seasonal cycles of the climate system best using NNRP2 boundary conditions is IBIS-AS (Table 3.2). IBIS-AS, BATS-FC, IBIS-FC, and BATS-AS accurately simulate incident and absorbed surface shortwave radiation. Values for downward and net longwave radiation produced by all models are in reasonable agreement with observations. 2-m temperature is well simulated by IBIS-AS, BATS-FC, and BATS-AS on average; IBIS-FC overestimates 2-m temperature during the summer. IBIS-AS, BATS-FC, IBIS-FC, and BATS-AS simulate a significant wet bias in the spring, summer, and fall. This enhancement of precipitation is a key limitation in the ability of each model to accurately capture the observed hydroclimatology of the American Midwest. Evapotranspiration is overestimated by IBIS-AS, BATS-FC, IBIS-FC, and BATS-AS in the spring and early summer. Total runoff, surface runoff, and groundwater runoff are well simulated by IBIS-AS. While BATS-FC and BATS-AS do model the seasonal cycle of total runoff well, gross errors in the partitioning of total runoff between surface runoff and groundwater runoff exist. The seasonal cycle of root zone soil moisture simulated by IBIS-AS is slightly dry, but otherwise agrees with observations. BATS-FC, IBIS-FC, and BATS-AS all significantly underestimate root zone soil moisture.

IBIS-AS also performs best using EH5OM boundary conditions, as shown in Table 3.3. Increased cloud cover caused by the EH5OM forcing reduces shortwave radiation incident in BATS-FC, resulting in a cold bias. The overestimation of IBIS-AS and BATS-FC precipitation is larger in the EH5OM experiments than the overestimation of IBIS-AS and BATS-FC precipitation in the NNRP2 experiments.

Table 3.2: Comparison of model performance using NNRP2 boundary conditions. Each number is the annual average over Illinois for the dates available, as described in Section 3.2.

	Obs	IBIS-AS	BATS-FC	IBIS-FC	BATS-AS
Incident shortwave [W m^{-2}]	178	180	169	192	156
Absorbed shortwave [W m^{-2}]	148	149	140	160	129
2-m temperature [°C]	12.5	12.9	11.1	13.6	10.8
Downward longwave [W m^{-2}]	330	317	319	315	322
Net longwave [W m^{-2}]	52.3	66.6	53.4	73.2	48.7
Evapotranspiration [mm d^{-1}]	1.66	2.10	2.32	2.05	2.30
Precipitation [mm d^{-1}]	2.56	2.92	3.01	2.87	3.14
Total runoff [mm d^{-1}]	0.83	0.82	0.70	0.83	0.85
Surface runoff [mm d^{-1}]	0.15	0.22	0.64	0.37	0.70
Groundwater runoff [mm d^{-1}]	0.67	0.60	0.06	0.45	0.15
Surface soil moisture [ ]	0.61	0.63	0.58	0.60	0.60
Root zone soil moisture [ ]	0.71	0.65	0.57	0.62	0.61

Table 3.3: Comparison of model performance using EH5OM boundary conditions. Each value is an annual average over Illinois for dates available, as described in Section 3.2.

	Obs	IBIS-AS	BATS-FC	EH5OM
Incident shortwave [W m^{-2}]	178	176	163	160
Absorbed shortwave [W m^{-2}]	148	146	135	132
2-m temperature [°C]	12.5	12.2	10.2	12.2
Downward longwave [W m^{-2}]	330	313	315	327
Net longwave [W m^{-2}]	52.3	65.3	51.5	51.5
Evapotranspiration [mm d^{-1}]	1.66	2.05	2.30	2.53
Precipitation [mm d^{-1}]	2.56	3.05	3.08	3.62
Total runoff [mm d^{-1}]	0.83	1.00	0.80	1.10
Surface runoff [mm d^{-1}]	0.15	0.28	0.69	0.67
Groundwater runoff [mm d^{-1}]	0.67	0.72	0.11	0.43
Surface soil moisture [ ]	0.61	0.65	0.60	0.79
Root zone soil moisture [ ]	0.71	0.67	0.61	0.79

Chapter 4

Sensitivity of Latent Heat Flux to Available Energy

4.1 Introduction

Whether prescribed as an explicit climate sensitivity or calculated using multiple parameterizations, the response of the surface to changes in the atmosphere is uncertain. One uncertainty in particular, the sensitivity of latent heat flux to an increase in available energy, is especially salient as it directly impacts the effect of climate change on surface temperature.

Given an increase in radiation at the surface, by what relative magnitudes should climate models increase fluxes of latent and sensible heat? Are the responses of all models similar? If the responses are different, which one is correct? And if it is correct, is it for the right reasons? To answer these questions, a thorough understanding of both the climatology and sensitivity of the surface energy budget is needed.

Many studies have been conducted to asses the ability of surface and climate models to simulate latent heat flux. One of the most comprehensive analyses of uncertainty in surface physics models to date is the Project for Intercomparison of Land Surface Parameterization Schemes (PILPS). The goal of PILPS was to improve the surface parameterizations used in numerical weather and climate prediction models [Henderson-Sellers et al., 1996]. PILPS evaluated an extensive range of variables using both offline and atmospheric GCM

forcings to quantify the variability between different models and between models and observations. Phase 1a included twenty-three models. Each model completed offline simulations over grassland and tropical forest vegetation types using synthetic forcings [Pitman and Henderson-Sellers, 1998]. Phase 1c was similar to Phase 1a, but models were screened based on their ability to close the water and energy budgets within certain tolerances, and parameter values were assigned in a more rigorous fashion [Pitman and Henderson-Sellers, 1998]. The range in simulated fluxes of latent heat over grassland among the sixteen models participating in Phase 1c was 40-70 W m^{-2}.

A related study comparing 10 GCMs, the Atmospheric Model Intercomparison Project (AMIP), found latent heat flux values spanning a range of 30-95 W m^{-2} [Henderson-Sellers et al., 1996].

The wide range of values for latent heat flux found in both PILPS and AMIP demonstrates that there is considerable uncertainty in simulating the climatology of latent heat flux. And while there have been few studies comparing the sensitivity of latent heat flux among models, given the variability in the climatology, it is likely that significant differences exist.

A framework based on the Penman-Monteith equation is developed to identify deficiencies in model predictions of the climatology of evapotranspiration and the response of latent heat flux to an increase in surface radiation. Note that the terms "latent heat flux" and "evapotranspiration" are used interchangeably throughout this thesis. The theoretical sensitivity of latent heat flux to available energy is calculated by taking the partial derivative of the Penman-Monteith formulation of evapotranspiration with respect to available energy. The theoretical sensitivity is shown to be primarily dependent on the ratio of surface resistance to aerodynamic resistance, which are both calculated to gain additional insight into model performance. Figure 4-1 illustrates the influence of surface resistance and aerodynamic resistance on both the climatology of evapotranspiration (λE) and the sensitivity of latent heat flux to available energy ($\frac{\partial \lambda E}{\partial A}$). Many combinations of resistances can produce a specific latent heat flux; however, to capture both the correct climatology and sensitivity, only one combination of surface resistance and aerodynamic resistance is valid. Therefore, tuning a model to produce the right climatology alone is not adequate to simulate the re-

sponse of an ecosystem to a changing atmosphere. The analysis proposed below addresses this problem.

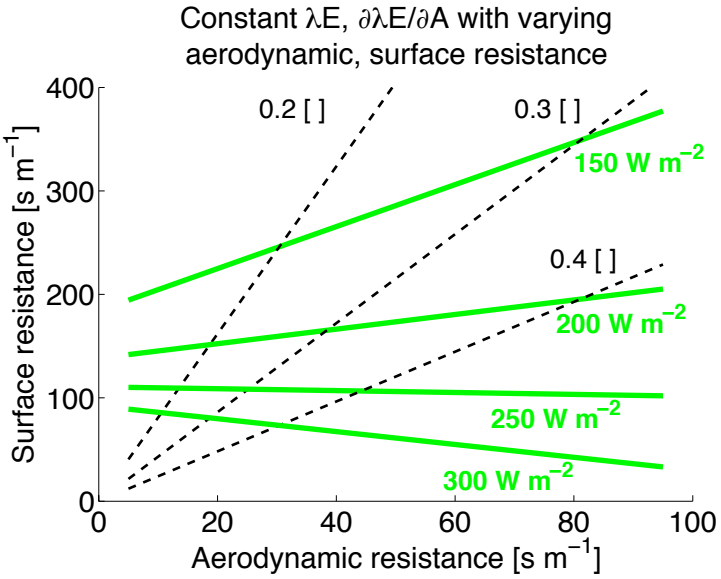

Figure 4-1: The relationship between surface, aerodynamic resistance and latent heat flux (green solid lines, green bold values), sensitivity of latent heat flux to available energy (black dashed lines, black values) derived using the Penman-Monteith equation. The slope of the saturation vapor pressure-temperature relationship, vapor pressure deficit, and available energy are assumed to be constant values of 150 Pa °C^{-1}, 1500 Pa, and 350 W m^{-2}, respectively.

4.2 Methodology

The Penman-Monteith equation was used to develop a consistent framework for comparing models and observations.

$$\lambda E = \frac{\Delta A + \frac{\rho c_p}{r_a}(e_{sat} - e)}{\Delta + \gamma\left(1 + \frac{r_s}{r_a}\right)} \tag{4.1}$$

λE is the latent heat flux, Δ is the slope of the saturation vapor pressure-temperature relationship, A is the available energy, ρ is the mean air density, c_p is the specific heat of air, r_a is the aerodynamic resistance, $(e_{sat} - e)$ is the vapor pressure deficit, γ is the psychometric constant, and r_s is the surface resistance [Shuttleworth, 1979].

All variables except r_s were acquired for each simulation and observational dataset. The Penman-Monteith equation was then used to calculate an implied surface resistance,

creating a uniform framework capable of comparing models of varying complexity as well as observations. In addition to r_s, r_a was carefully analyzed because of its strong influence on the partitioning of available energy between latent and sensible heat.

Since r_s and r_a are the two primary variables of interest, the partial derivative of latent heat flux was taken with respect to each.

$$\frac{\partial \lambda E}{\partial r_s} = \frac{-\Delta A r_a \gamma - \rho c_p \gamma \left(e_{sat} - e\right)}{\left(\Delta r_a + \gamma r_a + \gamma r_s\right)^2} \tag{4.2}$$

$$\frac{\partial \lambda E}{\partial r_a} = \frac{\Delta A r_s \gamma - \rho c_p \Delta \left(e_{sat} - e\right) - \rho c_p \gamma \left(e_{sat} - e\right)}{\left(\Delta r_a + \gamma r_a + \gamma r_s\right)^2} \tag{4.3}$$

Equation 4.2 shows that an increase in surface resistance suppresses latent heat flux. However, the effect of an increase in aerodynamic resistance is not immediately apparent. Both positive and negative terms exist in Equation 4.3, so the response of latent heat flux to a change in r_a is dependent on the variables describing the current system state.

$$r_s \uparrow \Longrightarrow \lambda E \downarrow \qquad\qquad r_a \uparrow \Longrightarrow \lambda E \downarrow \text{ or } \lambda E \uparrow \tag{4.4}$$

The sensitivity of latent heat flux to available energy is:

$$\frac{\partial \lambda E}{\partial A} = \frac{\Delta}{\Delta + \gamma \left(1 + \frac{r_s}{r_a}\right)}. \tag{4.5}$$

From Equation 4.5, it is clear that:

$$r_s \uparrow \Longrightarrow \frac{\partial \lambda E}{\partial A} \downarrow \qquad\qquad r_a \uparrow \Longrightarrow \frac{\partial \lambda E}{\partial A} \uparrow . \tag{4.6}$$

In order to better understand the climatology of latent heat flux and the sensitivity of latent heat flux to available energy simulated by RegCM3-IBIS and RegCM3-BATS1e, the developed framework is applied to model output and observations as described below.

4.3 Design of Experiments

RegCM3-IBIS and RegCM3-BATS1e were evaluated at two sites where extensive FLUXNET observations are available. FLUXNET is a network of over 400 micrometeorological tower sites that provides eddy covariance measurements of carbon, water vapor, and energy fluxes between the land surface and atmosphere [Baldocchi et al., 1998]. Bondville (BV), Illinois (40.0°N, 88.3°W) is an agricultural site with an annual rotation between soybeans (1998) and corn (1997,1999). Little Washita Watershed (LW), Oklahoma (35.0°N, 98.0°W) is a grassland located near Chickasha. The data used in this analysis are derived from the Marconi Conference Gap-Filled Flux and Meteorology Dataset [Falge et al., 2005].

It is important to acknowledge that errors exist in the FLUXNET observations of latent heat flux and sensible heat flux. Twine et al. [2000] found that uncertainty in the surface energy budget ranged from 10% to 30%, while uncertainty in measuring available energy was approximately 10%. To address errors in the measurements of latent and sensible heat, the methodology of Twine et al. [2000] was used to close the energy budget of FLUXNET observations. Specifically, ground heat flux was subtracted from net radiation to find available energy, and then latent and sensible heat fluxes were scaled to match available energy while preserving the Bowen ratio. The total annually averaged adjustments to available energy for Illinois and Oklahoma were 8 W m^{-2} and 17 W m^{-2}, respectively. In addition to FLUXNET observations, the seasonal cycles of surface temperature and precipitation were compared to the Climate Research Unit (CRU) Time Series 2.0 (TS2.0) and some aspects of the energy budget were evaluated using the National Aeronautics and Space Administration (NASA) Surface Radiation Budget (SRB) dataset, obtained from the NASA Langley Research Center Atmospheric Science Data Center [NASA, 2006].

RegCM3-IBIS and RegCM3-BATS1e were assessed using four years of simulated climate (1996-1999) chosen for maximum overlap with FLUXNET observations. Each numerical experiment was initialized April 1st, 1994 and allowed to spin-up for twenty-one months. The domain is centered at 40°N, 95°W and spans 100 points zonally, 60 points meridionally with a horizontal grid spacing of 60 km (Figure 4-2). The 40-year European Centre for Medium-Range Weather Forecasts (ECMWF) Re-Analysis (ERA40) dataset

[Uppala et al., 2005] was used to force the boundaries under the exponential relaxation of Davies and Turner [1977]. SSTs were prescribed using The National Oceanic and Atmospheric Administration Optimum Interpolation SST dataset [Reynolds et al., 2002].

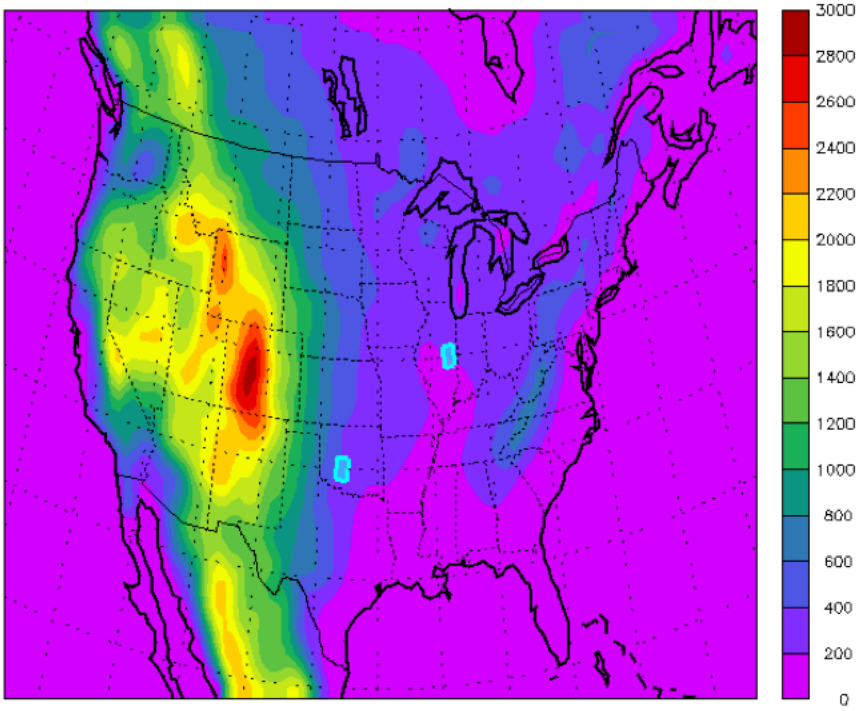

Figure 4-2: Domain and topography [m] with, from north to south, 1° x 1° cyan shaded boxes delineating the extent of spatial averaging over Bondville, IL and Little Washita Watershed, OK.

Vegetation, topography, soil temperature, and soil moisture were assigned using the methods described in Section 3.2. In all simulations presented, RegCM3-IBIS was run with static vegetation to create a consistent comparison among models. The vegetative cover (biomes for RegCM3-IBIS, vegetation classes for RegCM3-BATS1e) over each point examined is provided in Table 4.1.

RegCM3-IBIS and RegCM3-BATS1e were run using the configuration for convection that best simulated the hydroclimatology of Illinois in the NNRP2 control experiments described in Section 3.3.1. RegCM3-IBIS was run using the Grell parameterization for convection and AS74 convective closure (IBIS-AS). RegCM3-BATS1e was also run using the Grell parameterization for convection, but with the FC80 convective closure (BATS-FC).

Table 4.1: Biomes for RegCM3-IBIS, vegetation classes for RegCM3-BATS1e, over the domain examined (1.0° x 1.0° boxes shown in Figure 4-2). The distribution of biomes/vegetation classes within each box is given by the fraction in parentheses.

	RegCM3-IBIS	RegCM3-BATS1e
Bondville, IL	Cropland (5/6)	Cropland (5/6)
	Savanna (1/6)	Forest Field Mosaic (1/6)
Little Washita, OK	Grassland (3/6)	Short Grass (3/6)
	Savanna (2/6)	Forest Field Mosaic (3/6)
	Cropland (1/6)	—

FLUXNET observations and output from the IBIS-AS and BATS-FC simulations were averaged to create 6-hourly time series. Saturation vapor pressure was calculated using the empirical formula of Bolton [1980]. The slope of the saturation vapor pressure curve was obtained over a 0.2°C increment. FLUXNET relative humidity values were converted to vapor pressure with ERA40 surface pressure. Aerodynamic resistance was calculated using the mean canopy windspeed ($\bar{u}$) and the friction velocity (u_*):

$$r_a = \frac{\bar{u}}{u_*^2}. \tag{4.7}$$

Surface resistance was computed by solving the Penman-Monteith equation for r_s.

4.4 Results

Presented results for both models are 1.0° x 1.0° spatial averages centered over the boxes shown in Figure 4-2. The top box is centered over Bondville, IL and the bottom box over Little Washita Watershed, OK. Illinois has temporal coverage for January 1997 through December 1999, while data for the Oklahoma site is available May 1996 to December 1998. Variables from the Illinois and Oklahoma FLUXNET sites are measured at tower top: 8 and 3 m, respectively.

The sensitivity of latent heat flux to available energy was calculated for daylight hours (07:00-19:00 local time) from May to September, capturing most of the agricultural and

natural growing season as well as the increase, peak, and subsequent decline of the seasonal cycle of latent heat flux. Nighttime hours and time intervals with less than 10 W m^{-2} of evapotranspiration were eliminated from the analysis because their contribution to the total annual flux of latent heat is minimal. In addition to determining the sensitivity of latent heat flux to available energy using the partial derivative of the Penman-Monteith equation for evapotranspiration with respect to available energy ("theoretical"), a simple linear regression was also performed to provide an empirical estimate of the response of latent heat flux to changes in available energy ("empirical").

An assessment of the ability of IBIS-AS and BATS-FC to simulate the energy and water budgets of each site is presented in Section 4.4.1. The theoretical sensitivity of latent heat flux to available energy and the empirical response of latent heat flux to changes in available energy are discussed in Section 4.4.2. Finally, the applications of the Penman-Monteith framework are explored in Section 4.4.3.

4.4.1 Seasonal Cycle Analysis

Seasonal cycles of incident surface shortwave radiation, absorbed surface shortwave radiation, latent heat flux, sensible heat flux, 2-m temperature, and precipitation are presented in Figures 4-3 and 4-4 to provide background for the sensitivity analysis and identify errors in model simulations that may propagate through the Penman-Monteith framework. Values for FLUXNET are point measurements averaged over the dates available. Model, CRU TS2.0, and NASA SRB values are 1.0° x 1.0° spatial averages centered over the FLUXNET site for 1996-1999.

Both models overestimate incident surface shortwave radiation at the Illinois site during the summer months (June, July, August) by ≈30 W m^{-2}. IBIS-AS also simulates excess incident surface shortwave radiation throughout much of the year. Over Oklahoma, IBIS-AS and BATS-FC simulate some additional incident surface shortwave radiation when compared to FLUXNET, but are in general agreement NASA SRB. BATS-FC overestimates incident surface shortwave radiation by ≈18 W m^{-2} at the Oklahoma site during the month of June. Surface albedos appear relatively consistent across models and observations as

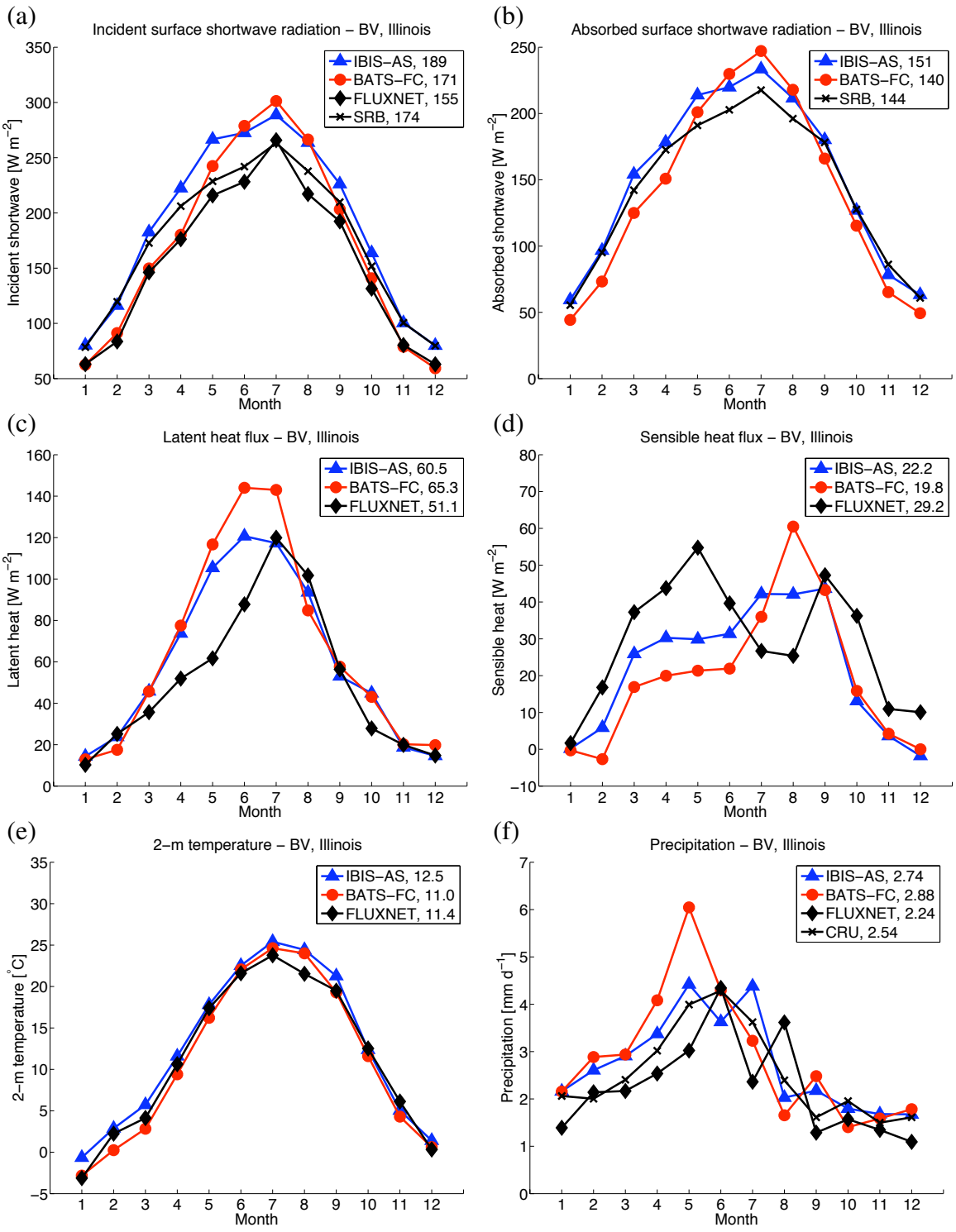

Figure 4-3: ERA40 control and observed seasonal cycles of: (a) incident surface shortwave radiation, (b) absorbed surface shortwave radiation, (c) latent heat flux, (d) sensible heat flux, (e) 2-m temperature, and (f) precipitation for Bondville, IL. Each point is a monthly average for the years 1996-1999 (FLUXNET 1997-1999). Annual averages for each variable examined are provided in the legend.

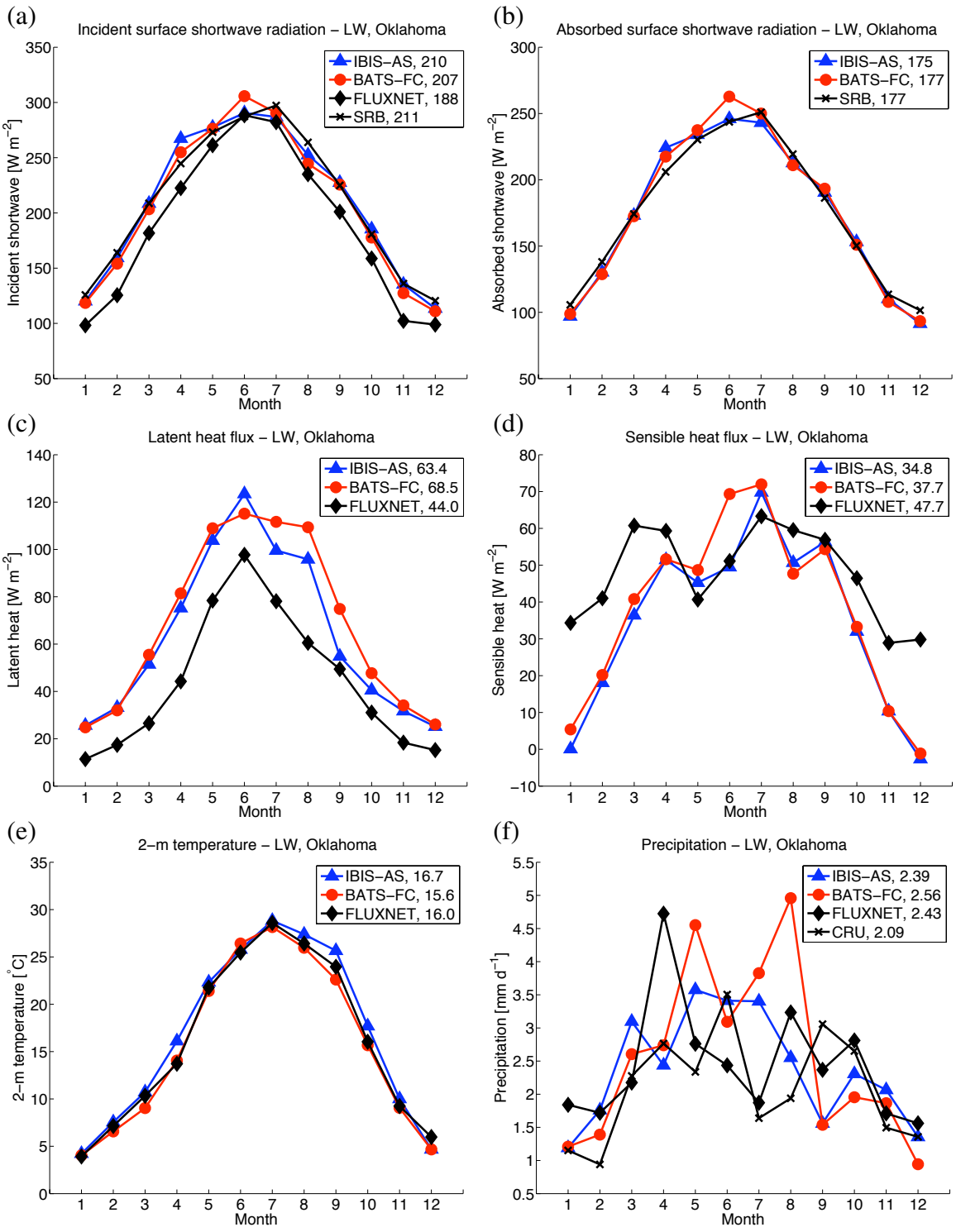

Figure 4-4: ERA40 control and observed seasonal cycles of: (a) incident surface shortwave radiation, (b) absorbed surface shortwave radiation, (c) latent heat flux, (d) sensible heat flux, (e) 2-m temperature, and (f) precipitation for Little Washita Watershed, OK. Each point is a monthly average for the years 1996-1999 (FLUXNET 5/1996-1998). Annual averages for each variable examined are provided in the legend.

errors in absorbed surface shortwave radiation are well correlated with errors in incident surface shortwave radiation.

Both models simulate excessive latent heat flux during the spring (March, April, May) at the Illinois and Oklahoma sites. Summer latent heat flux is overestimated by IBIS-AS (27 W m^{-2}) and BATS-FC (33 W m^{-2}) at the Oklahoma site and by BATS-FC (21 W m^{-2}) over Illinois. Both models miss the early summer (May, June, July) reduction of sensible heat flux found in the Illinois FLUXNET observations. IBIS-AS and BATS-FC overestimate sensible heat flux over Illinois during the summer, likely a result of increased surface temperatures from surplus incident surface shortwave radiation. BATS-FC underestimates the flux of sensible heat during the spring and fall (September, October, November) at the Illinois site. Sensible heat flux is overestimated by BATS-FC at the Oklahoma site by 18 W m^{-2} during the month of June. IBIS-AS and BATS-FC underestimate sensible heat flux during the winter (December, January, February), spring, and fall over Illinois and Oklahoma.

2-m temperature is well simulated by both models at the Oklahoma site and by BATS-FC over Illinois. IBIS-AS has a warm bias during the summer at the Illinois site, approximately 1.8°C, which is a result of the overestimation of incident shortwave radiation. The ability of IBIS-AS and BATS-FC to accurately simulate the seasonal cycles of precipitation over Illinois and Oklahoma is modest, and there are significant discrepancies between FLUXNET and CRU TS2.0 observations. Generally, both models tend to overestimate precipitation at the Illinois site. Monthly precipitation is highly variable over Oklahoma and there is little agreement between IBIS-AS, BATS-FC, FLUXNET, and CRU TS2.0.

4.4.2 Sensitivity of Latent Heat Flux to Available Energy

Figure 4-5 shows the theoretical sensitivity of latent heat flux to available energy and the empirical response of latent heat flux to changes in available energy for IBIS-AS, BATS-FC, and FLUXNET observations. Error bars denoting one standard deviation are included in the theoretical sensitivity figures and R^2 values that describe the correlation between evapotranspiration and available energy are included in the empirical response plots. Some

of the annual variations in the theoretical sensitivities of latent heat flux to available energy are reflected in the empirical responses of latent heat flux to changes in available energy; however, in general there is little agreement between the two methods. The most noticeable difference is that the theoretical sensitivities are always less than the empirical responses. Discrepancies between the theoretical sensitivity of latent heat flux to available energy and the empirical response of latent heat flux to changes in available energy are due in part to comparing a partial derivative to an approximation of the full derivative. In the Penman-Monteith framework, all variables except available energy are held constant. This is not true of a regression, which just examines the relationship between a response and explanatory variable, treating the influence of other factors as noise that degrades the R^2 value. Additional inaccuracies in the theoretical framework may result from applying the Penman-Monteith equation at such fine scales. However, as observational records continue to expand both spatially and temporally, errors in the application of this framework should be reduced.

IBIS-AS and BATS-FC overestimate the theoretical sensitivity of latent heat flux to available energy in May and June and underestimate the theoretical sensitivity of latent heat flux to available energy in the late summer (July, August, September) at the Illinois site; however, both models are in agreement with FLUXNET on average. The empirical responses of latent heat flux to changes in available energy simulated by IBIS-AS and BATS-FC over Illinois are also too high in May and June and too low in July, August, and September when compared to FLUXNET. The IBIS-AS and BATS-FC theoretical sensitivities of latent heat flux to available energy are similar to the observed theoretical sensitivity at the Oklahoma site; however, the empirical response of latent heat flux to changes in available energy are underestimated by IBIS-AS and BATS-FC.

The accumulation of greenhouse gasses (CO_2, CH_4, water vapor, etc.) in the atmosphere increases downward longwave radiation and available energy. Underestimating the sensitivity of latent heat flux to available energy has many potential consequences, including the retention of soil moisture, less water vapor in the canopy, a decrease in plant respiration, increased sensible heat flux, and warmer surface temperatures. This is apparent even in the control simulations, where IBIS-AS underestimates the sensitivity of latent heat flux

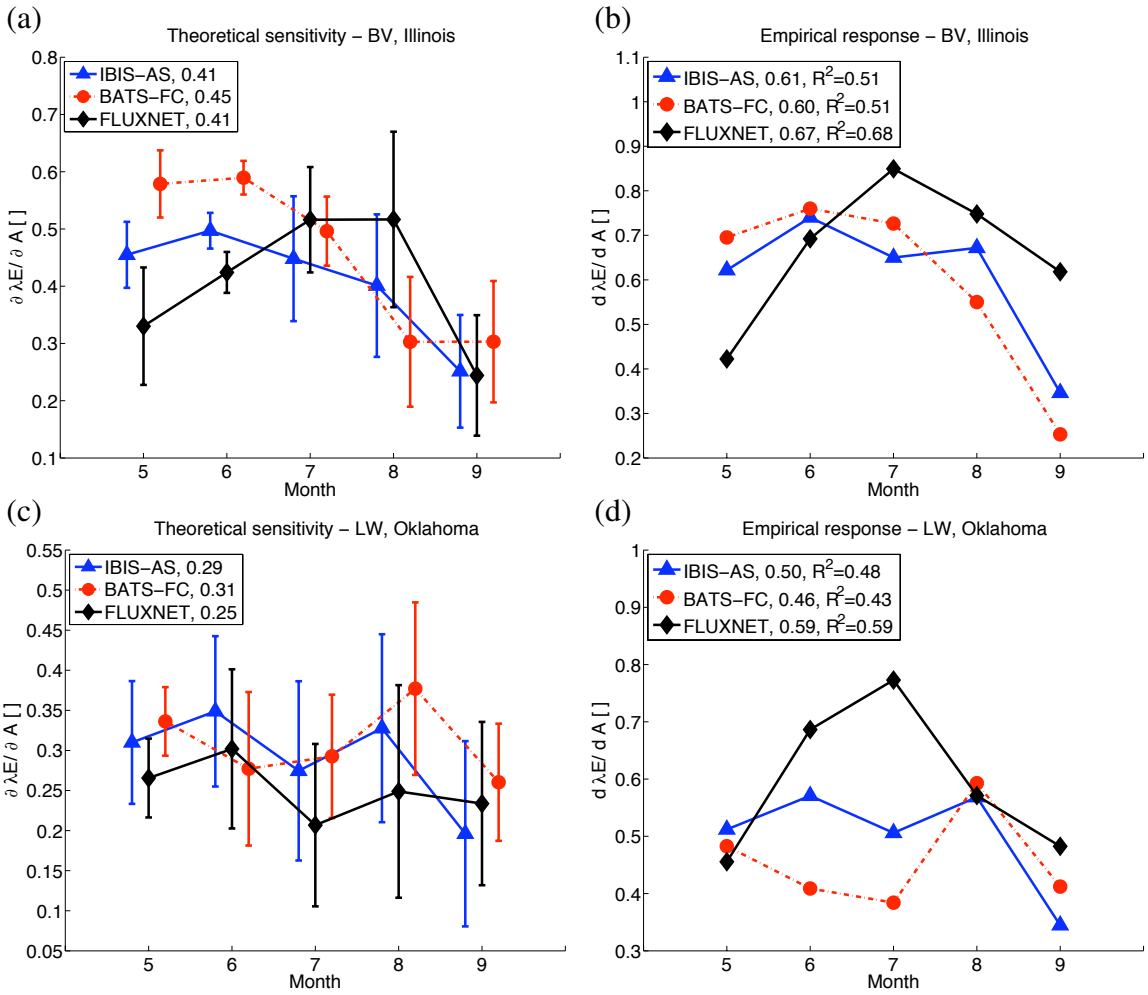

Figure 4-5: Theoretical sensitivity of latent heat flux to available energy with error bars denoting the standard deviation (a), (c); and empirical response of latent heat flux to changes in available energy with associated R^2 values (b), (d) using ERA40 boundary conditions for 1996-1999 (FLUXNET 1997-1999 for Illinois, 1996-1998 for Oklahoma). May-September averages for each variable examined are provided in the legend.

to available energy during the late summer over Illinois, which coincides with an increase in surface temperature and sensible heat flux. And while the results presented in Section 4.4.1 demonstrate that the simulation of 2-m temperature is fairly robust despite inaccuracies in latent heat flux, small changes in the simulation of temperature and water vapor could have significant implications for more sensitive variables, such as precipitation and cloudiness. Overestimating the sensitivity of latent heat flux to available energy could also be detrimental to the accuracy of model simulations. Excess latent heat flux will dampen the increase in surface temperature resulting from additional available energy, introducing a number of biases to the system.

As discussed above, to provide an accurate prediction of future climate, a model must capture both the correct climatology of evapotranspiration and the correct sensitivity of latent heat flux to available energy. Models with a higher climatology of latent heat flux will likely have a higher sensitivity based solely on the magnitude of the fluxes involved. To address this bias, Figure 4-6 shows the theoretical sensitivity of latent heat flux to available energy and the empirical response of latent heat flux to changes in available energy normalized by the latent heat flux, integrating the climatology of evapotranspiration and the theoretical sensitivity/empirical response of latent heat flux into a single seasonal cycle. The normalized theoretical sensitivities of latent heat flux to available energy and empirical responses of latent heat flux to changes in available energy of FLUXNET observations are largest, a result of the relatively low values of latent heat in the FLUXNET dataset. BATS-FC simulates high values of evapotranspiration, resulting in reduced normalized theoretical sensitivities and empirical responses when compared to IBIS-AS and FLUXNET.

4.4.3 Applying the Penman-Monteith Framework

One benefit of using the Penman-Monteith framework to calculate the sensitivity of latent heat flux to available energy is the additional analyses possible. The empirical response of latent heat flux to changes in available energy, derived from a regression, can at best show correlation. It addresses nothing past the variables considered nor provides any causal information. Using the Penman-Monteith equation is a mechanistic approach that allows

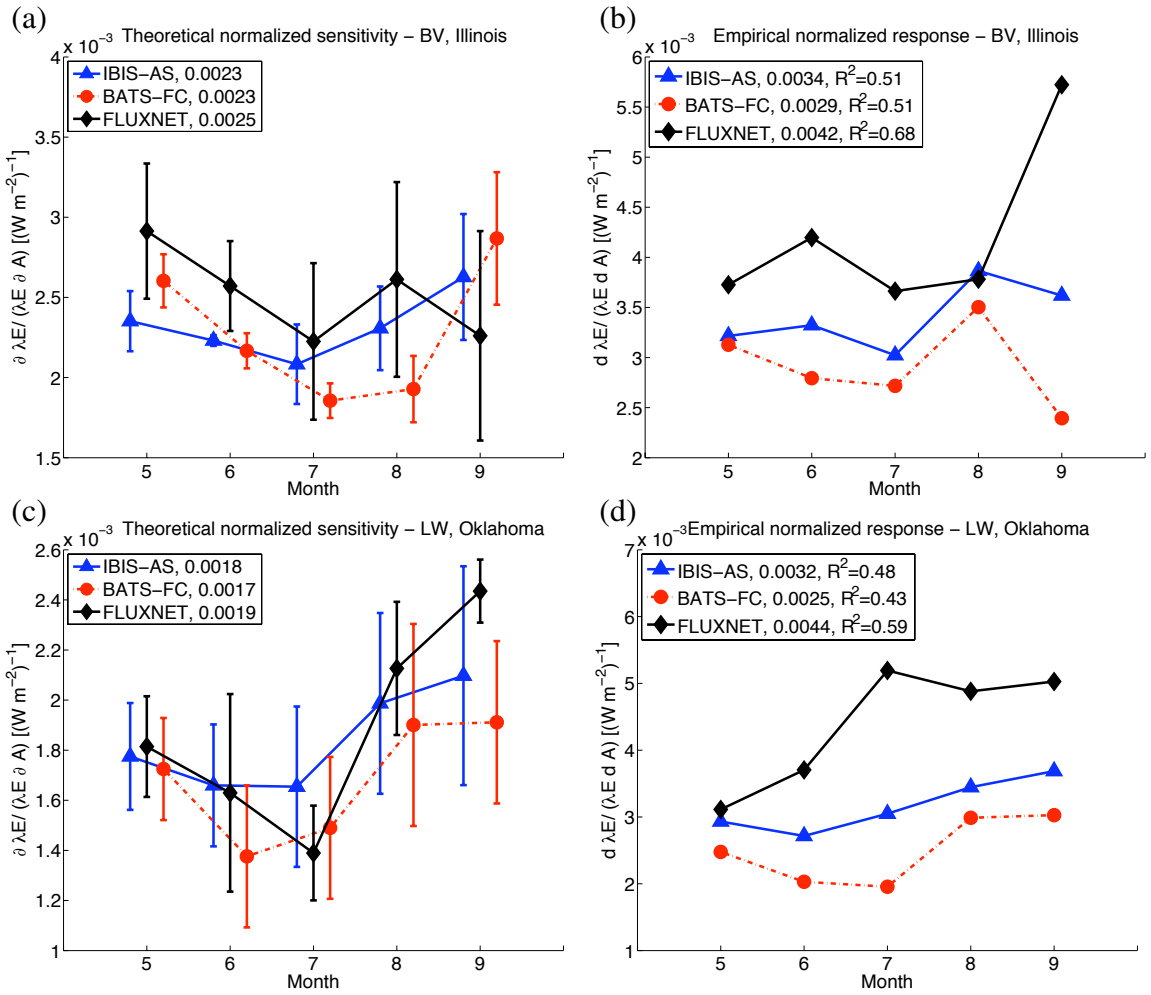

Figure 4-6: Theoretical normalized sensitivity of latent heat flux to available energy with error bars denoting the standard deviation (a), (c); and empirical normalized response of latent heat flux to changes in available energy with associated R^2 values (b), (d) using ERA40 boundary conditions for 1996-1999 (FLUXNET 1997-1999 for Illinois, 1996-1998 for Oklahoma). May-September averages for each variable examined are provided in the legend.

examination at every level. Equation 4.5 shows that the theoretical sensitivity of latent heat flux to available energy is a function of the ratio of surface resistance to aerodynamic resistance. While Δ is also variable, it remains relatively constant over the months considered.

The surface and aerodynamic resistances for both models are presented in Figure 4-7. Combined with Equation 4.5, these plots explain many of the differences illustrated in Figure 4-5. The increase in the surface resistance of IBIS-AS at the end of the summer over Illinois and Oklahoma increases the denominator of Equation 4.5, thus reducing the sensitivity of latent heat flux to available energy in IBIS-AS. This suggests an error within the model, as large values of surface resistance are not found in the FLUXNET observations. Aerodynamic resistance also plays an important role in the sensitivity of latent heat flux to available energy. IBIS-AS simulates high values of aerodynamic resistance at both sites, reducing the denominator of Equation 4.5 and increasing the sensitivity of the model. Larger values of aerodynamic resistance in IBIS-AS and BATS-FC at the Illinois site relative to the Oklahoma site are a result of both higher winds and lower friction velocities.

In addition to assessing the sensitivity of latent heat flux to available energy, the ratio of surface resistance to aerodynamic resistance can also be used to provide information about the climatology of evapotranspiration. For example, the low surface resistance simulated by BATS-FC is expected to produce large values of latent heat flux over Illinois during May, June, and July. In contrast, the higher values of surface resistance simulated by BATS-FC at the Illinois site in August and September should result in lower evapotranspiration. Both are observed, as evidenced in Figure 4-3.

Figure 4-8 is exactly the same as Figure 4-1, but includes the approximate position of IBIS-AS, BATS-FC, and FLUXNET during the early summer (May, June, July) at the Illinois site. IBIS-AS and BATS-FC simulate low surface resistances, large values of latent heat flux, and a high sensitivity of latent heat flux to available energy in May, June, and July over Illinois.

The natural extension of using the Penman-Monteith framework to evaluate disparities between models and observations is applying it to guide improvements. The normalized sensitivity of latent heat flux to available energy is underestimated by IBIS-AS and BATS-FC over Illinois. The surface resistances of IBIS-AS and BATS-FC are too high in the

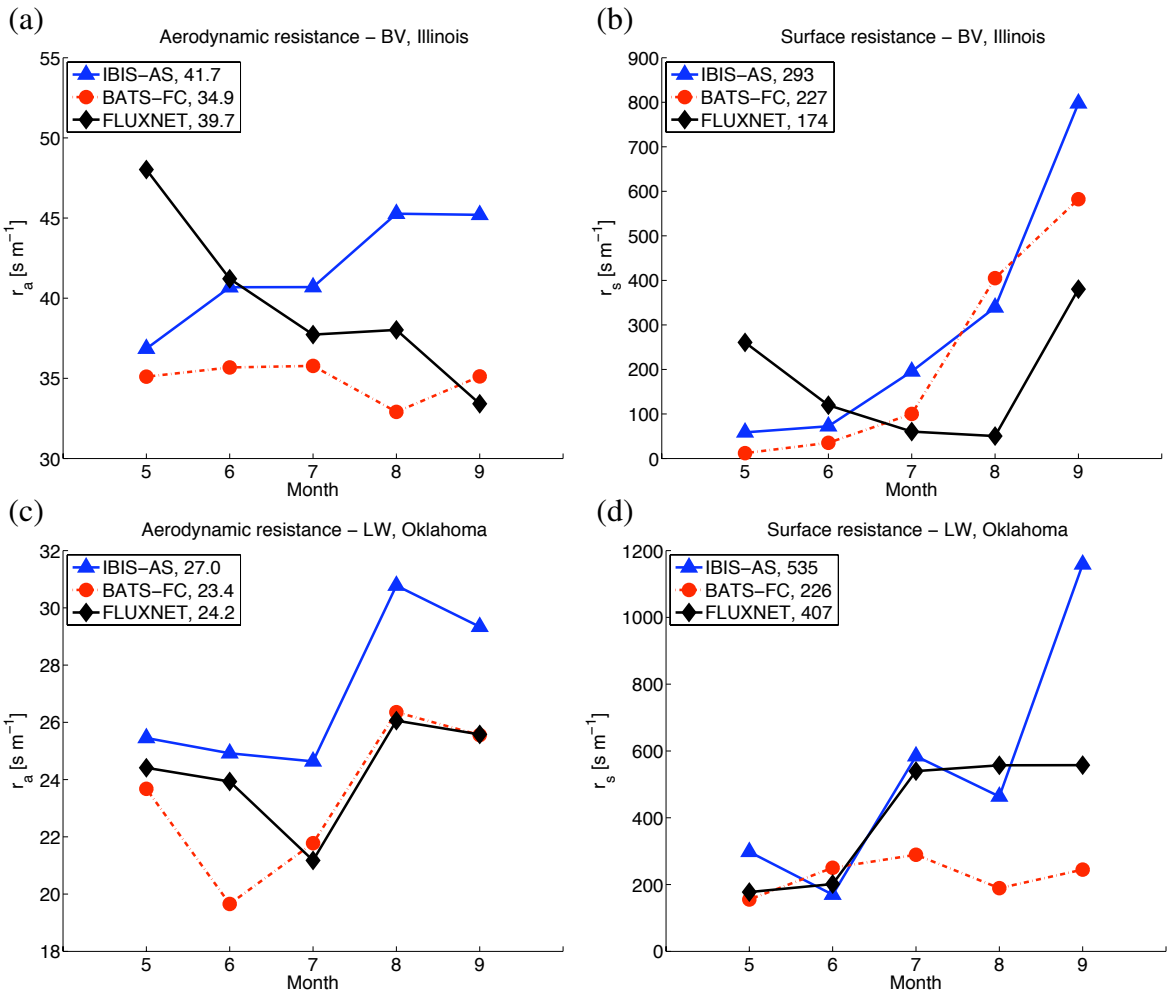

Figure 4-7: Aerodynamic resistance (a), (c); and surface resistance (b), (d) using ERA40 boundary conditions for 1996-1999 (FLUXNET 1997-1999 for Illinois, 1996-1998 for Oklahoma). May-September averages for each variable examined are provided in the legend.

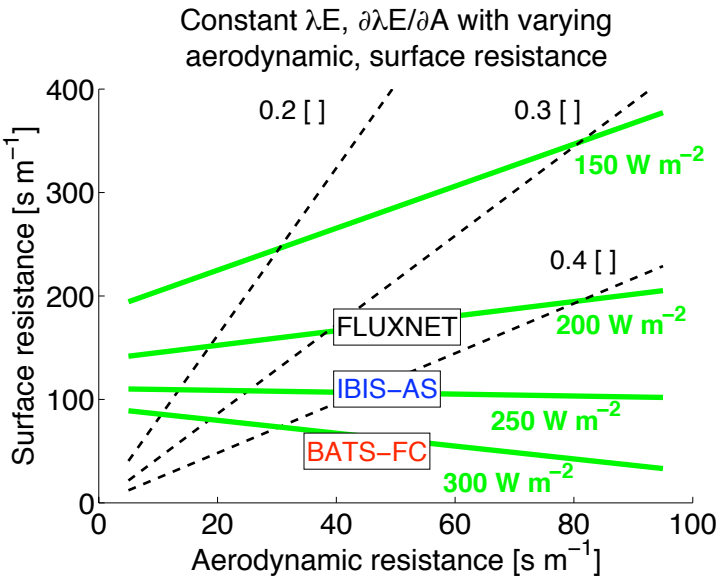

Figure 4-8: The relationship between surface, aerodynamic resistance and latent heat flux (green solid lines, green bold values), sensitivity of latent heat flux to available energy (black dashed lines, black values) derived using the Penman-Monteith equation. The slope of the saturation vapor pressure-temperature relationship, vapor pressure deficit, and available energy are assumed to be constant values of 150 Pa $^{\circ}$C^{-1}, 1500 Pa, and 350 W m^{-2}, respectively. The approximate positions of IBIS-AS, BATS-FC, and FLUXNET during the early summer (May, June, July) at the Illinois site are given.

late summer. This suggests that there needs to be a reduction of the controls on evapotranspiration. In IBIS-AS, surface resistance is a function of the photosynthetic rate, CO_2 concentration, and water vapor concentration. In BATS-FC, surface resistance is a function of solar radiation, saturation vapor pressure, seasonal temperature, and soil moisture. Each factor should be examined to see which is limiting, and that limiting factor should be assessed and revised if appropriate. IBIS-AS and BATS-FC underestimate surface resistance and aerodynamic resistance in the early summer, causing an overestimation of latent heat flux and thus reducing the normalized sensitivity. Again, each component of the resistance formulas in IBIS-AS and BATS-FC should be evaluated should be evaluated and revised if appropriate. It is important to note that errors in the energy budget must be fixed in conjunction with those in the surface physics scheme, as the accuracy of a simulation depends both on the correct flux of radiation into the system and the correct partitioning of that energy.

4.5 Conclusions

A thorough comparison of IBIS-AS, BATS-FC, and FLUXNET observations is presented. In addition to examining the climatology of energy and water fluxes over Bondville, IL and Little Washita Watershed, OK, a framework using the Penman-Monteith equation was developed to assess the theoretical sensitivity of latent heat flux to available energy. An empirical estimate of the response of latent heat flux to changes in available energy was calculated by regression. The theoretical and empirical values show limited agreement, with some differences attributable to comparing a partial derivative to an approximation of the full derivative.

The advantage of using the Penman-Monteith framework is the ability to expose relationships beyond a simple correlation. The physical basis of the Penman-Monteith equation makes it possible to tell not only if, but exactly why models differ. In addition, completing extensive assessments that reveal the mechanics of each model ensures that skillful simulations are the result of an accurate model, as opposed to merely getting the right answer for the wrong reason. Information derived from this analysis is also valuable for correcting er-

rors in parameterizations. It is expected that a comparison of models with less in common (different spatial resolutions, atmospheric representations, etc.) would yield more disparate sensitivities of latent heat flux to available energy and greater insight.

IBIS-AS and BATS-FC do a reasonable job of simulating the theoretical sensitivity of latent heat flux to available energy on average over the summer; however, there are significant differences between the seasonal cycles of both models and FLUXNET observations. IBIS-AS and BATS-FC underestimate the theoretical normalized sensitivity of latent heat flux to available energy at the Illinois site. The empirical responses of latent heat flux to changes in available energy are generally greater than the theoretical sensitivities of latent heat flux to available energy derived from the Penman-Monteith framework. Both models underestimate the response of latent heat flux to changes in available energy when compared to FLUXNET using the empirical method. This damped response of latent heat flux to an increase in the radiative forcing will have a substantial effect on the energy balance. Energy not partitioned to latent heat must leave the system as sensible heat. This would likely result in an overestimation of temperature and an exacerbation of temperature-dependent feedbacks in climate change simulations.

Ideally, models would be verified by comparing the state of the model to a past observed state; however, only a very small subset of state observations are available. Simple, intuitive equations can be leveraged to reveal a more complete picture of simulated and observed climate, expanding the scope of parameterization assessment and ultimately improving our ability to model the earth system.

Chapter 5

Modeling the American Midwest Under a Warmer Climate

5.1 Introduction

One of the first substantial analyses of the response of soil moisture to climate change was completed by Manabe et al. in 1981. Using the NOAA Geophysical Fluid Dynamics Laboratory (GFDL) general circulation model (GCM) with three different arrangements of topography and resolution, Manabe et al. [1981] observed significant soil moisture reductions in middle and high latitudes during the summer. Recently, in more detailed studies, Manabe and Wetherald [2002] and Manabe et al. [2004] conducted experiments with the coupled atmosphere-ocean-land model developed at the NOAA Geophysical Fluid Dynamics Laboratory to explore the effects of climate on the hydrologic cycle using the Intergovernmental Panel on Climate Change IS92a scenario and a quadrupling of CO_2, respectively. Under the IS92a scenario, the global mean surface air temperature by the middle of the 21st century was 2.3°C warmer than the pre-industrial global mean surface air temperature [Manabe and Wetherald, 2002]. In Manabe et al. [2004], the concentration of CO_2 was increased by 1% compounded each year until it reached 4 x CO_2 in year 140. The simulation was run to year 250, at which point the increase in global mean surface air temperature over the control (fixed CO_2) scenario was 5.5°C [Manabe et al., 2004].

Manabe and Wetherald [2002] and Manabe et al. [2004] concluded that semi-arid regions, such as the southwestern United States, are particularly susceptible to drying and that the American Midwest will experience summer drying and winter wetting. Mechanisms for both summer drying and winter wetting over the midwestern United States are given. In the winter, rainfall is enhanced by increased moisture transport from warmer oceans and cold surface temperatures cause additional available energy produced by climate change to be partitioned into sensible heat [Manabe et al., 2004]. In contrast, during the summer surface temperatures are warmer and latent heat flux is enhanced, outpacing any increase in precipitation from the oceans, thus drying the soils [Manabe et al., 2004]. In addition to changes in latent heat flux and precipitation, Manabe et al. [2004] find that the reduction of springtime surface albedo (from decreased snow cover), lengthened growing season, and soil moisture-cloud-rainfall feedback exacerbate summer drying over the midwestern United States.

Similar findings were reported by Wang [2005] in a comprehensive study on the potential for future agricultural drought using fifteen different GCMs. Wang examined both the average predictions across models and the consistency between model predictions. Additionally, she completed a focused analysis of four regions, including one that encompassed the midwestern United States. Consistent with Manabe et al. [2004], the majority of models examined predicted extensive summer drying and some winter wetting over mid-latitude North America. While most models did agree on the sign of soil moisture change with season, there were some differences in the distribution of soil moisture within each model's domain and disparities in the predicted soil moisture changes between models was large. The 15 GCMs were almost unanimous in predicting drier conditions throughout the year in southwestern North America and the Mediterranean [Wang, 2005].

However, this trend has not been found by all studies. A comparison of the GFDL and National Center for Atmospheric Research (NCAR) GCMs forced using a 2 x CO_2 climate change scenario concluded that land surface parameterizations play a pivotal role in the study of summer dryness [Meehl and Washington, 1988]. In Meehl and Washington [1988], the GFDL model retained less of the precipitation increase of the winter months than the NCAR GCM, partitioning it to runoff as opposed to groundwater recharge, making

the GFDL model drier in the spring and summer. In contrast, water added during the winter and early spring to the NCAR model reduced and sometimes eliminated summer drying [Meehl and Washington, 1988]. The response of both models was magnified by the observed soil moisture-cloud-rainfall feedback [Meehl and Washington, 1988].

In 2002, Seneviratne et al. found decreases in soil moisture over the midwestern United States to be weak compared to the warming forcing applied, on the order of 1% to 2% of saturation. Seneviratne et al. [2002] hypothesized that vegetative controls on transpiration and increased infiltration in the spring mitigate summer drying. The deviation of these results from those of Manabe et al. [1981] was explained through a series of experiments illustrating the differences between the land surface parameterizations used in the two studies.

Last year the U.S. Global Change Research Program released a study detailing the impacts of climate change on the United States. Karl et al. [2009] concludes that agriculture in the midwestern United States is likely to benefit from low levels of warming, a result of a longer growing season and CO_2 fertilization. However, larger changes in temperature and precipitation associated with higher levels of warming will be detrimental to crop growth and yields [Karl et al., 2009]. Precipitation is expected to increase in the winter and spring, and become more intense throughout the year, escalating the risk of flooding [Karl et al., 2009]. More intense rainfall during the summer is likely to result in longer periods of time between precipitation events, which coupled with enhanced evapotranspiration will increase the likelihood of drought [Karl et al., 2009; Wuebbles and Hayhoe, 2004]. Note that the terms "latent heat flux" and "evapotranspiration" are used interchangeably throughout this thesis.

Precipitation plays a pivotal role in the response of soil moisture to climate change. Observational evidence collected during the 20^{th} century (1900-2002) shows an increasing trend in precipitation across the contiguous United States on average [Groisman et al., 2004]. Regionally, enhanced precipitation is robust across much of the United States, with the exception the Southwest and parts of the Southeast. Over the state of Illinois, the linear trend in precipitation from 1900-2002 is approximately 15% [Groisman et al., 2004]. Positive trends in precipitation (3% per decade) across the United States were also found

by Kunkel et al. [1999] for the years of 1931-1996. Karl and Knight [1998] concluded that precipitation has increased ≈10% over the contiguous United States since 1910.

Groisman et al. [2001] examined the seasonal distribution of the linear trend in precipitation for the years 1910-1996. Changes in precipitation were confined to the spring, summer, and autumn, with the largest increase in precipitation occurring in autumn [Groisman et al., 2001]. This finding is consistent with the conclusions of Small and Islam [2009], who determined that the linear trend in total autumn precipitation for the years 1948-2004 throughout the Great Lakes and Mississippi regions is more than 5% per decade.

5.2 Design of Experiments

All climate change experiments are identical in domain to the control experiments described in Section 3.2. Simulations are centered at 40°N, 95°W and use a Rotated Mercator projection. The domain covers all of the United States, as well as parts of Mexico and Canada (Figure 5-1), spanning 100 points zonally, 60 points meridionally at a horizontal grid spacing of 60 km. Simulations were allowed to spin-up for 21 months. The region evaluated is shown by the 4.0° x 5.5° shaded box contained in Figure 5-1.

Initialization of vegetation, soil moisture, and soil temperature is identical to the control simulations and thoroughly described in Section 3.2. A brief review is included below for reference.

Vegetation classes in RegCM3-BATS1e were directly assigned using the USGS Global Land Cover Characterization (GLCC) dataset. In IBIS, each grid box was populated with plant functional types (PFTs) based on the potential global vegetation dataset of Ramankutty [1999] and two climate datasets. Croplands were then defined in RegCM3-IBIS using the USGS GLCC dataset. RegCM3-IBIS was run with static vegetation to create a consistent comparison between models. Topography for both models was given by the USGS Global 30-arc second elevation dataset [1996] aggregated to a 0.5° x 0.5° spatial resolution.

RegCM3-BATS1e initial soil moisture and soil temperature were set by the surface temperature boundary condition and vegetation type, respectively. Soil moisture, soil temperature, and soil ice were initialized in RegCM3-IBIS using an offline simulation of IBIS

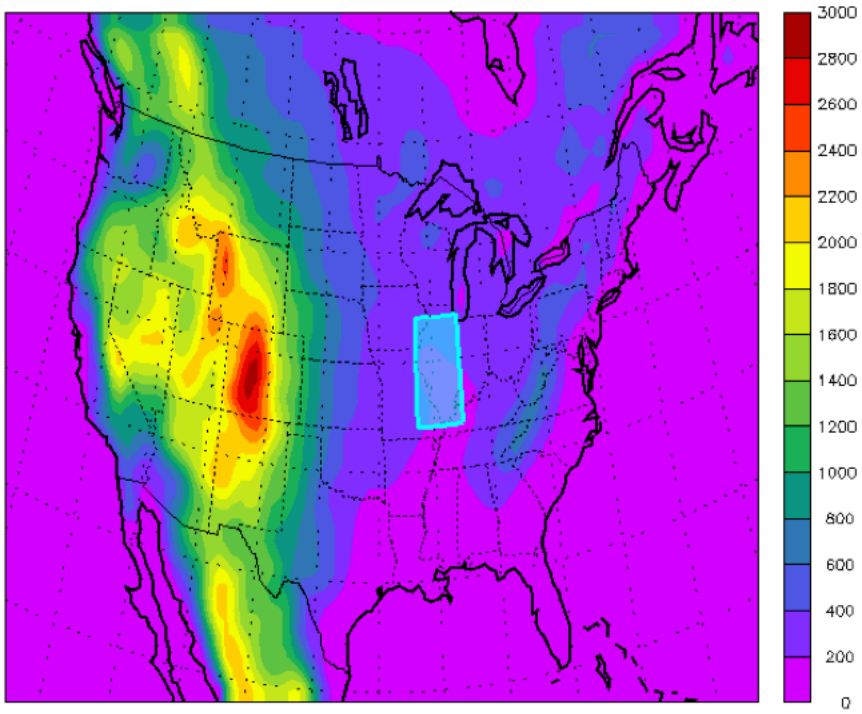

Figure 5-1: Domain and topography [m] of climate change experiments with a 4.0° x 5.5° cyan shaded box delineating the extent of spatial averaging over Illinois.

forced with monthly mean climatologies. Differences in the initialization of soil moisture and temperature in RegCM3-IBIS and RegCM3-BATS1e were shown to have a minimal impact on model results, as discussed in Section 3.2.

The RegCM3-IBIS and RegCM3-BATS1e control experiments (NNRP2 and EH5OM) were assessed using the NASA Surface Radiation Budget (SRB) dataset [NASA, 2006] and data compiled by Yeh [2003] (ISWS).

5.2.1 NCEP-DOE Reanalysis 2 Surrogate Climate Change

A surrogate climate change scenario was constructed based on the methodology of Schär et al. [1996] using the NCEP-DOE Reanalysis 2 (NNRP2) dataset. First, the boundaries were warmed by 3°C. Specifically, the NNRP2 dataset of temperature was increased by 3°C consistently throughout the atmospheric column, and sea surface temperatures derived from the NOAA OISST dataset were warmed by 3°C. Relative humidity fields were left unchanged, resulting in an increased flux of water vapor at the boundaries. A global

mean equilibrium surface temperature increase of 3°C corresponds approximately to a CO_2 equivalent concentration of 710 ppm [Randall et al., 2007]. Therefore, the NNRP2 surrogate climate change simulations were run with a constant CO_2 equivalent concentration of 710 ppm, double the concentration of CO_2 equivalent (355 ppm) used in the NNRP2 control experiments. NNRP2 surrogate climate change experiments were initialized April 1st, 1982 and allowed to spin-up for 21 months. The subsequent 22 years (1984-2005) of simulated climate were assessed.

Surrogate climate change scenarios have a number of advantages. First, boundary conditions are dynamically consistent with observed atmospheric flows [Schär et al., 1996]. By basing the climate change scenario on reanalysis data, which integrates observations, regional climate models are guaranteed to be constrained by realistic atmospheric flows. This is not true of GCM climate change predictions, which have complete freedom and could potentially introduce significant errors. Second, the procedure is model independent, and is therefore not subject to the biases of any particular GCM. And finally, surrogate climate change scenarios are intuitive and easy to implement [Schär et al., 1996].

To examine the model configuration variability of the NNRP2 surrogate climate change experiments, RegCM3-BATS1e and RegCM3-IBIS were run using the Grell parameterization of convection with the Fritsch & Chappell (FC80) and Arakawa & Schubert (AS74) convective closure assumptions. This produced an ensemble of four simulations: RegCM3-IBIS using AS74 (IBIS-AS), RegCM3-IBIS using FC80 (IBIS-FC), RegCM3-BATS1e using FC80 (BATS-FC), and RegCM3-BATS1e using AS74 (BATS-AS). Besides modified boundary conditions, SSTs, and an increased concentration of CO_2 equivalent; all other facets of the experimental design were identical to the NNRP2 control simulations, as described in Section 3.2.1.

5.2.2 ECHAM5 GCM A1B

A climate change simulation of the ECHAM5 GCM (EH5OM) driven by the A1B emissions scenario of Nakicenovic et al. [2000] was used to force the boundaries of RegCM3-IBIS and RegCM3-BATS1e. The EH5OM A1B emissions scenario is a continuation of the

20^{th} century experiment detailed in Section 3.2.2, and describes a world of rapid convergent economic growth from 2001-2100 [Roeckner et al., 2006b]. World population peaks mid-century and declines afterward, regional differences in per capita income are reduced significantly, and new and more efficient technologies spread quickly [Nakicenovic et al., 2000]. The energy portfolio is balanced in this scenario, with renewable resources and fossil fuels in use. Both boundary conditions and SSTs were derived from the EH5OM A1B experiment. The concentration of CO_2 equivalent was increased over time as described by the A1B emissions scenario. EH5OM A1B climate experiments were initialized April 1^{st}, 2076 and allowed to spin-up for 21 months. The subsequent 22 years (2078-2099) of simulated climate were assessed.

While climate change boundary conditions generated by EH5OM are more complex to construct and vulnerable to errors specific to EH5OM, there are several advantages to using a GCM-driven climate change experiment. First, it allows for a more sophisticated representation of climate change. For example, the temperature of the entire atmospheric column will not uniformly warm by 3°C as described by the surrogate climate change scenario. Using a GCM allows for vertical differentiation in temperature response. But more importantly, the GCM climate change scenario, unlike the surrogate climate change scenario, is not bound by current atmospheric flows. It is likely that climate change will significantly impact many aspects of the climate system at a variety of spatial scales. The EH5OM A1B scenario can include large-scale changes in atmospheric flows resulting from climate change while the surrogate scenario cannot.

RegCM3-IBIS and RegCM3-BATS1e were run using the configuration for convection that best simulated the hydroclimatology of Illinois in the NNRP2 control experiments presented in Section 3.3.1: the AS74 convective closure assumption for RegCM3-IBIS (IBIS-AS) and the FC80 convective closure assumption for RegCM3-BATS1e (BATS-FC). Besides modified boundary conditions, SSTs, and an increased concentration of CO_2 equivalent, all other facets of the experimental design were identical to the EH5OM control simulations as described in Section 3.2.2.

5.3 Results

5.3.1 NCEP-DOE Reanalysis 2 Surrogate Climate Change

Presented results are 4.0° x 5.5° spatial averages over the box contained in Figure 5-1. Changes in the hydroclimatology of the American Midwest resulting from the NNRP2 surrogate climate change scenario are described in Figures 5-2 to 5-13.

Figures 5-2 to 5-7 present each variable using a pair of panels, where the left panel shows the seasonal cycles of the NNRP2 control simulations and the right panel shows the difference between the NNRP2 surrogate climate change and NNRP2 control seasonal cycles.

Figure 5-2 contains the response of incident and absorbed surface shortwave radiation to the NNRP2 surrogate climate change forcing. Differences in surface shortwave radiation values are small relative to the model configuration variability of the NNRP2 control simulation ensemble. The FC80 convective closure loses significantly more clouds than the AS74 convective closure during the summer (June, July, August), resulting in additional incident surface shortwave radiation. NNRP2 surrogate climate change seasonal cycles are consistent with NNRP2 control experiments; IBIS-AS and BATS-AS generally cloudier and simulate less incident shortwave radiation during the summer months than IBIS-FC and BATS-FC.

IBIS-AS, BATS-FC, IBIS-FC, and BATS-AS simulate warmer 2-m temperatures throughout the year when forced using the NNRP2 surrogate climate change boundary conditions instead of the NNRP2 control boundary conditions. While the NNRP2 control seasonal cycle of 2-m temperature is a function of both the surface physics scheme and convective closure, warming under the NNRP2 surrogate climate change scenario is controlled by convective closure during June, July, and August. IBIS-FC and BATS-FC simulate approximately a 3.3°C warming over the summer months, while IBIS-AS and BATS-AS only increase 2-m temperature $\approx$2.1°C. This is in part a function of the reduced cloudiness and increased incident surface shortwave radiation simulated when using the FC80 closure assumption.

The response of net and downward longwave radiation to the NNRP2 surrogate climate

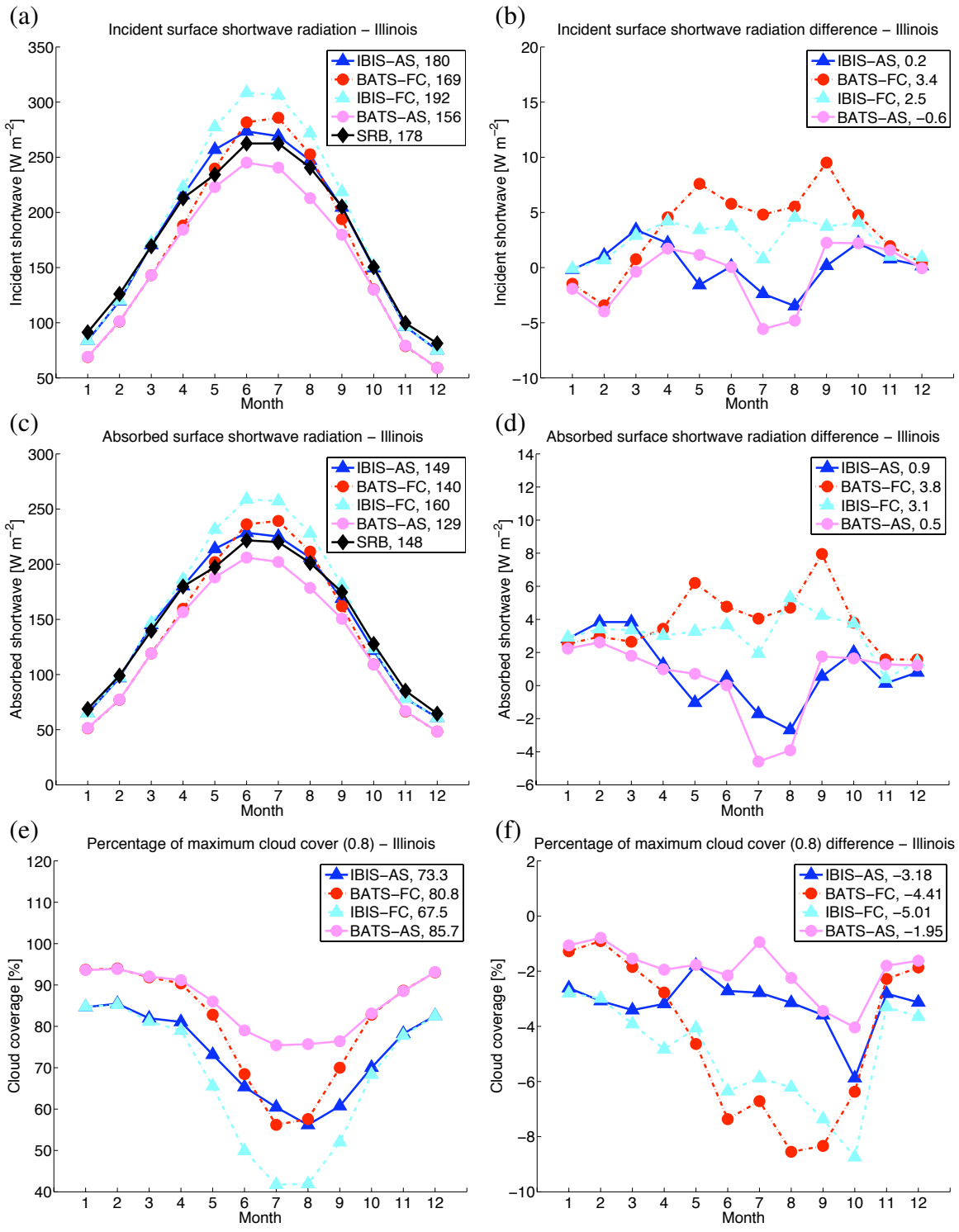

Figure 5-2: NNRP2 control and observed seasonal cycles of: (a) incident surface shortwave radiation, (c) absorbed surface shortwave radiation, (e) percentage of maximum model fractional cloud cover (0.8); and the difference between NNRP2 surrogate climate change and NNRP2 control seasonal cycles of: (b) incident surface shortwave radiation, (d) absorbed surface shortwave radiation, (f) percentage of maximum model fractional cloud cover (0.8) for 1984-2004. Annual averages for each variable examined are provided in the legend.

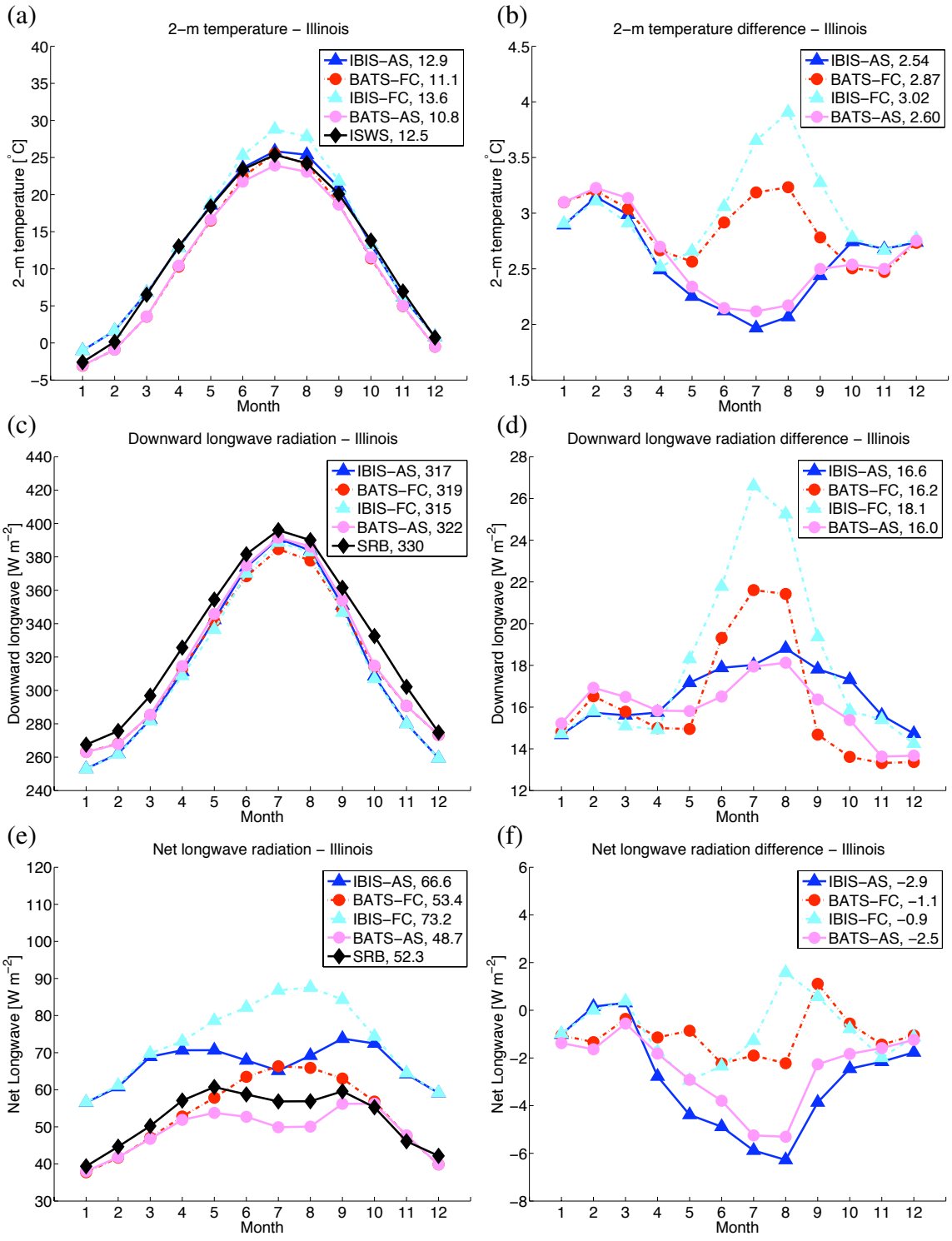

Figure 5-3: NNRP2 control and observed seasonal cycles of: (a) 2-m temperature, (c) downward longwave radiation, (e) net longwave radiation (defined as positive upward); and the difference between NNRP2 surrogate climate change and NNRP2 control seasonal cycles of: (b) 2-m temperature, (d) downward longwave radiation, (f) net longwave radiation (defined as positive upward) for 1984-2004 (2-m temperature 1984-2005). Annual averages for each variable examined are provided in the legend.

change scenario depends on both surface physics scheme and convective closure assumption (Figure 5-3). Downward longwave radiation is enhanced in all simulations, a result of increasing the concentration of CO_2 equivalent from 355 ppm to 710 ppm and additional water vapor in the atmosphere. Reduced cloudiness in IBIS-FC and BATS-FC allows more longwave radiation to reach the surface.

The difference between the NNRP2 surrogate climate change net longwave radiation (defined as positive upward) seasonal cycles and the NNRP2 control net longwave radiation seasonal cycles is a function of ground temperature and downward longwave radiation. The increase in downward longwave radiation reduces net longwave radiation; however, warmer surface temperatures increase net longwave radiation. Here, IBIS-AS and BATS-AS show the largest reduction in net longwave radiation, a result of the damped response of surface temperature relative to IBIS-FC and BATS-FC.

The response of evapotranspiration to the NNRP2 surrogate climate change scenario is muted overall. IBIS-AS, BATS-FC, IBIS-FC, and BATS-AS simulate less than a 7% increase in evapotranspiration annually averaged. While IBIS-FC simulates an increase in evapotranspiration throughout most of the year, during July and August evapotranspiration is reduced in the climate change simulation, a result of high surface temperatures and low precipitation values. IBIS-AS produces 0.16 mm d^{-1} of additional evapotranspiration averaged over the summer month when forced using the NNRP2 surrogate climate change scenario. Evapotranspiration in BATS-AS is relatively unchanged in June, July, and August while large increases in precipitation enhance evapotranspiration in BATS-FC by 0.27 mm d^{-1} during the summer.

Changes in sensible heat flux found under the NNRP2 surrogate climate change forcing were small when compared to the NNRP2 control simulation ensemble variability (Figure 5-4).

All models simulate increased precipitation under the climate change scenario; however, there are significant differences between each model's response based on convective closure assumption and surface physics scheme. BATS-FC enhances precipitation by 0.82 mm d^{-1} (21%) during June, July, and August. The summer precipitation increases in IBIS-AS and BATS-AS are 0.35 mm d^{-1} (10%) and 0.23 (6%), respectively. This is consistent

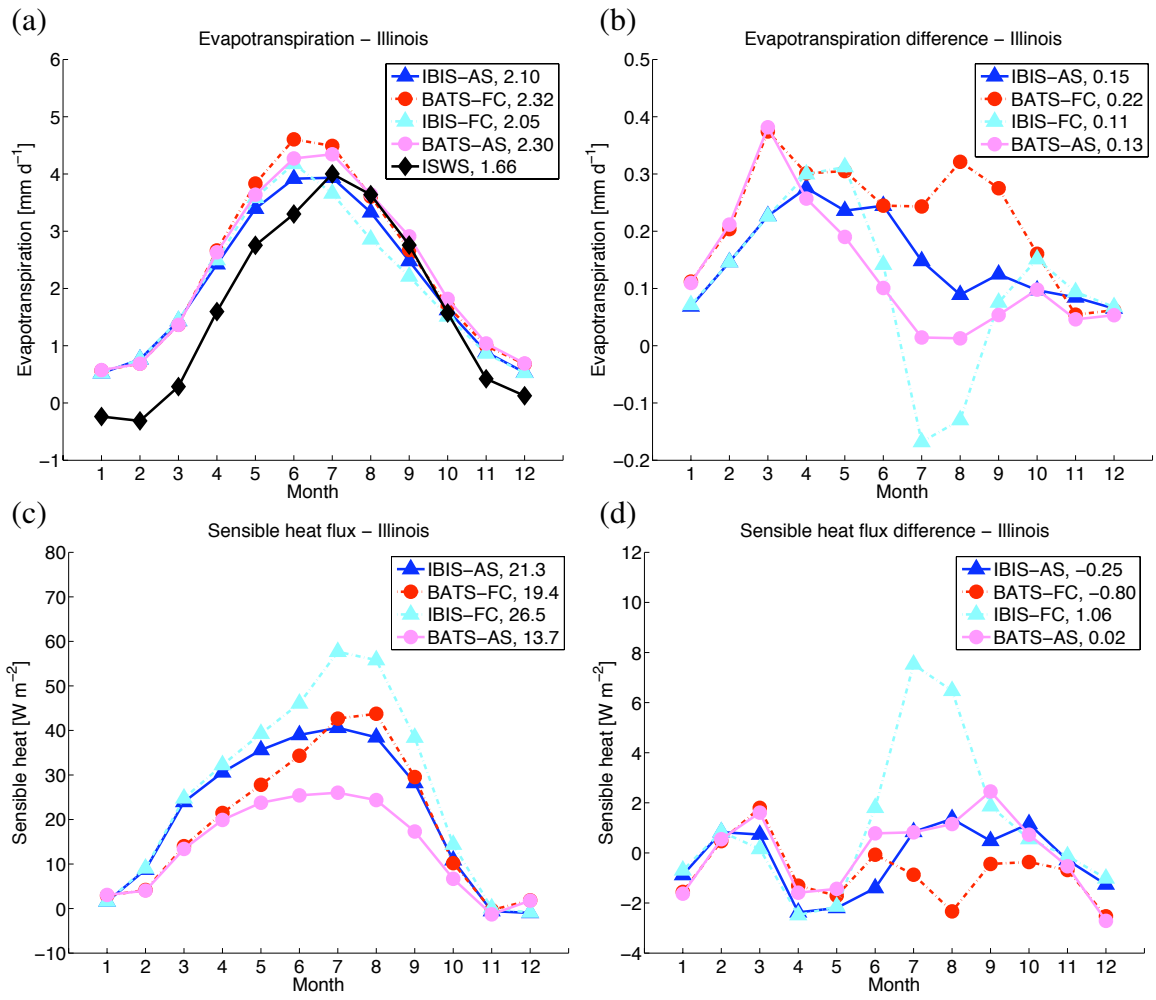

Figure 5-4: NNRP2 control and observed seasonal cycles of: (a) evapotranspiration, (c) sensible heat flux; and the difference between NNRP2 surrogate climate change and NNRP2 control seasonal cycles of: (b) evapotranspiration, (d) sensible heat flux for 1984-2005. Annual averages for each variable examined are provided in the legend.

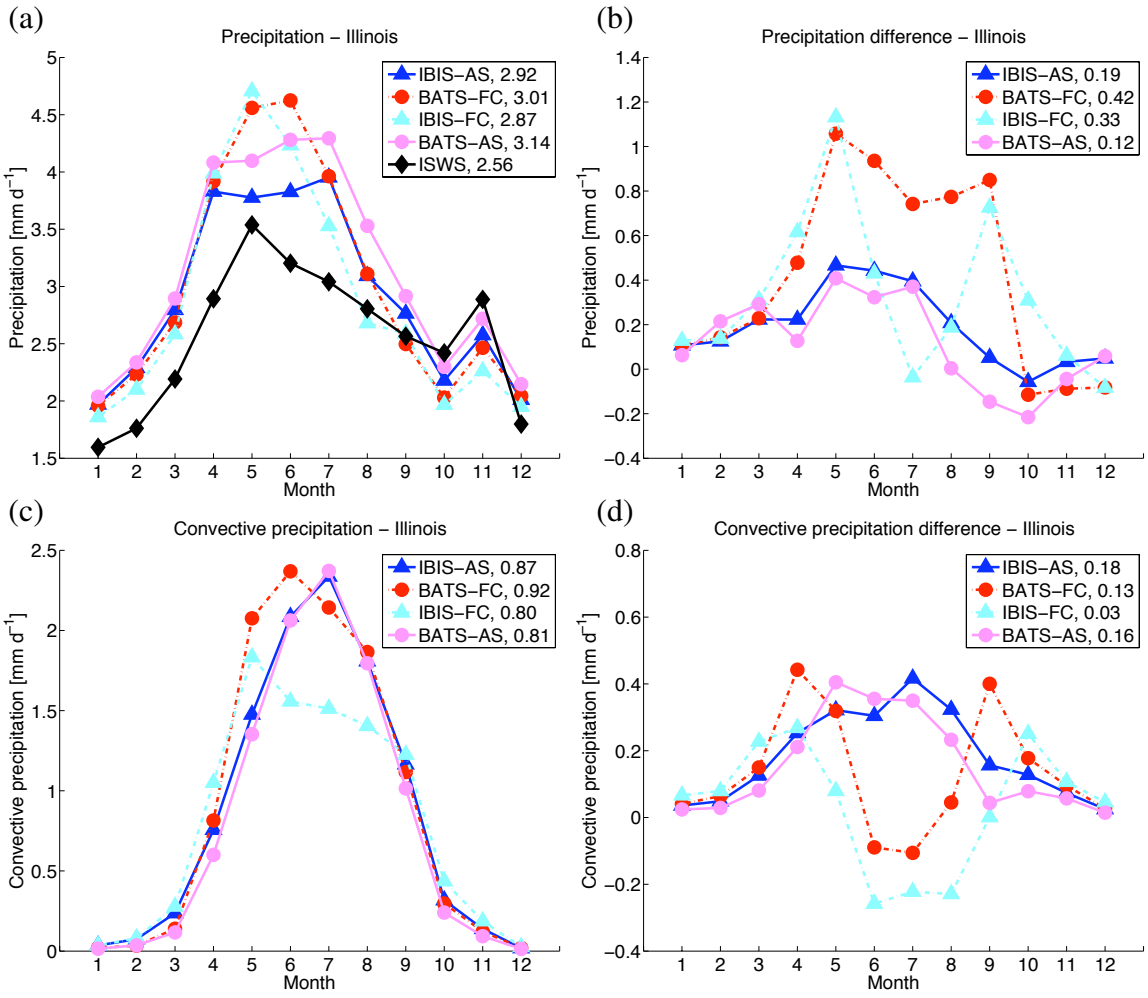

Figure 5-5: NNRP2 control and observed seasonal cycles of: (a) precipitation, (c) convective precipitation; and the difference between NNRP2 surrogate climate change and NNRP2 control seasonal cycles of: (b) precipitation, (d) convective precipitation for 1984-2005. Annual averages for each variable examined are provided in the legend.

with the tendency of the AS74 closure assumption to produce a narrower range of rainfall values and more clouds in the NNRP2 control simulations. In contrast, IBIS-FC simulates large precipitation increases during the spring (March, April, May) and fall (September, October, November), but increases precipitation only 0.20 mm d^{-1} during the summer. One surprising result of these simulations is the breakdown of precipitation between convective and large scale. IBIS-AS and BATS-AS show an increase in convective precipitation during the summer under the NNRP2 surrogate climate change scenario as expected, but BATS-FC and IBIS-FC only show an increase in convective precipitation during the spring and fall. This response is expected given the NNRP2 control simulation of IBIS-FC, where higher than observed surface temperatures reduce convective precipitation during the warmest months of the year.

The differences in total runoff between the NNRP2 surrogate climate change and NNRP2 control simulations of IBIS-AS and BATS-AS are minimal (Figure 5-6). Changes in BATS-FC and IBIS-FC total runoff are dominated by increases in surface runoff resulting from additional precipitation. Because precipitation is heavily influenced by convective closure assumption, the response of total runoff is sensitive to convective closure assumption. Annually averaged, total runoff increases under the NNRP2 surrogate climate change scenario in BATS-FC (0.19 mm d^{-1}) and IBIS-FC (0.22 mm d^{-1}). Over the summer months, the average increases in total runoff for BATS-FC and IBIS-FC are 0.44 mm d^{-1} (55%) and 0.32 mm d^{-1} (27%), respectively. Increased total runoff is consistent with previous studies detailed in Section 5.1. The implications of the response of runoff to climate change are discussed further in Section 6.2.2

The response of surface runoff to the NNRP2 surrogate climate change scenario is primarily dictated by convective closure assumption (Figure 5-6). The increase in IBIS-AS and BATS-AS surface runoff is small. In contrast, BATS-FC and IBIS-FC enhance late spring and summer precipitation, which increases surface runoff significantly during the summer in BATS-FC (0.39 mm d^{-1}) and IBIS-FC (0.35 mm d^{-1}). This result is in agreement with the work of Niemann and Eltahir [2005], who noted in their study of Illinois using a stochastic model that surface runoff amplified climate change signals.

Changes in groundwater runoff produced by the NNRP2 surrogate climate change forc-

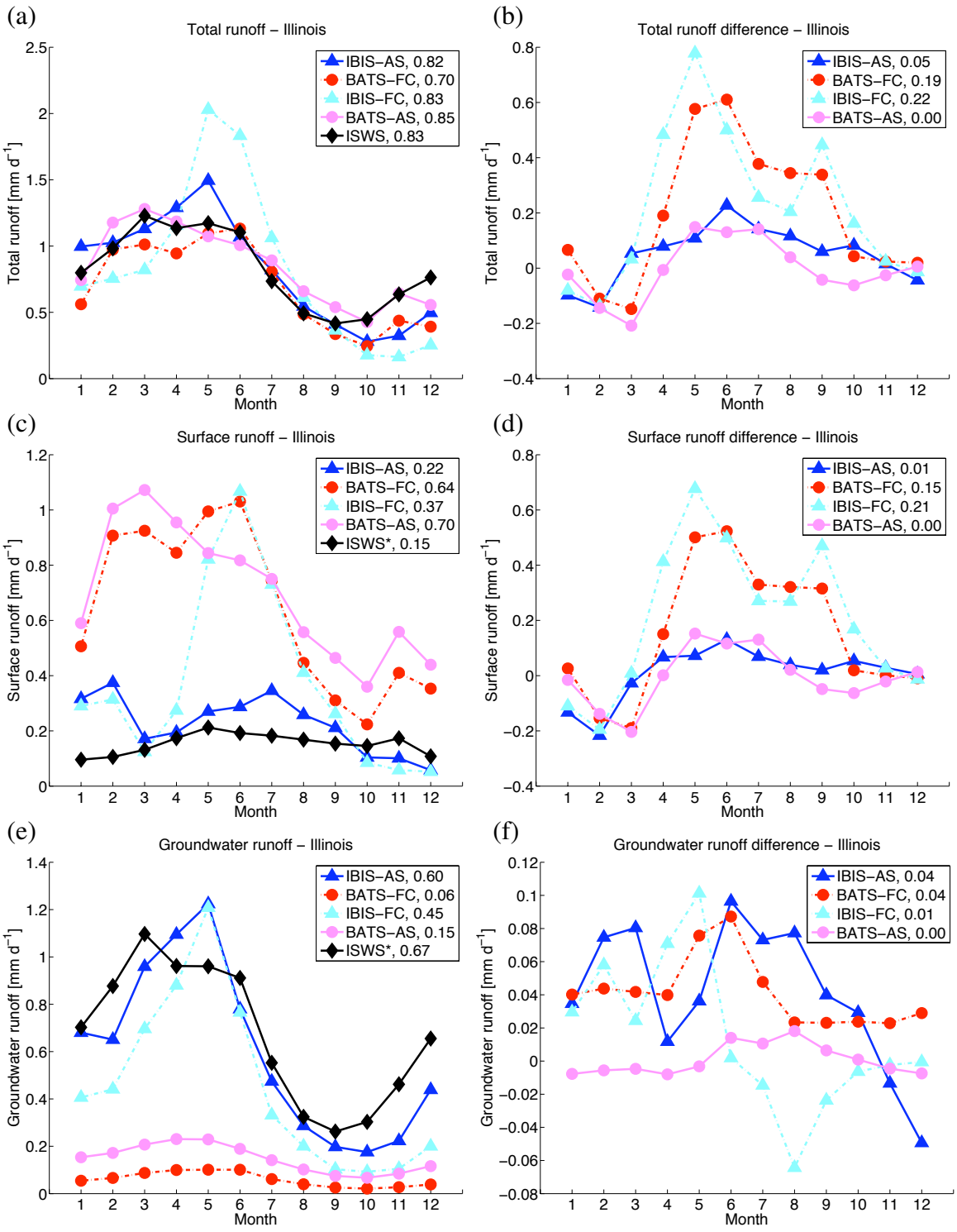

Figure 5-6: NNRP2 control and observed seasonal cycles of: (a) total runoff, (c) surface runoff, (e) groundwater runoff; and the difference between NNRP2 surrogate climate change and NNRP2 control seasonal cycles of: (b) total runoff, (d) surface runoff, (f) groundwater runoff for 1984-2005. Annual averages for each variable examined are provided in the legend. *estimate of runoff as described in Section 3.2

ing are damped when compared with surface runoff. The largest response is simulated by IBIS-AS and BATS-FC, but is only 0.04 mm d^{-1} annually averaged. Changes in groundwater runoff are determined by both surface physics scheme and precipitation. Note that relative to NNRP2 control seasonal cycles, the changes in IBIS-AS, BATS-AS, and IBIS-FC groundwater runoff are minimal, whereas the increase in groundwater runoff in BATS-FC is on the order of the seasonal cycle itself.

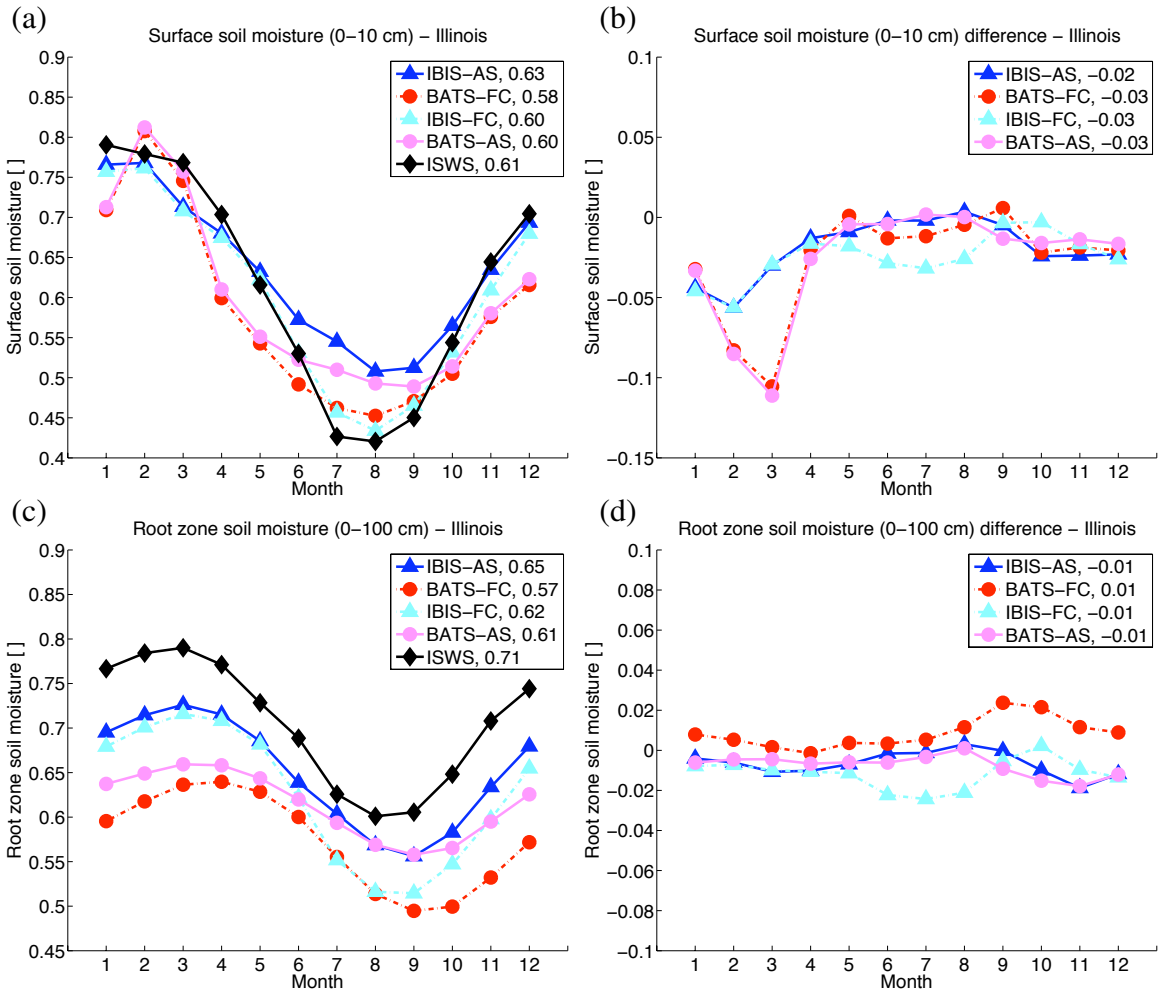

Figure 5-7: NNRP2 control and observed seasonal cycles of: (a) surface soil moisture, (c) root zone soil moisture; and the difference between NNRP2 surrogate climate change and NNRP2 control seasonal cycles of: (b) surface soil moisture, (d) root zone soil moisture for 1984-2003. Annual averages for each variable examined are provided in the legend.

The differences between the NNRP2 surrogate climate change and NNRP2 control seasonal cycles of surface soil moisture are very small and well within the variability of the NNRP2 control seasonal cycle ensemble (Figure 5-7). Changes in surface soil moisture

under the NNRP2 surrogate climate change scenario are primarily a function of surface physics scheme during the spring, winter (December, January, February), and fall. In summer, precipitation, and therefore convective closure, is a significant factor.

The response of root zone soil moisture to the NNRP2 surrogate climate change scenario is minimal. While there is some late summer and early fall wetting in BATS-FC and IBIS-AS, this wetting is trivial compared to the differences in root zone soil moisture across model configurations. The largest change in summer root zone soil moisture is simulated by IBIS-FC (-0.02 or -4.0%). This demonstrates the key finding of this study: there are no significant summer soil moisture reductions under a warmer climate in the midwestern United States.

Profiles of soil moisture also show negligible changes when forced using NNRP2 surrogate climate change boundary conditions instead of NNRP2 control boundary conditions (Figure 5-8). Annually, all models simulate slight drying in the first soil layer. Below that, BATS-AS and IBIS-FC are slightly drier and IBIS-AS and BATS-FC are slightly wetter. Note that changes in the annual soil moisture profile are extremely small relative to the NNRP2 control ensemble variability. During the summer IBIS-FC simulates drying throughout the soil column and IBIS-AS simulates wetting; however, these changes are insignificant compared with the model configuration variability found in the NNRP2 control runs.

Figures 5-9 and 5-10 show the response of key components of the hydrologic cycle to the NNRP2 surrogate climate change scenario within the context of interannual variability. Specifically, Figures 5-9 and 5-10 contain the IBIS-AS and BATS-FC seasonal cycles and seasonal cycle differences of Figures 5-4, 5-5, 5-6, and 5-7, but also have error bars denoting the standard deviations of the NNRP2 control seasonal cycles (a measure of interannual variability) and error bars denoting the sign and magnitude of the difference between the standard deviations of the NNRP2 surrogate climate change and NNRP2 control seasonal cycles. This analysis was conducted using the two model configurations that best reproduced the observed hydroclimatology of the midwestern United States in the NNRP2 control experiments presented in Section 3.3.1: IBIS-AS and BATS-FC.

Precipitation is highly variable throughout the year. The response of IBIS-AS to the

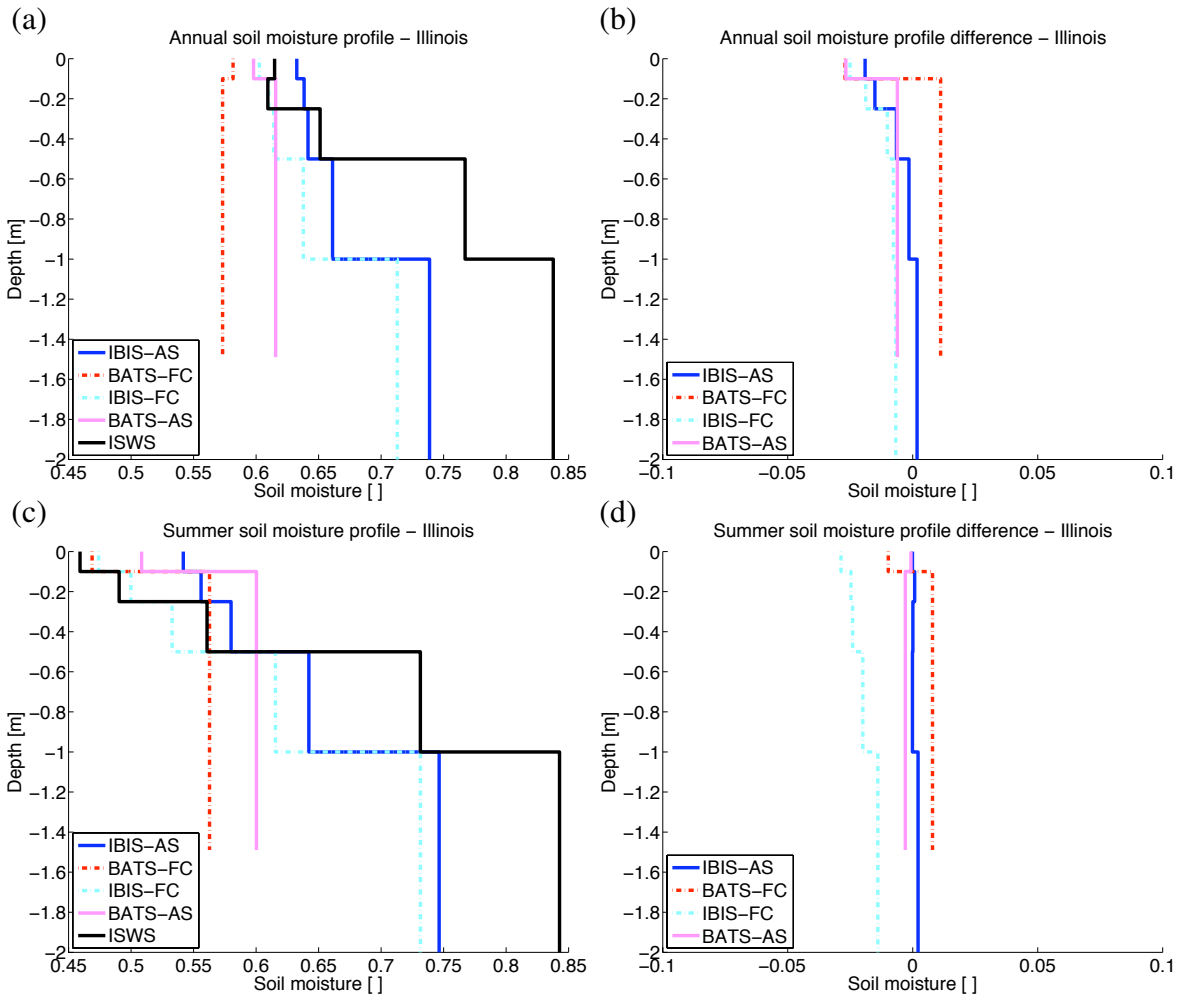

Figure 5-8: NNRP2 control and observed (a) annual, (c) summer (June, July, August) soil moisture profiles; and the difference between NNRP2 surrogate climate change and NNRP2 control (b) annual, (d) summer (June, July, August) soil moisture profiles for 1984-2003.

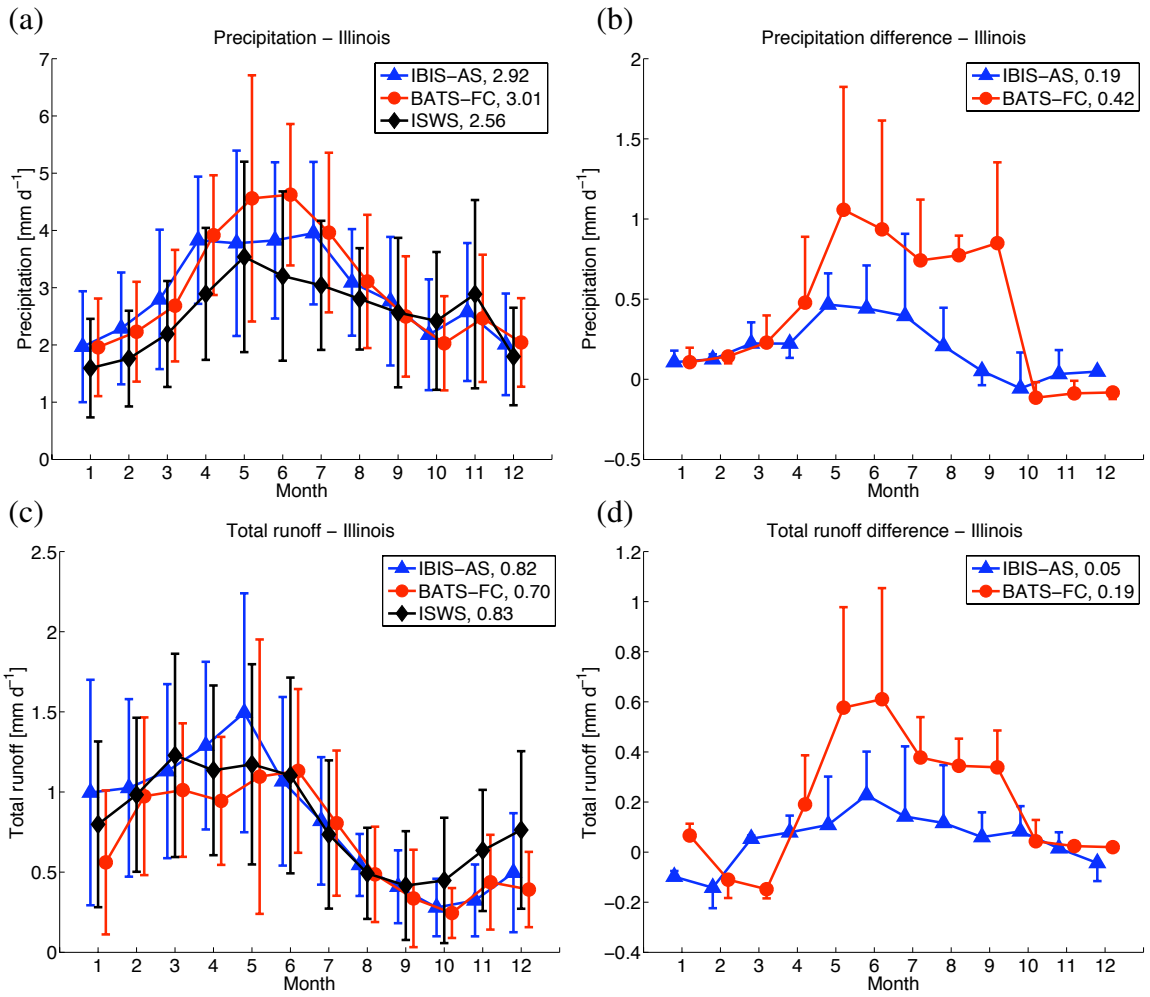

Figure 5-9: NNRP2 control and observed seasonal cycles of: (a) precipitation, (c) total runoff for 1984-2005. Error bars denote the standard deviations of the NNRP2 control seasonal cycles. The difference between NNRP2 surrogate climate change and NNRP2 control seasonal cycles of: (b) precipitation, (d) total runoff for 1984-2005. Error bars denote the difference between the standard deviations of NNRP2 surrogate climate change and NNRP2 control seasonal cycles. Annual averages for each variable examined are provided in the legend.

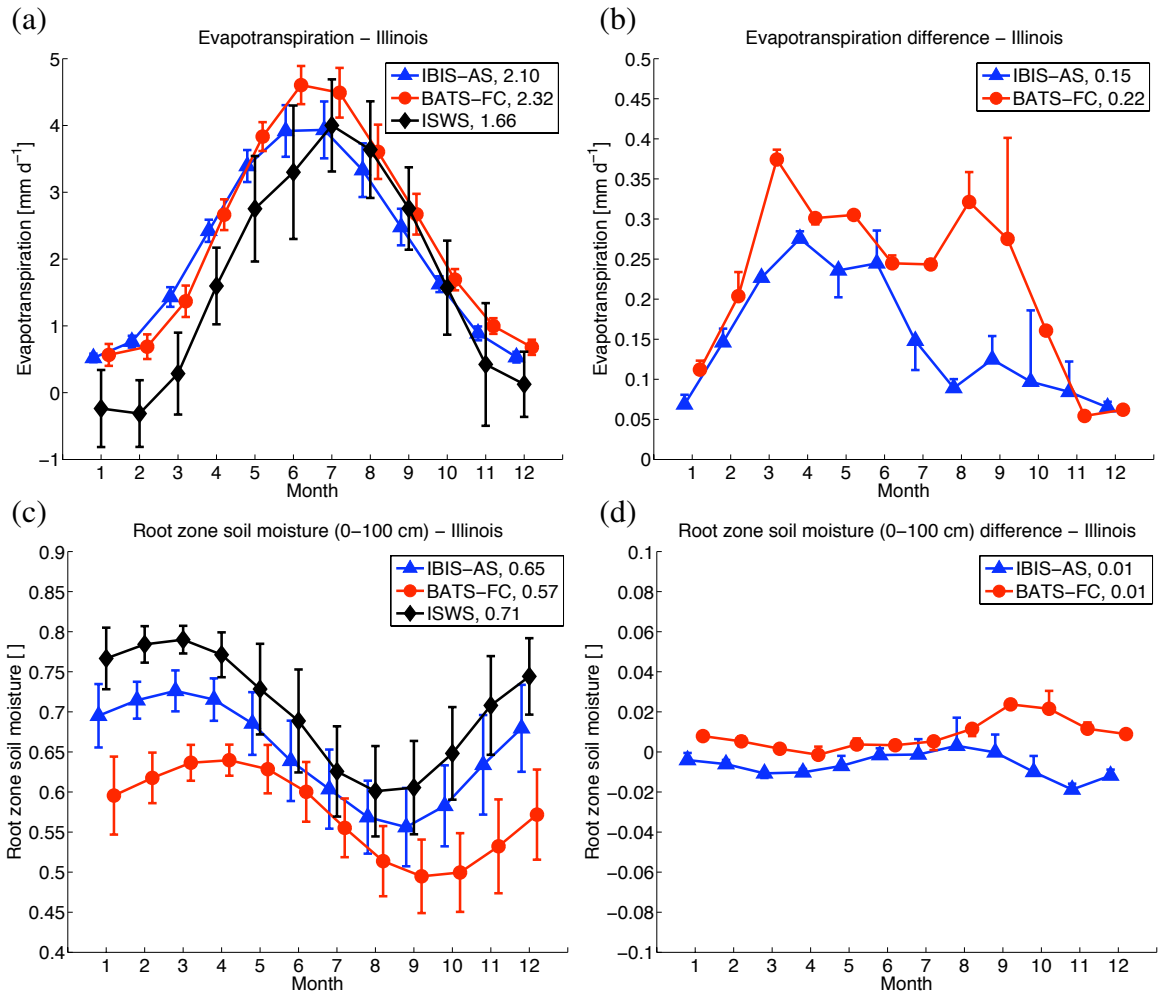

Figure 5-10: NNRP2 control and observed seasonal cycles of: (a) evapotranspiration (1984-2005), (c) root zone soil moisture (1984-2003). Error bars denote the standard deviations of the NNRP2 control seasonal cycles. The difference between NNRP2 surrogate climate change and NNRP2 control seasonal cycles of: (b) evapotranspiration (1984-2005), (d) root zone soil moisture (1984-2003). Error bars denote the difference between the standard deviations of NNRP2 surrogate climate change and NNRP2 control seasonal cycles. Annual averages for each variable examined are provided in the legend.

NNRP2 surrogate climate change scenario is generally less than the standard deviation of the IBIS-AS NNRP2 control precipitation seasonal cycle; however, the increase in precipitation simulated by BATS-FC during the summer is closer in magnitude to the standard deviation of the BATS-FC NNRP2 control precipitation seasonal cycle. Both IBIS-AS and BATS-FC simulate increased interannual variability when forced using NNRP2 surrogate climate change boundary conditions. This finding is consistent with the studies described in Section 5.1, which concluded that climate change will cause more intense precipitation events throughout the year over the American Midwest.

High interannual variability in IBIS-AS and BATS-FC precipitation drives high interannual variability in IBIS-AS and BATS-FC total runoff. Like precipitation, the standard deviation of the NNRP2 control total runoff seasonal cycle is greater than the response of total runoff to the NNRP2 surrogate climate change scenario in IBIS-AS, and approximately the same as the response of total runoff to the NNRP2 surrogate climate change scenario in BATS-FC. The interannual variability of IBIS-AS and BATS-FC total runoff increases throughout the year under the NNRP2 surrogate climate change forcing, a result of the increase in IBIS-AS and BATS-FC precipitation interannual variability under the NNRP2 surrogate climate change forcing.

While differences in evapotranspiration between the NNRP2 surrogate climate change and NNRP2 control seasonal cycles are relatively small compared to other components of the hydrologic cycle, throughout most of the year the enhancement of evapotranspiration is larger than the standard deviations of the IBIS-AS and BATS-FC NNRP2 control seasonal cycles. However, note that the interannual variability of the NNRP2 control evapotranspiration seasonal cycles simulated by both models is lower than observed.

The response of IBIS-AS and BATS-FC root zone soil moisture to the NNRP2 surrogate climate change scenario is very small compared to the standard deviations of the IBIS-AS and BATS-FC NNRP2 control seasonal cycles.

Figure 5-11 shows the differences between the summer (June, July, August) hydrologic cycles of the NNRP2 surrogate climate change and NNRP2 control simulations for IBIS-AS and BATS-FC throughout the United States.

IBIS-AS and BATS-FC simulate additional summer precipitation throughout the mid-

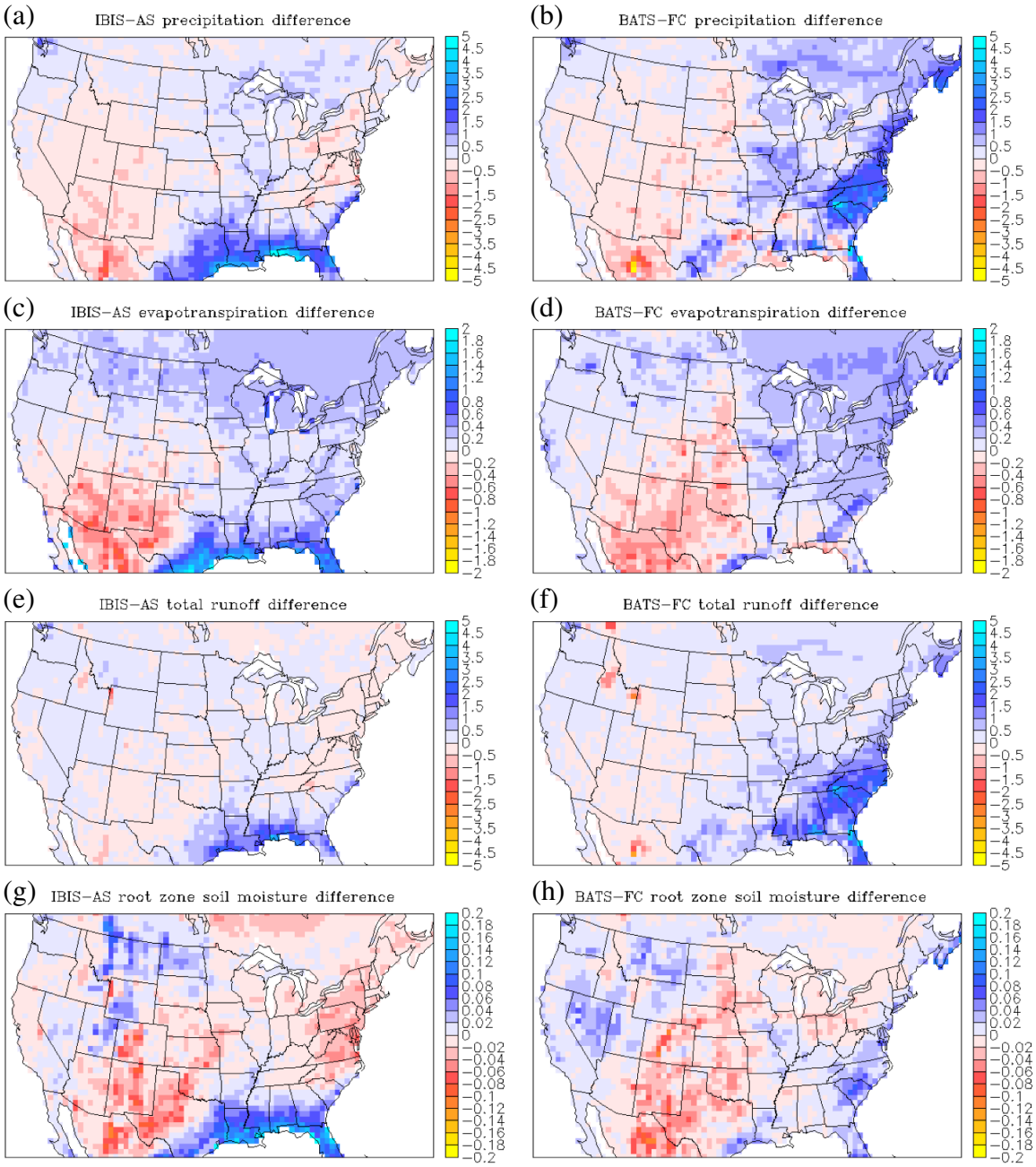

Figure 5-11: Difference between NNRP2 surrogate climate change and NNRP2 control simulations of summer (June, July, August): (a), (b) precipitation; (c), (d) evapotranspiration; (e), (f) total runoff; (g), (h) root zone soil moisture for the years 1984-2005.

western United States when forced using NNRP2 surrogate climate change boundary conditions. Large precipitation increases are predicted along the Gulf of Mexico by IBIS-AS and the East Coast by BATS-FC. The exception to enhanced precipitation is southwestern North America, where decreases in summer precipitation are found throughout Arizona, New Mexico, and western Mexico.

The spatial distribution of the summer evapotranspiration response to the NNRP2 surrogate climate change scenario is reasonably well correlated with changes in precipitation; however, the magnitude of the response is damped. IBIS-AS and BATS-FC simulate increased evapotranspiration throughout the northwestern, midwestern, and eastern United States. Both models decrease evapotranspiration across the southwestern United States and northern Mexico during the summer months, likely a result of reduced precipitation.

The increase in June, July, August total runoff resulting from the NNRP2 surrogate climate change scenario is greater in BATS-FC. Enhanced runoff simulated by BATS-FC is especially prominent over the southeastern and midwestern United States, and is generated by increased precipitation. Changes in IBIS-AS total runoff during the summer months are relatively small with the exception of the Gulf of Mexico, where large increases in June, July, August precipitation drive enhanced summer total runoff.

The differences in summer root zone soil moisture between the NNRP2 surrogate climate change and NNRP2 control simulations of IBIS-AS and BATS-FC are relatively small throughout much of the United States. Soil moisture increases along the Gulf of Mexico in IBIS-AS, and to a lesser extent the East Coast in BATS-FC, are substantial and a result of enhanced precipitation. Reduced summer soil moisture is significant over some parts of the southwestern United States and northern Mexico, especially relative to the dry soils contained in these areas.

One useful method for examining the response of the hydrologic cycle to climate change is examining the humidity index, which is the ratio of precipitation to potential evaporation, and the runoff coefficient, which is the ratio of total runoff to precipitation. Potential evaporation was calculated using the Penman-Monteith equation with the surface resistance (r_s) set to 0:

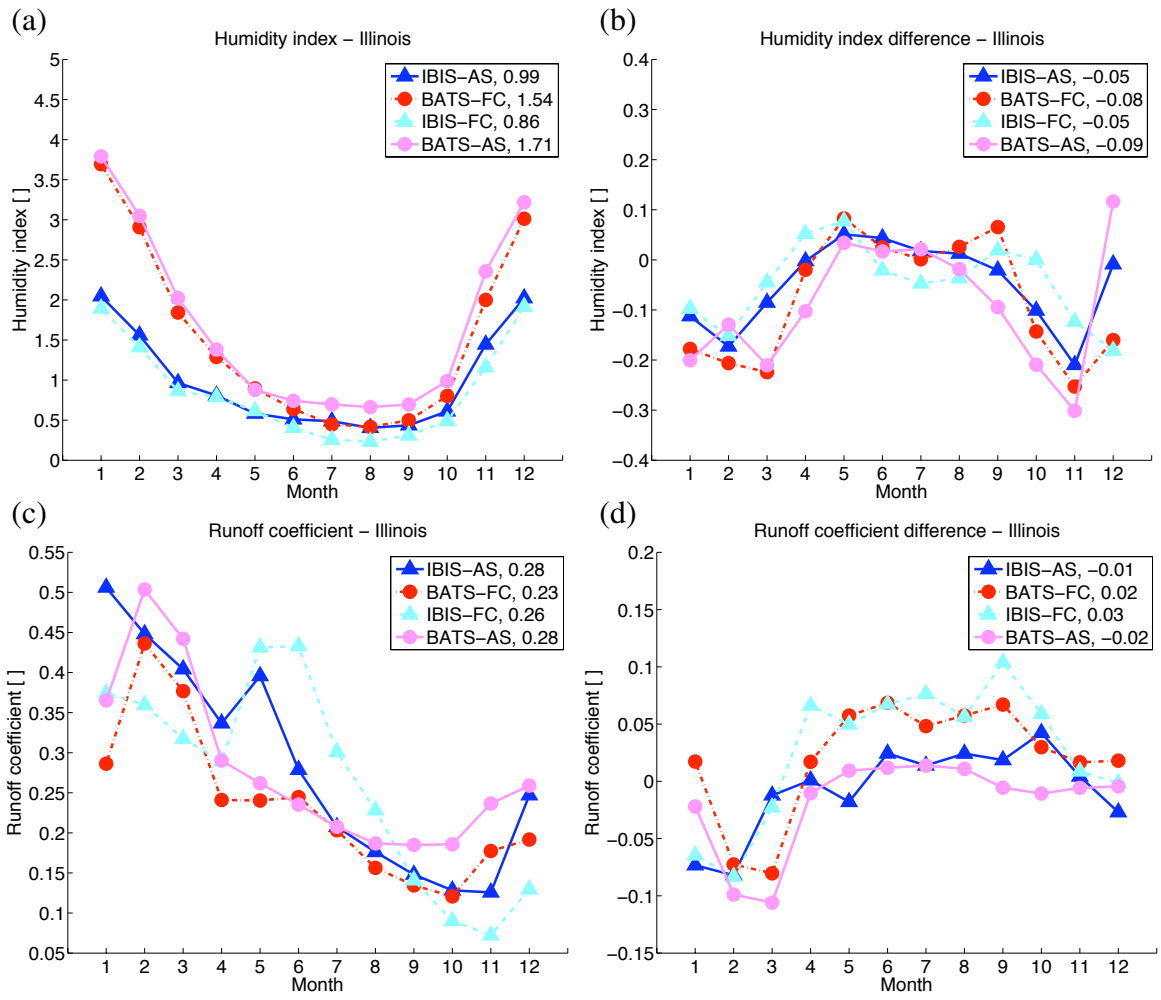

Figure 5-12: NNRP2 control and observed seasonal cycles of: (a) the humidity index, (c) the runoff coefficient; and the difference between NNRP2 surrogate climate change and NNRP2 control seasonal cycles of: (b) the humidity index, (d) the runoff coefficient for 1984-2005. Annual averages for each variable examined are provided in the legend.

$$\lambda E = \frac{\Delta A + \frac{\rho c_p}{r_a}(e_{sat} - e)}{\Delta + \gamma}, \tag{5.1}$$

where:

$$r_a = \frac{\bar{u}}{u_*^2}. \tag{5.2}$$

In Equations 5.1 and 5.2, λE is the latent heat flux, Δ is the slope of the saturation vapor pressure-temperature relationship, A is the available energy, ρ is the mean air density, c_p is the specific heat of air, r_a is the aerodynamic resistance, $(e_{sat} - e)$ is the vapor pressure deficit, γ is the psychometric constant, $\bar{u}$ is mean canopy wind speed, and u_* is the friction velocity [Shuttleworth, 1979]. Mean canopy wind speeds for all models were derived from CRU CL2.0, which is a climatology of wind speeds from 1961-1999 at a 10' spatial resolution [New et al., 2002].

The largest humidity indices are simulated by BATS-FC and BATS-AS; however, during the summer months the humidity indices of BATS-AS are similar to humidity indices of IBIS-AS and IBIS-FC. Discrepancies in the humidity index seasonal cycles of IBIS-AS, BATS-FC, IBIS-FC, and BATS-AS during the winter months are primarily a result of differences in the vapor pressure deficit $(e_{sat} - e)$. The simulation of both e_{sat} and e is strongly influenced by 2-m temperature, and BATS-AS and BATS-FC 2-m temperatures are significantly cooler than IBIS-AS for all months except June, July, and August.

All models simulate comparable runoff coefficient seasonal cycles. The large runoff coefficient values of IBIS-AS and IBIS-FC during the months of May and June are a result of groundwater runoff, which lags in response to early spring precipitation.

Limited changes in precipitation (numerator of the humidity index) coupled with increased potential evaporation caused primarily by warmer surface temperatures (denominator) results in a negative response of the humidity index to the NNRP2 surrogate climate change scenario in the winter months. In contrast, during the summer NNRP2 surrogate climate change and NNRP2 control humidity indices are similar, as increases in potential evaporation are approximately commensurate with enhanced precipitation.

The response of the runoff coefficient to the NNRP2 surrogate climate change scenario

is larger in IBIS-FC and BATS-FC during the spring and summer months. This is likely a result the intensity precipitation increase generated by the Fritsch & Chappell convective closure.

One concern raised in future climate scenarios is the possible transition to fewer, more intense rainfall events [Karl et al., 2009]. As discussed in Section 5.1, this could increase the likelihood of short-term droughts. To assess this potential problem, probability distribution functions (PDFs) of NNRP2 surrogate climate change and NNRP2 control 10-day averaged precipitation and root zone soil moisture for June, July, and August of 1984-2005 were constructed. If short-term changes to precipitation or root zone soil moisture occurred in the NNRP2 surrogate climate change scenarios during the summer months, they would be evidenced by a shift in the PDFs contained in Figure 5-13. This analysis was conducted using the two model configurations that best reproduced the observed hydroclimatology of the midwestern United States in the NNRP2 control experiments presented in Section 3.3.1: IBIS-AS and BATS-FC.

There are few differences between the precipitation PDF of IBIS-AS forced using the NNRP2 surrogate climate change scenario and the precipitation PDF of IBIS-AS forced using the NNRP2 control scenario. The number of 10-day increments that average between 3-5 mm d^{-1} decreases, and there is an increase in the number of higher intensity events, especially 10-day periods that experience 9-11 mm d^{-1}. The response of the precipitation PDF to the NNRP2 surrogate climate change scenario is more pronounced in BATS-FC. There is a decrease in the number of 10-day periods with less than 5 mm d^{-1} of precipitation and a corresponding increase in the days with more than 5 mm d^{-1} of precipitation. The BATS-FC NNRP2 surrogate climate change scenario also contains significantly more 10-day increments with 9-11 mm d^{-1} as well as some very large 10-day precipitation averages not found in the the NNRP2 control simulations.

Relative to the IBIS-AS root zone soil moisture PDF under the NNRP2 control scenario, the IBIS-AS root zone soil moisture PDF under the NNRP2 surrogate climate change scenario contains more dry (0.475-0.525) and more wet (0.725-0.825) 10-day periods as well as a reduction in the most frequently occurring value of fractional soil moisture. Increased precipitation in BATS-FC forced using NNRP2 surrogate climate change boundary condi-

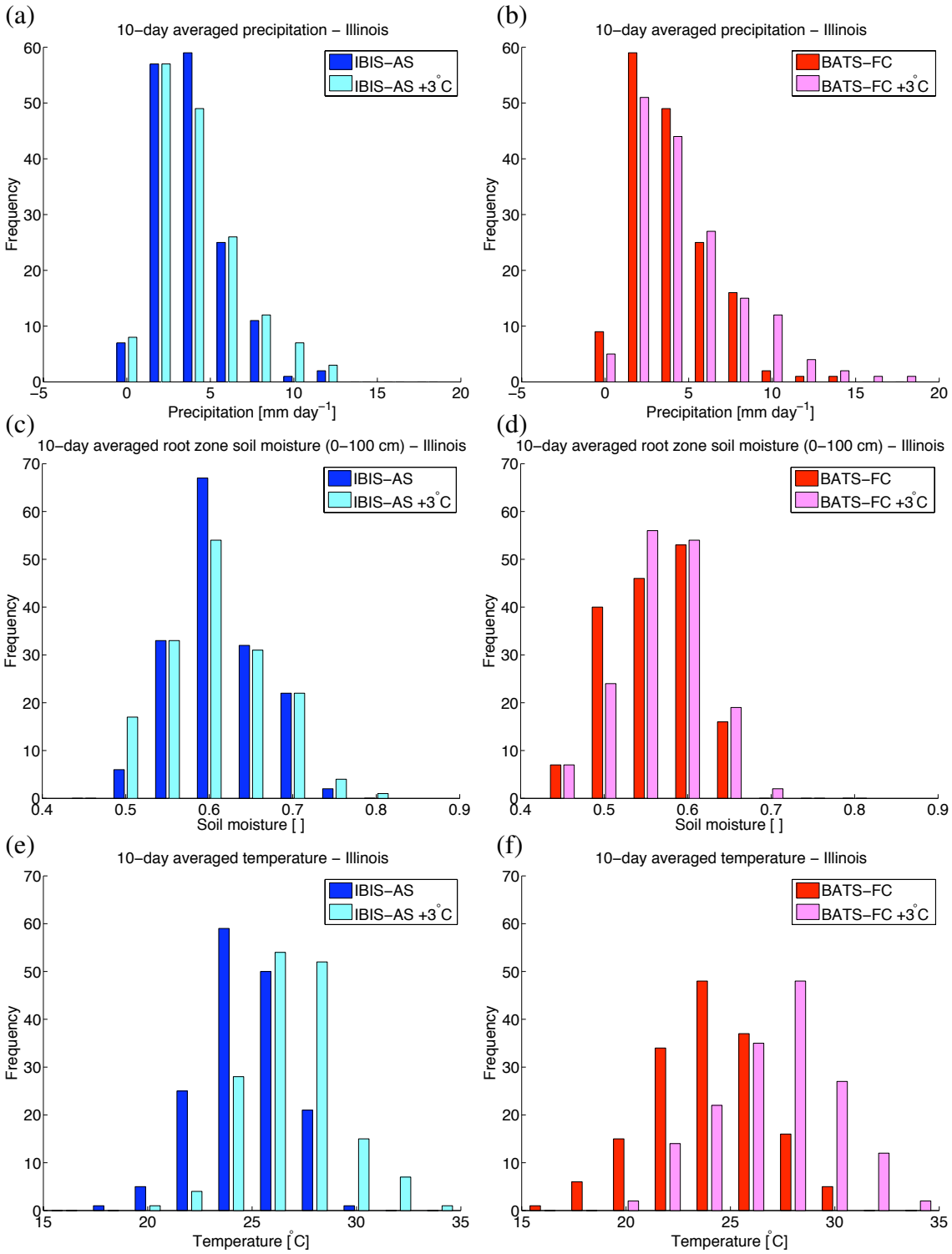

Figure 5-13: NNRP2 surrogate climate change and NNRP2 control probability distribution functions of summer (June, July, August) 10-day averaged: (a), (b) precipitation; (c), (d) root zone soil moisture; (e), (f) temperature for 1984-2005.

tions results in higher 10-day root zone soil moisture. Specifically, the number of 10-day periods with soil moisture values of 0.475-0.525 decreases and the frequency of 10-day increments with an average soil moisture of 0.525-0.725 increases.

Shifts in the 2-m temperature PDFs of both IBIS-AS and BATS-FC resulting from the NNRP2 surrogate climate change scenario are pronounced. Both models simulate warmer average 10-day temperatures throughout the summer, but the distribution of temperature, shown by the shape of the PDF, appears relatively unchanged. The most frequently occurring 10-day averaged 2-m temperature increases $\approx$2°C in IBIS-AS and $\approx$4°C in BATS-FC.

Sensitivity of Results to Precipitation

IBIS-AS, BATS-FC, IBIS-FC, and BATS-AS simulate excess precipitation when compared to observations. In theory, this overestimation of precipitation could bias results and hide soil drying. To address this concern, a subset of model output that best reproduced the seasonal cycles of precipitation over the American Midwest was analyzed. There are a total of 19 years simulated for which observations of soil moisture are available. Of those 19 years, the 10 years that contained the smallest late spring and summer (April, May, June, July, August) precipitation biases in both IBIS-AS and BATS-FC were selected, and 10-year seasonal cycles for precipitation and soil moisture were constructed.

The seasonal cycles of total and convective precipitation for the years that IBIS-AS and BATS-FC best simulate precipitation in the late spring and summer are presented in Figure 5-14. The summer precipitation biases of IBIS-AS and BATS-FC are reduced from 0.61 mm d^{-1} and 0.88 mm d^{-1} for the all-years average to 0.40 mm d^{-1} and 0.56 mm d^{-1} for the select-years average, respectively. The select-years response of precipitation to the NNRP2 surrogate climate scenario is similar in shape to the all-years response of precipitation in IBIS-AS, BATS-FC, IBIS-FC, and BATS-AS; however, the magnitude of the precipitation increase simulated by all models for the select years is slightly larger.

The seasonal cycles of surface and root zone soil moisture for the years that IBIS-AS and BATS-FC best simulate precipitation in the late spring and summer are presented in Figure 5-15. Differences between the select-years and all-years NNRP2 control seasonal cycles of both surface and root zone soil moisture are very slight and smaller than presented

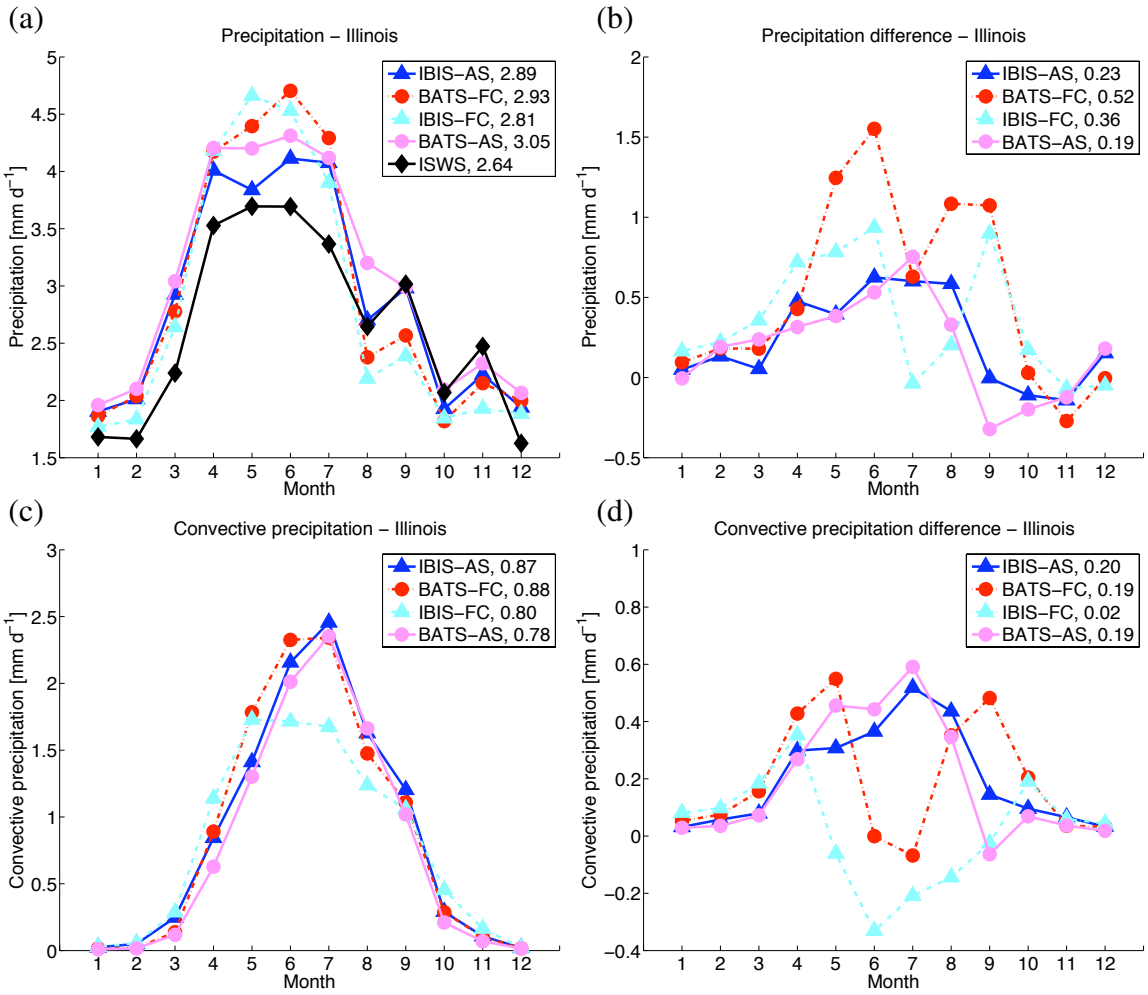

Figure 5-14: NNRP2 control and observed seasonal cycles of: (a) precipitation, (c) convective precipitation; and the difference between NNRP2 surrogate climate change and NNRP2 control seasonal cycles of: (b) precipitation, (d) convective precipitation for the 10 years (selected from 1984-2003) that best simulate late spring and summer (April, May, June, July, August) precipitation. Annual averages for each variable examined are provided in the legend.

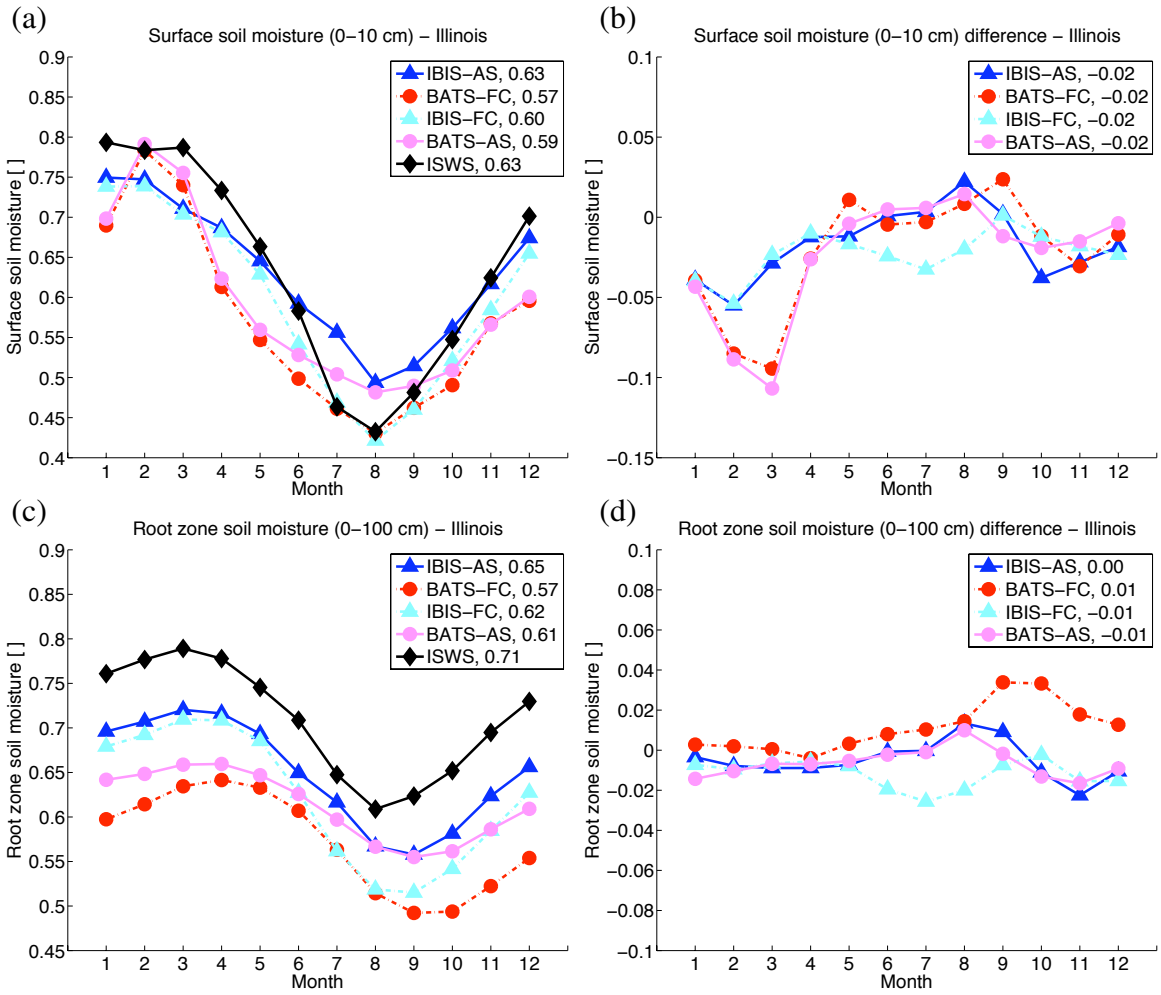

Figure 5-15: NNRP2 control and observed seasonal cycles of: (a) surface soil moisture, (c) root zone soil moisture; and the difference between NNRP2 surrogate climate change and NNRP2 control seasonal cycles of: (b) surface soil moisture, (d) root zone soil moisture for the 10 years (selected from 1984-2003) that best simulate late spring and summer (April, May, June, July, August) precipitation. Annual averages for each variable examined are provided in the legend.

significant figures annually averaged. The response of the select-year seasonal cycles of surface and root zone soil moisture to the NNRP2 surrogate climate change scenario was practically unchanged relative to the all-year response of surface and root zone soil moisture to the NNRP2 surrogate climate change scenario. This simple analysis demonstrates the robustness of predicted changes in precipitation and soil moisture under the NNRP2 surrogate climate change scenario as well as the low sensitivity of root zone soil moisture to corrections in the IBIS-AS, BATS-FC, IBIS-FC, and BATS-AS wet bias. However, additional research is necessary to further reduce the wet bias in all models and confirm the above findings.

5.3.2 ECHAM5 GCM A1B

Presented results are 4.0° x 5.5° spatial averages over the box contained in Figure 5-1. This set of simulations was run with the convective closure for RegCM3-IBIS and RegCM3-BATS1e that best reproduced the current water and energy budgets of the midwestern United States in the NNRP2 control experiments presented in Section 3.3.1: RegCM3-IBIS using the Arakawa & Schubert convective closure assumption (IBIS-AS) and RegCM3-BATS1e using the Fritsch & Chappell convective closure assumption (BATS-FC). Changes in the hydroclimatology of the American Midwest resulting from the EH5OM A1B climate change scenario are described in Figures 5-16 to 5-25.

Figures 5-16 through 5-21 present each variable using a pair of panels, where the left panel contains the seasonal cycles of the EH5OM control simulations and the right panel contains the difference between the EH5OM A1B climate change and EH5OM control seasonal cycles.

The responses of incident and absorbed surface shortwave radiation in IBIS-AS and BATS-FC to the EH5OM A1B climate change scenario are shown in Figure 5-16. Consistent with the results presented in Section 5.3.1, both models simulate a relatively small change in annually-averaged incident and absorbed shortwave radiation that is well within model configuration variability. However, IBIS-AS does simulate a 12.0 W m^{-2} reduction in absorbed shortwave radiation during the summer (June, July, August) when forced using

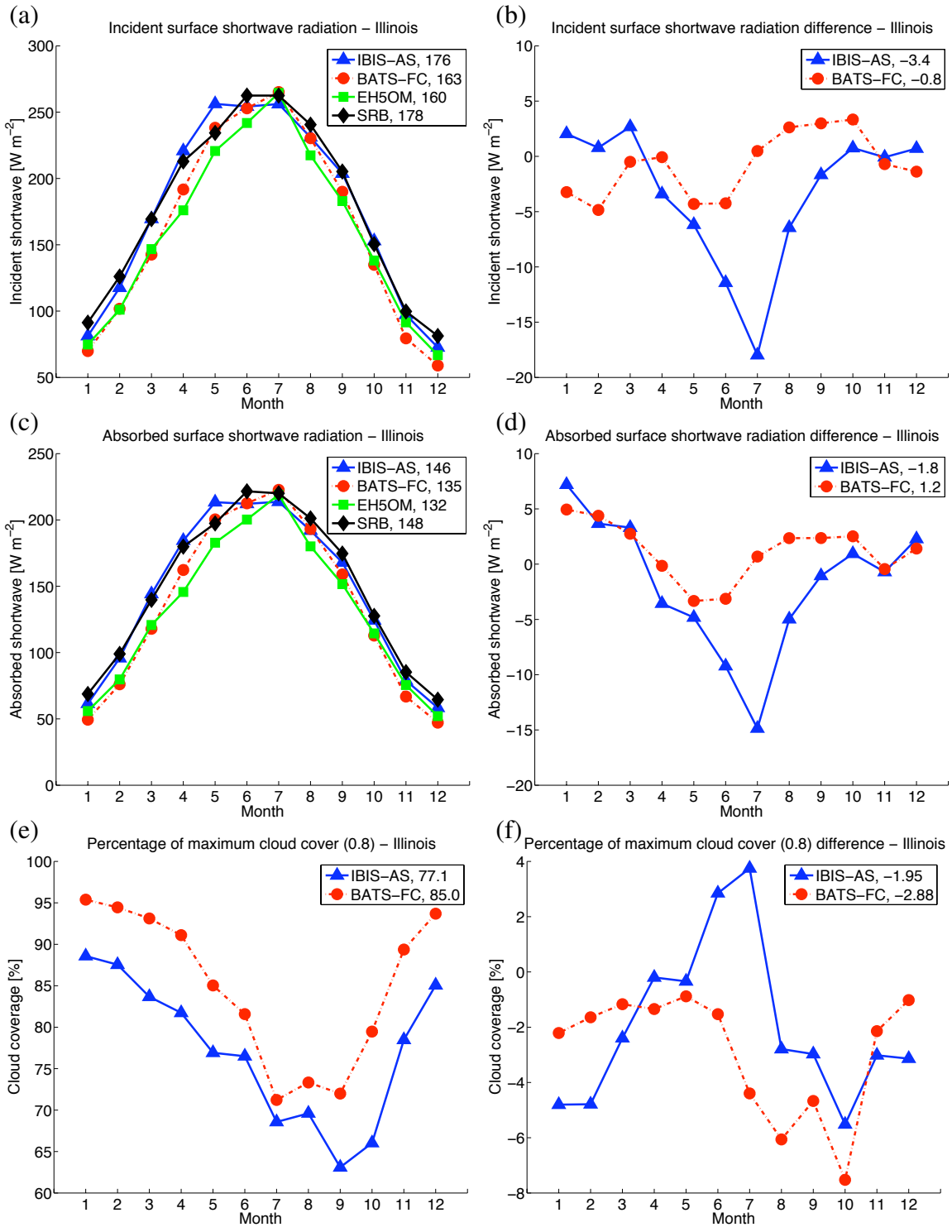

Figure 5-16: EH5OM control and observed seasonal cycles of: (a) incident surface shortwave radiation, (c) absorbed surface shortwave radiation, (e) percentage of maximum model fractional cloud cover (0.8) for 1984-2004; and the difference between EH5OM A1B climate change (2078-2098) and EH5OM control (1984-2004) seasonal cycles of: (b) incident surface shortwave radiation, (d) absorbed surface shortwave radiation, (f) percentage of maximum model fractional cloud cover (0.8). Annual averages for each variable examined are provided in the legend.

EH5OM A1B climate change boundary conditions, a result of increased cloud cover.

The EH5OM A1B climate change scenario produces a more significant warming than the NNRP2 surrogate climate change scenario. Annually averaged, the difference between the EH5OM A1B climate change and EH5OM control 2-m temperature seasonal cycles of IBIS-AS and BATS-FC are 2.93°C and 3.27°C, respectively. BATS-FC simulates a larger change in 2-m temperature, partly a result of reduced cloud cover and a slight increase in absorbed surface shortwave radiation (Figure 5-16). The variability in the EH5OM A1B climate change 2-m temperature seasonal cycles is greater than the variability in the NNRP2 surrogate climate change 2-m temperature seasonal cycles, and seems less dependent on convective closure assumption.

The response of downward longwave radiation to the EH5OM A1B climate change forcing is similar in IBIS-AS and BATS-FC (Figure 5-17). This suggests a strong control on downward longwave radiation by boundary conditions, as opposed to convective closure or surface physics scheme. The A1B scenario uses a balance of energy sources (fossil fuel and renewables) to support future growth, with levels of CO_2 equivalent varying from 624 ppm in 2076 to 700 ppm in 2100. The slightly larger increase in IBIS-AS and BATS-FC downward longwave radiation under the EH5OM A1B climate change scenario relative to the NNRP2 surrogate climate change scenario is likely a result of differences in water vapor and atmospheric temperatures.

The decrease in IBIS-AS and BATS-FC net longwave radiation (defined as positive upward) when forced using EH5OM A1B climate change boundary conditions is slightly larger than that found in Figure 5-3. IBIS-AS simulates a larger reduction in summer net longwave radiation (11.3 W m^{-2}) than BATS-FC (6.6 W m^{-2}). The increase in IBIS-AS 2-m temperature under the EH5OM A1B climate change scenario is smaller than the increase in BATS-FC 2-m temperature under the EH5OM A1B climate change scenario, which reduces the upward longwave radiation increase and results in a larger net longwave radiation decrease.

The increase in evapotranspiration under the EH5OM A1B climate change scenario is similar to the increase in evapotranspiration found under the NNRP2 surrogate climate change scenario. BATS-FC simulates a significant increase in evapotranspiration during

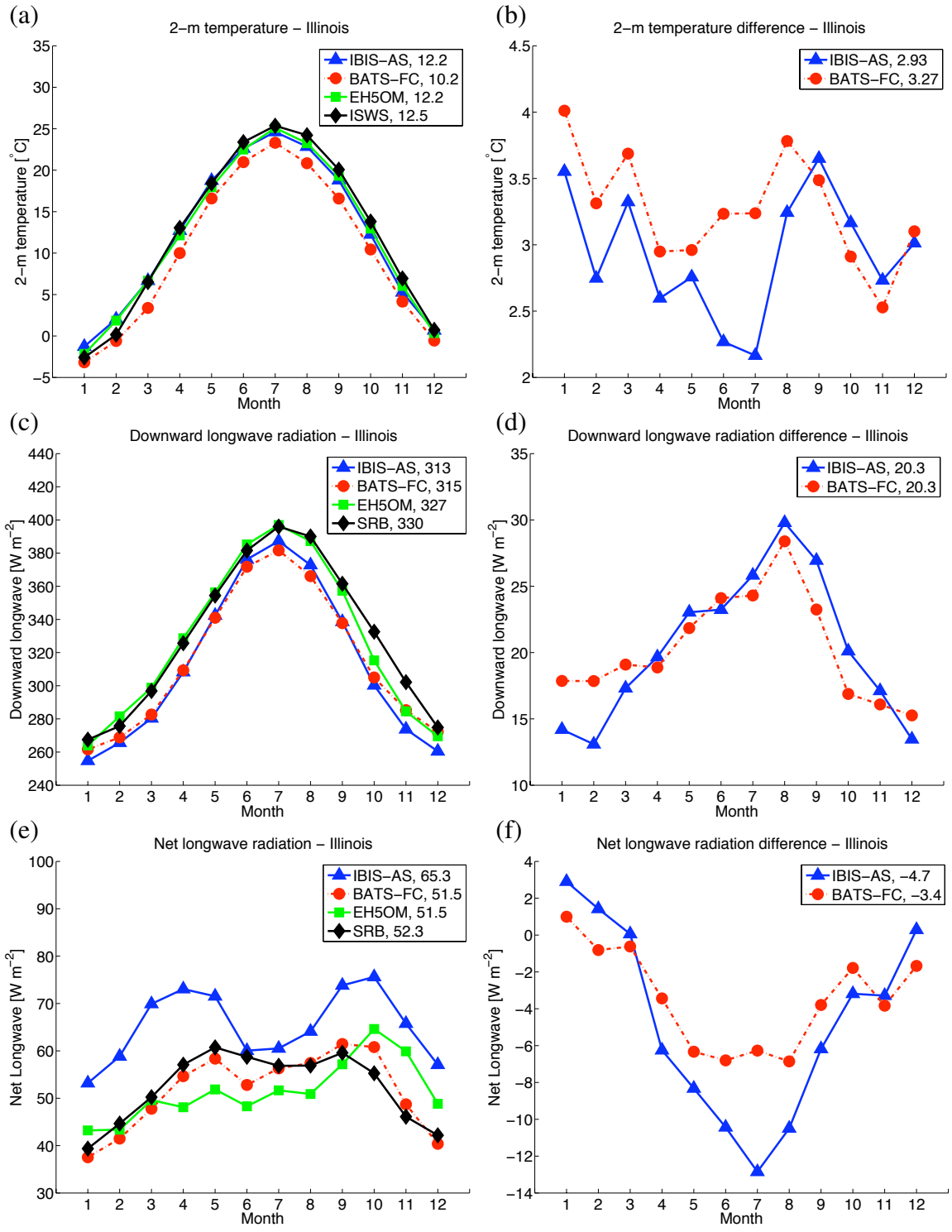

Figure 5-17: EH5OM control and observed seasonal cycles of: (a) 2-m temperature, (c) downward longwave radiation, (e) net longwave radiation (defined as positive upward) for 1984-2004 (2-m temperature 1984-2005); and the difference between the EH5OM A1B climate change (2078-2098, 2-m temperature 2078-2099) and EH5OM control (1984-2004, 2-m temperature 1984-2005) seasonal cycles of: (b) 2-m temperature, (d) downward longwave radiation, (f) net longwave radiation (defined as positive upward). Annual averages for each variable examined are provided in the legend.

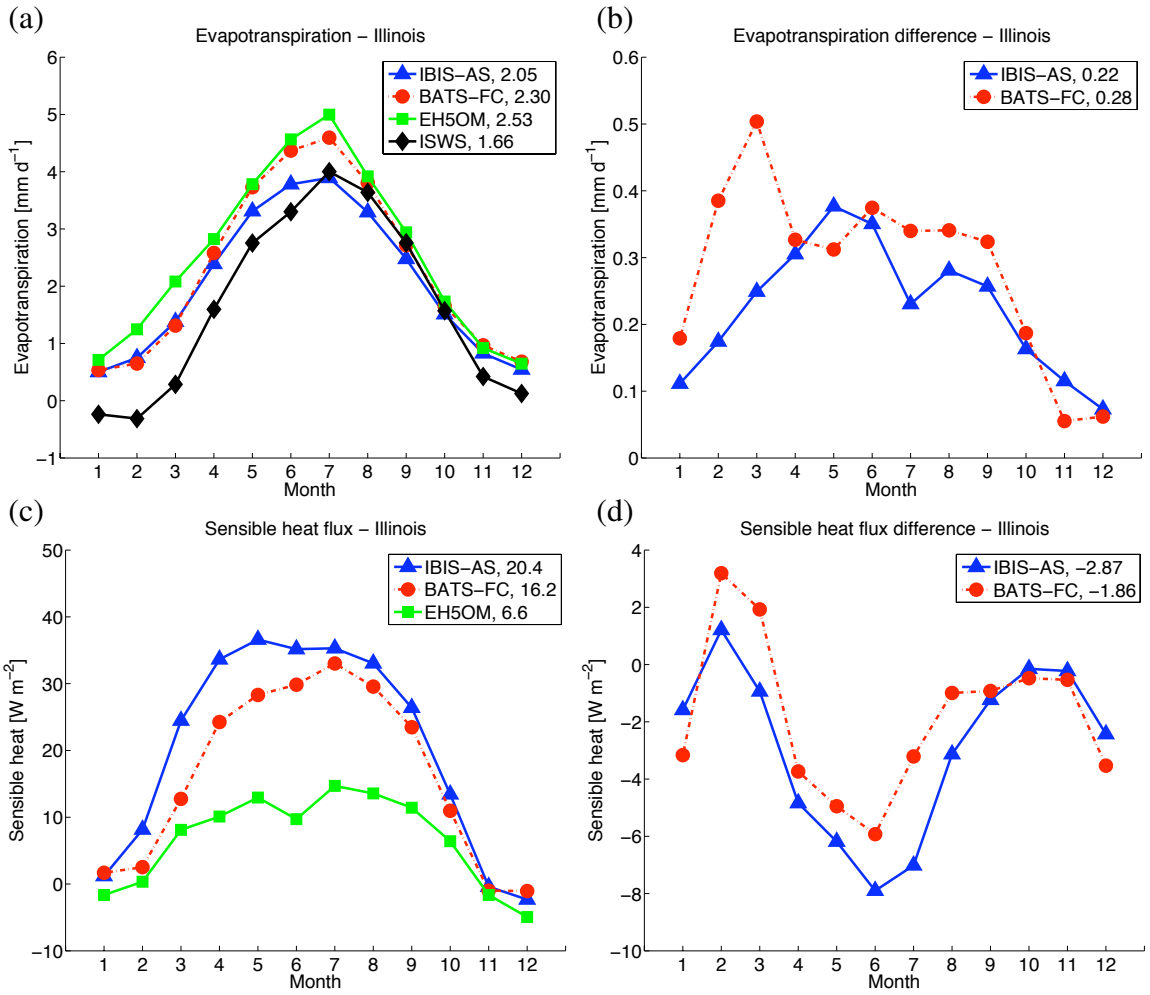

Figure 5-18: EH5OM control and observed seasonal cycles of: (a) evapotranspiration, (c) sensible heat flux for 1984-2005; and the difference between EH5OM A1B climate change (2078-2099) and EH5OM control (1984-2005) seasonal cycles of: (b) evapotranspiration, (d) sensible heat flux. Annual averages for each variable examined are provided in the legend.

the months of February and March, and therefore increases evapotranspiration more than IBIS-AS annually averaged.

The response of sensible heat flux in IBIS-AS and BATS-FC to the EH5OM A1B climate change scenario during the summer (June, July, August) is 6.0 W m^{-2} and 3.4 W m^{-2}, respectively. This is likely a result of the increased precipitation generated by the EH5OM A1B climate change forcing. The differences between the EH5OM A1B climate change and EH5OM control sensible heat flux seasonal cycles in IBIS-AS and BATS-FC are relatively similar, suggesting that the boundary conditions have significant control on the response of sensible heat flux.

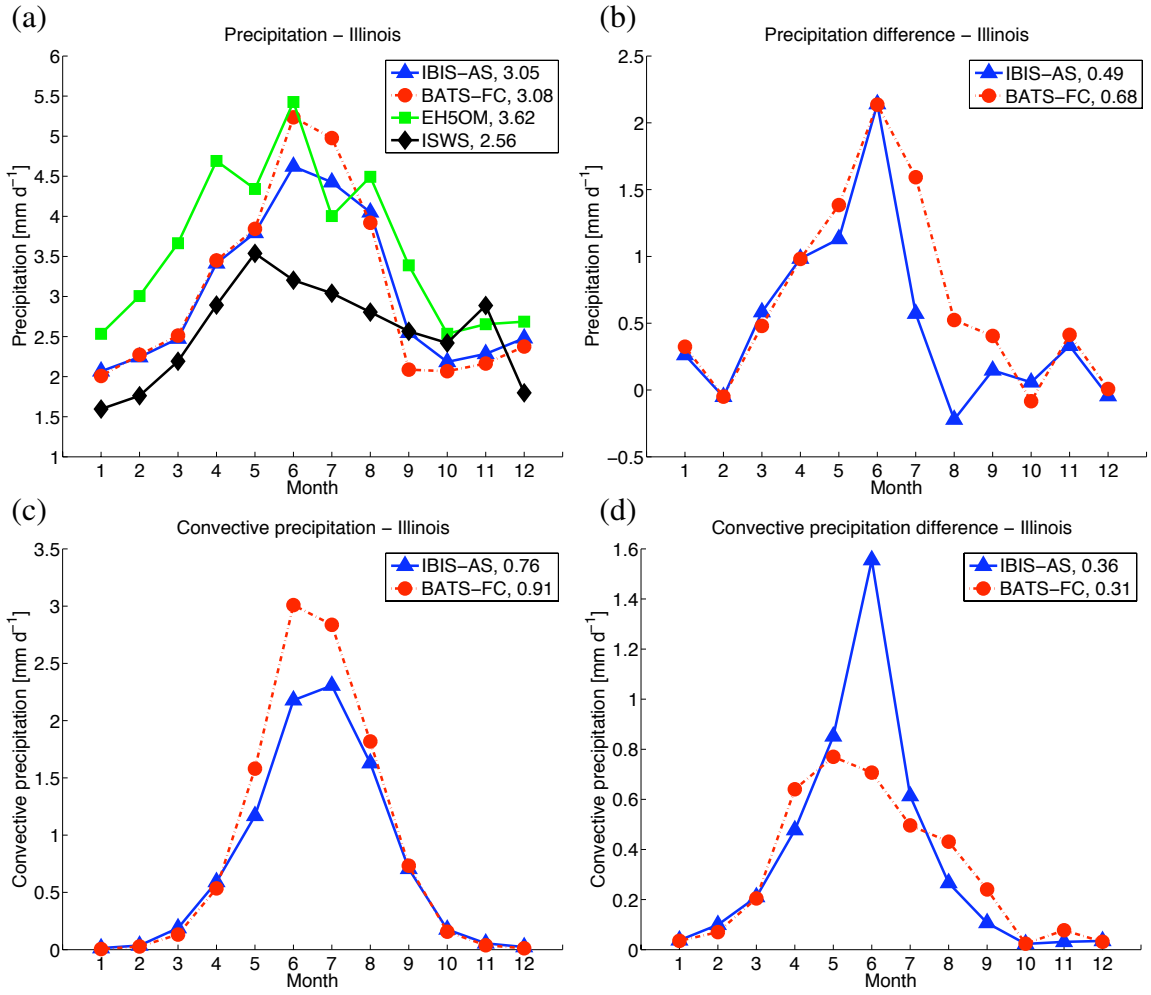

Figure 5-19: EH5OM control and observed seasonal cycles of: (a) precipitation, (c) convective precipitation for 1984-2005; and the difference between EH5OM A1B climate change (2078-2099) and EH5OM control (1984-2005) seasonal cycles of: (b) precipitation, (d) convective precipitation. Annual averages for each variable examined are provided in the legend.

The changes to the IBIS-AS and BATS-FC seasonal cycles of precipitation induced by the EH5OM A1B climate change forcing are similar. Both models simulate enhanced precipitation throughout most of the year, with a peak increase of 2.14 mm d^{-1} (46%) in IBIS-AS and 2.14 mm d^{-1} (41%) in BATS-FC during the month of June. The EH5OM A1B climate change boundary conditions produce a larger response of precipitation in IBIS-AS and BATS-FC than the NNRP2 surrogate climate change scenario. Annually averaged, BATS-FC increases precipitation more than IBIS-AS, which is consistent with the effects of the NNRP2 surrogate climate change scenario on BATS-FC and IBIS-AS precipitation. Enhanced precipitation is largely driven by increased large-scale precipitation in both models

Extremely large total runoff increases are produced by the EH5OM A1B climate change forcing, as shown in Figure 5-20. In the month of June total runoff almost doubles in IBIS-AS and BAT-FC, primarily in response to the approximate 50% increase in precipitation. Total runoff is enhanced during the summer in IBIS-AS and BATS-FC by 0.68 mm d^{-1} and 0.95 mm d^{-1}, respectively. Both models simulate small reductions of total runoff during the winter (December, January, February), a result of reduced precipitation as shown in Figure 5-19. Increases in IBIS-AS and BATS-FC total runoff generated by the EH5OM A1B climate change boundary conditions are significantly larger than increases IBIS-AS and BATS-FC total runoff resulting from the NNRP2 surrogate climate change scenario. Enhanced total runoff is consistent with previous studies detailed in Section 5.1, and the implications of the response of runoff to climate change are discussed further in Section 6.2.2

Under the EH5OM A1B climate change boundary conditions, BATS-FC simulates a 0.71 mm d^{-1} increase in surface runoff averaged over June, July, and August. The majority of total runoff in BATS-FC occurs as surface runoff. IBIS-AS has a more muted response of surface runoff to the EH5OM A1B climate change forcing than BATS-FC; however, compared to the seasonal cycle of surface runoff simulated by IBIS-AS, the increase during the summer (0.14 mm d^{-1}) is significant. In both IBIS-AS and BATS-FC, the EH5OM A1B climate change scenario produces a larger response in summer surface runoff than the NNRP2 surrogate climate change scenario.

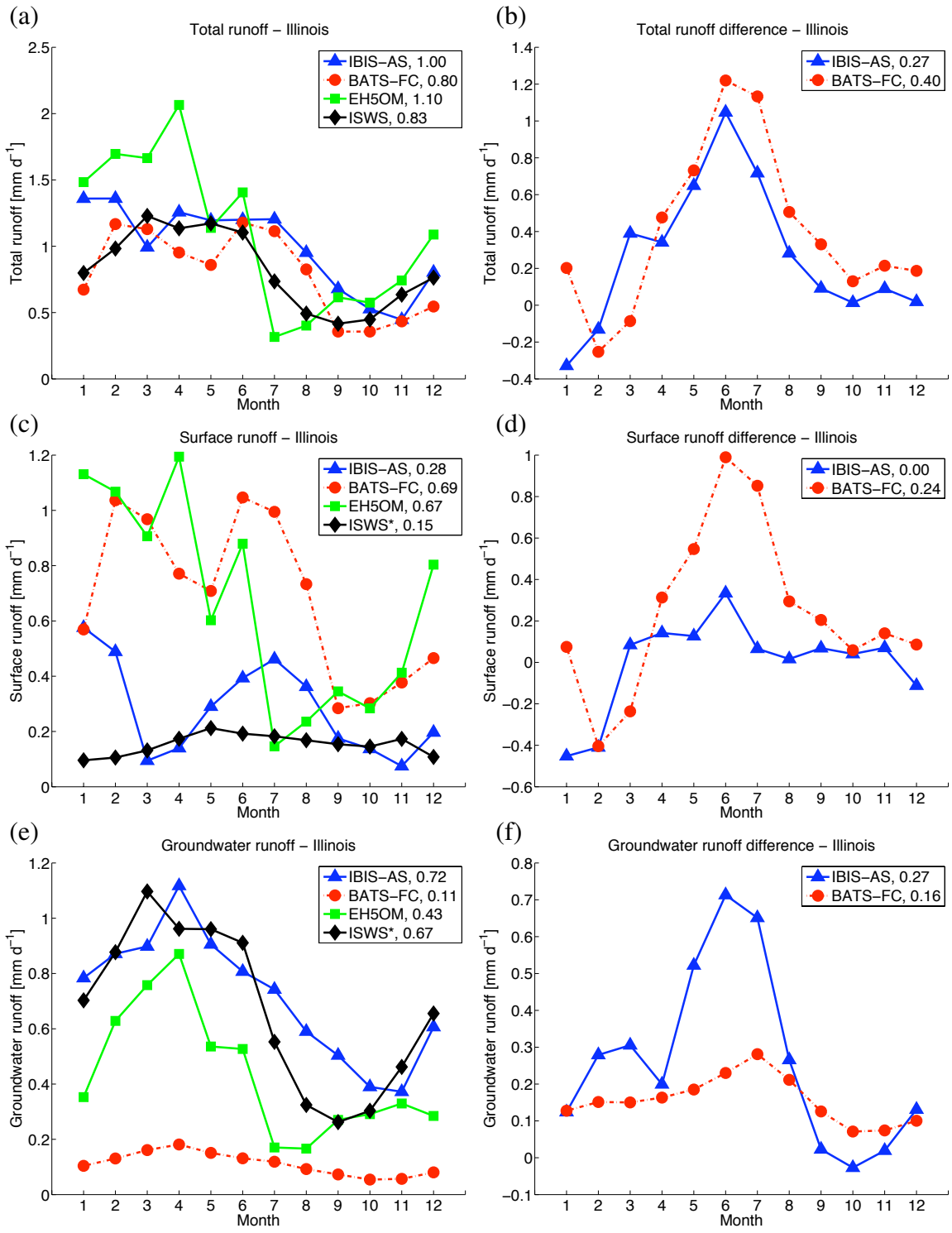

Figure 5-20: EH5OM control and observed seasonal cycles of: (a) total runoff, (c) surface runoff, (e) groundwater runoff for 1984-2005; and the difference between EH5OM A1B climate change (2078-2099) and EH5OM control (1984-2005) seasonal cycles of: (b) total runoff, (d) surface runoff, (f) groundwater runoff. Annual averages for each variable examined are provided in the legend. *estimate of runoff as described in Section 3.2

The annual average of the difference between the EH5OM A1B climate change and EH5OM control seasonal cycles of groundwater runoff in BATS-FC exceeds the magnitude of the EH5OM control seasonal cycle itself. However, groundwater runoff remains a relatively small component of total runoff in BATS-FC. In contrast, the response of groundwater runoff in IBIS-AS to the EH5OM A1B climate change scenario is significantly larger than the response of surface runoff, especially during May, June, and July (0.63 mm d^{-1}).

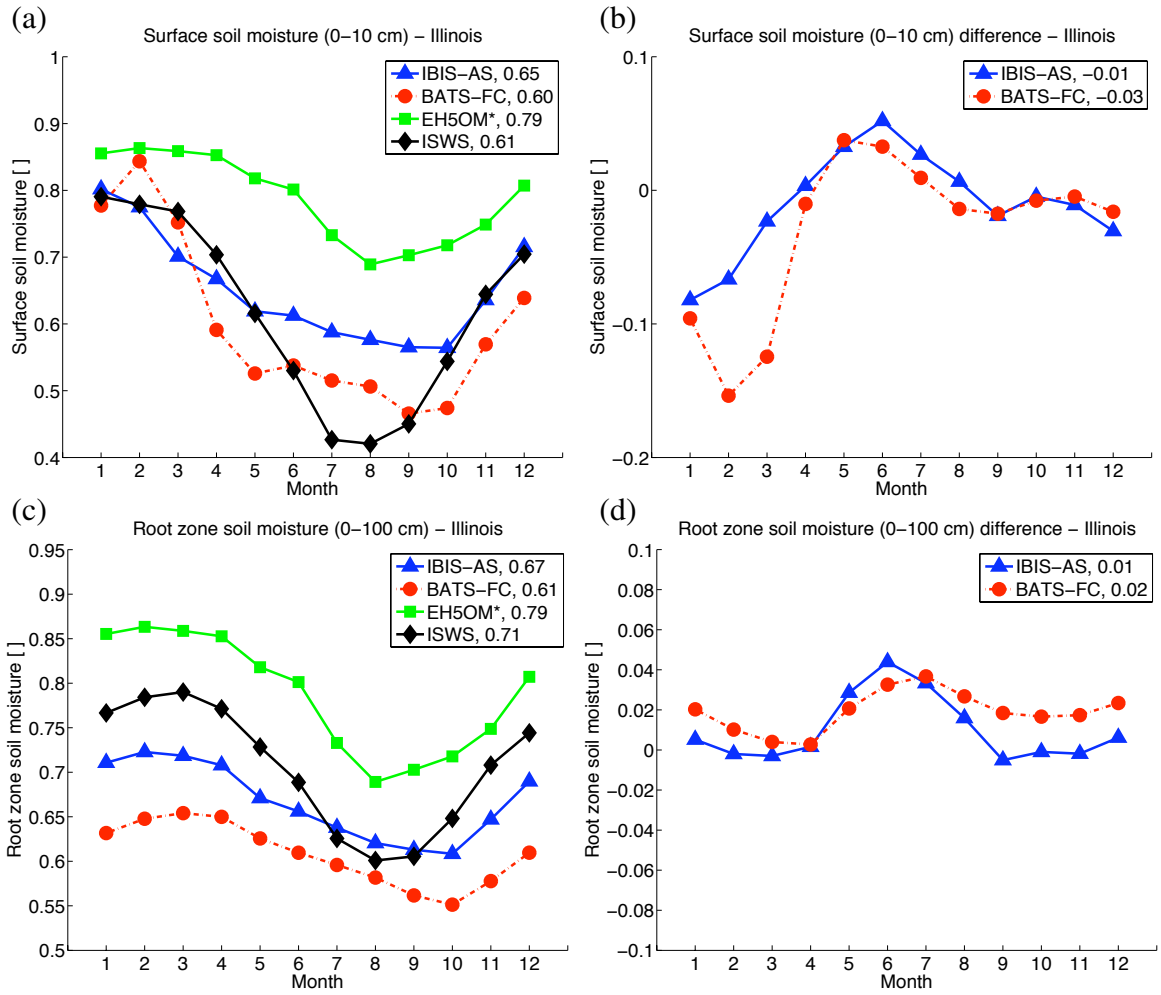

Figure 5-21: EH5OM control and observed seasonal cycles of: (a) surface soil moisture, (c) root zone soil moisture for 1984-2003; and the difference between EH5OM A1B climate change (2078-2097) and EH5OM control (1984-2003) seasonal cycles of: (b) surface soil moisture, (d) root zone soil moisture. Annual averages for each variable examined are provided in the legend.

Changes in IBIS-AS and BATS-FC summer surface soil moisture produced by the EH5OM A1B climate change scenario are insignificant; however, IBIS-AS and BATS-FC

surface soil moisture does show some drying during the winter months. During June, July, and August, the increase in surface soil moisture is 0.028 (4.7%) in IBIS-AS and 0.009 (1.8%) in BATS-FC.

The differences between the EH5OM A1B climate change and EH5OM control root zone soil moisture seasonal cycles of IBIS-AS and BATS-FC are very small, as shown in Figure 5-21. Increased precipitation is almost completely compensated for by enhanced runoff and evapotranspiration. During the summer, the change in IBIS-AS and BATS-FC root zone soil moisture is 0.031 (4.8%) and 0.032 (5.4%), respectively. The lack of response in root zone soil moisture to the EH5OM A1B climate change scenario reinforces the finding that summer soil moisture does not experience significant reductions under a warmer climate in the American Midwest.

Annually averaged, soils in IBIS-AS and BATS-FC are slightly drier at the surface and slightly wetter below 10 cm when forced using EH5OM A1B climate change boundary conditions. This response is consistent with the differences in soil moisture profiles generated by the NNRP2 surrogate climate change scenario. Drying at the surface is likely a result of increased 2-m temperatures and evapotranspiration, while wetting in deeper soil layers is a result of increased precipitation.

The EH5OM A1B climate change scenario produces increased soil moisture at all depths in IBIS-AS and BATS-FC during the summer; however, these changes are insignificant compared to the model configuration variability of the EH5OM control simulations.

Figures 5-23 and 5-24 show the response of key components of the hydrologic cycle to the EH5OM A1B climate change scenario within the context of interannual variability. Specifically, Figures 5-23 and 5-24 contain the IBIS-AS and BATS-FC seasonal cycles and seasonal cycle differences in Figures 5-18, 5-19, 5-20, and 5-21, but also have error bars denoting the standard deviations of the EH5OM control seasonal cycles (a measure of interannual variability) and error bars denoting the sign and magnitude of the difference between the standard deviations of the EH5OM A1B climate change and EH5OM control seasonal cycles.

The interannual variability of the IBIS-AS and BATS-FC precipitation seasonal cycles is relatively large compared to response of both models to the EH5OM A1B climate change

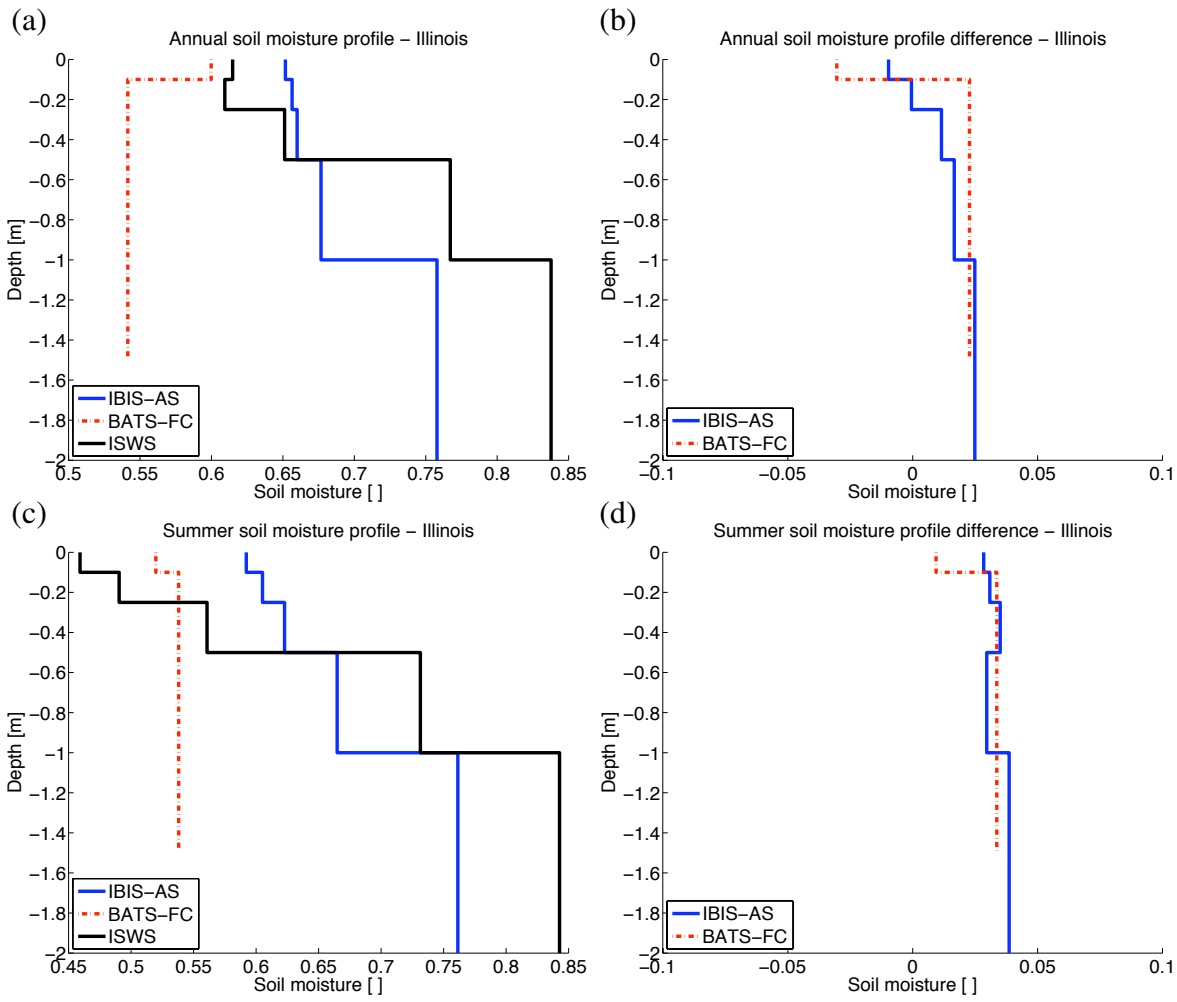

Figure 5-22: EH5OM control and observed (a) annual, (c) summer (June, July, August) soil moisture profiles for 1984-2003; and the difference between EH5OM A1B climate change (2078-2097) and EH5OM control (1984-2003) (b) annual, (d) summer (June, July, August) soil moisture profiles.

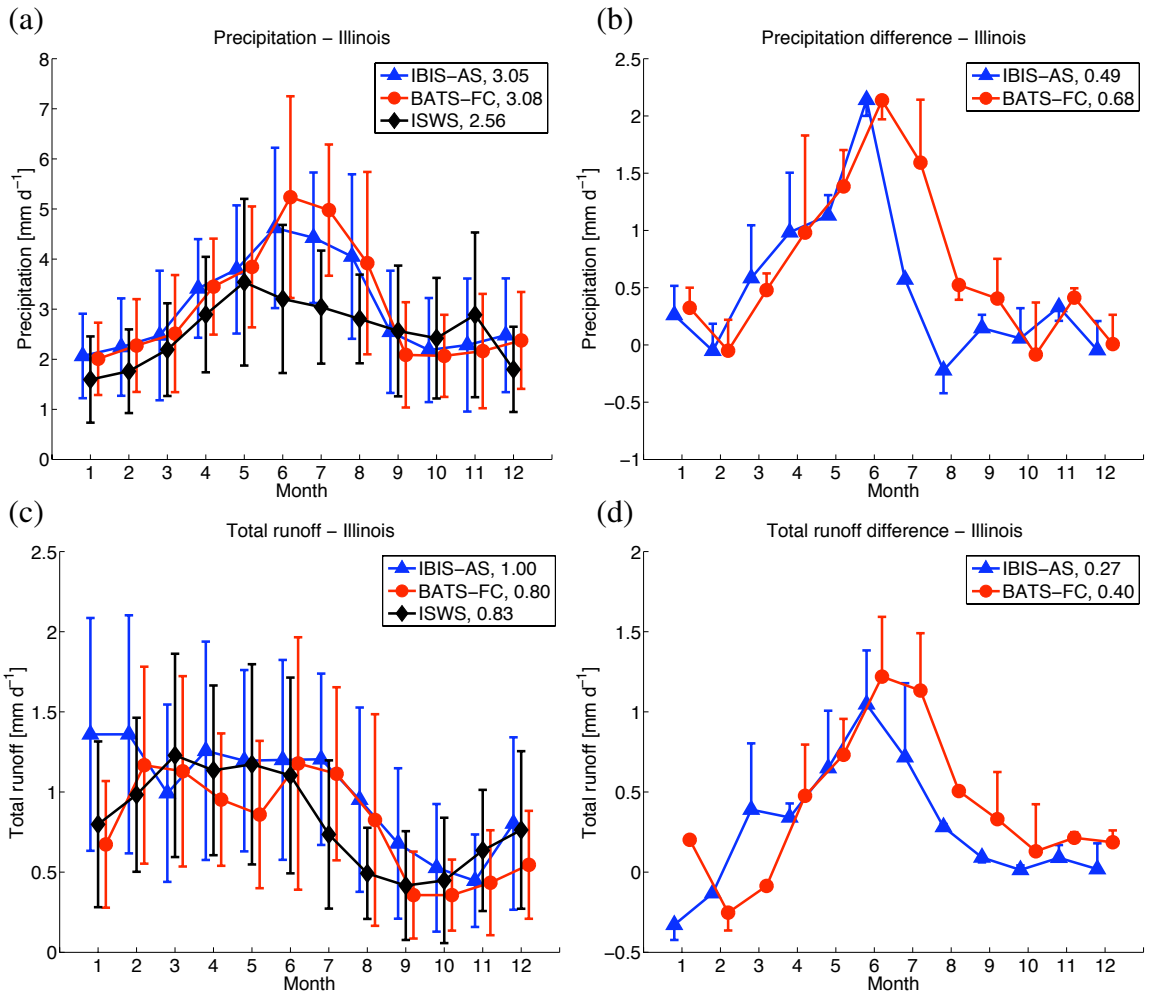

Figure 5-23: EH5OM control and observed seasonal cycles of: (a) precipitation, (c) total runoff for 1984-2005. Error bars denote the standard deviations of the EH5OM control seasonal cycles. The difference between EH5OM A1B climate change (2078-2099) and EH5OM control (1984-2005) seasonal cycles of: (b) precipitation, (d) total runoff. Error bars denote the difference between the standard deviations of EH5OM A1B climate change and EH5OM control seasonal cycles. Annual averages for each variable examined are provided in the legend.

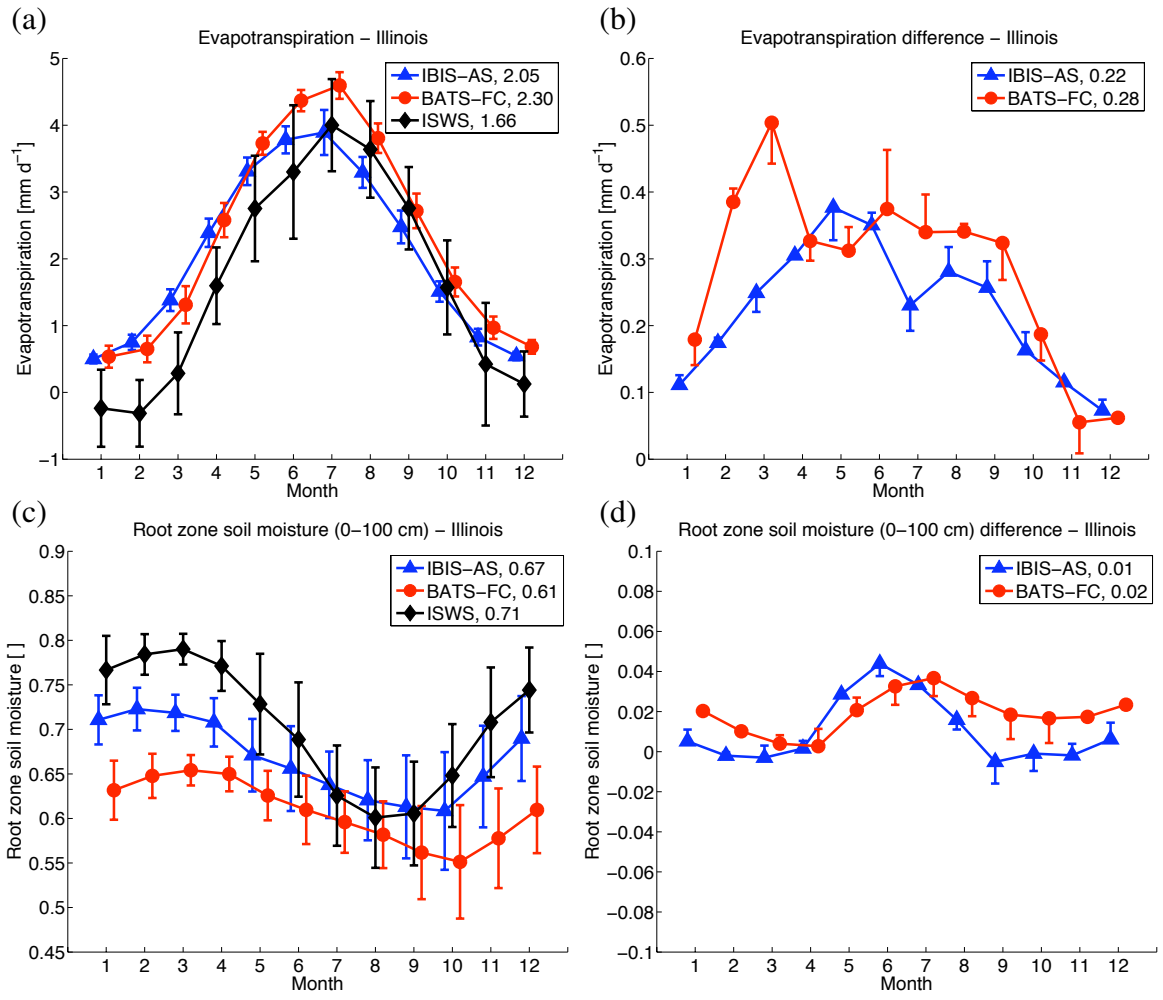

Figure 5-24: EH5OM control and observed seasonal cycles of: (a) evapotranspiration (1984-2005), (c) root zone soil moisture (1984-2003). Error bars denote the standard deviations of the EH5OM control seasonal cycles. The difference between EH5OM A1B climate change (2078-2099, root zone soil moisture 2078-2097) and EH5OM control (1984-2005, root zone soil moisture 1984-2003) seasonal cycles of: (b) evapotranspiration, (d) root zone soil moisture. Error bars denote the difference between the standard deviations of EH5OM A1B climate change and EH5OM control seasonal cycles. Annual averages for each variable examined are provided in the legend.

scenario. The largest enhancement of IBIS-AS and BATS-FC precipitation occurs in April, May, and June. During these months, precipitation increases are similar in magnitude to the seasonal cycle standard deviations.

Total runoff is largely a function of precipitation, and is therefore also highly variable throughout the year. During May, June, and July, the response of total runoff to the EH5OM A1B climate change scenario is significant relative to the interannual variability of total runoff in the EH5OM control simulations. The standard deviations of the IBIS-AS and BATS-FC EH5OM A1B climate change total runoff seasonal cycle are larger than the standard deviations of the EH5OM control total runoff seasonal cycle in the months of April, May, June, and July.

IBIS-AS and BATS-FC underestimate the interannual variability of evapotranspiration for all months. In both models, the response of evapotranspiration to the EH5OM A1B climate change scenario is comparable to the interannual variability of evapotranspiration in the EH5OM control simulations during the spring (March, April, May) and summer.

The interannual variability of the root zone soil moisture seasonal cycle is well simulated by IBIS-AS and IBIS-FC. Both models produce a small decrease in the standard deviation of the root zone soil moisture seasonal cycle under the EH5OM A1B climate change scenario during August, September, and October. The response of root zone soil moisture in IBIS-AS and BATS-FC to the EH5OM A1B climate change scenario is minimal compared to the interannual variability of root zone soil moisture in EH5OM control simulations.

Figure 5-25 shows the differences between the summer (June, July, August) hydrologic cycles of the EH5OM A1B climate change (2078-2099) and EH5OM control (1984-2005) simulations for IBIS-AS and BATS-FC throughout the United States.

Consistent with the response of summer precipitation to the NNRP2 surrogate climate change scenario, the EH5OM A1B climate change scenario enhances IBIS-AS and BATS-FC summer precipitation throughout the midwestern and southeastern United States and reduces summer precipitation over the Southwest. BATS-FC simulates large increases in summer precipitation throughout the Southeast and markedly reduced summer precipitation along Mississippi, Louisiana, and southeastern Texas.

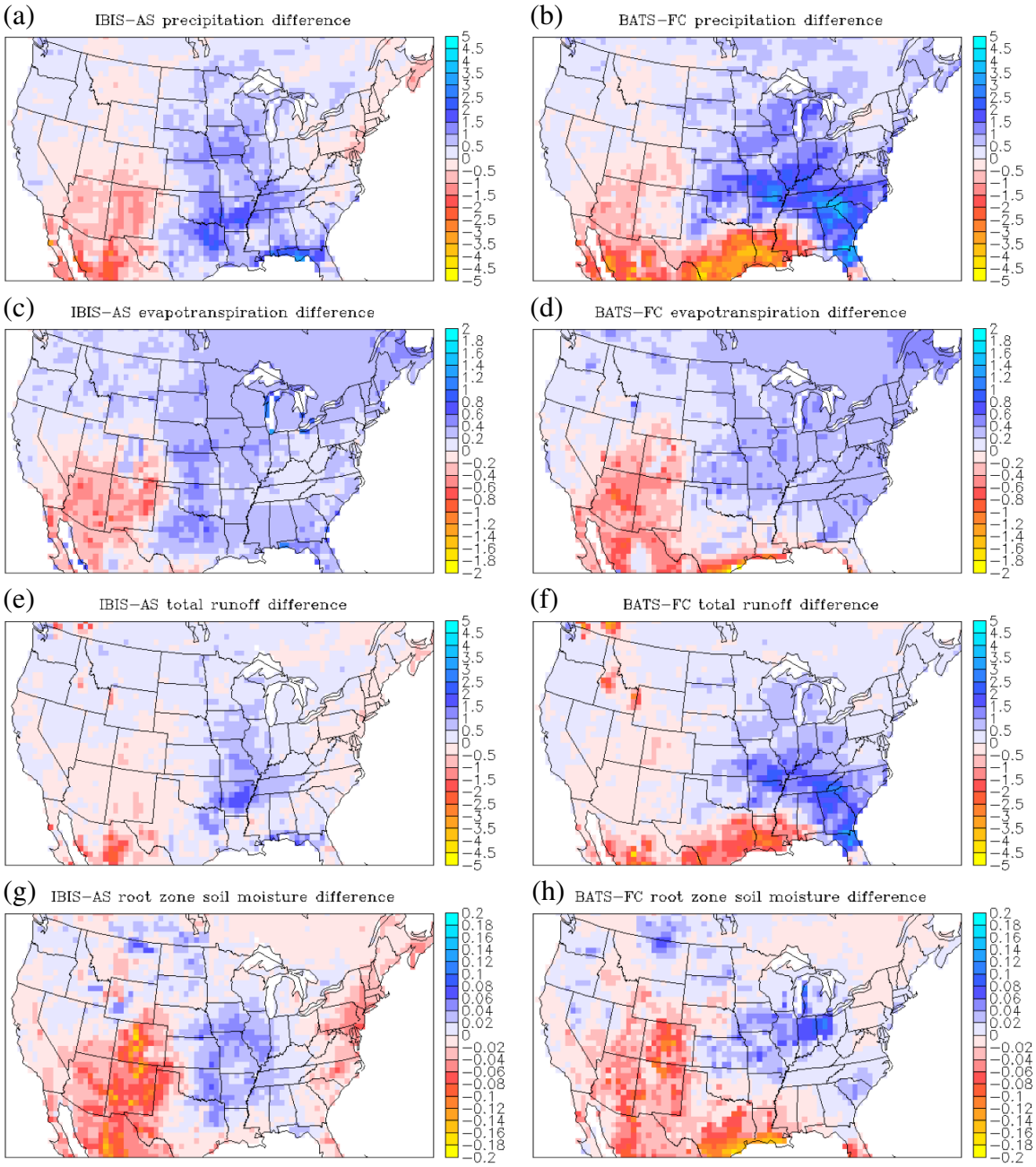

Figure 5-25: Difference between EH5OM A1B climate change (2078-2099) and EH5OM control (1984-2005) simulations of summer (June, July, August): (a), (b) precipitation; (c), (d) evapotranspiration; (e), (f) total runoff; (g), (h) root zone soil moisture.

Changes in summer evapotranspiration are relatively small in both the IBIS-AS and BATS-FC forced using EH5OM A1B climate change boundary conditions, with modest increases in evapotranspiration across much of the United States with the exception of the American Southwest. Reduced evapotranspiration across the southwestern United States and Northern Mexico is likely a result of decreased precipitation.

The changes in summer total runoff produced by the EH5OM A1B climate change scenario are tightly correlated with changes in precipitation. IBIS-AS simulates large increases in total runoff over the midwestern United States and BATS-FC simulates large increases in total runoff across the American Midwest and Southeast. While summer total runoff over the southwestern United States is reduced some in IBIS-AS under EH5OM A1B climate change boundary conditions, BATS-FC simulates significant decreases in summer total runoff throughout Mississippi, Louisiana, and southeast Texas.

IBIS-AS and BATS-FC forced using the EH5OM A1B climate change scenario contain more pronounced reductions in summer root zone soil moisture over the Southwest than IBIS-AS and BATS-FC forced using the NNRP2 surrogate climate change scenario. In addition, both models simulate increased summer root zone soil moisture across the midwestern United States and BATS-FC simulates reduced summer root zone soil moisture along southern Louisiana and southeastern Texas under the EH5OM A1B climate change scenario.

5.4 Conclusions

After extensively assessing the ability of RegCM3-IBIS and RegCM3-BATS1e to simulate the hydroclimatology of the American Midwest in Chapter 3 and exploring the sensitivity of latent heat flux to available energy in both models in Chapter 4, the response of RegCM3-IBIS and RegCM3-BATS1e to climate change is described in Chapter 5. Two sets of climate change experiments were conducted to evaluate this response. First, the surrogate climate change scenario of Schär et al. [1996] was used. Realistic boundary conditions (NNRP2) were warmed by 3°C with a corresponding increase in the concentration of CO_2 equivalent. Second, the boundaries of RegCM3-IBIS and RegCM3-BATS1e were

forced using output from the ECHAM5 GCM run under the A1B emissions scenario with a corresponding increase in CO_2 equivalent.

Qualitatively, both climate change experiments produced similar results. Several findings are robust across boundary conditions, surface physics schemes, and convective closures. These findings include: warmer 2-m temperatures, increased downward longwave radiation, reduced net longwave radiation (defined as positive upward), significantly enhanced summer precipitation, increased evapotranspiration, and increased total runoff.

As discussed in Chapter 1, one of the largest potential impacts of climate change is drought over agriculturally productive areas, such as the midwestern United States. The fundamental conclusion of these experiments is that there is no significant reduction in surface or root zone soil moisture under either of the climate change scenarios examined, as shown in Tables 5.1 and 5.2. While higher temperatures and increased downward longwave radiation do result in enhanced evapotranspiration, the coincident increase in precipitation more than balances larger fluxes of latent heat, and ultimately results in additional surface and groundwater runoff.

Table 5.1: Annual and summer (June, July, August) soil moisture differences between the NNRP2 surrogate climate change (1984-2003) and NNRP2 control (1984-2003) simulations over Illinois.

	IBIS-AS	BATS-FC	IBIS-FC	BATS-AS
Annual surface soil moisture	-0.02	-0.03	-0.03	-0.03
Annual root zone soil moisture	-0.01	0.01	-0.01	-0.01
JJA surface soil moisture	0.00	-0.01	-0.03	0.00
JJA root zone soil moisture	0.00	0.01	-0.02	0.00

Table 5.2: Annual and summer (June, July, August) soil moisture differences between the EH5OM A1B climate change (2078-2097) and EH5OM control (1984-2003) simulations over Illinois.

	IBIS-AS	BATS-FC
Annual surface soil moisture	-0.01	-0.03
Annual root zone soil moisture	0.01	0.02
JJA surface soil moisture	0.03	0.01
JJA root zone soil moisture	0.03	0.03

Chapter 6

Summary of Results, Conclusions, and Future Work

6.1 Summary of Results

6.1.1 Model Development

The coupling of Integrated Biosphere Simulator to Regional Climate Model version 3 significantly improves the ability of RegCM3 to simulate the subsurface hydrology and the partitioning of total runoff between surface runoff and groundwater runoff relative to RegCM3-BATS1e. IBIS also expands the functionality of RegCM3, adding vegetation dynamics, plant competition, more sophisticated phenology, and explicit modeling of soil/plant biogeochemistry.

Multiple errors were identified in the initial version of RegCM3-IBIS, including a significant warm bias, an underestimation of root zone soil moisture, and an overestimation of incident surface shortwave radiation, net longwave radiation, sensible heat flux, and total runoff [Winter et al., 2009]. Improvements were made to RegCM3-IBIS to address these deficiencies. The overestimation of incident surface shortwave radiation was reduced by updating the optical properties of water vapor, including background aerosols, and using the Arakawa & Schubert closure assumption for the Grell parameterization of convection. In addition, a cropland plant functional type based on the work of Kucharik and Brye

[2003] was added to RegCM3-IBIS to better represent the current vegetation cover of the midwestern United States.

6.1.2 Simulating the Hydroclimatology of the American Midwest

To illustrate the relative strengths and weaknesses of RegCM3-IBIS and RegCM3-BATS1e, an ensemble of 22-year numerical experiments was completed to assess the ability of both models to simulate the energy and water budgets of the American Midwest. The sensitivity of RegCM3-IBIS and RegCM3-BATS1e to convective closure and boundary conditions was examined. RegCM3-IBIS and RegCM3-BATS1e were run using the Arakawa & Schubert (IBIS-AS, IBIS-AS) and Fritsch & Chappell (BATS-FC, IBIS-FC) convective closure assumptions under NNRP2 boundary conditions. The best performing convective closure for each surface physics scheme (IBIS-AS, BATS-FC) was then forced using with boundary conditions derived from the EH5OM 20^{th} century (1984-2000) and EH5OM A1B (2001-2005) simulations. Model results were evaluated using the NASA SRB dataset [NASA, 2006], data compiled by Yeh [2003], and the Climate Research Unit Time Series 2.1 [Mitchell et al., 2004].

Overall, the model that simulates the observed energy and water budgets best using NNRP2 boundary conditions is IBIS-AS. BATS-FC and IBIS-FC produce too much incident surface shortwave radiation during the summer, while BATS-AS underestimates incident surface shortwave radiation throughout the year. IBIS-FC overestimates 2-m temperature while BATS-FC and BATS-AS underestimate 2-m temperature. The observed 2-m temperature seasonal cycle is captured by IBIS-AS. Evapotranspiration is best simulated by IBIS-AS and IBIS-FC, although all model configurations significantly overestimate evapotranspiration during the spring. IBIS-AS, BATS-FC, IBIS-FC, and BATS-AS contain a wet bias during the spring and summer. IBIS-AS and IBIS-FC simulate annually-averaged precipitation best. IBIS-AS, BATS-FC, and BATS-AS simulate total runoff reasonably well, but only IBIS-AS partitions total runoff correctly between surface runoff and groundwater runoff. BATS-FC and BATS-AS produce almost exclusively surface runoff, which is unrealistic. IBIS-AS simulates the observed seasonal cycle of root zone soil moisture best.

IBIS-AS outperforms BATS-FC under EH5OM boundary conditions as well. Increased water vapor in the atmosphere, likely a result of wetter boundary conditions, creates enhanced cloud cover which reduces the overestimation of incident surface shortwave radiation and 2-m temperature in IBIS-AS. In BATS-FC, this same additional water vapor causes an underestimation of incident shortwave radiation and a cold bias. EH5OM boundary conditions exacerbate the wet bias in both IBIS-AS and BATS-FC.

6.1.3 Sensitivity of Latent Heat Flux to Available Energy

A climate model must include an accurate surface physics scheme in order to examine the interactions between the land and atmosphere. Given an increase in the surface radiative forcing, the sensitivity of latent heat flux to available energy plays an important role in determining the energy budget and has a significant impact on the response of surface temperature. Note that the terms "latent heat flux" and "evapotranspiration" are used interchangeably throughout this thesis.

The Penman-Monteith equation was used to construct a theoretical framework for evaluating the climatology of evapotranspiration and the sensitivity of latent heat flux to available energy. RegCM3-IBIS (IBIS-AS), RegCM3-BATS1e (BATS-FC); and FLUXNET micrometeorological tower observations were compared and contrasted using the developed methodology.

IBIS-AS and BATS-FC simulate the observed sensitivity of latent heat flux to available energy reasonably well during the summer on average; however, there are significant variations in the monthly values. Additional information provided by the physically-based Penman-Monteith framework is employed for identifying deficiencies and guiding improvements in models, allowing calibration of both the climatology of evapotranspiration and the sensitivity of latent heat flux to available energy.

6.1.4 Modeling the American Midwest Under a Warmer Climate

The response of RegCM3-IBIS and RegCM3-BATS1e to a surrogate climate change scenario and the EH5OM A1B scenario was assessed.

Root zone soil moisture in the midwestern United States did not decrease in any of the climate change experiments conducted. Enhanced precipitation outpaces increases in evapotranspiration, which results in increased total runoff and unchanged root zone soil moisture.

Predictably, 2-m temperatures increased in all climate change experiments conducted, but the extent of warming is modulated by cloud cover, which is a function of both convective closure and boundary conditions. Summer precipitation increases significantly in all climate change simulations, a result of enhanced evapotranspiration, increased fluxes of water vapor at the boundaries, and additional energy at the surface to fuel both convective and large-scale precipitation. Enhanced precipitation is more pronounced in simulations using the Fritsch & Chappell convective closure and the EH5OM A1B boundary conditions. Increased precipitation, surface radiation, and 2-m temperatures produce enhanced evapotranspiration in all model configurations. Total runoff increases significantly in IBIS-AS, BATS-FC, IBIS-FC, and BATS-AS; however, while the response is dominated by surface runoff in BATS-FC, BATS-AS, and IBIS-FC, it is dominated by groundwater runoff in IBIS-AS.

6.2 Discussion

Ultimately, the change in soil moisture produced by climate change is a balance of modified fluxes of water in and out of the soil column. These fluxes include evapotranspiration, precipitation, surface runoff, and groundwater (subsurface) runoff, as shown in Figure. 6-1. While changes to the seasonal cycle of soil moisture under future climatic conditions were assessed directly, each flux of water in and out of the soil was also carefully examined.

The response of latent heat flux to climate change was assessed using both the theoretical framework based on the Penman-Monteith equation described in Chapter 4 and the simulations presented in Chapter 5. On average, the theoretical sensitivities of latent heat flux to available energy ($\frac{\partial \lambda E}{\partial A}$) simulated by IBIS-AS and BATS-FC were in agreement with observations. The approximate value of the theoretical sensitivity of latent heat flux to available energy over Bondville, IL was 0.5. Physically, this means that for a 10 W

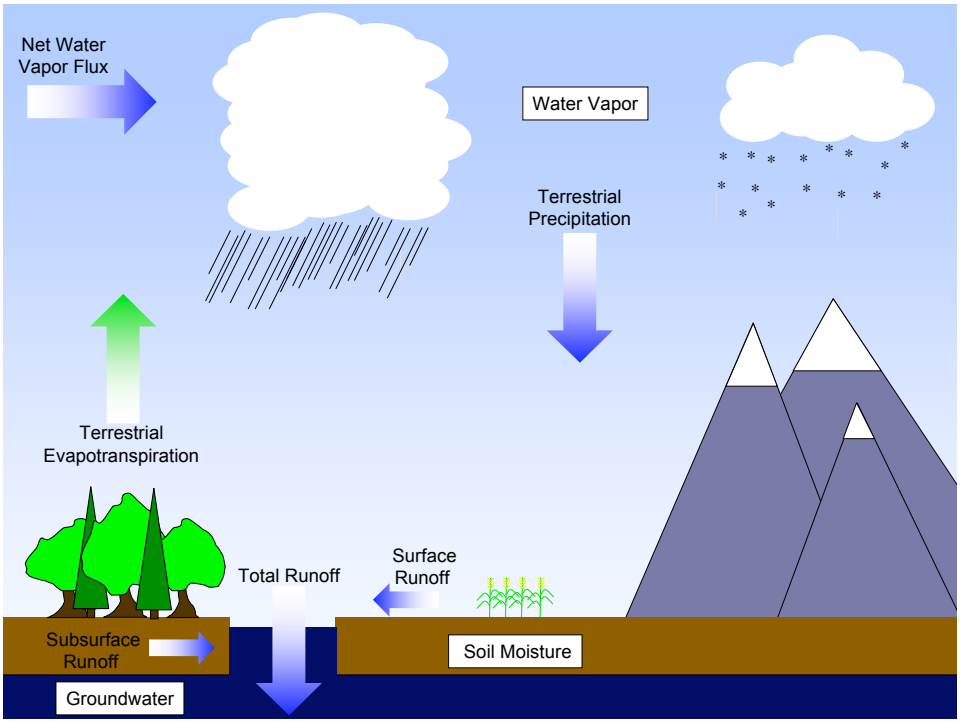

Figure 6-1: Components of the hydrologic cycle relevant to the simulation of soil moisture over the American Midwest.

m^{-2} increase in available energy, the response of latent heat flux will be 5 W m^{-2}. The empirical response of latent heat flux to changes in available energy over Illinois is slightly higher, approximately 0.6 on average. Note that the empirical response of latent heat flux to changes available energy is a full derivative in which no variables are held constant, while the theoretical sensitivity of latent heat flux to available energy is a partial derivative that holds all variables constant except for available energy. Increases in available energy during June, July, and August are relatively small under both the NNRP2 surrogate climate change and EH5OM A1B climate change scenarios, $\approx$5 W m^{-2} averaged across all simulations. While the increase in latent heat flux is also limited during the summer months, $\approx$5 W m^{-2}, it is similar to the increase in available energy. Therefore, the response of latent heat flux to changes in available energy found in the future climate scenarios (Chapter 5) is approximately unity. This demonstrates the importance of precipitation in simulating the response of latent heat flux to an increase in the surface radiative forcing.

Because precipitation is a key variable in determining the response of soil moisture to climate change, the sensitivity of its response to large-scale forcing, convective closure,

and surface physics scheme was explored. Boundary conditions and convective closure assumption had a strong influence on both the magnitude and shape of the precipitation seasonal cycle under both climate change scenarios, with a range of responses from 0.19 mm d^{-1} to 1.42 mm d^{-1} during the summer. And while inaccuracies in the simulation of precipitation represent a key limitation of regional and global climate models, it is important to note that in each numerical experiment conducted, the response of precipitation to the climate change scenario was larger than the response of evapotranspiration to the climate change scenario in June, July, and August. This finding reinforces the conclusion that climate change over the midwestern United States is unlikely to cause significant soil moisture drying.

As noted above, the simulated response of precipitation to climate change is larger than the simulated response of evapotranspiration to climate change in all experiments conducted. While this would seem to suggest wetter soil conditions, the balance of precipitation is removed from the system as runoff, leaving soil moisture unchanged. The response of total runoff is largely a function of precipitation, which is itself dependent on convective closure assumption and boundary conditions. However, the partitioning of total runoff between surface runoff and groundwater runoff is almost completely dictated by surface physics scheme. In BATS-FC and BATS-AS, the majority of total runoff occurs as surface runoff. Enhanced surface runoff is simulated by IBIS-FC forced using the NNRP2 surrogate climate change scenario, a result of large increases in rainfall during the late spring and summer. In contrast, the response of total runoff in IBIS-AS is balanced between surface and groundwater runoff. Physically, this means that while additional precipitation does move through the soil column, it is removed as the water content of the lowest soil layer increases. Again, despite some physical differences in model responses, the result of insignificant soil moisture drying under a warmer climate is consistent.

6.2.1 Comparison to Previous Studies

The difference between the results presented in this thesis and those of Manabe and Wetherald [2002] and Manabe et al. [2004] merits a more detailed discussion. A description of

the numerical experiments conducted by Manabe and Wetherald [2002] and Manabe et al. [2004] can be found in Section 5.1. Qualitatively both Manabe and Wetherald [2002] and Manabe et al. [2004] contain similar conclusions regarding soil moisture changes over the American Midwest; however, the climate change forcing of Manabe and Wetherald [2002] is the more consistent with the experiments presented in this thesis. Therefore, a brief summary of the pertinent findings of Manabe and Wetherald [2002] is provided below.

In the mid- to high-latitudes of the Northern Hemisphere, Manabe and Wetherald [2002] describes the response of soil moisture as summer drying and winter wetting. While seasonal cycles of precipitation and evapotranspiration are not included in the manuscript, the physical mechanism for changes in soil moisture is presented. During the winter enhanced evaporation over the oceans resulting from warmer sea surface temperatures (SSTs) increases precipitation across the American Midwest. Over the continents temperatures are low enough that climate change does not significantly increase the saturation vapor pressure due to the nonlinearity of the Clausius-Clapeyron equation [Manabe and Wetherald, 2002]. Thus the response of latent heat flux to climate change is relatively small. Increased precipitation and relatively unchanged evapotranspiration results in winter wetting of soil moisture [Manabe and Wetherald, 2002].

During the summer the surface is warmer, and the increase in temperature and available energy significantly enhances evapotranspiration due to a higher saturation vapor pressure. And while precipitation does increase during the summer, the additional rainfall at any given latitude over land is smaller than the additional rainfall over water [Manabe and Wetherald, 2002]. This modest enhancement of precipitation paired with higher latent heat flux values results in the summer drying of soils [Manabe and Wetherald, 2002]. And while there are some additional factors that contribute to summer drying, as discussed in Section 5.1, the primary response of soil moisture to climate change appears to depend on the balance between the change in precipitation and the change in evapotranspiration.

The relative changes of precipitation and evapotranspiration under a climate change scenario also play a major role in the response of soil moisture during the summer in the numerical experiments presented in Chapter 5; however, the actual predicted changes of precipitation and evapotranspiration (and therefore soil moisture) are very different from

those of Manabe and Wetherald [2002]. This difference is primarily a result of the response of precipitation. While the climate change simulations presented in Section 5.3 and Manabe and Wetherald [2002] both predict increases in evapotranspiration, the simulations in Section 5.3 conclude that this increase is relatively minor when compared to the increase in precipitation. This large response of precipitation relative to evapotranspiration coupled with increased runoff results in unchanged soil moisture. In contrast, the increase in latent heat flux described Manabe and Wetherald [2002] is greater than the increase in precipitation, resulting in soil moisture drying. This prompts many interesting areas for future work, some of which are described in Section 6.5.

6.2.2 Implications

Finding an insignificant change in soil moisture using multiple climate change scenarios and a variety of model configurations has numerous implications for agriculture and water resources management. However, it is important to caveat that only one regional climate model was used and that in-depth analysis was only performed over the state of Illinois, corresponding with observed data available. While the accuracy of temperature and precipitation simulated by IBIS-AS and BATS-FC was evaluated throughout the United States in Section 3.3, and a discussion of the response of the hydrologic cycle to climate change across the United States is included in Section 5.3, extensive comparison of control simulations to observations was only performed over Illinois.

The experiments conducted in Chapter 5 indicate that the agricultural industry is likely to benefit from mean climate change in the near-term (i.e. a warming of $\approx 3^{\circ}$C) over Illinois. Enhanced precipitation, a longer growing season, and CO_2 fertilization should increase crop yields. However, extreme events (specifically floods and heat waves), more intense changes in climate, and croplands not considered in this study could have a significant effect on the overall agricultural productivity of the United States.

Regional climate models have difficulty simulating the timing, intensity, and duration of precipitation events, which could have considerable implications for crop yields. Errors in simulating the time between precipitation events could cause an underestimation

of drought. Heat waves could also be potentially problematic for the agricultural industry. All simulations predict significantly increased 2-m temperatures with coincident changes in ground temperature. Excessive warming of corn, soybeans, and cotton was shown by Schlenker and Roberts [2009] to decrease agricultural productivity.

More extreme changes in climate resulting from more carbon-intensive scenarios or accumulation of CO_2 in the atmosphere over longer periods of time (i.e. centuries) are not considered in this thesis. Non-linear changes in the response of environmental variables to climate change makes extrapolating the results of Chapter 5 further than 100 years impractical. Any number of changes in future climate, including shifts in large-scale dynamics, local alterations of microclimate, and modified precipitation patterns could result in a different response of soil moisture to climate change.

Finally, it is important to note that agricultural areas that are more arid than Illinois will likely suffer from drought. Figures 5-11 and 5-25 show reductions in soil moisture over the southwestern United States. While the significance of this drying was not examined, it is certainly a cause for concern.

Water supply shortages in Illinois are unlikely based on the results of this study. While errors in simulating the timing, intensity, and duration of precipitation could have implications for water resources management; annually-averaged changes in precipitation, surface runoff, and groundwater runoff are positive and all simulations show increased precipitation during the dry summer months. It is important to note that this study considers only the supply of water, and an increase water use could stress water resources.

While the results of Section 5.3 indicate that in the near-term droughts are unlikely to become more common in the state of Illinois, the increase in surface temperature and precipitation suggests a potential for more severe heatwaves and floods. Heatwaves and floods can result in extensive losses of human life and economic productivity. For example, the record-breaking 2003 European heat wave was blamed for 35,000 deaths [Fischer et al., 2007a] and damages to agricultural areas resulting from the 1993 flood of the midwestern United States were estimated to be $6-8 billion [Rosenzweig et al., 2002]. Robust and significant increases of 2-m temperature, groundwater runoff, and surface runoff are troubling. Enhanced temperature and precipitation are consistent with multiple studies, in-

cluding Easterling et al. [2000], that have examined the impacts of climate change on the frequency and severity of floods and heatwaves.

By the end of the 21st century, Easterling et al. [2000] predict that higher maximum temperatures, an increase in the heat index, and more hot summer days are "very likely". Trends in 1-day and multi-day heavy precipitation events, the annual number of days with precipitation totals greater than 2 and 4 inches, and exceedance of station-specific precipitation thresholds have all increased over the midwestern United States during the 20th century [Easterling et al., 2000]. Model predictions indicate that this trend is likely to continue, with more heavy 1-day and multi-day precipitation events being "very likely" in the 21st century [Easterling et al., 2000].

6.3 Conclusions

The ability of RegCM3-IBIS and RegCM3-BATS1e to simulate the surface water and energy budgets–including temperature, precipitation, evapotranspiration, shortwave radiation, longwave radiation, runoff, and soil moisture–was extensively tested. To examine the sensitivity of simulations to model configuration, RegCM3-IBIS and RegCM3-BATS1e were run using the Fritsch & Chappell and Arakawa & Schubert convective closure assumptions.

The Arakawa & Schubert convective closure is shown to be superior in capturing the observed seasonal cycle of incident surface shortwave radiation. The Fritsch & Chappell convective closure simulates reduced cloud cover during the summer leading to an overestimation of absorbed surface shortwave radiation. This deficiency must be addressed in order for the Fritsch & Chappell convective closure to be valid over the midwestern United States.

RegCM3-IBIS simulates the partitioning of total runoff between surface runoff and groundwater runoff correctly. RegCM3-BATS1e does not, grossly overestimating surface runoff and underestimating groundwater runoff.

Both RegCM3-IBIS and RegCM3-BATS1e produce a significant wet bias in the spring and summer. Errors in simulating the timing and magnitude of precipitation are the single

most important uncertainty in the presented predictions of surface and subsurface hydrology under a warmer climate.

RegCM3-IBIS using the Arakawa & Schubert convective closure assumption (IBIS-AS) simulates the surface energy and water budgets of the state of Illinois accurately. The skill of IBIS-AS across a spectrum of observations creates confidence in the numerical experiments conducted.

The response of soil moisture in the midwestern United States to climate change was assessed by forcing RegCM3-IBIS and RegCM3-BATS1e with two different sets of boundary conditions: a surrogate climate change scenario and ECHAM5 GCM A1B model output. In addition, the sensitivity of latent heat flux to available energy was examined using a mechanistic framework based on the Penman-Monteith equation. While many studies have examined the response of soil moisture over the American Midwest to climate change, none have run a more comprehensive set of experiments with such a thoroughly evaluated regional climate model.

Precipitation is extremely sensitive to both climate change scenarios and increases in all numerical experiments conducted. This finding is consistent with the observed increases in annual total precipitation over the midwestern United States described in Section 5.1.

Evapotranspiration is less responsive to climate change than precipitation. Increases in available energy are small in experiments conducted, and while the empirical response of latent heat flux to increased available energy is significantly greater than the theoretical sensitivity of latent heat flux to available energy, changes in summer evapotranspiration are on average half of the changes in summer precipitation.

Total runoff increases in both models, removing most all of the difference between enhanced precipitation and enhanced evapotranspiration. The partitioning of the increase in total runoff between surface runoff and groundwater runoff is strongly influenced by surface physics scheme and convective closure assumption.

The response of soil moisture to both climate change scenarios is negligible compared to model configuration and interannual variability, and is relatively insensitive to surface physics, boundary conditions, convective closure assumption, and a reduction in the model wet bias. No summer drying in any simulation examined was found.

6.4 Contributions

Succinctly, the research presented in this thesis makes three important contributions to the field of regional climate modeling:

1. Completion of an extensive evaluation of a regional climate model over the state of Illinois, including: temperature, precipitation, incident top of atmosphere shortwave radiation, top of atmosphere albedo, incident surface shortwave radiation, absorbed surface shortwave radiation, downward longwave radiation, net longwave radiation, evapotranspiration, total runoff, surface runoff, groundwater runoff, surface soil moisture, and root zone soil moisture.

2. Construction of a regional climate model (IBIS-AS) that simulates the surface energy and water budgets of the state of Illinois accurately.

3. Assessment of the response of soil moisture in the midwestern United States to climate change using multiple model configurations and warming scenarios.

6.5 Future Work

There are several key lines of research that will continue to elucidate questions relevant to this thesis.

Larger ensembles should be run. Consistent with the Regional Climate Change Hyper-Matrix of Giorgi et al. [2008], more large-scale forcings, more regional climate models, and more model configurations need to be examined within the context of summer soil moisture drying over the midwestern United States.

Future improvements to RegCM3 should focus on correcting precipitation. Despite its importance to the climate system, of all variables examined precipitation is simulated poorest. Convective and large-scale precipitation schemes, as well as the effect that these parameterizations have on the shortwave energy budget, should be examined thoroughly.

Experiments using dynamic vegetation should be conducted. One of the strengths of IBIS is the dynamic vegetation module, which allows vegetation biomes to evolve over

time based on climate. Although dynamic vegetation was not used in this study, longer simulations using the parallel version of this model currently in development will yield valuable information about the relationship between vegetation and climate.

Enhance the accuracy and functionality of RegCM3-IBIS. A more sophisticated representation of crops, analogous to Kucharik et al. [2000], would allow RegCM3-IBIS to explicitly simulate agricultural yields. Adding a parameterization of groundwater would result in a more physically accurate representation of subsurface hydrology. Although the biogeochemical component of IBIS is largely neglected in this study, the ability of RegCM3-IBIS to simulate and predict fluxes of CO_2 should be explored. Finally, multiple smaller tasks including the construction of a high-resolution landuse initialization dataset, revised soil properties, as well as better documentation and compatibility across platforms would give RegCM3-IBIS more flexibility for use in future climate studies.

Appendix A

Figures

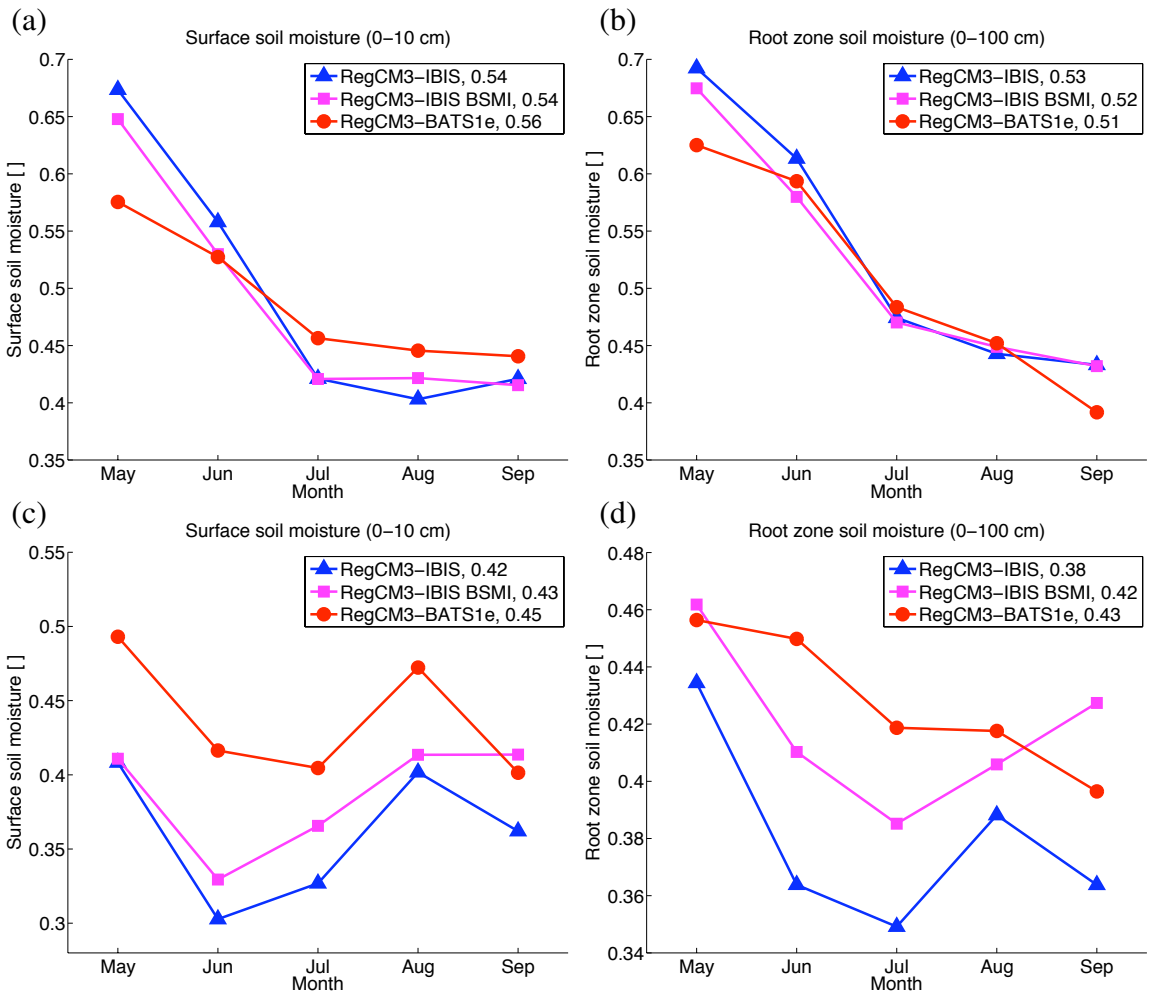

Figure A-1: May-September seasonal cycles of surface soil moisture (0-10 cm) and root zone soil moisture (0-100 cm) for: (a), (b) Bondville, IL; (c), (d) Little Washita Watershed, OK. Each value is a 1.0° x 1.0° spatial average over the FLUXNET site for 1996-1999. May-September averages for each variable examined are provided in the legend.

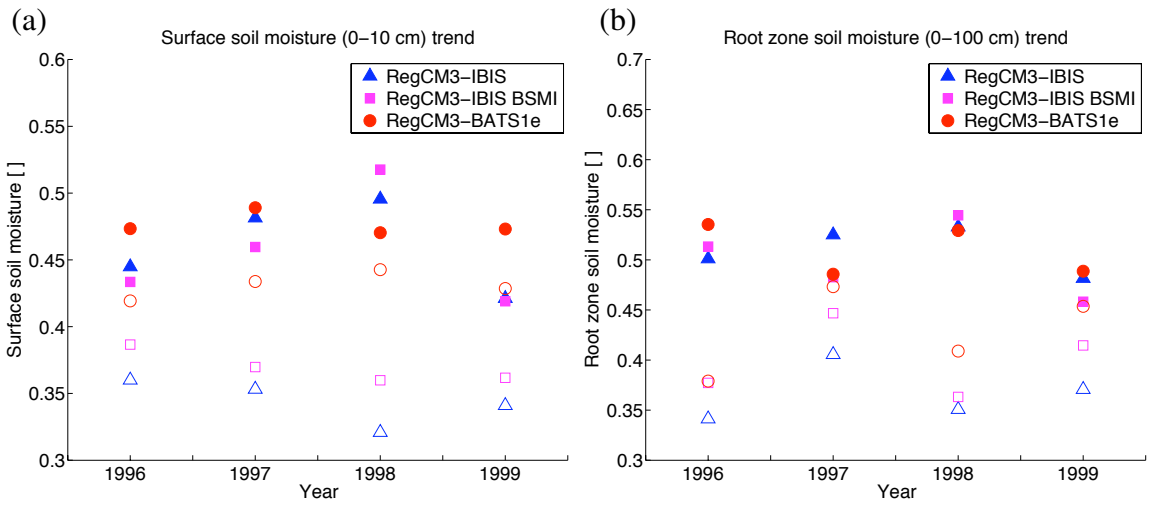

Figure A-2: Summer (June, July, August) (a) surface soil moisture (0-10 cm) and (b) root zone soil moisture (0-100 cm) for Bondville, IL (solid) and Little Washita Watershed, OK (outline). Each value is a 1.0° x 1.0° spatial average over the FLUXNET site for 1996-1999.

Bibliography

Amthor, J. S., 1984: The role of maintenance respiration in plant growth. *Plant, Cell and Environment*, **7**, 561–636.

Anthes, R., 1977: A cumulus parameterization scheme utilizing a one-dimensional cloud model. *Monthly Weather Review*, **105**, 270–286.

Anthes, R., E. Hsie, and Y.-H. Kuo, 1987: Description of the Penn State / NCAR Mesoscale Model version 4 (MM4). Technical Note TN-282+STR, National Center for Atmospheric Research.

Arakawa, A. and W. H. Schubert, 1974: Interaction of a cumulus cloud ensemble with large-scale environment, Part 1. *Journal of Atmospheric Sciences*, **31**, 674–701.

Baldocchi, D., E. Falge, L. Gu, R. Olson, D. Hollinger, S. Running, P. Anthoni, C. Bernhofer, K. Davis, R. Evans, J. Fuentes, A. Goldstein, G. Katul, B. Law, X. Lee, Y. Malhi, T. Meyers, W. Munger, W. Oechel, K. T. Paw, K. Pilegaard, H. P. Schmid, R. Valentini, S. Verma, T. Vesala, K. Wilson, and S. Wofsy, 1998: FLUXNET: A new tool to study the temporal and spatial variability of ecosystem-scale carbon dioxide, water vapor, and energy flux densities. *Bulletin of the American Meteorological Society*, **82**, 2415–2434, URL `http://www.fluxnet.ornl.gov/fluxnet/index.cfm`.

Ball, J. T., I. E. Woodrow, and J. A. Berry, 1986: A model predicting stomatal conductance and its contribution to the control of photosynthesis under different environmental conditions. *Progress in Photosynthesis Research*, International Congress on Photosynthesis, Martinus-Nijhoff, Dordecht, Netherlands, Vol. 4.

Barkstrom, B. R., 1984: The Earth Radiation Budget Experiment (ERBE). *Bulletin of the American Meteorological Society*, **65**, 1170–1185.

Bartlein, P., 2000: Absolute minimum temperature minus average of the coldest monthly mean temperature, sources include: Worldwide Airfield Summaries (NCDC TD-9647), Climatology of the U.S., No 20 (1951-80).

Bell, J. L., L. C. Sloan, and M. A. Snyder, 2004: Regional changes in extreme climatic events: A future climate scenario. *Journal of Climate*, **17**, 81–87.

Betts, A. K., 1986: A new convective scheme. Part 1: Observational and theoretical basis. *Quarterly Journal of the Royal Meteorological Society*, **112**, 677–691.

Bolton, D., 1980: The computation of equivalent potential temperature. *Monthly Weather Review*, **108**, 1046–1053.

Claassen, M. M., 1995: Managing drought: Crop strategies. Tech. rep., North Carolina Cooperative Extension Service.

Clapp, R. B. and G. M. Hornberger, 1978: Empirical equations for some soil hydraulic properties. *Water Resources Research*, **14**, 601–604.

Collins, W. D., J. M. Lee-Taylor, D. P. Edwards, and G. L. Francis, 2006: Effects of increased near-infrared absorption by water vapor on the climate system. *Journal of Geophysical Research*, **111**, D18 109.

Davies, H. and R. Turner, 1977: Updating prediction models by dynamical relaxation: An examination of the technique. *Quarterly Journal of the Royal Meteorological Society*, **103**, 225–245.

Deardorff, J. W., 1978: Efficient prediction of ground surface temperature and moisture, with inclusion of a layer of vegetation. *Journal of Geophysical Research*, **83**, 1889–1904.

Delire, C. and J. A. Foley, 1999: Evaluating the performance of a land surface ecosystem model with biophysical measurements from contrasting environments. *Journal of Geophysical Research*, **104**, 16,895–16,909.

Delire, C., S. Levis, G. Bonan, J. A. Foley, M. T. Coe, and S. Vavrus, 2002: Comparison of the climate simulated by the CCM3 coupled to two different land-surface models. *Climate Dynamics*, **19**, 657–669.

Delworth, T. L., R. J. Stouffer, K. W. Dixon, M. J. Spelman, T. R. Knutson, A. J. Broccoli, P. J. Kushner, and R. T. Wetherald, 2002: Review of simulations of climate variability and change with the GFDL R30 coupled climate model. *Climate Dynamics*, **19**, 555–574.

Dickinson, R., R. Errico, F. Giorgi, and G. Bates, 1989: A regional climate model for the western United States. *Climate Change*, **15**, 383–422.

Dickinson, R., A. Henderson-Sellers, and P. Kennedy, 1993: Biosphere Atmosphere Transfer Scheme (BATS) version 1E as coupled to the NCAR Community Climate Model. Technical Note TN-387+STR, National Center for Atmospheric Research.

Dickinson, R. E. and A. H. Sellers, 1988: Modelling tropical deforestation: A study of GCM land-surface parametrizations. *Quarterly Journal of the Royal Meteorological Society*, **114**, 439–462.

Easterling, D. R., G. A. Meehl, C. Parmesan, S. A. Chagnon, T. R. Karl, and L. O. Mearns, 2000: Climate extremes: Obervations, modeling, and impacts. *Science*, **289**, 2068–2074.

Eltahir, E. A. B. and R. L. Bras, 1994: Sensitivity of regional climate to deforestation in the Amazon Basin. *Quarterly Journal of the Royal Meteorological Society*, **17**, 101–115.

Emanuel, K. A., 1991: A scheme for representing cumulus convection in large-scale models. *Quarterly Journal of the Royal Meteorological Society*, **48**, 2313–2329.

Falge, E., M. Aubinet, P. Bakwin, D. Baldocchi, P. Berbigier, C. Bernhofer, A. Black, R. Ceulemans, A. Dolman, A. Goldstein, M. Goulden, A. Granier, D. Hollinger, P. Jarvis, N. Jensen, K. Pilegaard, G. Katul, K. T. Paw, B. Law, A. Lindroth, D. Loustau, Y. Mahli, R. Monson, P. Moncrieff, E. Moors, W. Munger, T. Meyers, W. Oechel, E. Schulze, H. Thorgeirsson, J. Tenhunen, R. Valentini, S. Verma, T. Vesala, and S. Wofsy, 2005:

FLUXNET Marconi Conference Gap-Filled Flux and Meteorology Data, 1992-2000. online, URL `http://www.daac.ornl.gov`.

Farquhar, G. D. and T. D. Sharkey, 1982: Stomatal conductance and photosynthesis. *Annual Review of Plant Physiology*, **33**, 317–345.

Farquhar, G. D., S. von Caemmerer, and J. A. Berry, 1980: A biogeochemical model of photosynthetic CO_2 assimilation in leaves of C_3 species. *Planta*, **149**, 78–90.

Federer, C. A., 1979: A soil-plant-atmosphere model for transpiration and availability of soil water. *Water Resources Research*, **15**, 555–562.

Fischer, E. M., S. I. Seneviratne, D. Lüthi, and C. Schär, 2007a: Contribution of land-atmosphere coupling to recent European summer heat waves. *Geophysical Research Letters*, **34**, L06 707.

Fischer, E. M., S. I. Seneviratne, P. L. Vidale, D. Lüthi, and C. Schär, 2007b: Soil-moisture-atmosphere interactions during the 2003 European summer heat wave. *Journal of Climate*, **20**, 5081–5099.

Foley, J. A., I. C. Prentice, N. Ramankutty, S. Levis, D. Pollard, S. Sitch, and A. Haxeltine, 1996: An integrated biosphere model of land surface processes, terrestrial carbon balance, and vegetation dynamics. *Global Biogeochemical Cycles*, **10**, 603–628.

Folland, C. K., T. R. Karl, J. R. Christy, R. A. Clarke, G. V. Gruza, J. Jouzel, M. E. Mann, J. Oerlemans, M. J. Salinger, and S.-W. Wang, 2001: *Observed Climate Variability and Change. In: Climate Change 2001: The Scientific Basis. Contribution of Working Group I to the Third Assessment Report of the Intergovernmental Panel on Climate Change*. Cambridge University Press.

Friend, A. D., 1995: PGEN: An integrated model of leaf photosynthesis, transpiration, and conductance. *Ecological Modelling*, **77**, 233–255.

Fritsch, J. M. and C. F. Chappell, 1980: Numerical prediction of convectively driven mesoscale pressure systems. Part I: Convective parameterizations. *Journal of Atmospheric Sciences*, **37**, 1722–1733.

Giorgi, F., 1990: Simulation of regional climate using a limited area model nested in a general circulation model. *Journal of Climate*, **3**, 941–963.

Giorgi, F. and G. Bates, 1989: The climatological skill of a regional model over complex terrain. *Monthly Weather Review*, **117**, 2325–2347.

Giorgi, F., N. S. Diffenbaugh, X. J. Gao, E. Coppola, S. K. Dash, O. Frumento, I. Seidou Sanda, S. A. Rauscher, A. Remedio, A. L. Steiner, B. Sylla, and A. Zakey, 2008: The regional climate change hyper-matrix framework. *Eos*, **89**, 445–446.

Global Soil Data Task, International Geosphere-Biosphere Programme, Data and Information System, 2000: Global soil data products CD-ROM. online, URL `http://www.daac.ornl.gov/SOILS.igbp.html`.

Grell, G. A., 1993: Prognostic evaluation of assumptions used by cumulus parameterizations. *Monthly Weather Review*, **121**, 764–787.

Grell, G. A., J. Dudhia, and D. Stauffer, 1994: A description of the fifth-generation Penn State/NCAR Mesoscale Model (MM5). Technical Note TN-398+IA, National Center for Atmospheric Research.

Groisman, P. Y., R. W. Knight, and T. R. Karl, 2001: Heavy precipitation and high streamflow in the contiguous United States: Trends in the twentieth century. *Bulletin of the American Meteorological Society*, **82**, 219–246.

Groisman, P. Y., R. W. Knight, T. R. Karl, D. R. Easterling, B. Sun, and J. H. Lawrimore, 2004: Contemporary changes of the hydrological cycle over the contiguous United States: Trends derived from in situ observations. *Journal of Hydrometeorology*, **5**, 64–85.

Harrison, P., J. Bruinsma, H. de Haen, N. Alexandratos, J. Schmidhuber, G. Bödeker, and M.-G. Ottaviani, 2002: World agriculture: Towards 2015/2030. online, URL `http://www.fao.org/documents/`.

Henderson-Sellers, A., K. McGuffie, and A. J. Pitman, 1996: The project for intercomparison of land-surface parameterization schemes (PILPS): 1992 to 1995. *Climate Dynamics*, **12**, 849–859.

Hillel, D., 1980: *Application of soil physics*. Academic Press, New York.

Hinckley, T. M., J. P. Lassoie, and S. W. Running, 1978: Temporal and spatial variations in the water status for forest trees. *Forest Science Monograph*, **20**, 1–72.

Holtslag, A. A. M., E. I. F. de Bruijn, and H. L. Pan, 1990: A high resolution air mass transformation model for short-range weather forecasting. *Monthly Weather Review*, **118**, 1561–1575.

Jarvis, P. G., 1976: The interpretation of the variations in leaf water potential and stomatal conductance found in canopies in the field. *Philisophical Transactions of the Royal Society of London. Series B, Biological Sciences*, **273**, 593–610.

Kanamitsu, M., W. Ebisuzaki, J. Woollen, S. K. Yang, J. J. Hnilo, M. Fiorino, and G. L. Potter, 2002: NCEP/DOE AMIP-II reanalysis (R-2). *Bulletin of the American Meteorological Society*, **83**, 1631–1643.

Karl, T. R. and R. W. Knight, 1998: Secular trends of preciptiation amount, frequency, and intensity in the United States. *Bulletin of the American Meteorological Society*, **79**, 231–241.

Karl, T. R., J. M. Melillo, and T. C. Peterson, (Eds.) , 2009: *Global Climate Change Impacts in the United States*. Cambridge University Press.

Kiehl, J., J. Hack, G. Bonan, B. Boville, B. Breigleb, D. Williamson, and P. J. Rasch, 1996: Description of the NCAR Community Climate Model (CCM3). Technical Note TN-420+STR, National Center for Atmospheric Research.

Kucharik, C. J. and K. R. Brye, 2003: Integrated BIosphere Simulator (IBIS) yield and nitrate loss predictions for Wisconsin maize receiving varied amounts of nitrogen fertilizer. *Journal of Environmental Quality*, **32**, 247–268.

Kucharik, C. J., J. A. Foley, C. Delire, V. A. Fisher, M. T. Coe, J. D. Lenters, C. Young-Molling, N. Ramankutty, J. M. Norman, and S. T. Gower, 2000: Testing the performance of a dynamic global ecosystem model: Water balance, carbon balance, and vegetation structure. *Global Biogeochemical Cycles*, **14**, 795–826.

Kunkel, K. E., K. Andsager, and D. R. Easterling, 1999: Long-term trends in extreme precipitation events over the conterminous United States and Canada. *Journal of Climate*, **12**, 2515–2527.

Leung, R. L., L. O. Mearns, F. Giorgi, and R. Wilby, 2003: Workshop on regional climate research: Need and opportunities. *Bulletin of the American Meteorological Society*, **84**, 89–95.

Leuning, R., 1995: A critical appraisal of a combined stomatal-photosynthesis model for C_3 plants. *Plant, Cell and Environment*, **18**, 339–355.

Lloyd, J., 1991: Modeling stomatal responses to environment in *Macadamia integrifolia*. *Australian Journal Plant Physiology*, **18**, 649–660.

Lloyd, J. and G. D. Farquhar, 1994: ^{13}C discrimination during CO_2 assimilation by the terrestrial biosphere. *Oecologia*, **99**, 201–215.

Manabe, S., 1969: Climate and the ocean circulation: The atmospheric circulation and the hydrology of the Earth's surface. *Monthly Weather Review*, **97**, 739–774.

Manabe, S., R. T. Weatherald, and R. J. Stouffer, 1981: Summer dryness due to an increase of atmospheric CO_2 concentration. *Climate Change*, **3**, 347–386.

Manabe, S. and R. T. Wetherald, 2002: Simulation of hydrologic changes associated with global warming. *Journal of Geophysical Research*, **107**, 4379.

Manabe, S., R. T. Wetherald, P. C. D. Milly, T. L. Delworth, and R. J. Stouffer, 2004: Century-scale changes in water availability: CO_2 quadrupling experiment. *Climate Change*, **64**, 59–76.

Marcella, M. P. and E. A. B. Eltahir, 2008: Modeling the hydroclimatology of Kuwait: The importance of subcould layer evaporation in semiarid climates. *Journal of Climate*, **12**, 2976–2989.

Massman, W. J., 1980: Water storage on forest foliage: A general model. *Water Resources Research*, **16**, 210–216.

Maykut, G. A. and N. Untersteiner, 1971: Some results from a time-dependent thermodynamic model of sea ice. *Journal of Geophysical Research*, **76**, 1550–1576.

Meehl, G. A. and W. M. Washington, 1988: A comparison of soil-moisture sensitivity in two global climate models. *Journal of Atmospheric Sciences*, **45**, 1476–1492.

Mitchell, T. D., T. R. Carter, P. D. Jones, M. Hulme, and M. New, 2004: A comprehensive set of high resolution grids of monthly climate for Europe and the globe: The observed record (1901-2000) and 16 scenarios (2001-2100). Tyndall Working Paper 55, URL `http://www.cru.uea.ac.uk/`.

Molz, F. J., 1981: Model of water transport in the soil-plant system: A review. *Water Resources Research*, **17**, 1245–1260.

Monteith, J. L., 1976: *Vegetation and the Atmosphere*, Vol. 1-2. Academic Press.

Nakicenovic, N., J. Alcamo, G. Davis, B. de Vries, J. Fenhann, S. Gaffin, K. Gregory, A. Grübler, T. Y. Jung, T. Kram, E. L. La Rovere, L. Michaelis, S. Mori, T. Morita, W. Pepper, H. Pitcher, L. Price, K. Raihi, A. Roehrl, H.-H. Rogner, A. Sankovski, M. Schlesinger, P. Shukla, S. Smith, R. Swart, S. van Rooijen, N. Victor, and Z. Dadi, 2000: *IPCC Special Report on Emissions Scenarios*. Cambridge University Press.

NASA, 2006: Surface Radiation Budget. online, URL `http://eosweb.larc.nasa.gov`.

New, M., M. Hulme, and P. D. Jones, 1999: Representing twentieth century space-time climate variablility. Part 1: Development of a 1961-90 mean monthly terrestrial climatology. *Journal of Climate*, **12**, 829–856.

New, M., D. Lister, M. Hulme, and I. Makin, 2002: A high-resolution data set of surface climate over global land areas. *Climate Research*, **21**, 1–25.

Niemann, J. D. and E. A. B. Eltahir, 2005: Sensitivity of regional hydrology to climate changes, with applicaiton to the Illinois River basin. *Water Resources Research*, **41**, W07 014.

Norman, J. M., 1993: Scaling processes between leaf and canopy levels. *Scaling Physiological Processes: Leaf to Globe*, Academic Press, San Diego, CA, 41–76.

Pal, J. S., 1997: The role of soil moisture conditions in the occurrence of floods and droughts over the Mississippi Basin. Master's thesis, Massachusetts Institute of Technology.

———, 2001: Modeling the role of soil moisture in North American summer climate. Ph.D. thesis, Massachusetts Institute of Technology.

Pal, J. S., F. Giorgi, and X. Bi, 2004: Consistency of recent European summer precipitation trends and extremes with future regional climate projections. *Geophysical Research Letters*, **31**, L13 202.

Pal, J. S., F. Giorgi, X. Bi, N. Elguindi, F. Solmon, X. Gao, S. A. Rauscher, R. Francisco, A. Zakey, J. Winter, M. Ashfaq, F. S. Syed, J. L. Bell, N. S. Diffenbaugh, J. Karmacharya, A. Konaré, D. Martinez, R. P. Da Rocha, L. C. Sloan, and A. L. Steiner, 2007: Regional climate modeling for the developing world: The ICTP RegCM3 and RegCNET. *Bulletin of the American Meteorological Society*, **88**, 1395–1409.

Pal, J. S., E. E. Small, and E. A. B. Eltahir, 2000: Simulation of regional-scale water and energy budgets: Representation of subgrid cloud and precipitation processes within RegCM. *Journal of Geophysical Research*, **105**, 29 579–29 594.

Pitman, A. J. and A. Henderson-Sellers, 1998: Recent progress and results from the project for the intercomparison of landsurface parameterization schemes. *Journal of Hydrology*, **212**, 128–135.

Pollard, D. and S. L. Thompson, 1995: Use of a land-surface-transfer scheme (LSX) in a global climate model (GENESIS): The response to doubling stomatal resistance. *Global and Planetary Change*, **10**, 129–161.

Ramankutty, N., 1999: Estimating historical changes in land cover: North American croplands from 1850 to 1992. *Global Ecology & Biogeography*, **8**, 381–396.

Randall, D. A., R. A. Wood, S. Bony, R. Colman, T. Fichefet, J. Fyfe, V. Kattsov, A. Pitman, J. Shukla, J. Srinivasan, R. J. Stouffer, A. Sumi, and K. E. Taylor, 2007: *Climate Models and Their Evaluation. In: Climate Change 2007: The Physical Science Basis. Contribution of Working Group I to the Fourth Assessment Report of the Intergovernmental Panel on Climate Change*. Cambridge University Press.

Reynolds, R. W., N. A. Rayner, T. M. Smith, D. C. Stokes, and W. Wang, 2002: An improved in situ and satellite SST analysis for climate. *Journal of Climate*, **15**, 1609–1625.

Roeckner, E., G. Bäuml, L. Bonaventura, R. Brokopf, M. Esch, M. Giorgetta, S. Hagemann, I. Kirchner, L. Kornblueh, E. Manzini, A. Rhodin, U. Schlese, U. Schulzweida, and A. Tompkins, 2003: The atmospheric general circulation model ECHAM5. Part I: Model description. Tech. rep., Max-Plank Institute for Meteorology.

Roeckner, E., M. Lautenschlager, and M. Esch, 2006a: IPCC-AR4 MPI-ECHAM5_T63L31 MPI-OM_GR1.5L40 20C3M run no.3: Atmosphere monthly mean values MPImet/MaD Germany. Tech. rep., World Data Center for Climate.

Roeckner, E., M. Lautenschlager, and H. Schneider, 2006b: IPCC-AR4 MPI-ECHAM5_T63L31 MPI-OM_GR1.5L40 SRESA1B run no.3: Atmosphere monthly mean values MPImet/MaD Germany. Tech. rep., World Data Center for Climate.

Rosenzweig, C., A. Iglesias, X. B. Yang, P. R. Epstein, and E. Chivian, 2001: Climate change and extreme weather events: Implications for food production, plant diseases, and pests. *Global Change and Human Health*, **2**, 90–104.

Rosenzweig, C., F. N. Tubiello, R. Goldberg, E. Mills, and J. Bloomfield, 2002: Increased

crop damage in the US from excess precipitation under climate change. *Global Environmental Change*, **12**, 197–202.

Rossow, W. B. and R. A. Schiffer, 1991: ISCCP cloud data products. *Bulletin of the American Meteorological Society*, **72**, 2–20.

Rothman, L. S., A. Goldman, J. R. Gillis, R. R. Gamache, H. M. Pickett, R. L. Poytner, N. Husson, and A. Chedin, 1983: Air Force Geophysical Laboratory trace gas compilation - 1982 version. *Applied Optics*, **22**, 1616–1627.

Schär, C., C. Frei, D. Lüthi, and H. Davies, 1996: Surrogate climate-change scenarios for regional climate models. *Geophysical Research Letters*, **23**, 669–672.

Schlenker, W. and M. J. Roberts, 2009: Nonlinear temperature effects indicate severe damages to U.S. crop yields under climate change. *Proceedings of the National Academy of Sciences*, **106**, 15,594–15,598.

Semtner Jr., A. J., 1976: A model for the thermodynamic growth of sea ice in numerical investigations of climate. *Journal of Physical Oceanography*, **6**, 379–389.

Seneviratne, S. I., J. S. Pal, E. A. B. Eltahir, and C. Schär, 2002: Summer dryness in a warmer climate: A process study with a regional climate model. *Climate Dynamics*, **20**, 69–85.

Shuttleworth, W., 1979: Evaporation. Tech. Rep. 56, Institute of Hydrology.

Small, D. and S. Islam, 2009: A synoptic view of trends and decadal variations in autumn precipitation across the United States from 1948 to 2004. *Journal of Geophysical Research*, **114**, D10 102.

Steiner, A. L., J. S. Pal, S. A. Rauscher, J. L. Bell, N. S. Diffenbaugh, A. Boone, L. C. Sloan, and F. Giorgi, 2009: Land surface coupling in regional climate model simulations of the West African monsoon. *Climate Dynamics*, **33**, 869–892.

Thom, A. S. and H. R. Oliver, 1977: On Penman's equation for estimating regional evaporation. *Quarterly Journal of the Royal Meteorological Society*, **103**, 345–357.

Thompson, S. L. and D. Pollard, 1995a: A global climate model (GENESIS) with a Land-Surface Transfer Scheme (LSX). Part I: Present climate simulation. *Journal of Climate*, **8**, 732–761.

———, 1995b: A global climate model (GENESIS) with a Land-Surface Transfer Scheme (LSX). Part II: CO_2 sensitivity. *Journal of Climate*, **8**, 1104–1121.

Twine, T. E., W. P. Kustas, J. M. Norman, D. R. Cook, P. R. Houser, T. P. Meyers, J. H. Prueger, P. J. Starks, and M. L. Wesely, 2000: Correcting eddy-covariance flux underestimates over a grassland. *Agricultural and Forest Meteorology*, **103**, 279–300.

Uppala, S. M., P. W. KÅllberg, A. J. Simmons, U. Andrae, V. D. C. Bechtold, M. Fiorino, J. K. Gibson, J. Haseler, A. Hernandez, G. A. Kelly, X. Li, K. Onogi, S. Saarinen, N. Sokka, R. P. Allan, E. Andersson, K. Arpe, M. A. Balmaseda, A. C. M. Beljaars, L. V. D. Berg, J. Bidlot, N. Bormann, S. Caires, F. Chevallier, A. Dethof, M. Dragosavac, M. Fisher, M. Fuentes, S. Hagemann, E. Hólm, B. J. Hoskins, L. Isaksen, P. A. E. M. Janssen, R. Jenne, A. P. McNally, J.-F. Mahfouf, J.-J. Morcrette, N. A. Rayner, R. W. Saunders, P. Simon, A. Sterl, K. E. Trenberth, A. Untch, D. Vasiljevic, P. Viterbo, and J. Woollen, 2005: The ERA-40 re-analysis. *Quarterly Journal of the Royal Meteorological Society*, **131**, 2961–3012.

USGS, 1996: Global 30-Arc Second Elevation Dataset (GTOPO30). online, URL `http://edc.usgs.gov/products/elevation/gtopo30/gtopo30.html`.

———, 1997: Global Land Cover Characterization. online, URL `http://edcsns17.cr.usgs.gov/glcc/`.

Wang, G., 2005: Agricultural drought in a future climate: Results from 15 global climate models participating the the 4^{th} assessment. *Climate Dynamics*, **25**, 739–753.

Winter, J. M., 2006: Coupling of Integrated Biosphere Simulator to Regional Climate Model version 3. Master's thesis, Massachusetts Institute of Technology.

Winter, J. M., J. S. Pal, and E. A. B. Eltahir, 2009: Coupling of Integrated Biosphere Simulator to Regional Climate Model Version 3. *Journal of Climate*, **22**, 2743–2757.

Wuebbles, D. J. and K. Hayhoe, 2004: Climate chance projections for the United States Midwest. *Mitigation and Adaptation Strategies for Global Change*, **9**, 335–363.

Yeh, P. J.-F., 2003: Representation of water table dynamics in a land surface scheme: Observations, models, and analyses. Ph.D. thesis, Massachusetts Institute of Technology.

Yeh, P. J.-F., M. Irizarry, and E. A. B. Eltahir, 1998: Hydroclimatology of Illinois: A comparison of monthly evaporation estimates based on atmospheric water and soil water balance. *Journal of Geophysical Research*, **103**, 19 823–19 837.

Zeng, X., M. Zhao, and R. E. Dickinson, 1998: Intercomparison of bulk aerodynamic algorithms for the computation of sea surface fluxes using TOGA COARE and TAO data. *Journal of Climate*, **11**, 2628–2644.